Measurement of Tau Polarisation in $Z/\gamma^* \to \tau\tau$ Decays in Proton–Proton Collisions at ATLAS

Dissertation
zur
Erlangung des Doktorgrades (Dr. rer. nat.)
der
Mathematisch-Naturwissenschaftlichen Fakultät
der
Rheinischen Friedrich-Wilhelms-Universität Bonn

von
Benedict Tobias Winter
aus
Bonn

Bonn, Oktober 2018

Dieser Forschungsbericht wurde als Dissertation von der Mathematisch-Naturwissenschaftlichen Fakultät der Universität Bonn angenommen und ist auf dem Hochschulschriftenserver der ULB Bonn `http://nbn-resolving.de/urn:nbn:de:hbz:5n-55461` elektronisch publiziert.

1. Gutachter:	Prof. Dr. Jochen Dingfelder
2. Gutachter:	Prof. Dr. Klaus Desch

Tag der Promotion:	14.06.2019
Erscheinungsjahr:	2019

Abstract

This thesis presents a measurement of the tau polarisation in $Z/\gamma^* \rightarrow \tau\tau$ decays at ATLAS using a dataset of proton–proton collisions recorded at a centre-of-mass energy of $\sqrt{s} = 8\,\text{TeV}$ that amounts to an integrated luminosity of $20.2\,\text{fb}^{-1}$. A signal region enhanced with $Z/\gamma^* \rightarrow \tau\tau$ decays is selected that are followed by one leptonic and one hadronic tau decay. Information about the tau spin states is gained from the hadronic decays. A tau polarisation of $P_\tau = -0.27 \pm 0.02\ \text{(stat)} \pm 0.04\ \text{(syst)}$ is measured in a fiducial region that resembles the signal region and is defined on generator level. An extrapolation to the full phase-space for ditau masses of 66–116 GeV yields $P_\tau = -0.14 \pm 0.02\ \text{(stat)} \pm 0.04\ \text{(syst)}$. The results agree with Standard Model predictions of $P_\tau = -0.270 \pm 0.006$ for the fiducial region and $P_\tau = -0.1536 \pm 0.0014$ for the ditau mass range. An approximate weak mixing angle of $\sin^2 \theta_\text{W}^\text{eff} \approx 0.232 \pm 0.005$ is determined by neglecting the photon contribution and its interference with the dominant Z boson contribution. The measurement complements previous precision ones in electron–positron collisions at the Z boson pole.

Furthermore, an upgraded reconstruction for hadronic tau decays is presented that allows for the determination of decay modes and of the four-momenta of the individual hadrons from these decays. Five decay modes are distinguished, and the classification is accurate for 75% of the hadronic tau decays in $Z/\gamma^* \rightarrow \tau\tau$ events. Particle-flow methods are used to determine the visible tau four-momentum. In comparison with the previous reconstruction, the visible energy resolution is improved by up to a factor of two. The directional resolution is improved by up to a factor of five. Information about the decay modes and reconstructed neutral pions is provided to physics analyses for the first time at ATLAS. A planned measurement of the Higgs boson's CP properties in $H \rightarrow \tau\tau$ decays, for example, relies on this type of information. The simulation reproduces the performance of the upgraded reconstruction in data well.

Contents

CHAPTER 1

Introduction

The launch of the Large Hadron Collider (LHC) at the European Organisation for Nuclear Research (CERN) in 2009 triggered a new era of physics at the energy frontier. The LHC challenges our understanding of fundamental physics at the electroweak scale in an unprecedented manner, and may provide insight into mysteries like the matter–antimatter asymmetry in the universe or the nature of dark matter.

The early LHC particle physics programme has been based on proton–proton collisions at centre-of-mass energies of $\sqrt{s} = 7$, 8, and 13 TeV. The general-purpose experiments ATLAS and CMS each collected datasets corresponding to an integrated luminosity of about $120\,\mathrm{fb}^{-1}$ before 2018. The discovery of a Higgs boson [1, 2], which appears to be consistent with the final elementary particle predicted by the Standard Model of particle physics (SM), highlights the rich harvest of results. The rapidly increasing datasets and continuous refinements of analysis techniques have revolutionised the understanding of SM processes, and bounds on allowed deviations from the SM have tightened severely. The further anticipated improvements may open a window to physics beyond the SM. The centre-of-mass energy will increase to the design value of $\sqrt{s} = 14$ TeV in 2021. The ATLAS and CMS datasets are expected to double by 2023, and a further tenfold increase is expected by around 2040.

Leptons are among the most important signatures for interesting processes at the LHC because they are not present in the initial state at hadron colliders. Muons and electrons can be identified more reliably and reconstructed more accurately than tau leptons. In turn, taus couple much stronger to the Higgs boson providing a unique opportunity to study its Yukawa couplings to leptons [3–6], and one of the best to search for Higgs boson pair production [7, 8]. Limits on allowed contributions from physics beyond the SM are considerably weaker for processes involving third generation fermions, which favours scenarios involving new particles with enhanced couplings to taus. ATLAS has searched for additional Higgs or gauge bosons [9–11], tau sleptons and other sparticles [12–18], leptoquarks [19], for further new particles, and for lepton flavour violation involving taus [20–22]. CMS has presented equally impressive results. Taus also provide access to their spin via their decays, which enables measurements of the tau polarisation or of spin correlations in ditau production processes.

The tau polarisation in $Z/\gamma^* \to \tau\tau$ decays at the Z boson pole was used to precisely measure the weak mixing angle at the Large Electron–Positron Collider (LEP) [23]. The tau spin is more difficult to access in hadron collisions because the backgrounds are much larger and the initial state is known less accurately. The only tau polarisation measurement at a hadron collider prior to this thesis was performed in $W \to \tau\nu$ decays using $24\,\mathrm{pb}^{-1}$ of proton–proton collision data collected by ATLAS [24]. Information about the tau spin may be used to measure the Higgs boson's CP properties in decays to tau pairs [6], and measurements of the tau polarisation in $Z^*/\gamma^* \to \tau\tau$ and $W^* \to \tau\nu$ decays far beyond the Z and W boson poles may soon be feasible at the LHC. Tau spin observables can also be used to select signals that share final states involving taus with a large SM background if the tau helicity configurations differ [10].

This thesis presents a measurement of the tau polarisation in $Z/\gamma^* \to \tau\tau$ decays with ditau masses close to the Z boson pole [25]. It is based on the ATLAS dataset of proton–proton collisions recorded at a centre-of-mass energy of $\sqrt{s} = 8$ TeV, which corresponds to an integrated luminosity of 20.2 fb^{-1}. The tau polarisation is measured in a fiducial region that resembles the selected signal region, and an extrapolation to the full phase space within the mass-selected region 66 GeV $< m_{Z/\gamma^*} <$ 116 GeV is performed. The measured tau polarisation is compared with SM predictions, and the weak mixing angle is estimated by neglecting the photon contribution. New analysis techniques provide a comprehensive understanding of the systematic uncertainties in the modelling of the signal, and estimate the large backgrounds present in ditau final states accurately. The measurements at the LHC and at LEP are complementary because the Z bosons are produced via qqZ and eeZ vertices, respectively.

The ATLAS collaboration's physics programme for final states with tau leptons relies on its ability to reconstruct hadronic tau decays accurately. This thesis presents an extension of their reconstruction that determines the decay mode and the individual four-momenta of the hadrons [26]. The reconstruction of the visible tau four-momentum is improved using particle-flow techniques that combine information about the individual hadrons from complementary detector components. Possible future analyses aiming to access tau spins are expected to benefit significantly from being able to exploit reconstructed tau decay modes and individual hadron four-momenta, which were not provided before at ATLAS. For example, the planned measurement of the Higgs boson's CP properties in $H \to \tau\tau$ decays using observables such as those discussed in Ref. [6] relies on this type of information.

The thesis is structured as follows. The theory is introduced in Chapter 2. The CERN LHC and the ATLAS experiment are described in Chapter 3. Chapter 4 provides techniques for data analysis. Chapter 5 documents the reconstruction of hadronic decay products in tau decays. The measurement of the tau polarisation in $Z/\gamma^* \to \tau\tau$ decays is presented in Chapter 6. Chapter 7 concludes.

CHAPTER 2

Theory

This chapter provides the theoretical background for the works presented in this thesis. The Standard Model is summarised in Section 2.1. Features of high-energy proton–proton collisions are shown in Section 2.2. The chapter closes with a discussion of taus and of the tau polarisation in $Z/\gamma^* \to \tau\tau$ decays.

2.1 The Standard Model

The Standard Model of particle physics (SM) is the state-of-the-art theory of matter and of interactions on the fundamental level. It is a renormalisable Lorentz-invariant quantum field theory that simultaneously describes the electromagnetic, weak, and strong interactions. The electromagnetic and weak interactions are unified. The SM was completed in the 1970's, and has provided impressively reliable predictions for the outcome of numerous measurements. All elementary particles in the SM have been observed, many of which were predicted years before their discovery. There are various reviews and textbooks providing detailed descriptions of the SM. The summary on hand is based on Refs. [27–32]. For clarity and brevity, it is given from today's perspective. Theoretical ideas are shown in a different order than they were developed, and experimental results are considered irrespective of when they became available.

2.1.1 Elementary Fermions

The SM describes elementary matter as excitations of fermion fields with spin $\frac{1}{2}$. Their propagation is described by the Dirac equation. In free space, it reads

$$\left(i\gamma^\mu \partial_\mu - m\right)\psi = 0, \tag{2.1}$$

where m is the fermion mass, γ^μ are the γ-matrices, and the solutions, ψ, are four-component vectors called spinors. Greek-letter indices run over the four space-time components. Repeated indices are contracted following the Einstein summation convention. The spinors can be decomposed into two components each that have positive energy if they propagate forward or backward in time, respectively. The former (latter) are attributed to particles (antiparticles). The two (anti-)particle components can be decomposed into eigenstates of the helicity operator

$$\hat{\lambda} = \frac{\hat{S} \cdot \hat{p}}{|\hat{p}|} \qquad \text{with eigenvalues} \qquad \lambda = \pm\frac{1}{2},$$

Fermion type		1st Generation			2nd Generation			3rd Generation		
		Symbol	Name	Mass	Symbol	Name	Mass	Symbol	Name	Mass
Quark	up-type	u	up	2.2	c	charm	1 275	t	top	173 000
	down-type	d	down	4.7	s	strange	95	b	bottom	4 180
Lepton	neutrino	ν_e	electron n.	0	ν_μ	muon n.	0	ν_τ	tau n.	0
	charged	e	electron	0.511	μ	muon	106	τ	tau	1 777

Table 2.1: Elementary fermions in the SM. The masses are given in MeV. The neutrinos are called electron neutrino, muon neutrino, and tau neutrino, respectively. They are listed with zero mass as predicted by the SM even though they have been experimentally confirmed to have non-zero mass [27]. Each fermion has a corresponding antifermion. Masses taken from [27].

where $\hat{S}$ and $\hat{p}$ are the spin and three-momentum operators, respectively. Intuitively, the helicity quantifies whether a particle's spin is aligned with ($\lambda = +\frac{1}{2}$) or opposite to ($\lambda = -\frac{1}{2}$) its momentum. Helicity states are preserved in free space as time evolves. The helicity states are related to the chiral states, which are the eigenstates of the projection operators $\frac{1}{2}(1-\gamma^5)$ and $\frac{1}{2}(1+\gamma^5)$ with $\gamma^5 = i\gamma^0\gamma^1\gamma^2\gamma^3$. The former (latter) operator selects the left-handed (right-handed) chiral fermion and right-handed (left-handed) antifermion states. The chiral states are invariant under proper Lorentz transformations. The polarisation

$$P = \text{probability}\left(\lambda = +\frac{1}{2}\right) - \text{probability}\left(\lambda = -\frac{1}{2}\right) \tag{2.2}$$

is $-\beta = -\frac{v}{c}$ for left-handed chiral fermions and $+\beta$ for left-handed antifermions. The signs are opposite for the right-handed chiral states. It follows that in the ultra-relativistic limit, $\beta \to 1$, the left-handed (right-handed) chiral fermion state corresponds to the one with negative (positive) helicity, and vice versa for antifermions.

The types (flavours) of elementary fermions are listed in Table 2.1. They appear in three generations that each contain an up-type quark, a down-type quark, a charged lepton, and a neutrino. The assignment into one of these categories and the chiral state determine the charges of an elementary fermion, and consequently how it interacts (see Table 2.2). The quarks carry a colour charge, so they participate in the strong interaction. All fermions except the neutrinos carry a non-vanishing electric charge, Q, and interact electromagnetically. The leptons have integer electric charges, and the quark charges are multiples of $1/3$. The third component of the weak isospin, T_3, and the hypercharge, Y, define how a particle participates in the weak interaction, and they imply the electric charge via

$$Y = 2Q - 2T_3. \tag{2.3}$$

The antifermion charge signs are opposite to the fermion ones shown in Table 2.2.

The fermion fields interact via gauge fields, which are the consequence of local symmetries that are postulated in the SM. The gauge fields give rise to gauge bosons with unit spin that mediate the interactions (see Table 2.3). The principle is shown for the strong interaction and then for the electroweak interaction, which is more complex in this regard. Thereafter, the descriptions of the interactions are combined resulting in the SM.

Fermion type		Colour charge either chirality	Electric charge either chirality	T_3		Hypercharge	
				left	right	left	right
Quark	up-type	red/green/blue	+2/3	+1/2	0	+1/3	+4/3
	down-type		−1/3	−1/2	0	+1/3	−2/3
Lepton	neutrino	none	0	+1/2	non-existent	−1	non-existent
	charged		−1	−1/2	0	−1	−2

Table 2.2: Charges of elementary fermions in the SM. The left-handed and right-handed chiral states are denoted as left and right, respectively. The electric charges are given in units of the negative electron charge. The weak isospin is $T = 1/2$ ($T = 0$) for the left-handed (right-handed) chiral states. The third component of the weak isospin, T_3, is given in the table. Right-handed neutrinos would not interact and do not exist in the SM.

Name	Symbol	Mediates interaction	Multiplicity	Spin	Mass [GeV]	Q	Colour charge
Photon	γ	electromagnetic	1	1	0	0	no
Gluon	g	strong	8	1	0	0	yes
W boson	$W^\pm$	weak (charged current)	2	1	80.4	±1	no
Z boson	Z	weak (neutral current)	1	1	91.2	0	no
Higgs boson	H	none	1	0	125.2	0	no

Table 2.3: Elementary bosons in the SM. The gauge bosons are shown above the line. The gluons carry independent linear combinations of colour and anticolour charges. Masses taken from [27].

2.1.2 The Strong Interaction

The strong interaction is described by Quantum Chromodynamics (QCD). The leptons are omitted in its description because they do not carry a colour charge. The quark fields are written as three-vectors of spinors, $q = (\psi_\mathrm{r}, \psi_\mathrm{g}, \psi_\mathrm{b})^T$, where the indices label the colour charges red, green, and blue. The theory is required to be invariant under local SU(3) transformations in colour space,

$$q \xrightarrow{\mathrm{SU(3)_C}} e^{ig_\mathrm{s}\alpha^\mathrm{a}(x)T^\mathrm{a}} q, \tag{2.4}$$

where g_s is the coupling strength of the strong interaction, T^a are the eight generators of the SU(3) group, and α^a is an eight-component function of the space-time coordinate x. The x-dependence makes the transformation local, the repeated roman indices are summed, and the index "C" in $\mathrm{SU(3)_C}$ specifies that the transformation is in colour space. The generators T^a correspond to halves of the Gell–Mann matrices, and they satisfy the commutator relations

$$[T^\mathrm{a}, T^\mathrm{b}] = T^\mathrm{a}T^\mathrm{b} - T^\mathrm{b}T^\mathrm{a} = if^\mathrm{abc}T^\mathrm{c}, \tag{2.5}$$

where f^abc are the structure constants of the SU(3) group. In particular, the generators T^a do not commute making QCD a non-Abelian theory. The free-space Dirac Eq. (2.1) is made invariant under gauge transformations of the form (2.4) by introducing eight gauge boson fields, G^a_μ, and replacing ∂_μ with the covariant derivative

$$D_\mu = \partial_\mu - ig_\mathrm{s}T^\mathrm{a}G^\mathrm{a}_\mu. \tag{2.6}$$

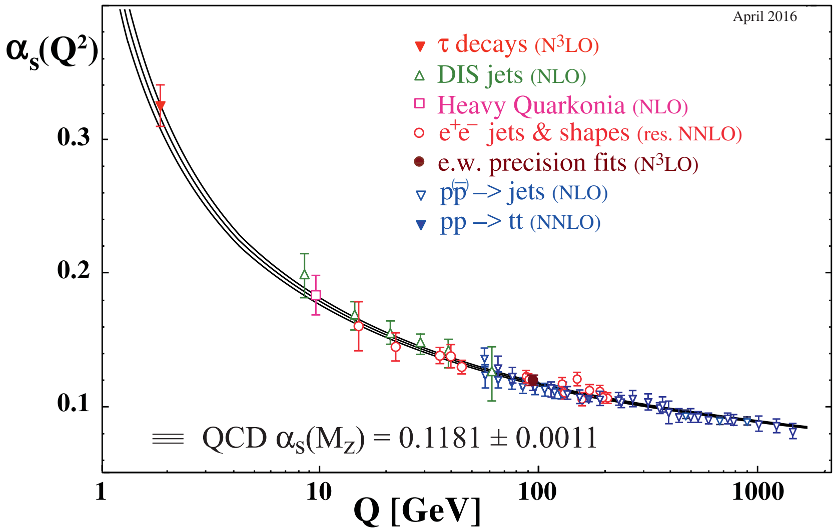

Figure 2.1: Running of α_s as a function of the momentum transfer. Various measured values and a parametrisation are shown. In the parametrisation, the value at the mass of the Z boson (91.2 GeV) is set to the world average, which is also given. Taken from [27].

The excitations of the G_μ^a fields are the gluons (see Table 2.3). The gluon fields transform as follows to ensure gauge invariance:

$$G_\mu^\mathrm{c} \xrightarrow{\mathrm{SU(3)_C}} G_\mu^\mathrm{c} - \partial_\mu \alpha^\mathrm{c} - g_\mathrm{s} f^\mathrm{abc} \alpha^\mathrm{a} G_\mu^\mathrm{b}.$$

The last term is dictated by the commutator relations (2.5), and it leads to interactions among the gluons. The strong interaction is fully described by the Lagrangian density

$$\mathcal{L}_\mathrm{QCD} = \sum_f \overline{q_f} \left(i\gamma^\mu D_\mu - m_f \right) q_f - \frac{1}{4} G^a_{\mu\nu} G^{a\mu\nu}, \tag{2.7}$$

where the sum runs over the quark flavours, $\overline{q_f}$ is the vector containing the adjoint quark spinors, and

$$G^a_{\mu\nu} = \partial_\mu G_\nu^\mathrm{a} - \partial_\nu G_\mu^\mathrm{a} + g_\mathrm{s} f^\mathrm{abc} G_\mu^\mathrm{b} G_\nu^\mathrm{c}.$$

The term $\overline{q_f}(i\gamma^\mu D_\mu - m_f) q_f$ describes the free propagation of quarks as well as their interactions with gluons. The gauge-invariant Dirac equation can be obtained by applying Hamilton's principle to this term. The additional term in Eq. (2.7) describes the propagation of gluons as well as interactions of three or four gluons.

The free parameters of QCD are the six quark masses and g_s. The gluons are massless because they result from an unbroken local gauge symmetry. The g_s parameter is often replaced by the so-called strong coupling constant, $\alpha_\mathrm{s} = g_\mathrm{s}^2/4\pi$. The coupling constant "runs" as a function of the momentum transferred in an interaction, Q (see Figure 2.1). Once specified at a given Q value, α_s can be extrapolated following QCD predictions.

At low Q values, α_s is of order unity as a result of the gluon self-couplings. This makes it impossible to perform perturbative calculations of low-Q interactions, for which methods like lattice QCD are employed instead. The large α_s values have drastic phenomenological consequences as well. QCD forces colour-charged objects to be bound in colour-neutral hadrons, which is referred to as confinement. Hadrons consist of valence quarks that determine its flavour quantum numbers, and of virtual gluons and virtual quark–antiquark pairs that are permanently produced and annihilated. The latter are called sea quarks. Baryons contain three valence quarks, one of each colour. Protons, for example, are baryons with two u and one d valence quarks. Analogously, antibaryons contain three valence antiquarks. Mesons contain one valence quark and one valence antiquark of the corresponding anticolour. The elementary constituents of hadrons are referred to as partons. Coloured objects are less strongly bound ("quasi free") at large momenta. This is referred to as asymptotic freedom.

2.1.3 The Electroweak Interaction

The electroweak force results from the combination of a local SU(2) symmetry in weak isospin space and a U(1) symmetry in hypercharge space. The $\mathrm{SU(2)_L} \times \mathrm{U(1)_Y}$[1] symmetry is spontaneously broken. This makes the mediators of the weak force massive and introduces a scalar boson. A U(1) symmetry in electric-charge space is preserved, and labelled $\mathrm{U(1)_{EM}}$. It leads to the electromagnetic interaction, which is mediated by the massless photon and described by Quantum Electrodynamics (QED).

The left-handed fermion fields are arranged in $\mathrm{SU(2)_L}$ doublets, f_L. One doublet per generation contains the neutrino fields and the left-handed chiral charged-lepton fields. An additional doublet per generation contains the left-handed chiral quark fields.[2] A $\mathrm{SU(2)_L} \times \mathrm{U(1)_Y}$ transformation has the following effect on an $\mathrm{SU(2)_L}$ doublet

$$f_\mathrm{L} \xrightarrow{\mathrm{SU(2)_L \times U(1)_Y}} e^{ig\alpha^\mathrm{a}(x)T^\mathrm{a} + ig'\beta(x)Y/2} f_\mathrm{L},$$

where T^a are the three generators of SU(2), Y generates the U(1) group, α^a is a three-component function, and β is a one-component function. The parameters g and g' are the coupling strengths of $\mathrm{SU(2)_L}$ and $\mathrm{U(1)_Y}$, respectively. The generators T^a correspond to halves of the Pauli matrices, and they satisfy the commutator relations

$$[T^\mathrm{a}, T^\mathrm{b}] = i\epsilon^\mathrm{abc} T^\mathrm{c}, \tag{2.8}$$

where ϵ^abc is the Levi–Civita symbol. The right-handed fields are $\mathrm{SU(2)_L}$ singlets, f_R, and transform like this

$$f_\mathrm{R} \xrightarrow{\mathrm{SU(2)_L \times U(1)_Y}} e^{ig'\beta(x)Y/2} f_\mathrm{R}.$$

Gauge invariance is ensured by replacing ∂_μ with the covariant derivative

$$D_\mu = \partial_\mu - igT^\mathrm{a} W^\mathrm{a}_\mu - ig' \frac{Y}{2} B_\mu, \tag{2.9}$$

where the $igT^\mathrm{a} W^\mathrm{a}_\mu$ term is only relevant for left-handed fermions. The three fields W^a_μ and the field B_μ are

---

[1] The index "L" specifies that the left-handed chiral states, those with $T \neq 0$, are affected by the $\mathrm{SU(2)_L}$ transformations.

[2] The quarks are massless before electroweak symmetry breaking, so the weak eigenstates are mass eigenstates at this point.

introduced to preserve the $\mathrm{SU(2)_L}$ and $\mathrm{U(1)_Y}$ symmetries, respectively. These fields transform as follows

$$W^{\mathrm{c}}_\mu \xrightarrow{\mathrm{SU(2)_L}} W^{\mathrm{c}}_\mu - \partial_\mu \alpha^{\mathrm{c}} - g\epsilon^{\mathrm{abc}}\alpha^{\mathrm{a}} W^{\mathrm{b}}_\mu \qquad W^{\mathrm{c}}_\mu \xrightarrow{\mathrm{U(1)_Y}} W^{\mathrm{c}}_\mu$$
$$B_\mu \xrightarrow{\mathrm{SU(2)_L}} B_\mu \qquad B_\mu \xrightarrow{\mathrm{U(1)_Y}} B_\mu - \partial_\mu \beta.$$

The $\epsilon^{\mathrm{abc}}\alpha^{\mathrm{a}} W^{\mathrm{b}}_\mu$ term results from the non-Abelian nature of the SU(2) group (see Eq. (2.8)), and it introduces interactions among the W^{a}_μ fields.

The resulting Lagrangian density of the electroweak sector before the symmetry breaking is

$$\begin{aligned}\mathcal{L} &= \overline{f_{\mathrm{L}}} i\gamma^\mu D_\mu f_{\mathrm{L}} + \overline{f_{\mathrm{R}}} i\gamma^\mu D_\mu f_{\mathrm{R}} - \frac{1}{4} W^a_{\mu\nu} W^{a\mu\nu} - \frac{1}{4} B_{\mu\nu} B^{\mu\nu} \\ &= \overline{\ell_{\mathrm{L}}} i\gamma^\mu D_\mu \ell_{\mathrm{L}} + \overline{e_{\mathrm{R}}} i\gamma^\mu D_\mu e_{\mathrm{R}} + \overline{q_{\mathrm{L}}} i\gamma^\mu D_\mu q_{\mathrm{L}} + \overline{u_{\mathrm{R}}} i\gamma^\mu D_\mu u_{\mathrm{R}} + \overline{d_{\mathrm{R}}} i\gamma^\mu D_\mu d_{\mathrm{R}} \\ &\quad - \frac{1}{4} W^a_{\mu\nu} W^{a\mu\nu} - \frac{1}{4} B_{\mu\nu} B^{\mu\nu},\end{aligned} \tag{2.10}$$

where in the second row the left-handed lepton (ℓ_{L}) and quark (q_{L}) doublets as well as the right-handed charged lepton (e_{R}), up-type quark (u_{R}), and down-type quark (d_{R}) singlets are shown separately. The field terms are

$$\begin{aligned} W^a_{\mu\nu} &= \partial_\mu W^{\mathrm{a}}_\nu - \partial_\nu W^{\mathrm{a}}_\mu + g\epsilon^{\mathrm{abc}} W^{\mathrm{b}}_\mu W^{\mathrm{c}}_\nu \qquad \text{and} \\ B_{\mu\nu} &= \partial_\mu B_\nu - \partial_\nu B_\mu. \end{aligned} \tag{2.11}$$

The gauge bosons and the fermions in Eq. (2.10) are all massless. Introducing gauge boson mass terms by hand would break the respective gauge symmetries. The theory would become non-renormalisable, i.e. unrecoverable divergencies would make calculations meaningless. Fermion mass terms like those in the QCD Lagrangian (2.7) would break the $\mathrm{SU(2)_L}$ symmetry because the left-handed components of the spinors are members of $\mathrm{SU(2)_L}$ doublets but the right-handed components are not. In the SM, massive gauge bosons and fermions, as observed in nature, are obtained via the Brout–Englert–Higgs (BEH) mechanism. The BEH mechanism is first demonstrated for a simple case.

A scalar field ϕ in a potential $V(\phi) = \mu^2\phi^*\phi - \lambda(\phi^*\phi)^2$ that interacts with a U(1) gauge field, A_μ, is described by the Lagrangian density

$$L = (\partial_\mu - ieA_\mu)\phi^*(\partial^\mu + ieA^\mu)\phi - \mu^2\phi^*\phi - \lambda(\phi^*\phi)^2 - \frac{1}{4} F_{\mu\nu}F^{\mu\nu},$$

where $\partial_\mu - ieA_\mu$ is the covariant derivative, and $F_{\mu\nu}$ takes the same form as $B_{\mu\nu}$ in Eq. (2.11). The Lagrangian is invariant under local gauge transformations

$$\phi \xrightarrow{\mathrm{U(1)}} e^{ie\alpha(x)}\phi \qquad A_\mu \xrightarrow{\mathrm{U(1)}} A_\mu - \partial_\mu\alpha(x).$$

If $\mu^2 > 0$ and $\lambda > 0$, the potential has exactly one minimum at $\phi = 0$, and the Lagrangian simply describes a self-interacting massive scalar in a U(1) gauge field. The interesting case is $\mu^2 < 0$ and $\lambda > 0$. Then the potential has the minima

$$|\phi| = \frac{v}{\sqrt{2}} = \sqrt{\frac{-\mu^2}{2\lambda}} \neq 0. \tag{2.12}$$

The minima correspond to ground states and v is called the vacuum expectation value. The ground states are linked via global U(1) transformations and they are hence equivalent. One ground state is chosen by nature. This breaks the U(1) symmetry because ϕ is no longer symmetric around the ground states.

The physics interactions after the spontaneous symmetry breaking are obtained by analysing small variations from one of the equivalent ground states of the Lagrangian. Performing the expansion around the ground state in which ϕ is real and positive, $\phi = (v + \eta(x))e^{i\zeta(x)/v}/\sqrt{2}$, and moving to the unitary gauge, $A_\mu \to A_\mu - \frac{1}{v}\partial_\mu\zeta(x)$, yields

$$L' = \frac{1}{2}(\partial_\mu\eta)^2 - \lambda v^2\eta^2 + \frac{1}{2}(ev)^2A_\mu^2 - \lambda v\eta^3 - \frac{1}{4}\lambda\eta^4 + \frac{1}{2}e^2A_\mu^2\eta^2 + ve^2A_\mu^2\eta - \frac{1}{4}F_{\mu\nu}F^{\mu\nu}.$$

The term $\frac{1}{2}(ev)^2A_\mu^2$ makes the gauge boson massive as intended ($m_A = ev$). The gauge boson has acquired a longitudinal degree of freedom by becoming massive. For this, the gauge boson has absorbed the $\zeta(x)$ degree of freedom. The η degree of freedom gives rise to a massive Higgs boson. The presence of such a particle is the key prediction of the BEH mechanism.

In the SM, an $\mathrm{SU(2)_L}$ doublet of scalar fields, Φ, is introduced. Its hypercharge is set to $Y_\Phi = 1$, so one of the components is electrically charged and the other is neutral (see Eq. (2.3)). The gauge invariant terms for the scalar field

$$(D_\mu\Phi)^\dagger(D^\mu\Phi) - \mu^2\Phi^\dagger\Phi - \lambda(\Phi^\dagger\Phi)^2$$

are added to the Lagrangian (2.10), and $\mu^2 < 0$ and $\lambda > 0$ are assumed. Only the neutral component of Φ is chosen to acquire a vacuum expectation value. Expanding around the ground state, $\Phi_0 = \frac{1}{\sqrt{2}}(0, v + H(x))^T$ with v as in Eq. (2.12), and moving to the appropriate unitary gauge leads to

$$|D_\mu\Phi|^2 = \frac{1}{2}(\partial_\mu H)^2 + \frac{1}{8}g^2(v+H)^2\left|W_\mu^1 + iW_\mu^2\right|^2 + \frac{1}{8}(v+H)^2\left|gW_\mu^3 - g'B_\mu\right|^2, \tag{2.13}$$

where $|(\ )|^2$ denotes $(\ )^\dagger(\ )$. The combinations

$$W_\mu^\pm = \frac{1}{\sqrt{2}}(W_\mu^1 \mp iW_\mu^2) \qquad Z_\mu = \frac{gW_\mu^3 - g'B_\mu}{\sqrt{g^2 + g'^2}} \qquad A_\mu = \frac{g'W_\mu^3 + gB_\mu}{\sqrt{g^2 + g'^2}} \tag{2.14}$$

correspond to the mediators of the weak interaction and to the photon, respectively (see Table 2.3). The masses are

$$m_W = \frac{1}{2}vg \qquad m_Z = \frac{1}{2}v\sqrt{g^2 + g'^2} \qquad m_A = 0. \tag{2.15}$$

The $\mathrm{U(1)_{EM}}$ symmetry is still present after the symmetry breaking because Φ_0 is electrically neutral. The massless photon confirms this. Three of the four degrees of freedom of Φ are absorbed by the W and Z bosons. The fourth gives rise to a Higgs boson (see Table 2.3). The related terms in the Lagrangian are

$$\frac{1}{2}(\partial_\mu H)^2 - \lambda v^2H^2 - \lambda vH^3 - \frac{\lambda}{4}H^4.$$

The first term, a kinetic term, stems from Eq. (2.13). The second is a mass term with $m_H^2 = 2\lambda v^2$. The last two terms describe self-interactions.

The interaction terms of the elementary fermions and the W^a and B bosons are (see Eqs. (2.9) and (2.10))

$$\sum_f \bar{f}\gamma^\mu\left(-igT^\mathrm{a}W_\mu^\mathrm{a} - ig'\frac{Y}{2}B_\mu\right)f = -igJ^{a\mu}W_\mu^\mathrm{a} - ig'\frac{j^{Y\mu}}{2}B_\mu,$$

where f are the fermion doublet and singlet states, and the currents $J^{a\mu}$ and $j^{Y\mu}$ are introduced. The $W^\pm$ bosons are the $\mathrm{SU(2)_L}$ ladder operators, so they transfer the $T^3 = \pm1/2$ states into each other. They exclusively couple to the left-handed chiral states, which implies that parity is maximally violated in couplings of W bosons to fermions. The neutral-current interactions are expressed using the weak mixing angle, θ_W, with

$$\begin{aligned} A_\mu &= \cos\theta_\mathrm{W} B_\mu + \sin\theta_\mathrm{W} W_\mu^3 \\ Z_\mu &= -\sin\theta_\mathrm{W} B_\mu + \cos\theta_\mathrm{W} W_\mu^3. \end{aligned}$$

Eqs. (2.14) and (2.15) imply

$$\sin\theta_\mathrm{W} = \frac{g'}{\sqrt{g^2+g'^2}} \qquad \cos\theta_\mathrm{W} = \frac{g}{\sqrt{g^2+g'^2}} = \frac{m_W}{m_Z} \qquad \tan\theta_\mathrm{W} = \frac{g'}{g}.$$

The neutral-current interactions are

$$\begin{aligned} -igJ^{3\mu}W_\mu^3 - i\frac{g'}{2}j^{Y\mu}B_\mu &= -i\left(g\sin\theta_\mathrm{W}J^{3\mu} + g'\cos\theta_\mathrm{W}\frac{j^{Y\mu}}{2}\right)A_\mu - i\left(g\cos\theta_\mathrm{W}J^{3\mu} - g'\sin\theta_\mathrm{W}\frac{j^{Y\mu}}{2}\right)Z_\mu \\ &= -iej^{\mathrm{EM}\mu}A_\mu - \frac{ie}{\sin\theta_\mathrm{W}\cos\theta_\mathrm{W}}\left(J^{3\mu} - \sin^2\theta_\mathrm{W}j^{\mathrm{EM}\mu}\right)Z_\mu, \end{aligned}$$

where $j^{\mathrm{EM}\mu} = J^{3\mu} + \frac{1}{2}j^{Y\mu}$ is the electromagnetic current, and $e = g\sin\theta_\mathrm{W}$ is the negative electron charge.

The Z boson current is

$$J^{3\mu} - \sin^2\theta_\mathrm{W}j^{\mathrm{EM}\mu} = \sum_f g_{f\mathrm{L}}\overline{\psi_{f\mathrm{L}}}\gamma^\mu\psi_{f\mathrm{L}} + g_{f\mathrm{R}}\overline{\psi_{f\mathrm{R}}}\gamma^\mu\psi_{f\mathrm{R}},$$

where $\psi_{f\mathrm{L}}$ and $\psi_{f\mathrm{R}}$ are the left- and right-handed chiral states, respectively. The couplings are

$$g_{f\mathrm{L}} = T^3 - \sin^2\theta_\mathrm{W}Q \qquad g_{f\mathrm{R}} = -\sin^2\theta_\mathrm{W}Q.$$

The Z boson couples differently to the left- and right-handed chiral states, and parity is violated. Hence, fermions produced in Z boson decays are polarised. This is elaborated in Section 2.3.2 to provide a foundation for Chapter 6. The photon couplings conserve parity because both chiral states have the same $T^3 + \frac{1}{2}Y = Q$.

The BEH mechanism is also used to make the charged leptons and quarks massive. For this, the Yukawa interaction terms

$$-\lambda_\ell\overline{\ell_\mathrm{L}}\Phi e_\mathrm{R} - \lambda_d\overline{q_\mathrm{L}}\Phi d_\mathrm{R} - \lambda_u\overline{q_\mathrm{L}}\tilde{\Phi}u_\mathrm{R} + \text{h.c.}$$

are added to the Lagrangian, where $\tilde{\Phi} = iT^2\Phi^*$. The mass of a fermion is $m_f = 1/\sqrt{2}\lambda_f v$. The new terms are gauge invariant and keep the SM renormalisable. However, the nine λ_f parameters are not predicted. They must be set to match the fermion masses in Table 2.1.

After introducing the masses, the weak eigenstates of the charged leptons and quarks are linear combinations of the mass eigenstates. Ultimately, only rotations of the left-handed down-type quarks are relevant. They are described by the unitary Cabibbo–Kobayashi–Maskawa (CKM) matrix. Charged-current interactions of quarks are proportional to

$$\begin{pmatrix} u & c & t \end{pmatrix}_\mathrm{L}\gamma_\mu\begin{pmatrix} d' \\ s' \\ b' \end{pmatrix}_\mathrm{L} = \begin{pmatrix} u & c & t \end{pmatrix}_\mathrm{L}\gamma_\mu V_\mathrm{CKM}\begin{pmatrix} d \\ s \\ b \end{pmatrix}_\mathrm{L} = \begin{pmatrix} u & c & t \end{pmatrix}_\mathrm{L}\gamma_\mu\begin{pmatrix} V_{ud} & V_{us} & V_{ub} \\ V_{cd} & V_{cs} & V_{cb} \\ V_{td} & V_{ts} & V_{tb} \end{pmatrix}\begin{pmatrix} d \\ s \\ b \end{pmatrix}_\mathrm{L}.$$

The off-diagonal elements introduce transitions between the generations. Five of the nine degrees of freedom of a general unitary matrix are effectless quark phases. Three real angles and one imaginary phase are physically relevant. The imaginary phase is the only source of CP violation in the SM. It introduces phenomenological differences between matter and antimatter on the fundamental level. The phenomenological structure of the CKM matrix is captured by the Wolfenstein parametrisation

$$V_{\mathrm{CKM}} = \begin{pmatrix} 1-\lambda^2/2 & \lambda & A\lambda^3(\rho - i\eta) \\ -\lambda & 1-\lambda^2/2 & A\lambda^2 \\ A\lambda^3(1-\rho-i\eta) & -A\lambda^2 & 1 \end{pmatrix} + O(\lambda^4),$$

an expansion in powers of $\lambda = \sin\theta_{\mathrm{C}} \approx 0.22$, where θ_{C} is called the Cabibbo angle. Transitions between the generations are suppressed. The CKM matrix has no effect on neutral-current interactions because

$$\begin{pmatrix} d' & s' & b' \end{pmatrix}_{\mathrm{L}} \gamma_\mu \begin{pmatrix} d' \\ s' \\ b' \end{pmatrix}_{\mathrm{L}} = \begin{pmatrix} d & s & b \end{pmatrix}_{\mathrm{L}} \gamma_\mu V^\dagger_{\mathrm{CKM}} V_{\mathrm{CKM}} \begin{pmatrix} d \\ s \\ b \end{pmatrix}_{\mathrm{L}} .$$

In general, there are no flavour-changing neutral-current interactions in the SM.

2.1.4 The Standard Model Lagrangian

The SM combines the previous descriptions of the electroweak and strong interactions. The quark–gluon interaction term in Eq. (2.6) completes the covariant derivative (2.9). The full SM Lagrangian is

$$\begin{aligned} \mathcal{L}_{\mathrm{SM}} = {} & \overline{f_{\mathrm{L}}} i\gamma^\mu D_\mu f_{\mathrm{L}} + \overline{f_{\mathrm{R}}} i\gamma^\mu D_\mu f_{\mathrm{R}} \\ & - \left(\lambda_\ell \overline{\ell_{\mathrm{L}}} \Phi e_{\mathrm{R}} + \lambda_d \overline{q_{\mathrm{L}}} \Phi d_{\mathrm{R}} + \lambda_u \overline{q_{\mathrm{L}}} \tilde{\Phi} u_{\mathrm{R}} + \text{h.c.}\right) \\ & - \frac{1}{4} W^a_{\mu\nu} W^{a\mu\nu} - \frac{1}{4} B_{\mu\nu} B^{\mu\nu} - \frac{1}{4} G^a_{\mu\nu} G^{a\mu\nu} \\ & + |D_\mu \Phi|^2 - \mu^2 \Phi^\dagger \Phi - \lambda(\Phi^\dagger\Phi)^2 . \end{aligned}$$

Overall, the SM has 18 degrees of freedom:

- the couplings g_{s}, g, and g'. Alternatively, α_{s}, $\alpha_{\mathrm{EM}} = \frac{g^2 \sin^2\theta_{\mathrm{W}}}{4\pi}$, and $G_{\mathrm{F}} = \frac{g^2}{4\sqrt{2} m_W^2}$ are often used,
- the parameters μ and λ of the Higgs potential or, equivalently, v and m_H,
- the nine Yukawa coupling parameters λ_f or, equivalently, the fermion masses,
- the four parameters of the CKM matrix.

2.1.5 Shortcomings of the Standard Model

The SM is extraordinarily successful in describing the experimental data in particle physics experiments. Some properties of nature, however, are inconsistent with SM predictions, so there must be beyond-SM (BSM) physics on the fundamental level. Additionally, the SM has some theoretically unfavourable features, an issue that may be resolved in more complete models. Because it successfully describes particle physics in past and present-day experiments, most BSM models are conceptually extensions of the SM. An in-depth discussion of the shortcomings of the SM and of BSM models is beyond the scope of this thesis. The following implicitly subjective list names some of the main issues, and examples for proposed solutions.

Matter–antimatter asymmetry There are no regions with significant matter–antimatter annihilation observed in the universe, so matter must be much more common in general. CP violation is a necessary condition for such an asymmetry, and the amount of CP violation in the SM is insufficient to account for the observed asymmetry. CP violation is being studied in various experiments.

Neutrino masses Neutrino oscillations [33, 34] imply non-zero neutrino masses contradicting SM predictions. Neutrino masses can be incorporated in the SM. The neutrinos are, however, known to be much lighter than the other fermions ($< 2\,\text{eV}$ in electron-based measurements [27]). A possible explanation is the seesaw mechanism. It predicts additional heavy leptons that are being searched for, for example in Ref. [35].[3]

Dark matter and dark energy Measurements of the cosmic microwave background are accurately described by the Standard Model of cosmology if ~25% of the energy in the universe are attributed to dark matter, and ~70% to dark energy that creates to a non-zero cosmological constant [36]. Rotation curves of galaxies independently suggest the presence of dark matter. Supersymmetry models, axion models, and others provide candidates for dark matter particles while addressing other shortcomings of the SM. Dark matter particles are being searched for at the LHC and elsewhere. Dark energy leads to an accelerated expansion of the universe. Its nature is a mystery.

Hierarchy problem The Higgs boson mass obtains various corrections from so-called loop diagrams. Unless these corrections are fine-tuned, m_H is expected to be of the order of the energy scale up to which the SM is valid. This may be the Planck scale, $m_{\text{Planck}} \approx 10^{19}\,\text{GeV}$ [27]. The amount of fine-tuning necessary can be reduced severely by introducing supersymmetry, a symmetry between elementary fermions and bosons. Supersymmetry models predict a large number of new particles that, in order to solve the hierarchy problem, should not be much heavier than the electroweak scale. They are being searched for at the LHC. The superpartners of particles are collectively referred to as sparticles and, for example, the partner of the tau lepton is called the tau slepton.

Strong CP problem A term of the form $\theta_{\text{QCD}}\epsilon^{\mu\nu\rho\sigma}G^{\text{a}}_{\mu\nu}G^{\text{a}}_{\rho\sigma}$ can be added to the SM Lagrangian without violating gauge invariance. It would lead to CP violation in strong interactions. The parameter $|\theta_{\text{QCD}}|$ is known to be $\lesssim 10^{-10}$ [27] from measurements of the electric dipole moment of the neutron. It is unclear why it is that small. A proposed solution is to introduce a spontaneously broken chiral symmetry. It would give rise to a new pseudoscalar particle, the axion, which is being searched for.

Gravity Gravity is not included in the SM. In interactions of few elementary particles, it is typically expected to be negligible for energies far below m_{Planck}. However, in models with extra dimensions, quantum gravity effects may be observable at the LHC.

2.2 Properties of Proton–Proton Collisions

The relevant hard interactions in high-energy proton–proton collisions take place between one parton per proton. The probability to find a specific type of parton carrying a specific fraction x of the proton momentum is inferred from scale-dependent parton distribution functions (PDF). Examples are shown in Figure 2.2. The initial-state partons may be gluons or (anti-)quarks of any flavour except top.[4] The momenta carried by the initial-state partons, the centre-of-mass energy, and the spin configuration differ and are unknown for a given proton–proton collision. Hence, numerous processes can occur and are

---

[3] I contributed to this result and publication in parallel to working on the analysis presented in this thesis.

[4] The top quark contribution is negligible due to the large top mass.

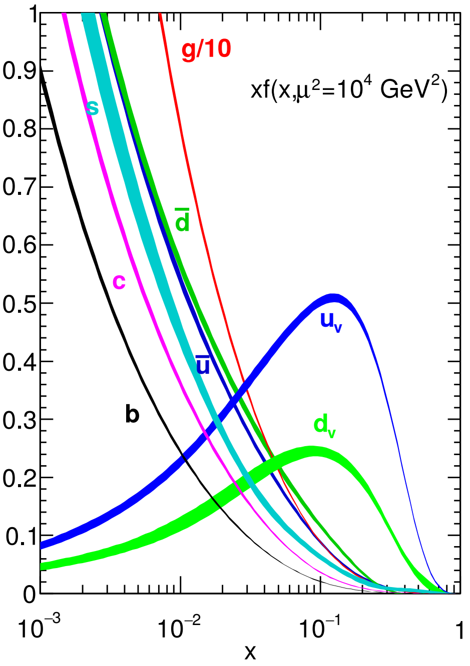

Figure 2.2: Parton distribution functions in the proton. The bands are x times the unpolarised PDF and their uncertainties obtained in the next-to-next-to-leading-order NNPDF3.0 global analysis [37] at a scale $\mu^2 = 10^4$ GeV^2 with $\alpha_\mathrm{s}(m_Z) = 0.118$. The PDF for up ($u_\mathrm{v}$) and down ($u_\mathrm{v}$) valence quarks, for $\overline{u}$, $\overline{d}$, s, c, and b sea (anti-)quarks, and for gluons (g) are shown. The sea quark and antiquark contributions match for each flavour. Taken from [27].

examinable. In turn, the accuracy of measurements may be affected by larger background levels and fewer exploitable kinematic constraints in comparison with electron–positron collisions.

At the LHC, protons collide head-on with equal momenta. The processes studied at different proton-level centre-of-mass energies, $\sqrt{s}$, are summarised in Figure 2.3. The production cross-section is a measure for the probability for a certain process to occur. Inelastic collisions account for about three quarters [38] of the total cross-section (pp in Figure 2.3). The inelastic cross-section is dominated by QCD processes with low Q^2 ($\lesssim 1$ GeV^2), in which partons are extracted from the protons. The extracted partons have small momenta transverse to the initial proton momenta ($p_\mathrm{T} \lesssim 1$ GeV). Multijet events result from QCD processes with (potentially much) larger Q^2 and, consequently, with larger p_T quarks or gluons. The term multijet is explained below. While the multijet cross-section depends on the requested Q^2 to a large extend, QCD processes dominate at any Q^2. They are mostly considered backgrounds because no heavy ($m \gtrsim 20$ GeV) particles are produced. The QCD processes are the dominant contributions in minimum-bias events, which are events recorded with as little trigger bias as possible. The most commonly produced heavy particles are W and Z bosons followed by top quarks. Possible Feynman diagrams are shown in Figure 2.4. Heavy particles are frequently produced in association with one or more high-p_T quarks or gluons like in the shown t-channel diagram. The decays of W and Z bosons are given in Table 2.4. Top quarks decay almost exclusively to a b quark and a W boson. Top quarks and W and Z bosons have lifetimes $< 10^{-24}$ s and unobservable small flight length.

If a parton is extracted from a proton or produced in the decay of a heavy particle, it interacts with the proton-remnants and with other partons produced in the collision. A parton shower is created. It terminates when the partons have hadronised, i.e. when they are bound in hadrons. The four-momentum-sum of the created hadrons is typically close to that of the initial parton, and most of the hadrons fly in

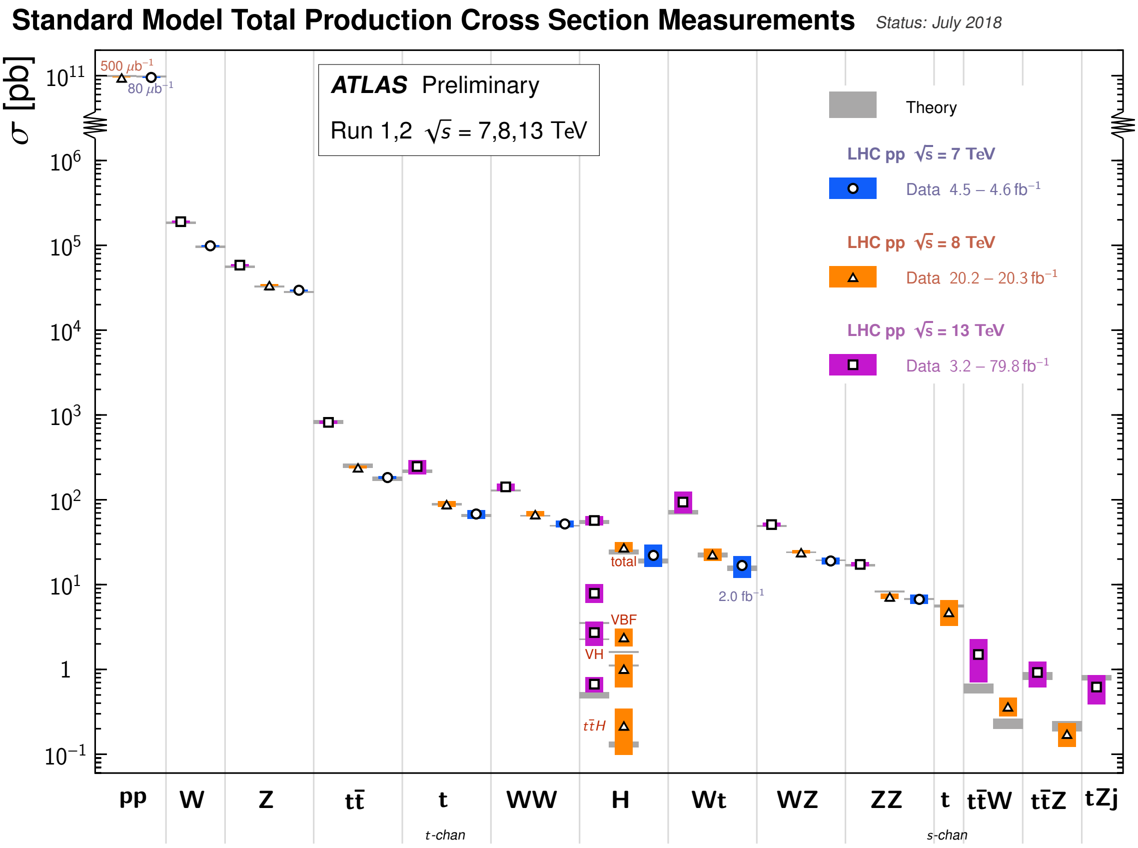

Figure 2.3: Summary of measurements of total production cross-sections at ATLAS. The cross-sections are corrected for leptonic branching fractions, and compared with the corresponding theoretical expectations. Taken from [39].

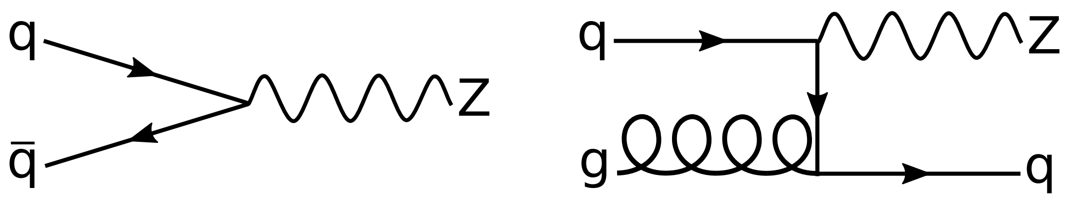

Figure 2.4: Lowest-order s-channel (left) and t-channel (right) Feynman diagrams for Z boson production. Time proceeds from left to right. The symbol q denotes a quark of arbitrary flavour. The initial state partons originate from the colliding protons. W bosons can be produced via analogous diagrams except that the quark flavour changes at the qqW vertex.

W bosons		Z bosons	
Decay	$\mathcal{B}$ [%]	Decay	$\mathcal{B}$ [%]
$W \to \ell_\tau \nu$	10.9	$Z \to \ell_\tau \ell_\tau$	3.37
$W \to qq$	67.4	$Z \to \nu\nu$	20.00
		$Z \to qq$	69.91

Table 2.4: Common decays of W and Z bosons. The branching fraction, $\mathcal{B}$, is the probability for the respective decay to occur. Antiparticles are not specified, and neutrinos are collectively referred to as ν. The branching fractions of decays involving charged leptons, ℓ_τ, are given per flavour. The branching fractions for $Z \to \nu\nu$ decays as well as for decays into quarks are flavour inclusive. Branching fractions taken from [27].

a similar direction. The resulting signature is called a quark- or gluon-initiated jet and very common in proton–proton collisions. Multijet events are named after this signature. Hadrons created in the hadronisation of the proton remnants are collectively referred to as the underlying event.

Many processes of interest at the LHC, such as top quark production and electroweak processes, can result in the production of leptons with transverse momenta of several GeV. The leptons are produced in decays of much heavier particles, such as W or Z bosons, and they are mostly geometrically isolated from other high-p_T particles. Such leptons are rarely produced in multijet events, which makes them valuable signatures for the rare events in which heavy particles are produced. Electrons, muons, and taus can be observed and identified using appropriate particle detectors. Neutrinos, however, are undetectable because they interact extremely rarely. Information about them is inferred as follows. The initial-state partons have $p_\mathrm{T} \lesssim 1\,\mathrm{GeV}$, and, due to momentum conservation, the vectorial p_T-sum of the final state particles is also small. Consequently, the negative p_T-sum of the visible particles, $E_\mathrm{T}^\mathrm{miss}$,[5] corresponds to the p_T-sum of invisible particles. In practice, the $E_\mathrm{T}^\mathrm{miss}$ reconstruction is affected by accumulating acceptance, efficiency, and resolution effects. The component collinear with the proton momenta cannot be used because the initial-state partons carry unknown fractions of the proton momenta.

The number of events expected for a certain process in a dataset collected at a particle collider is the product of the cross-section and the integrated luminosity. The latter is a measure for the size of the dataset. It is given by the time integral of the instantaneous luminosity, $\mathcal{L}$, which is determined by the properties of the collider.

2.3 Taus and Tau Polarisation

2.3.1 Taus and Tau Decays

Taus, the heaviest known leptons ($m = 1.777\,\mathrm{GeV}$), were discovered in 1975 [40]. Taus have a lifetime of 290 ps [27], and they decay via the weak interaction (see Figure 2.5). In the foreseeable future $H \to \tau\tau$ decays [3–5] will offer the best access to the Yukawa couplings of the Higgs boson alongside complementary measurements in ttH events [41, 42]. Furthermore, taus provide unique opportunities to search for BSM physics. Precision measurements set strict limits on deviations from the SM in processes involving leptons.[6] The corresponding limits are considerably weaker for processes involving

---

[5] This common notation may be considered confusing given that $E_\mathrm{T}^\mathrm{miss}$ is an inherently vectorial quantity. It reflects that $E_\mathrm{T}^\mathrm{miss}$ is primarily determined using calorimeters, which measure the energy of particles and their direction (see Section 3.2).

[6] In the following, lepton exclusively refers to electrons or muons unless stated otherwise. Leptons are denoted as ℓ in formulas. Leptons and taus are collectively referred to as ℓ_τ.

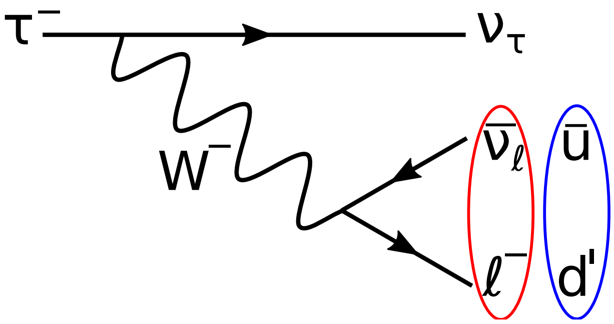

Figure 2.5: Leading-order Feynman diagram for τ^- decays. Time proceeds from left to right. Leptonic decays (red) involve an electron or muon (ℓ^-). Hadronic decays (blue) involve a quark–antiquark pair, which hadronises subsequently. The d' is $\cos\theta_C d + \sin\theta_C s$, where θ_C is the Cabibbo angle.

taus. Various BSM models predict new particles with enhanced couplings to third-generation fermions. Consequently, numerous searches for BSM physics in processes involving taus have been performed. ATLAS, for example, has searched for additional Higgs or gauge bosons [9–11], Higgs boson pair production [7, 8], tau sleptons and other sparticles [12–18], leptoquarks [19], lepton flavour violation [20–22], and more.

Taus must have transverse momenta of several GeV to be observable at the LHC. This is for example necessary for the visible momentum, the share carried by particles other than neutrinos, to be large enough for a candidate to stand out from backgrounds. Most observable taus have flight lengths of a few mm. The innermost sensors are a few cm away from the interaction point, so information about taus is gained from their decay products. For comparison, electrons are stable and muons with momenta $\gtrsim 1$ GeV have flight lengths of several km, so they can effectively be considered stable in high-energy experiments. Leptons have a cleaner experimental signature than taus, which makes them preferable in measurements in which leptons and taus are interchangeable. In turn, the helicity of taus is accessible via their parity-violating decays, which provides access to the Lorentz structure of tau production processes.

Tau decays and their properties providing access to the tau helicity are discussed in the following. The tau decays are assumed to be mediated by W bosons like in the SM. Decays of ultra-relativistic taus are considered. For example, taus emerging from decays of stationary Z bosons have $\beta_\tau = 0.9992$. A related assumption is that the tau decay products are collinear (collinear limit). The helicity states are called left-handed and right-handed referring to the chiral state they match in the ultra-relativistic limit. For example, left-handed fermions (antifermions) have $\lambda = -1/2$ ($\lambda = +1/2$).[7] CP violation is negligible in tau decays, so decays of left-handed τ^- particles and τ^+ antiparticles have the same kinematic properties. This also applies to right-handed τ^- particles and τ^+ antiparticles. Decays of τ^- particles are described explicitly here. Table 2.5 summarises the decay modes. Hadronic decays (τ_had decays) are possible because taus are heavier than the lightest mesons (see Table 2.6). Leptonic decays (τ_lep decays) are rarer than τ_had decays because the quarks appear in three colour states. Decays with kaons are Cabibbo suppressed, and decays with hadron multiplicities above three are phase-space suppressed. Charged pions and kaons are effectively stable and not distinguished in tau decays at ATLAS. Their individual momenta can be determined accurately up to ~100 GeV. Neutral pions have negligible flight lengths, and they decay to photon pairs with a branching fraction of $\mathcal{B} = 99\%$ [27].

---

[7] Left-handed (right-handed) typically means $\lambda = -1/2$ ($\lambda = +1/2$) in the literature. This, however, is inconvenient for this thesis.

Type	Decay topology	Decay	Mostly via resonances	$\mathcal{B}$ [%]
Leptonic		$\tau^- \to e^- \bar{\nu}_e \nu_\tau$		17.82
		$\tau^- \to \mu^- \bar{\nu}_\mu \nu_\tau$		17.39
Hadronic single-prong	$\tau \to h^\pm \nu$	$\tau^- \to \pi^- \nu_\tau$		10.82
		$\tau^- \to K^- \nu_\tau$		0.70
	$\tau \to h^\pm \pi^0 \nu$	$\tau^- \to \pi^- \pi^0 \nu_\tau$	$\rho^- \to \pi^- \pi^0$	25.49
		$\tau^- \to K^- \pi^0 \nu_\tau$	$K^{-*} \to K^- \pi^0$	0.43
	$\tau \to h^\pm \geq 2\pi^0 \nu$	$\tau^- \to \pi^- \pi^0 \pi^0 \nu_\tau$	$a_1^- \to \rho^- \pi^0 \to \pi^- \pi^0 \pi^0$	9.26
		other $\tau^- \to h^- \geq 2\pi^0 \nu_\tau$		1.32
		$\tau^- \to h^- K^0 N \nu_\tau$		0.99
Hadronic three-prong	$\tau \to h^\pm h^+ h^- \nu$	$\tau^- \to \pi^- \pi^+ \pi^- \nu_\tau$	$a_1^- \to \pi^- \rho^0 \to \pi^- \pi^+ \pi^-$	9.02
		other $\tau^- \to h^- h^+ h^- \nu_\tau$		0.44
	$\tau \to h^\pm h^+ h^- \geq 1\pi^0 \nu$	$\tau^- \to h^- h^+ h^- \geq 1\pi^0 \nu_\tau$		5.09

Table 2.5: Common τ^- decay modes. The symbol $h^\pm$ denotes $\pi^\pm$ or $K^\pm$, and N denotes possible additional neutral particles. The decay modes with $\geq 5h^\pm$ combined have a branching fraction of $\mathcal{B} \approx 0.1\%$. The τ^+ decay modes are analogous. The decay topologies categorise τ_{had} decays by their experimental signature. Data taken from [27].

Symbol	Wave function	Spin	m [MeV]	τ [s] or Γ [MeV]
π^+, π^-	$u\bar{d}, \bar{u}d$	0	140	2.6×10^{-8}
π^0	$(d\bar{d} - u\bar{u})/\sqrt{2}$	0	135	8.5×10^{-17}
K^+, K^-	$u\bar{s}, \bar{u}s$	0	494	1.2×10^{-8}
$K^0, \bar{K}^0$	$d\bar{s}, \bar{d}s$	0	498	(see caption)
ρ^+, ρ^-	$u\bar{d}, \bar{u}d$	1	775	149
ρ^0	$(d\bar{d} - u\bar{u})/\sqrt{2}$	1	775	149
K^{+*}, K^{-*}	$u\bar{s}, \bar{u}s$	1	896	46
a_1^+, a_1^-	$u\bar{d}, \bar{u}d$	1	1230	250–600

Table 2.6: Compilation of mesons in τ_{had} decays. The minimum-quark-content part of the wave function and the spin are shown in all cases. The lifetime is given for the mesons that decay via the weak or electromagnetic interaction (above the line). The decay width is given instead for the resonances. Neutral kaons have two states with different lifetimes that mostly agree with the CP eigenstates. Data taken from [27].

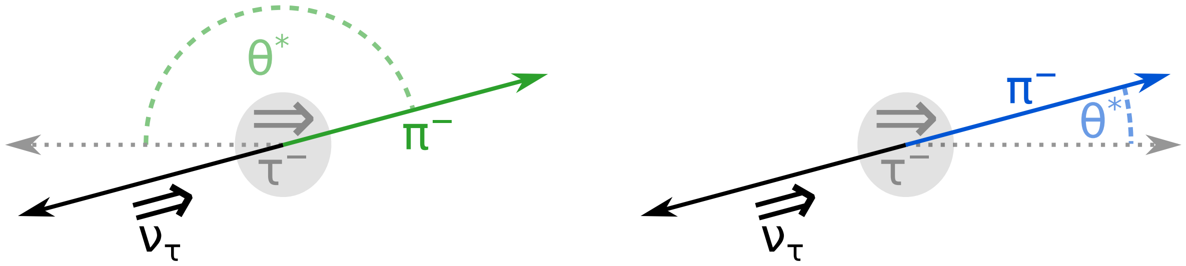

Figure 2.6: Schematic of $\tau^- \to \pi^- \nu_\tau$ decays. Arrows with a single (double) solid line indicate momentum (spin) directions in the tau rest frame. Left-handed (left) and right-handed (right) taus are boosted as indicated by the respective dotted grey arrow. The respective decay angle, θ^*, between the pion momentum in the tau rest frame and the tau momentum in the laboratory frame is indicated by the dashed arcs. Adapted from [44].

The $\tau^- \to \pi^- \nu_\tau$ decays are two-body decays. The tau spin is taken on by the neutrino because the pion is spinless. Information about the tau helicity is preserved because the neutrino is left-handed. The distribution of the decay angle, θ^* (see Figure 2.6), is [43]

$$\frac{\mathrm{d}\Gamma}{\mathrm{d}\cos\theta^*} \propto \frac{1}{2}(1 + \lambda_\tau \cos\theta^*), \tag{2.16}$$

where λ_τ is the τ^- helicity. The pion momentum is preferentially opposite to (aligned with) the boost for left-handed (right-handed) taus, so the pion is typically low (highly) energetic in the laboratory. Information about the tau helicity is accessible via the visible-energy fraction, $x_{\text{vis}} = E^{\tau_{\text{had-vis}}}/E^\tau$, where $E^{\tau_{\text{had-vis}}}$ and E^τ are the visible energy and the tau energy, respectively. The former is the pion energy in $\tau^- \to \pi^- \nu_\tau$ decays. The helicity-dependent distribution in the laboratory frame is [43]

$$\frac{1}{\Gamma}\frac{\mathrm{d}\Gamma}{\mathrm{d}x_{\text{vis}}} = \frac{1}{\beta_\tau(1 - m_\pi^2/m_\tau^2)}\left(1 + \lambda_\tau \frac{2x_{\text{vis}} - 1 - m_\pi^2/m_\tau^2}{\beta_\tau(1 - m_\pi^2/m_\tau^2)}\right) \approx 1 + \lambda_\tau(2x_{\text{vis}} - 1). \tag{2.17}$$

Terms of order m_π^2/m_τ^2 are neglected in the last expression and $\beta_\tau \to 1$ is used. The distribution is shown in Figure 2.7. The $\tau^- \to K^- \nu_\tau$ decays are analogous but m_K^2/m_τ^2 is no longer negligible.

Part of the information encoded in x_{vis} is accessible via $E^{\tau_{\text{had-vis}}}$. The rest is difficult to extract at the LHC. Events with taus involve multiple neutrinos due to lepton flavour conservation. Heavy particles like Z bosons typically have low p_{T}, so the neutrinos eventuating from their decays are back-to-back in the transverse plane. The $E_{\text{T}}^{\text{miss}}$ magnitude is the difference of the neutrino p_{T} magnitudes. The amount of cancellation is unknown. These and other reasons prevent accurate measurements of E^τ, and x_{vis}.

The $\tau^- \to \pi^- \pi^0 \nu_\tau$ decays via the ρ resonance ($\rho^- \to \pi^- \pi^0$) offer access to the tau helicity via x_{vis} and via the charged energy asymmetry observable, Υ, which is experimentally more accessible and introduced in the following. The $\tau^- \to \rho^- \nu_\tau$ decays are more complex than $\tau^- \to \pi^- \nu_\tau$ decays because the rho meson has unit spin. Taking the boost direction as the quantisation axis, the spin state is $(1/2, -1/2)$ and $(1/2, +1/2)$ for left-handed and right-handed τ^- particles, respectively. The rho meson and the neutrino can assume the spin states

- left-handed τ^-: $S_\rho = (1,\ 0)$, $S_\nu = (1/2, -1/2)$; right-handed τ^-: $S_\rho = (1, 0)$, $S_\nu = (1/2, +1/2)$;
- left-handed τ^-: $S_\rho = (1, -1)$, $S_\nu = (1/2, +1/2)$; right-handed τ^-: $S_\rho = (1, 1)$, $S_\nu = (1/2, -1/2)$.

Both options are shown in Figure 2.8. The former is analogous to $\tau^- \to \pi^- \nu_\tau$ decays in terms of the

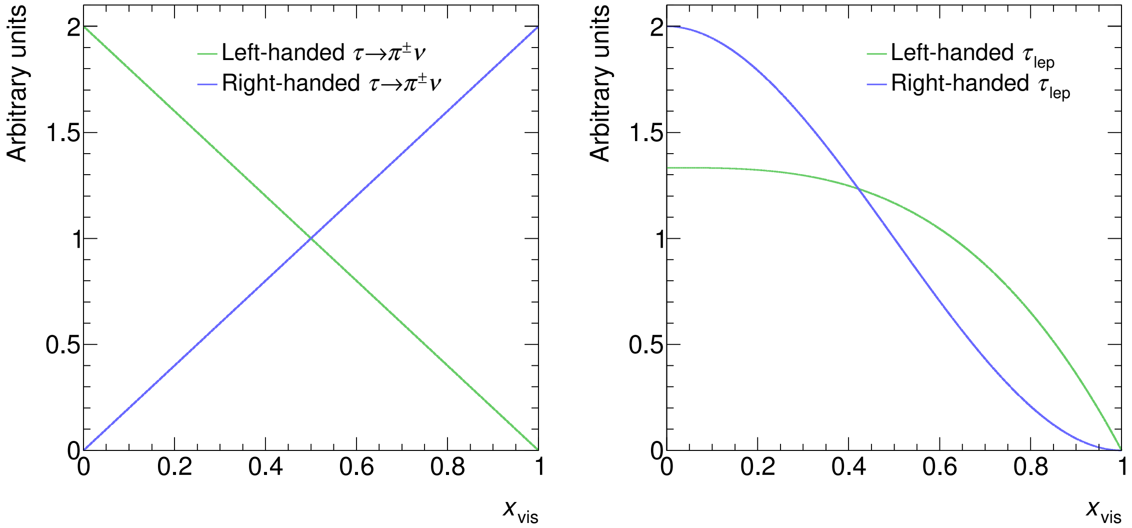

Figure 2.7: Distribution of x_vis in $\tau \to \pi^\pm\nu$ (left) and τ_lep (right) decays.

neutrino spin and the neutrino momentum in the tau rest frame. It features a longitudinal rho meson. The latter features a transverse rho meson, and the neutrino spin and momentum are opposite. The rho decay angle distributions are [43]

$$\begin{aligned} \frac{\mathrm{d}\Gamma}{\mathrm{d}\cos\theta^*} &\propto \frac{m_\tau^2}{2m_\rho^2}(1+\lambda_\tau\cos\theta^*) && \text{longitudinal } \rho \\ \frac{\mathrm{d}\Gamma}{\mathrm{d}\cos\theta^*} &\propto (1-\lambda_\tau\cos\theta^*) && \text{transverse } \rho. \end{aligned} \tag{2.18}$$

The mass-dependent relative factor originates from the helicity amplitudes [43]. The summed distribution is

$$\frac{\mathrm{d}\Gamma}{\mathrm{d}\cos\theta^*} \propto \frac{1}{2}(1+\alpha_\rho\lambda_\tau\cos\theta^*) \qquad \text{with } \alpha_\rho = \frac{m_\tau^2 - 2m_\rho^2}{m_\tau^2 + 2m_\rho^2} = 0.45. \tag{2.19}$$

The given α_ρ value applies to the rho pole mass. Expressions for the x_vis distributions in the laboratory frame are relatively lengthy [43]. Their key features can be read off from Eqs. (2.18) and (2.19). The contributions with longitudinal and transverse rho mesons cancel partially, so the summed x_vis distribution is less helicity dependent than Eq. (2.16). Transverse rho mesons are preferentially highly (low) energetic in decays of left-handed (right-handed) taus. The opposite is true for longitudinal rho mesons.

Information about the rho helicity is accessible via the subsequent $\rho^- \to \pi^-\pi^0$ decay (see Figure 2.8). The rho spin is transformed into angular momentum because the pions are spinless. The distributions of the rho decay angle, ω^*, are [43]

$$\begin{aligned} \frac{\mathrm{d}\Gamma}{\mathrm{d}\cos\omega^*} &\propto \cos^2\omega^* && \text{longitudinal } \rho \\ \frac{\mathrm{d}\Gamma}{\mathrm{d}\cos\omega^*} &\propto \frac{1}{2}\sin^2\omega^* && \text{transverse } \rho. \end{aligned}$$

In the laboratory frame this information is available via the charged energy asymmetry:

$$\Upsilon = \frac{E^{\pi^-} - E^{\pi^0}}{E^{\pi^-} + E^{\pi^0}} = 2\frac{E^{\pi^-}}{E_{\mathrm{T}}^{\tau_{\text{had-vis}}}} - 1. \tag{2.20}$$

The distributions in the collinear limit are [43][8]

$$\begin{aligned} \frac{\mathrm{d}\Gamma}{\mathrm{d}\Upsilon} &\propto \Upsilon^2 && \text{longitudinal } \rho \\ \frac{\mathrm{d}\Gamma}{\mathrm{d}\Upsilon} &\propto \frac{1}{2}(1-\Upsilon^2) - \frac{2m_\pi^2}{m_\rho^2} && \text{transverse } \rho. \end{aligned}$$

Transverse (longitudinal) rho mesons preferentially decay to pions that have similar (significantly different) energy in the laboratory frame. Exemplary Υ distributions are shown in Figure 2.9. They are clearly different between left-handed and right-handed taus.

It is straightforward to generalise Eq. (2.20) to single-prong τ_{had} decays of τ^- particles and τ^+ antiparticles:

$$\Upsilon = 2\frac{E^{h^\pm}}{E^{\tau_{\text{had-vis}}}} - 1 \approx 2\frac{p_{\mathrm{T}}^{h^\pm}}{p_{\mathrm{T}}^{\tau_{\text{had-vis}}}} - 1. \tag{2.21}$$

Energies can be approximated with the corresponding p_{T} values if the taus and their decay products are highly boosted. The Υ observable in this form has been effective in the first tau polarisation measurement at a hadron collider, which studied $W \to \tau\nu$ decays [24]. It is also used in Chapter 6.

The $\tau \to K^\pm\pi^0\nu$ decays via the K^* resonance are similar to $\tau \to \pi^\pm\pi^0\nu$ decays. The $\tau \to \pi^\pm\pi^0\pi^0\nu$ decays proceed via one more step. Information about the tau helicity is encoded in the momenta of the individual pions, and some is encoded in x_{vis}. The Υ observable exploits part of the information. Accurate knowledge about the neutral pion momenta would be needed to extract the rest of it. The $\tau \to \pi^\pm\pi^+\pi^-\nu$ decays are kinematically analogous to $\tau \to \pi^\pm\pi^0\pi^0\nu$ decays but the final state with charged pions is experimentally favourable. Possible observables are discussed in Refs. [23, 43]. The measurement in Chapter 6 utilises single-prong decays, which are more sensitive overall. Future analyses may gain some sensitivity by adding $\tau \to \pi^\pm\pi^+\pi^-\nu$ decays.

The τ_{lep} decays are three-body decays into three left-handed fermions. Different spin configurations are possible. The individual neutrino momenta are unobservable, which reduces the sensitivity to the tau helicity. The laboratory distributions of x_{vis} are [27]

$$\frac{\mathrm{d}\Gamma}{\mathrm{d}x_{\text{vis}}} = \frac{G_{\mathrm{F}}^2 m_\tau^5}{192\pi^3}\left(\frac{5}{3} - 3x_{\text{vis}}^2 + \frac{4}{3}x_{\text{vis}}^3 - \lambda_\tau\left(-\frac{1}{3} + 3x_{\text{vis}}^2 - \frac{8}{3}x_{\text{vis}}^3\right)\right), \tag{2.22}$$

and shown in Figure 2.7. Radiative corrections as well as terms of order m_ℓ^2/m_τ^2 and m_τ^2/E_τ^2 are neglected.

2.3.2 Tau Polarisation in $Z/\gamma^* \to \tau\tau$ Decays

Ditau production at the LHC is dominated by diagrams involving a Z boson or a photon (see Figure 2.10). The Z and γ^* diagrams contribute and interfere. The resulting process is referred to as $Z/\gamma^* \to \tau\tau$. The $Z \to \tau\tau$ component dominates around the Z boson pole, which is the mass range of interest in this thesis.

---

[8] The distributions are given in terms of the energy fraction of one of the pions, E_π/E_ρ, in Ref. [43].

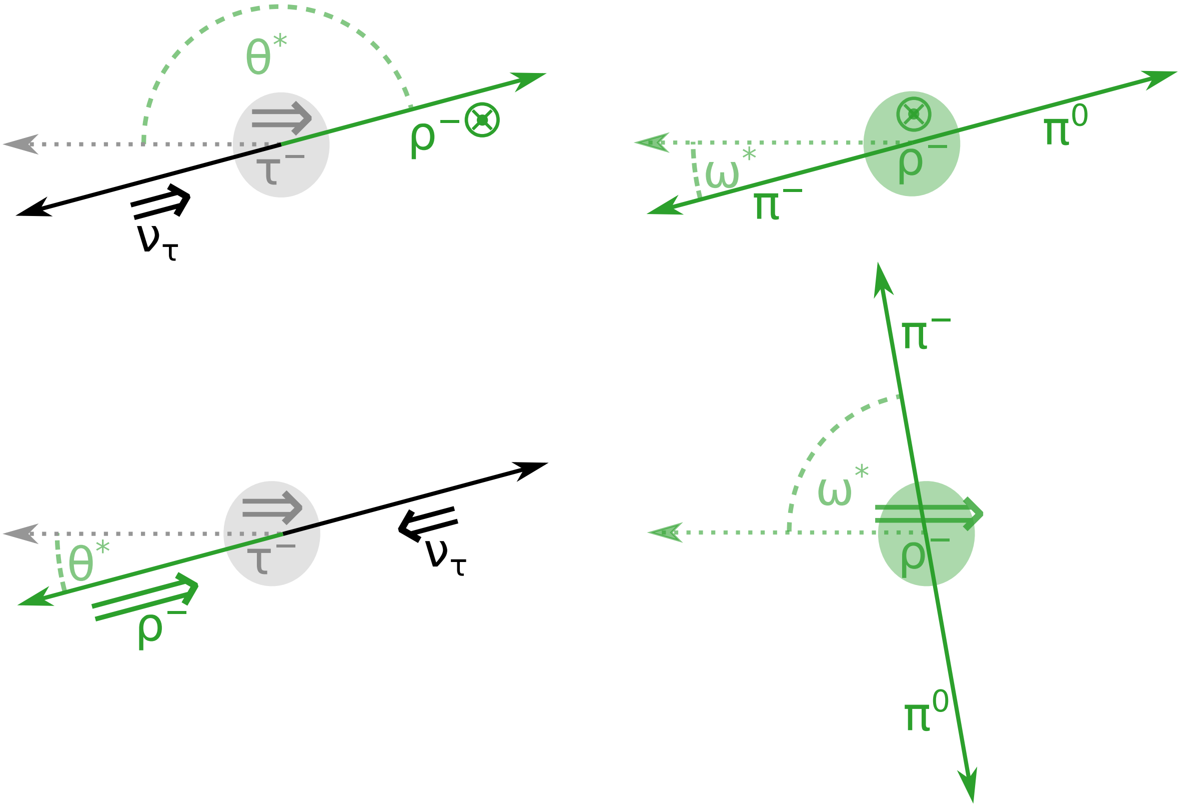

Figure 2.8: Schematic of $\tau^- \to \rho^- \nu_\tau$ decays of left-handed taus in the tau rest frame (left), and of the subsequent rho decays in the rho rest frame (right). The top (bottom) shows decays involving longitudinal (transverse) rho mesons. Arrows with a single (double) solid line indicate momentum (spin) directions in the rest frame of the respective decaying particle. Circles filled by a cross and a dot denote unit spin perpendicular to the drawing plane. Boosts are indicated by dotted arrows. The boost directions of the tau and the rho meson agree in the collinear limit. The tau (rho) decay angles, θ^* (ω^*), are indicated by dashed arcs.

The average tau polarisation in $Z \to \tau\tau$ decays is directly related to the weak mixing angle. The relation is discussed before effects resulting from the presence of the $\gamma^* \to \tau\tau$ diagram are introduced.

Possible spin configurations and the respective relevant couplings in $Z \to \tau\tau$ decays are shown in Figure 2.11. It is convenient to define the vector and axial vector couplings

$$g_{f\mathrm{V}} = g_{f\mathrm{L}} + g_{f\mathrm{R}} = T^3 - 2Q\sin^2\theta_\mathrm{W} \approx -0.04 \qquad g_{f\mathrm{A}} = g_{f\mathrm{L}} - g_{f\mathrm{R}} = T^3 = -0.5.$$

The given numerical values apply to taus (and leptons) for $\sin^2\theta_\mathrm{W} = 0.23$, which is about the measured value. The couplings enter quadratically, so the leading-order coupling asymmetry is

$$A_\tau = P_\mathrm{L} - P_\mathrm{R} = \frac{g_{\tau\mathrm{L}}^2 - g_{\tau\mathrm{R}}^2}{g_{\tau\mathrm{L}}^2 + g_{\tau\mathrm{R}}^2} = \frac{2g_{\tau\mathrm{V}}g_{\tau\mathrm{A}}}{g_{\tau\mathrm{V}}^2 + g_{\tau\mathrm{A}}^2} = \frac{1 - 4\sin^2\theta_\mathrm{W}}{1 + 4\sin^2\theta_\mathrm{W}(2\sin^2\theta_\mathrm{W} - 1)},$$

where P_L and P_R denote the probabilities for decays to the left-handed and right-handed chiral states,

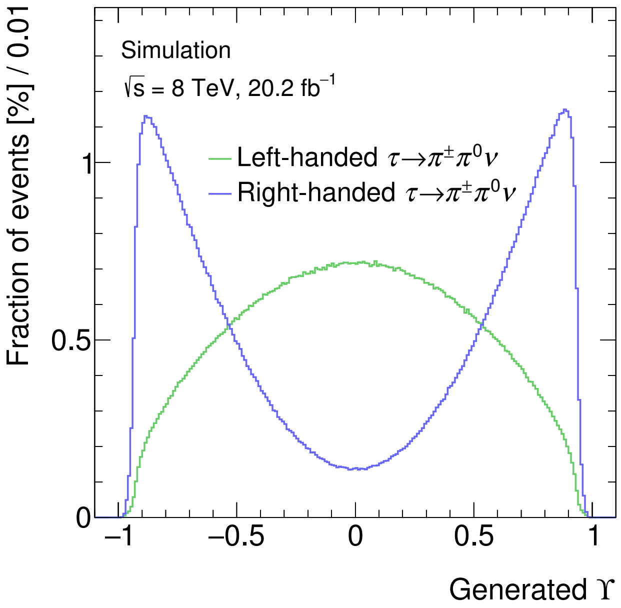

Figure 2.9: Stable-particle level Υ distribution in simulated $\tau \rightarrow \pi^{\pm}\pi^{0}\nu$ decays with $p_{\mathrm{T}}^{\tau_{\text{had-vis}}} > 20\,\text{GeV}$. The distributions are obtained from the nominal simulated sample described in Section 6.1.

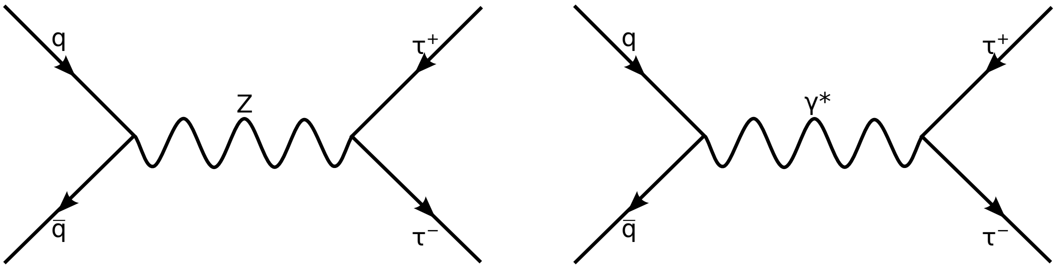

Figure 2.10: Feynman diagrams for ditau production via a Z boson (left) or a photon (right). The star indicates that the photon is far off its mass shell.

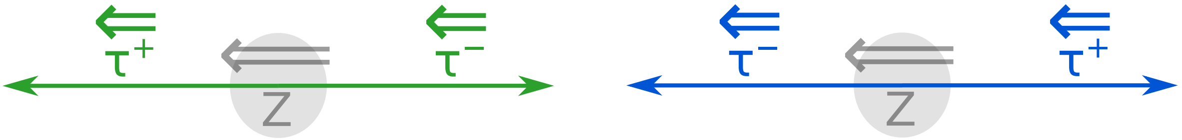

Figure 2.11: Possible spin configurations in $Z \to \tau\tau$ decays shown in the rest frame of the Z boson. The decay into the left-handed chiral states (left) is mediated by the $g_{\tau\mathrm{L}}$ coupling. That into the right-handed chiral states (right) is mediated by the $g_{\tau\mathrm{R}}$ coupling.

respectively. Neglecting $g_{\tau\mathrm{V}}^2$ leads to the simple relation

$$A_\tau = \frac{2g_{\tau\mathrm{V}}}{g_{\tau\mathrm{A}}} = 2 - 8\sin^2\theta_\mathrm{W}. \tag{2.23}$$

Higher-order corrections in the $Z\tau\tau$ coupling are absorbed in the effective weak mixing angle, $\sin^2\theta_\mathrm{W}^\mathrm{eff}$, preserving the form of Eq. (2.23). The current world average is $\sin^2\theta_\mathrm{W}^\mathrm{eff} = 0.23155 \pm 0.00004$ [27].

The polarisation (see Eq. (2.2)) is opposite for τ^- particles and τ^+ antiparticles. The τ^- polarisation is used by convention. It is $P_\tau = -A_\tau$ in the ultra-relativistic limit, so

$$P_\tau = 8\sin^2\theta_\mathrm{W}^\mathrm{eff} - 2 = -0.148. \tag{2.24}$$

Information about τ^+ decays can be considered with opposite helicity sign in a measurement. The measured polarisation can be conveniently expressed as

$$P_\tau = \frac{\sigma_\mathrm{RH} - \sigma_\mathrm{LH}}{\sigma_\mathrm{LH} + \sigma_\mathrm{RH}},$$

where σ is the production cross section and LH (RH) denotes left-handed (right-handed) τ^- particles or τ^+ antiparticles in the sense introduced in the previous section.

Parity is not only violated in the Z boson decay but also in its production. This is apparent in the dependence of the tau polarisation in $Z/\gamma^* \to \tau\tau$ decays in electron–positron collisions on the polar angle, which can be used to measure the asymmetry in the eeZ coupling [23]. In proton–proton collisions the initial quark and antiquark may come from either direction, and the tau polarisation is predicted to be nearly angle independent. The simulated dependency can be found in Figure B.1.

The simulated mass spectrum and the mass dependence of the average tau polarisation in $Z/\gamma^* \to \tau\tau$ decays are shown in Figure 2.12. The $Z \to \tau\tau$ contribution visibly dominates and the expected polarisation is close to that in Eq. (2.24) at the Z boson pole. The mass dependence of the polarisation is caused by the interference of Z and γ^* diagrams. The variation is large over the full mass range shown, but it is approximately constant around the Z boson pole. Hence, the average polarisation in a range around the pole is close to that on the pole. For example it is 0.154 in the range within 25 GeV of the pole ($66\,\mathrm{GeV} < m_{Z/\gamma^*} < 116\,\mathrm{GeV}$).

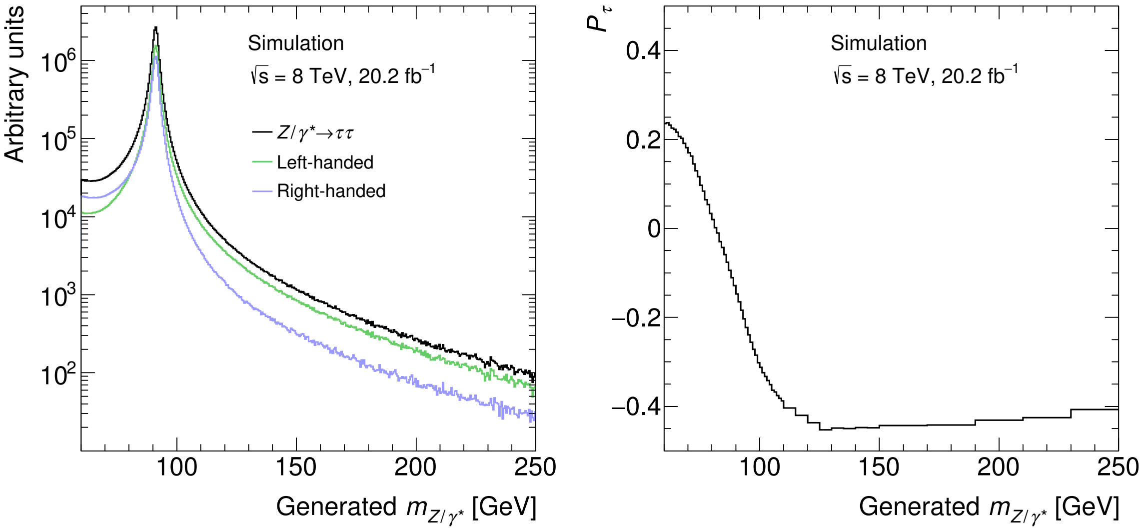

Figure 2.12: Expected m_{Z/γ^*} spectrum (left) and dependency of the tau polarisation on m_{Z/γ^*} (right) in proton–proton collisions. The distributions are taken from the nominal simulated sample described in Section 6.1.

CHAPTER 3

The ATLAS Experiment

The data utilised in this thesis stem from proton–proton collisions recorded by the ATLAS experiment at the Large Hadron Collider (LHC) of the European Organisation for Nuclear Research (CERN). CERN, the LHC, and ATLAS are described in this section.

3.1 CERN and the LHC

CERN was founded in 1954 by twelve Western European countries joining forces to perform world-class fundamental physics research, and is located north-west of Geneva at the French–Swiss border. To date over 600 institutes and universities and half the particle physicists around the world use its facilities [45]. Important scientific achievements include, in chronological order, the observation of antideuteron [46, 47], the invention of the multiwire proportional chamber [48], the direct observation of the weak neutral current [49, 50], the invention of stochastic cooling [51], the discovery of the W [52, 53] and Z [54, 55] bosons, the first production of antihydrogen [56], precision measurements of the electroweak interaction [23],[1] and the discovery of the Higgs boson [1, 2]. The World Wide Web was also invented at CERN [57].

Most research at CERN has been performed with an evolving complex of particle accelerators (see Figure 3.1). The protons collided in the LHC are initially accelerated to an energy of 50 MeV in LINAC 2 [58]. They are further accelerated to 1.4 GeV in the Proton Synchrotron Booster (PSB), to 25 GeV in the Proton Synchrotron (PS), and to 450 GeV in the Super Proton Synchrotron (SPS) before being injected into the LHC. Previous flagship accelerators serve as pre-accelerators for their successors because the accelerators can accept more particles if they are injected at a higher energy. For example, the muon neutrinos used to observe the weak neutral current were produced using a PS beam, and the W and Z bosons were discovered at the SPS. The PSB was specifically built to increase the injection energy of the PS allowing it to accept over 100 times more protons.

The LHC [60] is the largest and most powerful particle accelerator in the world. It is circular, has a circumference of 27 km, and is located 100 m under ground on average in the tunnel that previously housed the Large Electron–Positron Collider (LEP). One particle beam orbits the LHC in each direction. The beams are composed of particles grouped in bunches. They are guided by close to 10 000 magnets including 1 232 superconducting main dipole magnets, which provide magnetic fields of up to 8.3 T that keep the particles on a circular trajectory. The LHC is divided into octands. One octand houses the acceleration system, which consists of eight superconducting radiofrequency cavities for each beam.

---

[1] Cited to represent the many papers produced in this effort by the experiments at the Large Electron–Positron Collider that ran from 1989 to 2000.

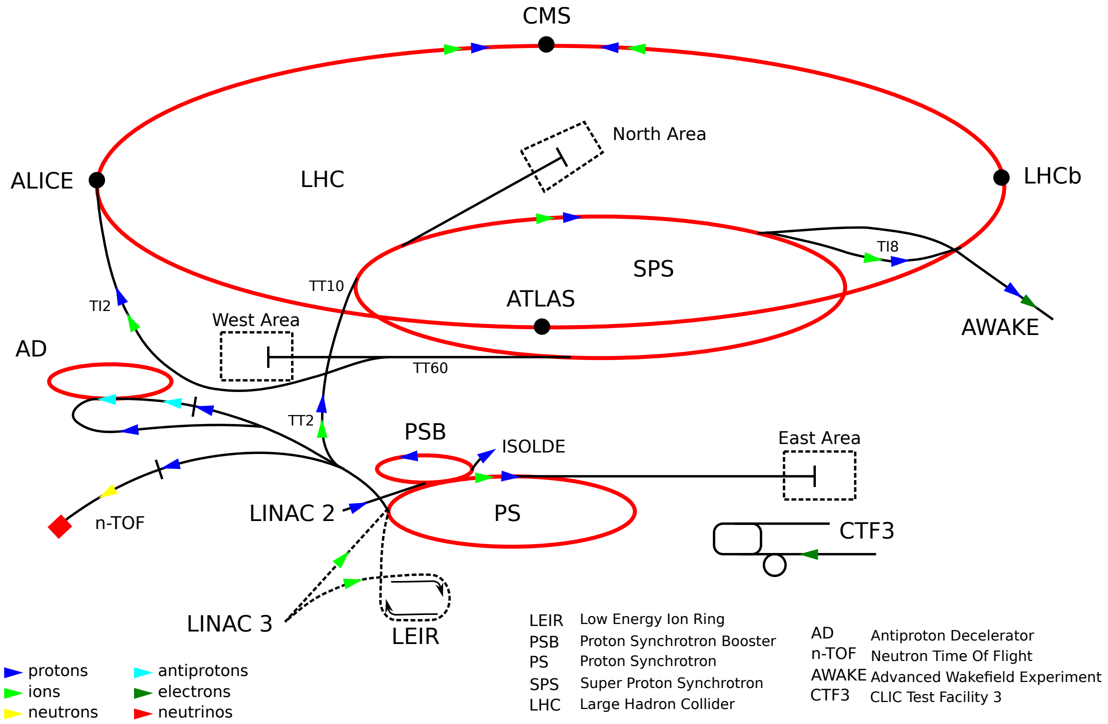

Figure 3.1: Schematic of the CERN accelerator complex. Adapted from [59].

In addition to increasing their energy, it also reduces energy differences between the particles. Two octands house the beam cleaning systems, in which particles with large momentum offset or betatron amplitudes are removed. One octand houses the beam abort systems, which end each LHC run. They extract the remaining particles and direct them into beam dumps. Four octands provide interaction points at which the particles are collided, and house the experiments. There are two high-luminosity interaction points, which are utilised by the general-purpose experiments ATLAS [61] and CMS [62]. The remaining interaction points provide medium luminosity, and are used by the more specialised LHCb [63] and ALICE [64] experiments. The beam injection lines are located in the octands with medium-luminosity interaction points.

The LHC can accelerate protons or heavier ions. It is mostly run with two proton beams to provide data for particle physics research. ATLAS and CMS aim to study the widest range of processes in proton–proton collisions possible. The two collaborations work independently and cross-check each other's results. LHCb is dedicated to *b* hadron decays, which provide insight into mechanisms for *CP* violation, and also searches for *b* hadron decays that are rare in the SM and possibly enhanced by physics beyond the SM. ALICE specialises in investigating a phase of matter called quark–gluon plasma. It is created in collisions involving heavy ions, which create energy densities similar to those immediately after the Big Bang. The data are provided in dedicated LHC runs in which one or both proton beams are replaced by beams of fully ionised lead nuclei. A run with two xenon nucleus beams was also performed. Three further, smaller experiments are operated at the LHC. TOTEM [65] measures the total interaction cross-section as well as elastic and diffractive scattering processes. LHCf [66] studies neutral-particle production cross-sections at low scattering angles to improve the understanding of atmospheric showers induced by cosmic rays. MoEDAL [67] searches for magnetic monopoles, and for highly-ionising, stable, massive particles.

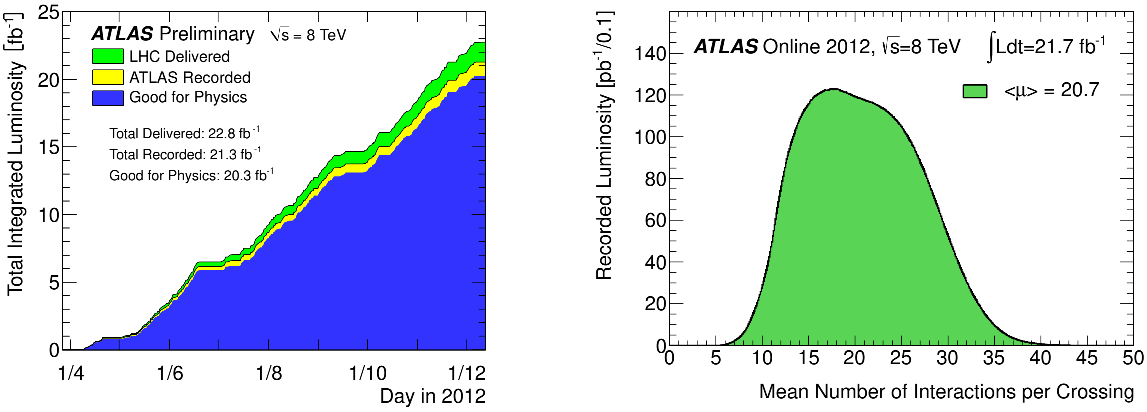

Figure 3.2: Cumulative luminosity versus time (left) and luminosity-weighted mean number of interactions per bunch crossing (right) in the $\sqrt{s} = 8$ TeV ATLAS dataset. The cumulative luminosities delivered (green), recorded (blue), and certified to be good quality data (blue) are shown. The values are taken from a preliminary luminosity calibration [68]. The mean number of interactions per crossing is taken from the instantaneous per-bunch luminosity assuming an inelastic cross-section of 73 mb. Taken from [68].

The LHC provided first proton–proton collisions in late 2009 at a centre-of-mass energy of $\sqrt{s} = 7$ TeV. This energy was maintained until 2012, when collisions at $\sqrt{s} = 8$ TeV were recorded. The data-taking period 2009–2012 is called Run 1 and was followed by a shutdown in which the LHC and the experiments were upgraded. The LHC has collided protons at $\sqrt{s} = 13$ TeV since 2015. The ongoing Run 2 will conclude in late 2018. After a second shutdown in 2019–2020 and further upgrades, the LHC will collide protons at the design centre-of-mass energy of $\sqrt{s} = 14$ TeV. Until the end of 2017, the LHC delivered integrated luminosities of 5.5, 22.8, and 93 fb^{-1} at $\sqrt{s} = 7$, 8, and 13 TeV, respectively, to ATLAS [68, 69]. The highest instantaneous luminosity to date, $2.05 \times 10^{34}\,\text{cm}^{-2}\text{s}^{-1}$ [70], is more than twice the design value.

The ATLAS dataset of proton–proton collisions at $\sqrt{s} = 8$ TeV is used in this thesis. The cumulative luminosity is shown in Figure 3.2. ATLAS recorded 89% of the delivered data with a fully operational detector making them suitable for physics analyses. The maximum instantaneous luminosity was $7.7 \times 10^{33}\,\text{cm}^{-2}\text{s}^{-1}$, and two successive bunch crossings were separated by 50 ns. The instantaneous luminosity was already so high that several inelastic proton–proton collisions took place simultaneously (see Figure 3.2). Signals in the detector that overlap with those created by a proton–proton collision of interest are called pile-up. The signals from successive crossings may pile up in detector systems with signal pulse lengths of $\gtrsim 50$ ns. Pile-up originating from the same (a different) crossing is called in-time (out-of-time) pile-up. Pile-up may affect the accuracy with which events of interest can be reconstructed. Its effect has been limited by choosing suitable detector designs and reconstruction techniques. ATLAS and CMS operate with the highest instantaneous luminosity to collect as much data as possible. The LHCb and ALICE experiments operate with smaller luminosities to keep the level of pile-up low. Pile-up is dominated by low-Q^2 QCD processes as they have by far the highest cross-section.

3.2 The ATLAS Experiment

ATLAS [61] is a general-purpose experiment. It investigates numerous processes involving the Higgs, W or Z bosons, top quarks, b hadron decays, and more to test the SM and to determine its parameters. It aims to discover physics beyond the SM if accessible at the LHC.

The ATLAS detector provides information about the particles emerging from the collisions, in particular about their type and momenta. Information about isolated leptons, taus, and photons is of exceptional importance, because they are commonly produced in interesting processes but relatively rarely in QCD processes. The most frequent signatures are quark- or gluon-initiated jets. ATLAS is designed to measure their momenta accurately, and to identify jets involving b hadrons. Candidates for interesting events are selected in real time because it is impossible to store the data from all bunch crossings. Collisions take place at a nominal bunch-crossing rate of 40 MHz and around a thousand particles are produced per crossing. ATLAS is designed to cope with the large particle multiplicities and with the harsh radiation doses.

The detector layout (see Figure 3.3) is forward-backward symmetric with a cylindrical geometry. The collisions take place in the centre of the detector. The components are arranged in an onion-like design and provide near 4π coverage in solid angle. The beryllium beam pipe holds the vacuum in the LHC, and is as thin as possible to minimise interactions with traversing particles. It is surrounded by the inner detector (ID), which is immersed in an axial magnetic field. The ID detects charged particles at different radii, which makes it possible to reconstruct their initial direction, p_{T}, and origin. The next component is the calorimeter system, which is divided into an electromagnetic (Ecal) and a hadronic (Hcal) calorimeter. Electrons and photons deposit their energy and are stopped in the Ecal, and their energy is measured. Hadrons are stopped in the Ecal or Hcal and may deposit a large fraction of their energy in either. Their energy is determined with the Ecal and Hcal. Muons are the only detectable particles that pass the calorimeter system. They are measured in the muon system. This outermost component is a tracking detector immersed in a magnetic field. It provides a measurement of the muon momentum complementary to that from the ID.

The coordinate system is defined in Section 3.2.1. The detector layout and trigger system in Run 1, which are relevant for the data analysed in this thesis, are described further in Sections 3.2.2–3.2.5. The descriptions are based on Refs. [61, 71–74]. The largest upgrades for Run 2 are the insertable B-layer in the pixel detector [75], and in the trigger system [76]. The reconstruction of physics objects from the recorded data is discussed in Section 3.2.6.

3.2.1 The Coordinate System

The following definition of the coordinate system is adapted from that commonly used in publications by ATLAS (see for example Refs. [25, 26]). ATLAS uses a right-handed coordinate system with its origin at the nominal interaction point in the centre of the detector and the z-axis along the beam pipe. The x-axis points from the nominal interaction point to the centre of the LHC ring, and the y-axis points upwards. Cylindrical coordinates (r, ϕ) are used in the transverse plane, $\phi \in (-\pi, \pi]$ being the azimuthal angle around the z-axis. The pseudorapidity is defined in terms of the polar angle, θ, as $\eta = -\ln\tan(\theta/2)$. Angular distance between physics objects is defined as $\Delta R \equiv \sqrt{(\Delta\eta)^2 + (\Delta\phi\ [\mathrm{rad}])^2}$. The $\Delta\phi$ separation is defined as $\min(|\phi_1 - \phi_2|, 2\pi - |\phi_1 - \phi_2|)$.

3.2.2 The Inner Detector

The ID consists of a pixel detector, a silicon-microstrip tracker (SCT), and a transition-radiation tracker (TRT). It is shown in Figure 3.4. The pixel detector and the SCT cover the region $|\eta| < 2.5$. The TRT covers $|\eta| < 2.0$. The ID is embedded in a thin, superconducting solenoid magnet that provides an axial 2 T field.

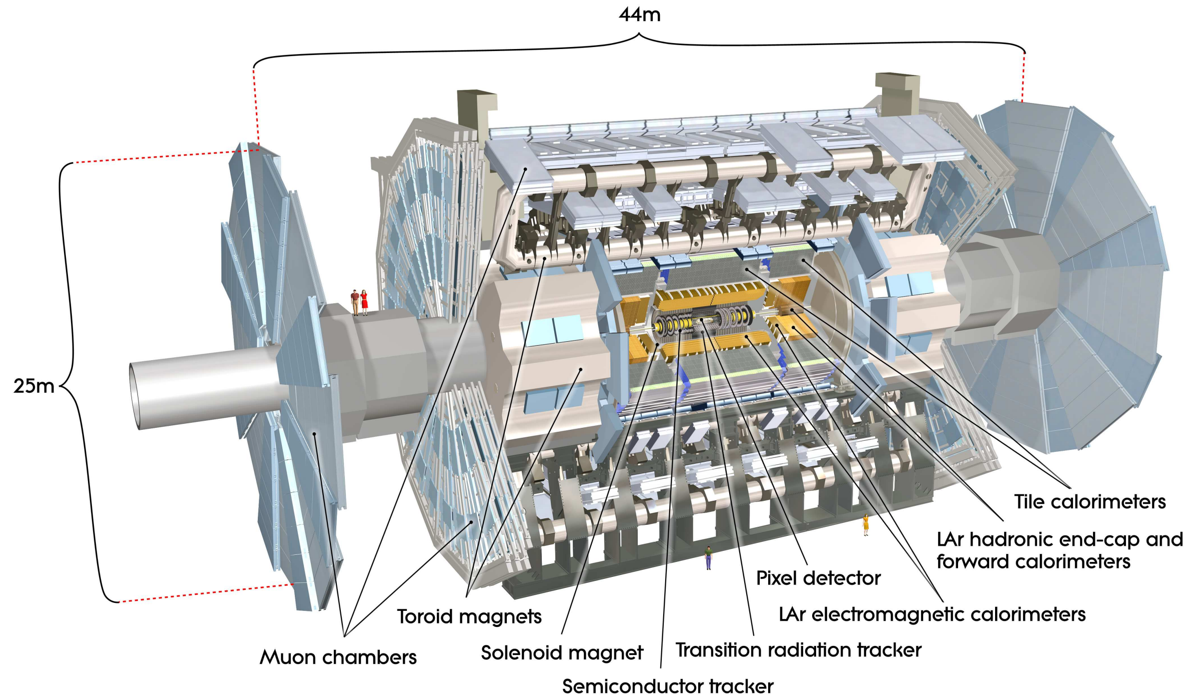

Figure 3.3: Cut-away view of the ATLAS detector. Taken from [61].

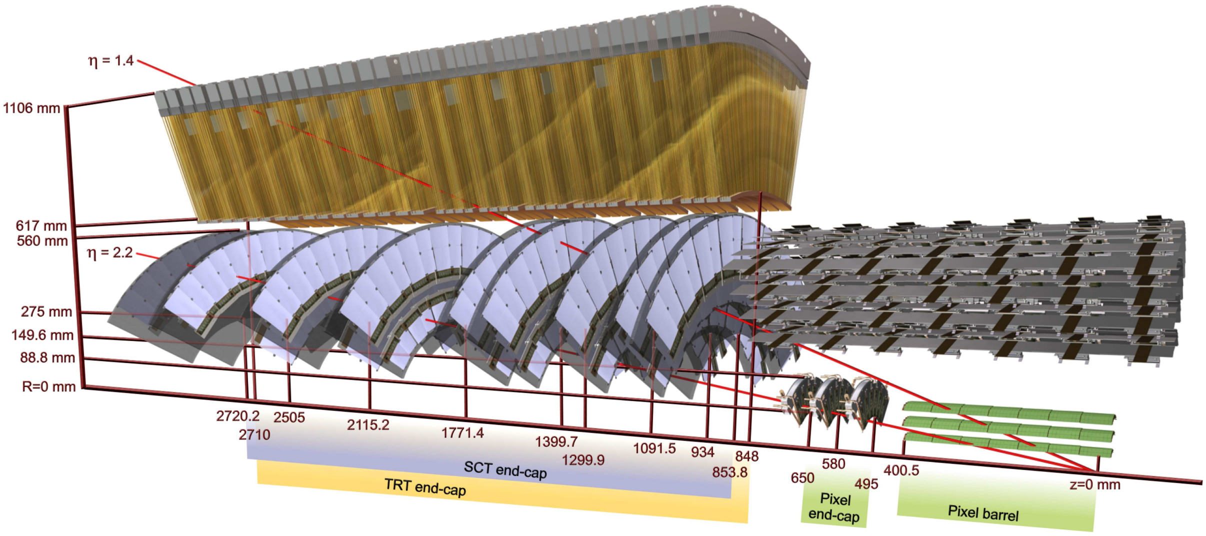

Figure 3.4: Layout of the ID in Run 1. The ID sensors and structural elements in this figure are traversed by two charged particles with $p_{\mathrm{T}} = 10\,\mathrm{GeV}$ each, and at $|\eta| = 1.4$ and 2.2, respectively. The particle at $|\eta| = 1.4$ traverses the three barrel pixel layers, the first four SCT endcap discs, and approximately 40 straws of the endcap TRT wheels. The particle at $|\eta| = 2.2$ traverses the first pixel barrel layer, two endcap pixel disks, and the last four SCT endcap disks. The latter track is not detected by the TRT. The four SCT barrel layers are visible above the three barrel pixel layers. The barrel TRT is located outside the barrel SCT but not shown. A fourth pixel detector layer [75] has been inserted before Run 2. Taken from [61].

The pixel detector is the innermost active component of ATLAS and detects charged particles at radii of a few cm. Identical silicon sensors with pixel sizes of $50 \times 400\,\mu\text{m}^2$ are used in the three barrel layers and in the two endcaps, which have three layers each. The intrinsic accuracy per hit is $10\,\mu\text{m}$ and $115\,\mu\text{m}$ in $R - \phi$ and z (in $R - \phi$ and R) in the barrel (endcaps), respectively. Particles within the acceptance typically pass three pixel layers. The pixel detector provides ability to extrapolate charged-particle tracks to the interaction region accurately. This makes it possible to assign particles to specific collisions, and provides valuable information for the identification of b hadrons and taus. These particles typically decay a few mm from where they were produced, so their decay products do not originate precisely from a proton–proton collision. The pixel detector has featured the insertable B-layer (IBL) [75] as its innermost layer since the start of Run 2.

The SCT consists of double layers of silicon-strip sensors with a pitch of $80\,\mu\text{m}$ and a pitch angle of 40 mrad. Each double layer measures a discrete space point. There are four double layers in the barrel region and nine in each endcap. Most particles within the acceptance traverse four double layers. In the barrel region one set of strips is aligned with the z-axis, and the intrinsic accuracy per double layer is $17\,\mu\text{m}$ in $R - \phi$ and $580\,\mu\text{m}$ in z. In the endcaps one set of strips runs radially, and the intrinsic accuracy is $17\,\mu\text{m}$ in $R - \phi$ and $580\,\mu\text{m}$ in R. The SCT significantly contributes to track p_T and direction measurements.

The TRT detects traversing charged particles via gas-filled straw tubes with a diameter of 4 mm. The barrel TRT contains up to 73 layers of straw tubes and each endcap contains 160 straw-tube planes. The TRT provides about 30 measurements in $R - \phi$ direction per track with an intrinsic resolution of $130\,\mu\text{m}$, each. The straw tubes are interleaved with material in which electrons create transition radiation, and the gas mixture is xenon-based to detect transition radiation efficiently. The TRT significantly contributes to track p_T measurements and to electron identification within its acceptance.

The hundreds of charged particles that emerge from each bunch crossing create thousands of hits in the ID, which results in an enormous combinatorial background for real charged-particle tracks. The discrete space points at inner radii measured by the pixel detector and SCT combined with the many consecutive $R - \phi$ measurements by the TRT provide comprehensive information for pattern recognition to identify and precisely reconstruct charged-particle trajectories (tracks).

The track p_T resolution of the ID is parametrised as [61]

$$\sigma\left(\frac{1}{p_\text{T}}\right) \cdot p_\text{T} = \sigma_\infty \cdot \left(p_\text{T} \oplus p_\text{T}^\text{match}\right), \tag{3.1}$$

where $\oplus$ denotes addition in quadrature, $\sigma_\infty = 0.34\,\text{TeV}^{-1}$ ($0.41\,\text{TeV}^{-1}$) is the asymptotic resolution expected at infinite momentum, and $p_\text{T}^\text{match} = 0.044\,\text{TeV}$ ($0.080\,\text{TeV}$) is where the intrinsic and multiple-scattering contributions match. The given values [61] apply for $0.25 < |\eta| < 0.50$ ($1.50 < |\eta| < 1.75$).

3.2.3 The Calorimeter System

The ATLAS calorimeter system (see Figure 3.5) consists of various subsystems to match the requirements in terms of performance, rate capability, and radiation hardness specific to each location and purpose.

The presampler is the innermost calorimeter subsystem. It features liquid argon as active and no dedicated absorber material, and it is thin. Its purpose is to estimate previous energy losses of electrons and photons. The material in front of the presampler corresponds to 2–4 radiation lengths (X_0) over most of its acceptance. The barrel and endcap presampler components cover $|\eta| < 1.5$ and $1.52 < |\eta| < 1.8$, respectively.

The electromagnetic calorimeter (Ecal) consists of a barrel and two endcap components that cover

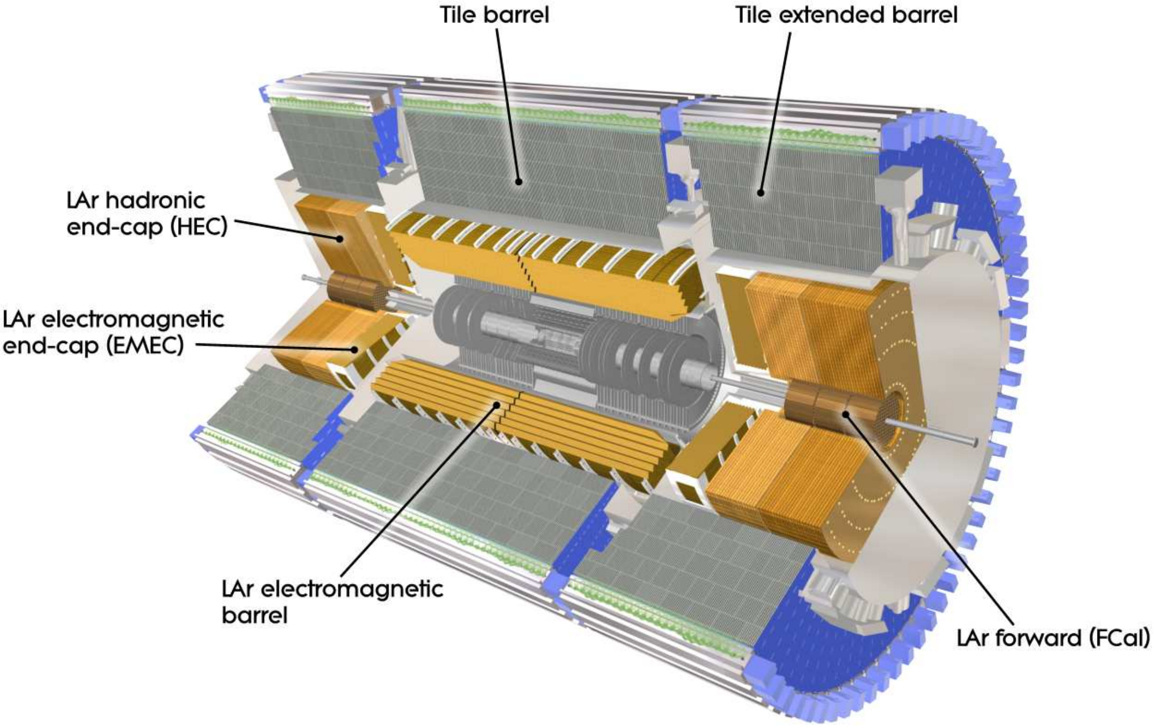

Figure 3.5: Cut-away view of the ATLAS calorimeter system. Taken from [61].

$|\eta| < 1.475$ and $1.375 < |\eta| < 3.2$, respectively. It is a sampling calorimeter with liquid argon as active and lead as absorber material. The region covered by the ID, $|\eta| < 2.5$, provides fine granularity to further aid the reconstruction and identification of, in particular, electrons, photons, and taus. The layout of the Ecal in this region is of interest for the reconstruction of neutral pions in τ_{had} decays discussed in Chapter 5.

An Ecal barrel module is shown in Figure 3.6. It has accordion-shaped absorbers and is segmented into three layers. The first layer, called strip layer, provides very fine granularity in η direction (see Table 3.1), and it is relatively thin. The strip layer detects electromagnetic showers in their early phase, where they are still very narrow, providing excellent η resolution for photons and electrons. Furthermore, isolated high-energy photons can be distinguished from neutral-pion decays to photon pairs. The cells in the second layer, Ecal2, are equally wide in η and ϕ providing good resolution in both directions. Ecal2 is by far the thickest Ecal layer and contains most of the energy of electrons and photons. The third layer, Ecal3, serves as a tail catcher for high-energy electromagnetic showers. The range $2.5 < |\eta| < 3.2$ is covered by two layers, the second of which is a tail catcher for electromagnetic showers. The material in front of the Ecal corresponds to 2.5–5X_0 for most of its acceptance. It corresponds to up to $11X_0$ in the transition regions between the barrel and endcaps, which are filled with cables and services for the ID and barrel Ecal. This degrades the performance in the transition regions.

The Hcal measures the energy of hadrons remaining after the Ecal, and limits punch-through into the muon system. The amount of material in front of and within the Hcal is shown in Figure 3.7. Tile calorimeters cover the regions $|\eta| < 1.0$ (barrel) and $0.8 < |\eta| < 1.7$ (extended barrel components). They are sampling calorimeters with scintillating tiles as active and steel as absorber material. Each endcap

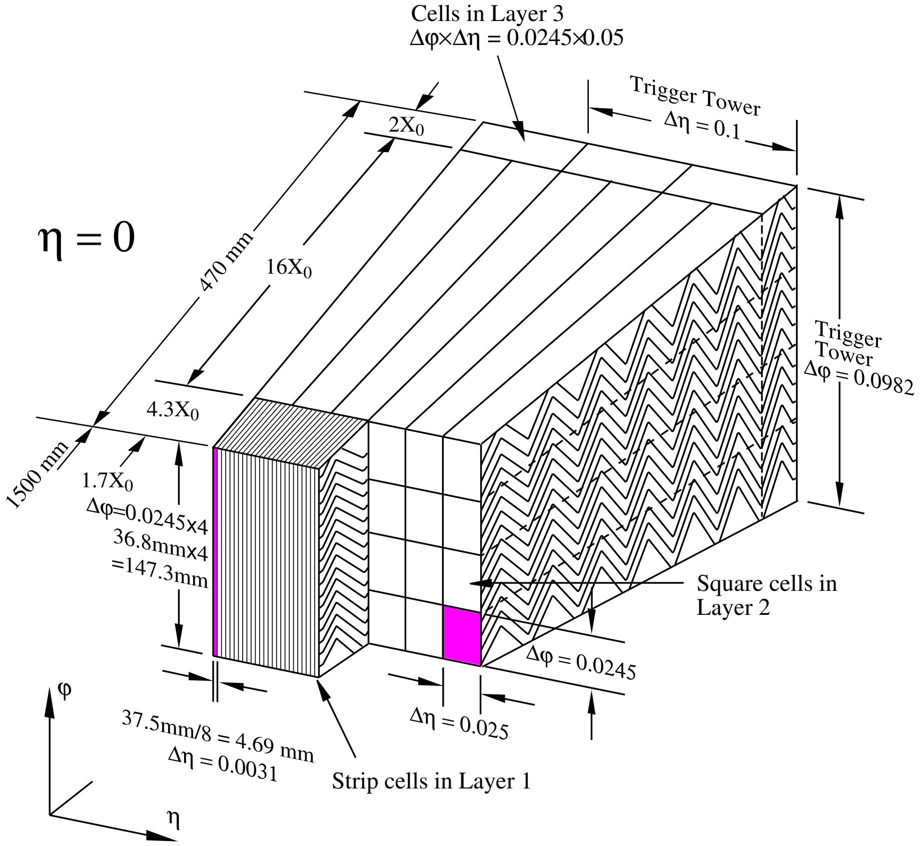

Figure 3.6: Layout of an Ecal barrel module. The cell and trigger-tower granularities are specified. The $\Delta\phi$ values are given in rad. Taken from [61].

Presampler		Strip layer		Ecal2		Ecal3	
$\lvert\eta\rvert$ range	$\Delta\eta \times \Delta\phi$	$\lvert\eta\rvert$ range	$\Delta\eta \times \Delta\phi$	$\lvert\eta\rvert$ range	$\Delta\eta \times \Delta\phi$	$\lvert\eta\rvert$ range	$\Delta\eta \times \Delta\phi$
0.0–1.52	**0.025 × 0.1**	**0.0 –1.4**	**0.025/8 × 0.1**	**0.0 –1.4**	**0.025 × 0.025**	**0.0–1.35**	**0.05 × 0.25**
		1.4 –1.475	0.025 × 0.025	1.4 –1.475	0.075 × 0.025		
1.5–1.8	**0.025 × 0.1**	1.375–1.425	0.05 × 0.1	1.375–1.425	0.05 × 0.1	**1.5–2.5**	**0.05 × 0.25**
		1.425–1.5	0.025 × 0.1	**1.425–2.5**	**0.025 × 0.025**		
		1.5 –1.8	**0.025/8 × 0.1**	2.5 –3.2	0.1 × 0.1		
		1.8 –2.0	0.025/6 × 0.1				
		2.0 –2.4	0.025/4 × 0.1				
		2.4 –2.5	0.025 × 0.1				
		2.5 –3.2	0.1 × 0.1				

Table 3.1: Granularity and acceptance of the presampler and the Ecal layers. The values for the barrel (endcaps) are shown above (below) the horizontal line. The $\Delta\phi$ values are given in rad. The most common granularity for each layer in terms of the number of cells is highlighted. Adapted from [61].

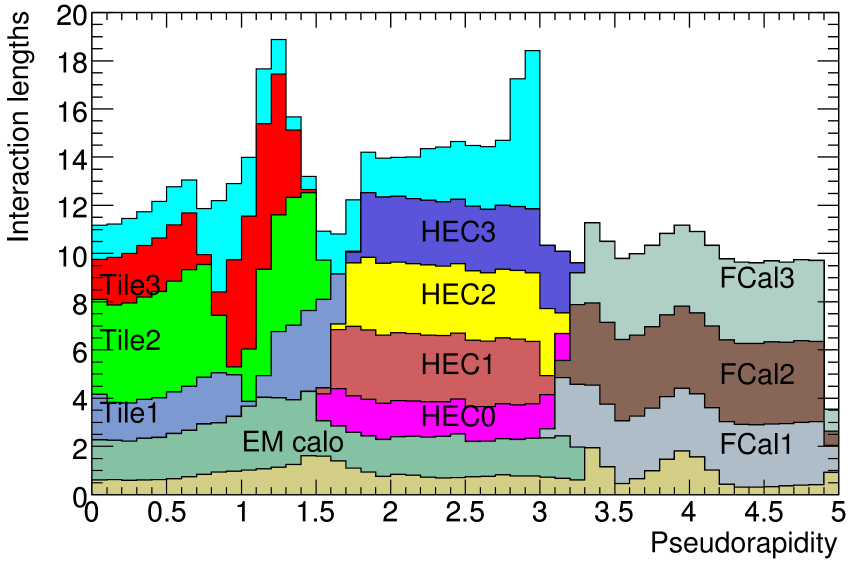

Figure 3.7: Cumulative amount of material in front of and within the calorimeter system in units of interaction length. The amounts within the Ecal, the three layers of the Tile Hcal, the four layers of the liquid-argon hadronic endcap (HEC), and the three layers of the liquid-argon forward (FCal) calorimeters are shown separately. Additional material in front of the first active layer of the muon system is shown in light blue. Taken from [61].

contains one liquid-argon hadronic endcap calorimeter with copper absorbers. They cover $1.5 < |\eta| < 3.2$. Liquid-argon forward calorimeters (FCal) cover the regions $3.2 < |\eta| < 4.9$. Their first layer is optimised to measure electromagnetic showers complementing the Ecal acceptance, and contains copper absorbers. The remaining two layers predominantly measure the energy of hadrons and utilise tungsten absorbers for their higher density.

The energy resolution is parametrised as [61]

$$\frac{\sigma(E)}{E} = \frac{a}{\sqrt{E}/\mathrm{GeV}} \oplus b, \tag{3.2}$$

where $a = 0.10$ (0.56) reflects the stochastic contribution, and $b = 0.007$ (0.055) reflects local non-uniformities in the energy response. The given values apply for electromagnetic showers in the barrel and endcap Ecal (for single charged pions in the tile Hcal at $|\eta| = 0.35$), and the values are $a = 0.50$ and $b = 0.03$ for jets measured with the Ecal and Hcal [61].

The calorimeter system rapidly provides reduced-granularity information to the trigger system via dedicated readout channels. The energy of cells within each so-called trigger tower is summed separately for the Ecal and Hcal. The trigger towers have the same size, $\Delta\eta \times \Delta\phi \approx 0.1 \times 0.1$ rad, in the Ecal and Hcal for $|\eta| < 2.5$, and cover the remaining pseudorapidity range with coarser and less regular granularity.

3.2.4 The Muon System

The muon system (see Figure 3.8) features three large superconducting air-core toroid magnets as well as two endcap toroids. The comparably light structure creates field integrals of about 2.5 T·m (up to 6.0 T·m) in the barrel (endcap) regions, and reduces multiple scattering.

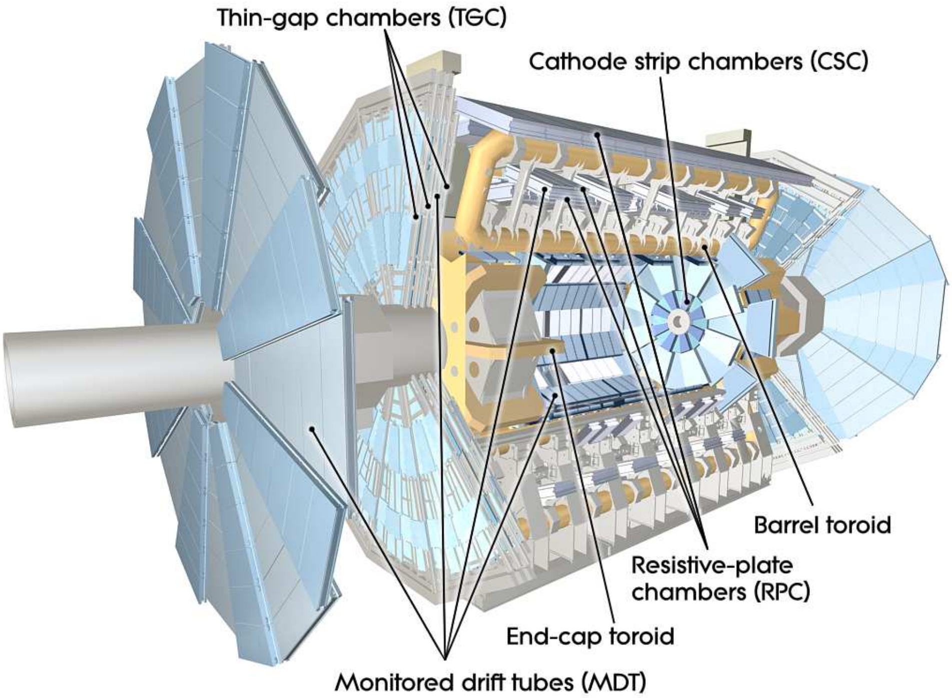

Figure 3.8: Cut-away view of the muon system. Taken from [61].

The muon system has dedicated subsystems that provide information to the trigger system rapidly. Specifically, these are resistive plate chambers in the range $|\eta| < 1.05$, and thin gap chambers in the range $1.00 < |\eta| < 2.4$. They measure the position of muons both in the bending (η) and non-bending (ϕ) planes with a typical resolution of 5–10 mm. Complementary precision subsystems provide η measurements and cover a wider range, $|\eta| < 2.7$. Three layers of monitored drift tube chambers are used. An exception is the innermost layer in the range $|\eta| > 2.0$, where cathode strip chambers provide better rate capability. The intrinsic resolution per hit in the bending plane is 60–80 µm. All subsystems are utilised in the offline muon reconstruction. The muon system can provide standalone muon momentum measurements for $p_{\mathrm{T}} > 3$ GeV. It can measure momenta of 1 TeV with an accuracy of about 10%, and determine the charge sign reliably up to a few TeV.

3.2.5 The Trigger System

Events are selected using a three-level trigger system. The levels exploit an increasing amount of information and reduce the event rate successively. The first level is implemented in hardware and exploits only rapidly accessible data. Specifically, it utilises the calorimeter trigger towers and the fast muon subsystems. It preselects events with one of the following signatures or combinations of them: high p_{T} muon, electron, photon, tau, jet candidate, high $E_{\mathrm{T}}^{\mathrm{miss}}$, or high total transverse momentum. The first level reduces the event rate to 75 kHz, and has a processing time of 2.5 µs. The second level utilises all detector elements within regions of interest defined by the first level. It is implemented in software and reduces the event rate to about ≤ 3 kHz. The third level utilises the entire detector, and the algorithms are similar or identical to the offline algorithms. The rate of accepted events varies with the data-taking conditions and was 400 Hz on average in 2012. The trigger system has been upgraded before Run 2 [76].

3.2.6 Reconstruction of Physics Objects

This section describes the physics objects used in this thesis with a focus on τ_{had} decays. Systematic uncertainties are discussed in the chapters in which they are relevant.

Charged-Particle Tracks in the ID and Primary Vertices

Tracks from particles directly produced in a proton–proton collision are initially reconstructed in the pixel and SCT detectors [77]. They are extrapolated to the TRT, and combined with track segments reconstructed separately therein.

A vertex position is calculated from the available tracks. The calculation is repeated iteratively, and the weight of tracks compatible with the vertex is increased in each step. After the first vertex is found, incompatible tracks are removed from it. The described procedure is repeated using the tracks not associated with a previously found vertex until no more vertices are found. The vertex with the highest sum of squared track p_{T} in an event is called the primary vertex.

Energy Clusters

Topological clusters [72] are the most widely used energy clusters in the ATLAS event reconstruction. They are for example used to reconstruct τ_{had} decays. Topological clusters are seeded by calorimeter cells with absolute[2] energy $|E^{\mathrm{cell}}| > 4\sigma_{\mathrm{noise}}$, where σ_{noise} is the average noise in the respective cell. Each seed cell forms a proto-cluster to which all neighbouring cells are added. Neighbouring cells are

- those in the same layer and subsystem that are directly adjacent,
- those in the next or previous layer of the same calorimeter subsystem that have at least partial overlap in η and ϕ,
- adjoining cells in a different subsystem in transition regions between subsystems.

The neighbours of proto-cluster cells with $|E^{\mathrm{cell}}| > 2\sigma_{\mathrm{noise}}$ are added iteratively. Proto-clusters are merged if they are connected by neighbouring cells that have $|E^{\mathrm{cell}}| > 2\sigma_{\mathrm{noise}}$.

The resulting proto-clusters may be large and contain energy of several particles, which is particularly likely for the collimated products of τ_{had} decays. Local maxima with $|E^{\mathrm{cell}}| > 500$ MeV and higher energy than all their neighbours are identified. The proto-clusters are split amongst them [72] to obtain the final topological clusters.

The cluster direction is the energy-weighted mean of the cell directions from the nominal interaction point. It may be recalculated with respect to another point, for example the primary vertex, during the reconstruction of higher-level physics objects. A local hadronic calibration [72] is applied to determine the cluster energy. The cluster mass is set to zero.

Jets

Jets are reconstructed by combining energy clusters using the anti-k_t algorithm [78] as implemented in the FastJet package [79]. The clusters are considered initial pseudojets, and processed as follows:

---

[2] Negative energy signals can result from out-of-time pile-up because signals from previous bunch crossings can contribute negative due to the pulse shape, or from noise. Keeping them randomly cancels positive signals from the same sources, and reduces biases.

- The distance between pseudojets with indices i and j is[3]

  $$d^{\mathrm{i,j}} = \min\left((p_{\mathrm{T}}^{\mathrm{i}})^{2p}, (p_{\mathrm{T}}^{\mathrm{j}})^{2p}\right)\frac{\Delta R}{R^2},$$

  where $p = -1$ for the anti-k_t algorithm,[4] and $R = 0.4$ for the jets used in this thesis. Additionally, $d^{\mathrm{i}} = (p_{\mathrm{T}}^{\mathrm{i}})^{2p}$ is set for each pseudojet.

- If the smallest of the $d^{\mathrm{i,j}}$ and d^{i} values is a $d^{\mathrm{i,j}}$ distance, the pseudojets i and j are combined. Otherwise, the pseudojet with the smallest d^{i} value is considered a jet instead of a pseudojet. This is repeated until no pseudojets are left.

The anti-k_t algorithm is infrared and collinear safe, and the jets are conical with radius R in terms of ΔR [78]. Energy clusters within possible overlaps of jet cones are mostly assigned to the jet with the highest energy.

The momenta of the reconstructed jets are corrected for pile-up and calibrated using simulation, followed by a final data-driven correction [80].

Electrons

Electron candidates are reconstructed by geometrically matching charged-particle tracks in the ID to energy clusters found in the Ecal and presampler [81]. The clusters are reconstructed with a sliding-window algorithm. While the cluster reconstruction is highly efficient, the track reconstruction may be affected by bremsstrahlung. Incomplete track segments in the pixel and SCT detectors are recovered by performing additional track fits, which allow for energy loss at each material surface, near candidate clusters. If multiple tracks are geometrically matched to a cluster a primary track is chosen. The electron energy is taken from the cluster, and its direction is taken from the primary track.

Electron candidates are identified using multivariate techniques. Analyses can further suppress candidates from quark- or gluon-initiated jets using

$$\begin{aligned} f_{p_{\mathrm{T}},\mathrm{iso}} &= (p_{\mathrm{T}}\text{-sum of tracks with } \Delta R(\text{track, electron}) < 0.4) \,/\, (\text{electron } p_{\mathrm{T}}) \qquad \text{and} \\ f_{E_{\mathrm{T}},\mathrm{iso}} &= (E_{\mathrm{T}}\text{-sum of calorimeter cells with } \Delta R(\text{cell, electron}) < 0.2) \,/\, (\text{electron } E_{\mathrm{T}})\,, \end{aligned} \tag{3.3}$$

where the primary electron track and energy associated with an electron are excluded in the numerators, and the numerator of $f_{E_{\mathrm{T}},\mathrm{iso}}$ is corrected for pile-up.

Muons

Tracks in the muon system are reconstructed by combining track segments found in its individual layers [73]. Muon candidates are reconstructed by successfully combining muon-system tracks with tracks in the ID that pass the following requirements:

- At least one hit in the pixel detector and at least five in the SCT. This requirement is loosened if the trajectory passes a sensor known to be inactive,

---

[3] It is assumed that the pseudojets are made massless by setting the absolute three-momentum to the energy. This is the case for the jets used in this thesis. For pseudojets with non-zero masses, the pseudorapidity separation, $\Delta\eta$, must be replaced by the rapidity separation, $\Delta y = y^1 - y^2$ with $y = \frac{1}{2}\ln\frac{E+p_z}{E-p_z}$, when evaluating ΔR for this equation.

[4] The k_t and Cambridge/Aachen algorithms are analogous to the anti-k_t algorithm except that $p = 1$ and 0, respectively.

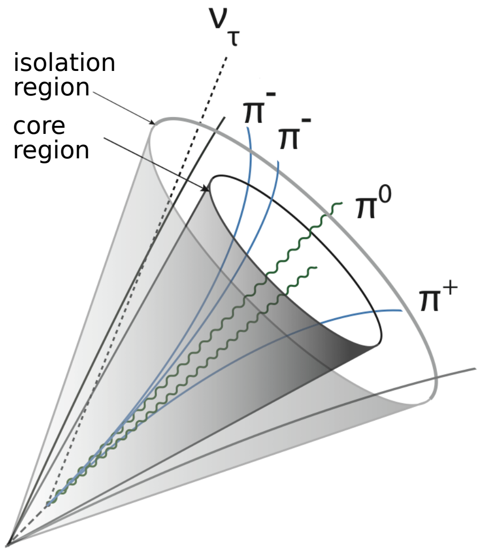

Figure 3.9: Depiction of a representative $\tau^- \to \pi^-\pi^+\pi^-\pi^0\nu_\tau$ decay at high momentum. The core and isolation regions are indicated. Adapted from [83].

- At most two active pixel and SCT sensors are traversed without a hit,
- Tracks within $0.1 < |\eta| < 1.9$ must have at least six TRT hits.

The $f_{p_{\mathrm{T}},\mathrm{iso}}$ and $f_{E_{\mathrm{T}},\mathrm{iso}}$ variables are defined in the same way as for electrons.

Hadronic Tau Decays

The reconstruction of τ_{had} decays [82] is seeded by jets with $p_{\mathrm{T}} > 10\,\mathrm{GeV}$ and $|\eta| < 2.5$. The next step is identifying the tau production vertex because, for example in processes like $W \to \tau\nu$ or $Z/\gamma^* \to \tau\tau$, the reconstructed primary vertex may stem from in-time pile-up: the momentum carried by charged particles may be as small as in typical minimum-bias processes if most momentum is transferred to the neutrinos or to neutral hadrons in the tau decays. All vertices found as described above are considered as tau production vertex candidates, and that with the highest p_{T}-sum of tracks with $p_{\mathrm{T}} > 1\,\mathrm{GeV}$ located in the cone of radius $\Delta R = 0.2$ around the jet seed is chosen. The τ_{had} candidate is assumed to originate from the chosen tau production vertex in the following. The three-momenta of the energy clusters within a cone of radius $\Delta R = 0.2$ around the jet seed are summed, and a preliminary $\tau_{\mathrm{had\text{-}vis}}$ four momentum is obtained by assuming a mass of zero. The cone of radius $\Delta R = 0.2$ around the preliminary $\tau_{\mathrm{had\text{-}vis}}$ momentum is called the core region (see Figure 3.9). It typically contains the decay products of boosted taus. The annulus $0.2 < \Delta R < 0.4$ is the isolation region.

The following criteria are applied to charged-particle tracks in the ID:

- $p_{\mathrm{T}} > 1\,\mathrm{GeV}$,
- at least two hits in the pixel detector, and at least seven hits in the pixel and SCT detectors combined,

Symbol	Description
f_{cent}	Pile-up corrected ratio of E_{T} found in cells within the region $\Delta R < 0.1$ around the preliminary $\tau_{\text{had-vis}}$ momentum and E_{T} found in the full core region. Only energy in clustered cells is considered
f_{track}	Pile-up corrected ratio of core track p_{T} and $p_{\mathrm{T}}^{\tau_{\text{had-vis}}}$
R_{track}	The p_{T}-weighted distance of the tracks in the core and isolation regions to the tau candidate direction
S_{track}	Distance of closest approach of the core track to the tau production vertex in the transverse plane divided by its estimated uncertainty
$N_{\mathrm{track}}^{\mathrm{iso}}$	Track multiplicity in the isolation region
$m_{\pi^0+\mathrm{track}}$	Invariant mass of the system composed of the core track and the reconstructed neutral pions
N_{π^0}	Reconstructed neutral-pion multiplicity
$p_{\mathrm{T}}^{\pi^0+\mathrm{track}}/p_{\mathrm{T}}$	The p_{T}-sum of the core track and reconstructed neutral pions divided by $p_{\mathrm{T}}^{\tau_{\text{had-vis}}}$

Table 3.2: Variables used to identify single-prong τ_{had} candidates as defined in Ref [82].

- the distance of closest approach of the track to the tau production vertex must be less than 1.0 mm in the transverse plane and less than 1.5 mm longitudinally.

The selected tracks within the core region (“core tracks”) define the charged-particle multiplicity and the electric charge of the τ_{had} candidate. Selected tracks within the isolation region are used to suppress backgrounds for τ_{had} decays.

In Run 1, information about neutral pions was used to suppress background τ_{had} candidates but it was otherwise inaccessible to physics analyses. The neutral-pion multiplicity and neutral-pion four-momenta were reconstructed by the Pi0Finder algorithm [26, 84], which proceeds as follows. A multiplicity of zero, one, or two is determined with multivariate techniques that utilise global τ_{had} candidate features obtained from the energy clusters and core tracks. Neutral-pion clusters are selected among the energy clusters, and their energy is corrected for charged-hadron energy deposits. The performance of the Pi0Finder algorithm provides a reference for the algorithms that reconstruct neutral pions in Run 2 (see Chapter 5).

The main backgrounds for τ_{had} decays are quark- or gluon-initiated jets. Their suppression with multivariate techniques is referred to as “τ_{had} identification”. The low particle multiplicity in τ_{had} decays, the fact that tau decay products are typically more collimated than particles in jets, and the often observable lifetime of taus are exploited. The variables used to identify τ_{had} candidates with a single core track (“single-prong candidates”) are of interest in Section 6.5.1 and listed in Table 3.2. A different set of variables, including some of the above, is used to identify candidates with multiple core tracks (“multi-prong candidates”). There are three levels of τ_{had} identification: *loose*, *medium*, and *tight*. The respective identification efficiencies are approximately 65%, 55%, and 40% (45%, 40%, and 25%) for single-prong (multi-prong) τ_{had} decays [82]. The background efficiency significantly depends on the type of parton initiating a jet as well as on p_{T} and η. The inverse background efficiency for the *tight* level is about 60 for single-prong τ_{had} candidates in multijet events with $20 < p_{\mathrm{T}}^{\mathrm{jet}} < 40\,\mathrm{GeV}$ and $|\eta| < 2.5$ [82].

Another significant background stems from electrons. It is also suppressed with multivariate techniques with *loose*, *medium*, and *tight* levels. A minor background from muons may be suppressed with a set of cuts on single variables. These methods are referred to as electron and muon vetoes, respectively.

The $\tau_{\text{had-vis}}$ energy is calibrated using simulation, and corrected for pile-up contributions. A small correction is applied to the η component of the direction. The ϕ component and the zero mass are taken on from the preliminary $\tau_{\text{had-vis}}$ momentum.

Missing Transverse Momentum

The reconstructed $E_{\mathrm{T}}^{\mathrm{miss}}$ component along the x (y) axis is [85]

$$E_{x(y)}^{\mathrm{miss}} = E_{x(y)}^{\mathrm{miss},e} + E_{x(y)}^{\mathrm{miss},\gamma} + E_{x(y)}^{\mathrm{miss},\tau_{\text{had-vis}}} + E_{x(y)}^{\mathrm{miss,jets}} + E_{x(y)}^{\mathrm{miss},\mu} + E_{x(y)}^{\mathrm{miss,soft}},$$

where the first five summands are the negative summed projections onto the x (y) axis of the calibrated electron, photon,[5] $\tau_{\text{had-vis}}$, jet, and muon momenta, respectively. The final summand accounts for the energy deposits in the calorimeter that are not associated with another object and pass criteria to suppress pile-up contributions. The reconstructed $E_{\mathrm{T}}^{\mathrm{miss}}$ is the vectorial sum of the x and y components along the respective axes.

---

[5] The photon reconstruction is described in Ref. [86].

CHAPTER 4

Data Analysis Techniques

This chapter describes the multivariate analysis and fitting techniques used in this thesis. Specifically, boosted decision tree (BDT) classifiers and maximum-likelihood fits are used in Chapters 5 and 6, respectively.

4.1 Boosted Decision Trees

BDT classifiers are multivariate classifiers based on machine learning techniques. BDT and other multivariate classifiers often provide better classification performance than simple sets of cuts or linear models. In particular, they are typically superior in exploiting sets of potentially correlated variables with non-linear relationships that provide little separation individually. The BDT classifiers used in this thesis [87] are provided with the same set of variables per object, and classify objects into signal and background. In order to adapt them to their application, they are trained with data in which objects are labelled as signal or background. This is known as supervised learning. Thereafter, the BDT classifiers are used to classify unseen data.

A decision tree iteratively cuts the parameter space spanned by the input variables into mutually exclusive regions (see Figure 4.1). The cuts are chosen by a greedy algorithm that minimises the yield-weighted mean of the Gini impurities, I, in the resulting nodes with

$$I = 2p \cdot (1 - p), \qquad \text{and} \qquad p = \frac{\text{signal yield}}{\text{total yield}}.$$

The choice of each cut is solely based on the training data in the respective node, which becomes sparser with each iteration. This makes large decision trees susceptible to adapting to statistical fluctuations in the training data. Hence, stopping conditions for example based on the training-data yield in a node are applied. Conditions on the impurity reduction are disfavoured because cuts that cause small improvements initially may create opportunities for powerful cuts. The response of a tree to an unseen object is $+1$ (-1) if there are more signal (background) than background (signal) training objects in the terminal node it reaches.

One small decision tree does usually not exploit the available information effectively. So-called boosting methods create powerful classifiers by combining multiple weak classifiers like small decision trees. Two types of boosting are relevant for this thesis. Adaptive boosting [89] alters the weights of the objects in the training data after creating each tree. The weights are increased for objects that are misclassified by the former tree, so the next tree prioritises them. The trees are weighted based on their individual classification performance. Gradient boosting [89] utilises a loss function, L, to rate the

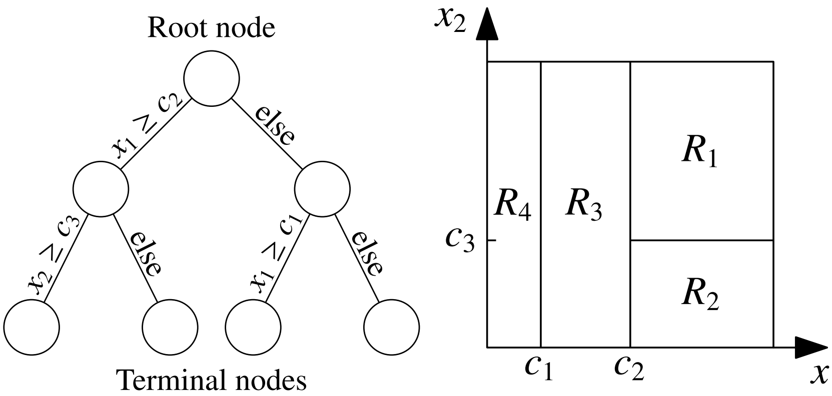

Figure 4.1: A decision tree (left) divides the parameter space spanned by the input variables (right). The cuts are applied starting from the root node until a terminal node is reached. Taken from [88].

classification performance via

$$\sum_{\mathrm{i}} L(y_{\mathrm{i}}, f(\boldsymbol{x}_{\mathrm{i}})), \tag{4.1}$$

where y_{i} is the label of object i (+1 for signal and −1 for background), $\boldsymbol{x}_{\mathrm{i}}$ are that object's variable values, and $f(\boldsymbol{x}_{\mathrm{i}}) \in [-1, 1]$ is the response of the BDT classifier. Adaptive boosting is equivalent to minimising the expression in Eq. (4.1) for $L = \exp(-y \cdot f(\boldsymbol{x}_{\mathrm{i}}))$ each time when creating a new tree [89]. The effect of outliers, statistical fluctuations, and mislabelled objects can be reduced by choosing a shallower loss function for $y \cdot f(\boldsymbol{x}_{\mathrm{i}}) < 0$. The binomial deviance loss function, $L = \log(1 + \exp(-2y \cdot f(\boldsymbol{x}_{\mathrm{i}})))$, is used by the gradient-boosted BDT classifiers in this thesis. It is asymptotically linear for $y \cdot f(\boldsymbol{x}_{\mathrm{i}}) < 0$ instead of exponential. Here, the expression in Eq. (4.1) cannot be minimised as described for adaptive boosting, so a gradient-descent approach is used.

4.2 Maximum-Likelihood Fits

This section introduces maximum-likelihood fits as implemented in the HistFactory tool [90] within the RooFit/RooStats framework [91, 92]. These fits can extract parameters of interest from one or more distributions that may be composed of multiple signal and background contributions, such as those in Figure 4.2. Different types of systematic uncertainties, which are described below, can be modelled via nuisance parameters. These features make it possible to construct an accurate statistical model of the tau polarisation measurement presented in Chapter 6.

A statistical model, $P(\boldsymbol{x}|\boldsymbol{\theta})$, quantifies the probability to obtain data values $\boldsymbol{x}$ dependent on model parameters $\boldsymbol{\theta}$. An example is the Poisson model

$$\mathrm{Pois}(x|\theta) = \theta^x \frac{e^{-\theta}}{x!}, \tag{4.2}$$

which describes a simple counting experiment with a single data value, the observed yield x, and a single parameter, the mean θ. The probability to obtain specific data for a given parameter set is quantified by the probability distribution. In turn, the likelihood, $L(\boldsymbol{\theta})$, describes how consistent a hypothesised parameter set is with given data. The probability distribution and the likelihood have the same functional form, for a simple counting experiment it is Eq. (4.2), but the former (latter) is a function of the data

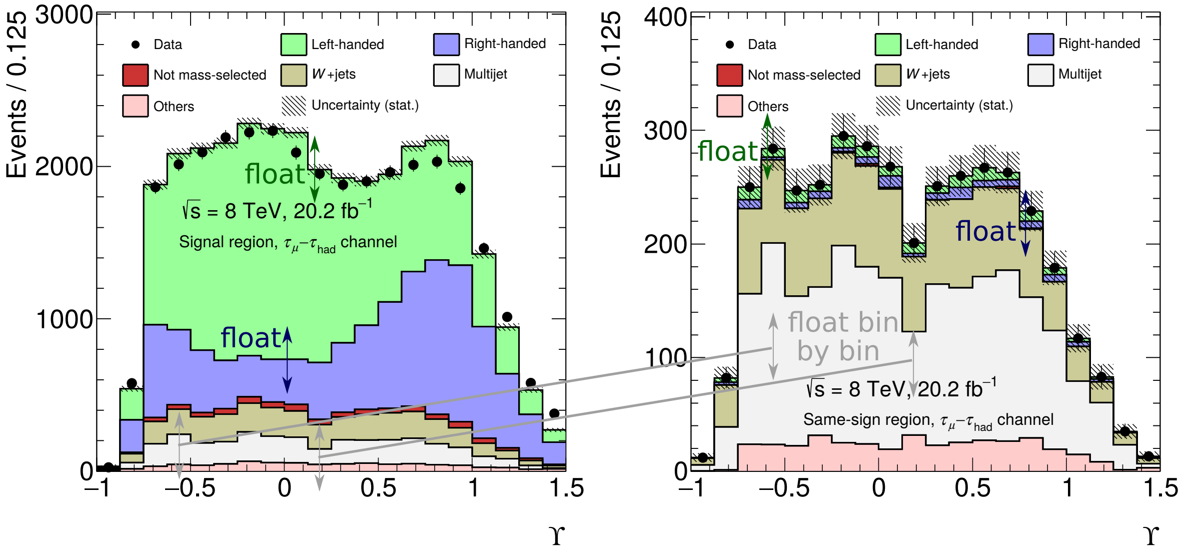

Figure 4.2: Example pre-fit distributions in the tau polarisation measurement (see Chapter 6). Shown are the reconstruction-level Υ distributions (see Eq. (2.21)) for the signal region for the τ_μ–$\tau_{\rm had}$ channel (left, see Table 6.4) and for the corresponding same-sign region (right, see Table 6.7). The former provides sensitivity to the tau polarisation, and the latter is a control region used to estimate the multijet background. The $Z/\gamma^* \to \tau\tau$ contributions with left- and right-handed taus inside the mass-selected region ($66\,\text{GeV} < m_{Z/\gamma^*} < 116\,\text{GeV}$) and the $Z/\gamma^* \to \tau\tau$ contribution outside the mass-selected region are shown separately. The relative normalisation of the left- and right-handed contributions is bound to a free fit parameter to determine the tau polarisation. One free parameter per bin represents the multijet contribution, such that the fitted multijet contribution agrees in the two regions up to a previously determined normalisation factor. The contributions of the W+jets and other, minor backgrounds are also shown and considered in the fit. In this figure, the tau polarisation in $Z/\gamma^* \to \tau\tau$ events is taken from the simulation, and the multijet contribution in the same-sign region is the difference of the data and the remaining contributions.

(of the model parameters). Maximising the likelihood for the observed data provides an estimate of the parameters. Likelihood functions typically contain series of products, so it is in practice easier to minimise the negative logarithm of the likelihood (NLL).[1] This is already visible for the model describing simple counting experiments:

$$-\frac{\mathrm{d}}{\mathrm{d}\theta}\ln L(\theta)\bigg|_{\hat\theta} = \frac{\mathrm{d}}{\mathrm{d}\theta}\left(\theta - x\ln\theta + \ln x!\right)\bigg|_{\hat\theta} = 0 \Leftrightarrow \hat\theta = x,$$

where $\hat\theta$ is the estimate of θ. Minimising the NLL is equivalent to maximising the likelihood because the logarithm function grows strictly monotonously.

In the large-sample limit, the likelihood is Gaussian and the NLL is (hyper)parabolic. The s-standard-deviation uncertainties can be read off from the hypersurface at which [27]

$$-\ln L(\boldsymbol{\theta}) = \mathrm{NLL}_{\min} + \frac{s^2}{2},$$

---

[1] In principle, it is as easy to maximise the positive logarithm. However, numerical tools like MINUIT [92] minimise functions, so the NLL is used by convention.

where $\mathrm{NLL}_{\mathrm{min}}$ is the minimum of the NLL. In particular, the 1σ uncertainty in a parameter θ can be read off from where

$$2 \cdot \Delta\mathrm{NLL} = 2 \cdot (-\ln L(\theta) - \mathrm{NLL}_{\mathrm{min}}) = 1. \tag{4.3}$$

Maximum-likelihood estimators are unbiased and efficient in the large-sample limit under rather general conditions [27]. Hence, they are commonly used in particle physics experiments.

The HistFactory tool builds statistical models for binned distributions. Contributions of individual processes are input via histograms that serve as templates. A modular approach allows the consideration of several processes and systematic uncertainties in a statistical model. Statistical models constructed with HistFactory can be written as [90]

$$\mathcal{P}(n_{\mathrm{cb}}, a_{\mathrm{p}}|\phi_{\mathrm{u}}, \alpha_{\mathrm{p}}) = \prod_{\mathrm{c}} \prod_{\mathrm{b}} \mathrm{Pois}(n_{\mathrm{cb}}|\nu_{\mathrm{cb}}(\boldsymbol{\phi}, \boldsymbol{\alpha})) \cdot \prod_{\mathrm{p}} f_{\mathrm{p}}(a_{\mathrm{p}}|\alpha_{\mathrm{p}}),$$

where

- n_{cb} is the number of events observed in channel c and bin b. A channel is a set of event selection requirements. The channels are assumed to be orthogonal,
- a_{p} is an observation that constrains the nuisance parameter $\alpha_{\mathrm{p}} \in \boldsymbol{\alpha}$. The constraint is $f_{\mathrm{p}}(a_{\mathrm{p}}|\alpha_{\mathrm{p}})$. Nuisance parameters are constrained parameters that model systematic uncertainties. For example, α_{p} may model the uncertainty in an energy scale and a_{p} may be a measurement of that scale.
- $\phi_{\mathrm{u}} \in \boldsymbol{\phi}$ is an unconstrained parameter that affects the normalisation of one or multiple templates,
- $\mathrm{Pois}(n_{\mathrm{cb}}|\nu_{\mathrm{cb}}(\boldsymbol{\phi}, \boldsymbol{\alpha}))$ models the probability to count n_{cb} events in channel c and bin b for an expected number of events ν_{cb}. The ν_{cb} are the summed expected contributions from the individual processes in the respective channel and bin.

The following types of constrained parameters are used in this thesis:

- Parameters that affect the normalisation of templates. Such a parameter may for example model the uncertainty in a trigger efficiency. The relative normalisation changes caused by $\pm 1\sigma$ variations are input for each template and channel when introducing a normalisation uncertainty parameter. These parameters have Gaussian constraints. Piecewise-exponential interpolations and exponential extrapolations [90] are performed to compute normalisation changes for variations other than by 0 and $\pm 1\sigma$.
- Parameters that affect the shape of templates. Such a parameter may for example model the uncertainty in an energy scale, which affects the shape of mass distributions and others. The effect of $\pm 1\sigma$ variations is specified for each template and channel when introducing a shape uncertainty parameter. These parameters have Gaussian constraints. Piecewise-linear interpolations and linear extrapolations are performed.
- Statistical uncertainties in templates taken from simulation are accounted for with a variation of the Barlow–Beeston treatment [93]. One parameter with a Poissonian constraint is introduced per bin and channel in order to model the respective combined uncertainties in that bin. These parameters have Poissonian constraints.

Additionally, sets of unconstrained parameters can be introduced to model the following type of data-driven background estimates that is also illustrated in Figure 4.2. A so-called control region is used to estimate the template shape of a background, which is then transferred to a so-called signal region, in which the signal properties of interest are measured. The template shape of the background is assumed to be equal in the control and signal regions. The signal and control regions are modelled by two channels in the fit with equal binning. One unconstrained parameter models the common relative contribution of the background in corresponding bins of the two channels.

CHAPTER 5

Reconstruction of Hadronic Tau Lepton Decay Products

The τ_{had} reconstruction used at ATLAS in Run 1 [82] determines the $\tau_{\text{had-vis}}$ momentum, the charged-hadron multiplicity and momenta, and the electric charge of a τ_{had} candidate. Backgrounds from quark- or gluon-initiated jets, electrons, and muons are suppressed. The reconstruction and identification methods have been refined continuously, and have provided essential foundation for many measurements and searches with tau leptons at ATLAS. Examples[1] are measurements of SM processes [24, 25, 94–98], searches for and measurements of the Higgs boson discovered at the LHC in 2012 [3, 7, 20, 99–101], searches for further Higgs bosons [102–104], as well as searches for supersymmetry [105–108], for heavy gauge bosons [109], for third generation leptoquarks [19], and in multi-lepton final states [110].

For Run 2, ATLAS has extended the τ_{had} reconstruction to classify the decay topology and to determine the individual four-momenta of all visible decay products [26]. In particular, information about reconstructed neutral pions is now available to physics analyses. Neutral pion reconstruction improves the sensitivity to tau spin effects, and is utilised to improve the $\tau_{\text{had-vis}}$ momentum reconstruction. For the latter, information from the ID and calorimeter is combined, which is called "particle flow". Particle flow has been used to reconstruct τ_{had} decays in other experiments, such as at LEP [111–114], at the Tevatron [115, 116], and by CMS at the LHC [117]. "Tau Particle Flow" refers to the reconstruction of the visible decay products and the corresponding $\tau_{\text{had-vis}}$ momentum at ATLAS. It is designed to exploit the signature of τ_{had} decays at ATLAS and inherently robust against pile-up. The latter feature is highly beneficial because pile-up levels will increase further at the LHC.

Tau Particle Flow is primarily aimed at τ_{had} decays with $p_{\text{T}}^{\tau_{\text{had-vis}}} \lesssim 100\,\text{GeV}$, which are the vast majority of τ_{had} decays at the LHC. In this kinematic range, the momenta of charged hadrons are measured more accurately in the ID than in the calorimeter (see Figure 5.1), which is the basis for improving the $\tau_{\text{had-vis}}$ momentum reconstruction. Neutral pions are reconstructed from electromagnetic showers in the Ecal that are created by the photon pairs emerging from their decays. The typical separation of hadrons emerging a τ_{had} decay (see Figure 5.2) is similar to shower widths in the Ecal, so energy deposits of neutral pions may be merged with those of other particles. The neutral pions often have transverse momenta of a few GeV (see Figure 5.2), in which case they do not strongly stand out from the underlying event, and pile-up. They are reconstructed and identified by exploiting the lateral and longitudinal segmentation of the ATLAS calorimeter system as well as its good energy resolution, and the precision information about charged hadrons provided by the ID. The photons emerging from a neutral-pion decay are mostly

---

[1] The following results are based on the τ_{had} reconstruction [82] and ATLAS data in Run 1. Examples for results based on Run 2 data are mentioned in Section 2.3.1.

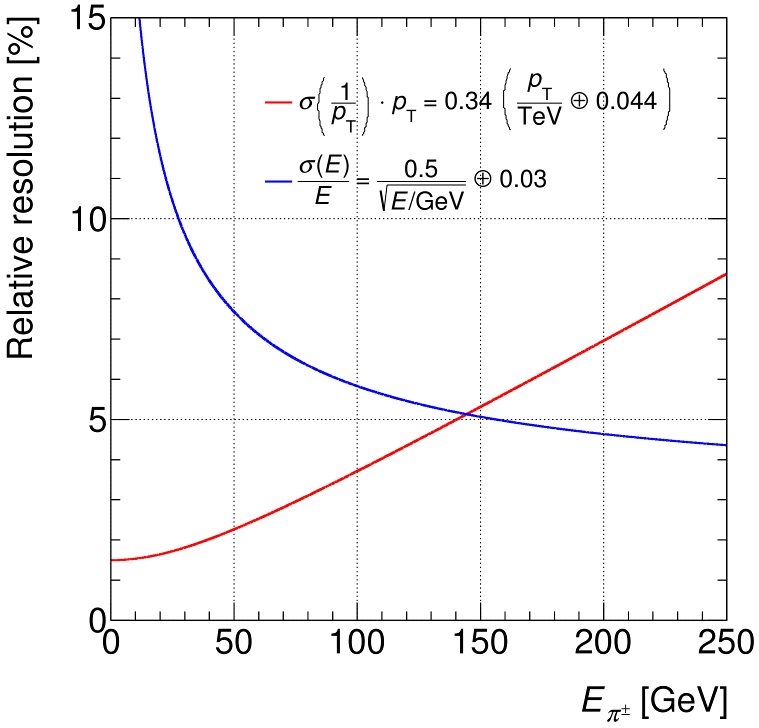

Figure 5.1: Comparison of the relative inverse p_T resolution of charged particles in the ID (red, see Eq. (3.1)) and the relative jet energy resolution in the Ecal and Hcal (blue, see Eq. (3.2)). The latter is qualitatively similar for single charged pions. The parameter values are taken from [61].

so close (see Figure 5.2) that their showers are merged on cluster level. In the few cases in which their separation is very large ($\Delta R \gtrsim 0.1$), at most one photon is energetic enough to be detectable.

This chapter describes the Tau Particle Flow reconstruction. Focus is the TauPi0Rec algorithm [26], which was created in my master thesis [119] and improved as part of this thesis. It subtracts charged-hadron energy deposits from the tau's energy deposits in the Ecal, identifies remaining neutral-pion candidates using a BDT classifier that recognises energy deposits with shapes characteristic for electromagnetic showers, and performs a preliminary decay topology classification. In Tau Particle Flow, the TauPi0Rec algorithm is combined with a method that reconstructs energy deposits of individual photons in the Ecal strip layer [120], and with the PanTau algorithm [121]. The PanTau algorithm combines information about charged-particle tracks, neutral-pion candidates, and energy deposits in the strip layer to perform the final decay topology classification. In particular, kinematic variables are utilised in addition to neutral-pion identification. For the purpose of this thesis, it may be assumed that Tau Particle Flow runs after the remaining τ_{had} reconstruction. Selection requirements are placed on the baseline $\tau_{\text{had-vis}}$ momentum that is calculated using the calorimeter only.

The data and simulated samples are introduced in Section 5.1. The status of the TauPi0Rec algorithm after my master thesis is recapitulated in Section 5.2, and Section 5.3 documents its subsequent development. The reconstruction of energy deposits in the strip layer is described in Section 5.4. The PanTau algorithm and the four-momentum reconstruction are covered in Section 5.5. A validation with data is shown in Section 5.6. Section 5.7 summarises recent developments and gives an outlook.

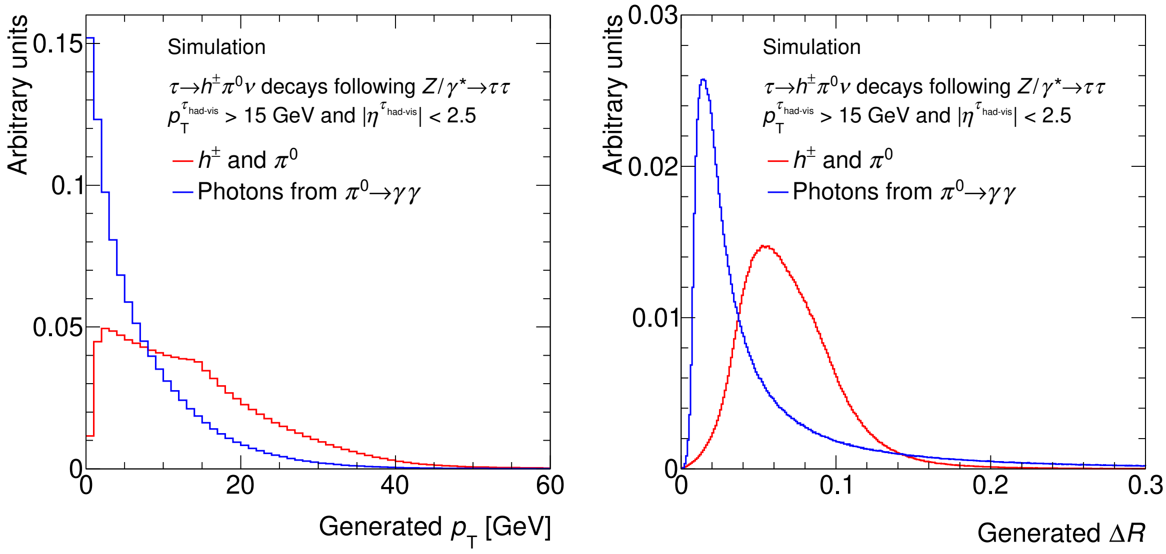

Figure 5.2: The stable-particle (=generator) level p_T (left) and ΔR (right) distributions for the particles emerging from $\tau \to h^{\pm}\pi^0\nu$ decays subsequent to $Z/\gamma^* \to \tau\tau$ decays: the charged hadrons and neutral pions, and the photons from the $\pi^0 \to \gamma\gamma$ decays. The $p_\mathrm{T}^{\tau_{\text{had-vis}}} > 15\,\mathrm{GeV}$ and $|\eta^{\tau_{\text{had-vis}}}| < 2.5$ cuts, which resemble the kinematic acceptance, are applied. The $Z/\gamma^* \to \tau\tau$ sample was produced using the Pythia8 [118] generator (see Section 5.1).

5.1 Data and Simulated Samples

An ATLAS data sample of proton–proton collisions at $\sqrt{s} = 8\,\mathrm{TeV}$ is used to validate Tau Particle Flow. It corresponds to an integrated luminosity of $5.0\,\mathrm{fb}^{-1}$ and is a subset[2] of the full $\sqrt{s} = 8\,\mathrm{TeV}$ sample. The maximum instantaneous luminosity is $3 \times 10^{33}\,\mathrm{cm}^{-2}\mathrm{s}^{-1}$ and there are 19 proton–proton interactions per bunch crossing on average. Events were selected by a trigger that requires an isolated muon with $p_\mathrm{T} > 24\,\mathrm{GeV}$ [74].

A sample of $Z/\gamma^* \to \tau\tau$ decays was simulated with the Pythia8 [118] event generator, which also models the tau decays. It is used to study the reconstruction of τ_{had} decays. Other processes are simulated to account for the respective contributions in the data, which enables comparisons of the data to a meaningful estimate for validation purposes. The simulated samples are summarised in Table 5.1. The tau decays in the top pair and $W \to \tau\nu$ + jets samples were modelled with the Tauola [122] decay library. Photon radiation was modelled with the Photos [123] algorithm in all simulated samples.

The response of the ATLAS detector was simulated [124] using the Geant4 toolkit [125]. The simulated events were overlaid with additional minimum-bias events created with the Pythia8 event generator, which account for in-time and out-of-time pile-up interactions. When comparing to the data, each simulated sample is reweighted such that the spectrum of the average number of pile-up interactions per bunch crossing matches that in the data. The data and simulated samples are processed through the same reconstruction. The trigger requirement is only applied to simulated events when comparing to the data.

---

[2] The data were reprocessed with Tau Particle Flow for this study. Reprocessing data is computationally very expensive, so it was only done for part of the dataset.

Process	Generator	PDF	UE tune
$Z/\gamma^* \to \tau\tau$	Pythia8 [118]	CTEQ6L1 [126]	AU2 [127]
$W \to \mu\nu$ + jets	Alpgen [128]+Pythia8	CTEQ6L1	Perugia2011C [129]
$W \to \tau\nu$ + jets	Alpgen+Pythia8	CTEQ6L1	Perugia2011C
$Z/\gamma^* \to \mu\mu$	Alpgen+Pythia8	CTEQ6L1	Perugia2011C
Top pair	MC@NLO [130–132]+Herwig [133, 134]	CT10 [135]	AUET2 [127]

Table 5.1: List of simulated samples. The following information is provided for each sample: the generator of the hard interaction, parton shower, hadronisation and multiple parton interactions; the set of parton distribution functions (PDF) and the underlying event (UE) tune of the Monte Carlo. Adapted from Ref. [26].

5.2 Initial Version of TauPi0Rec Algorithm

The initial version of the TauPi0Rec algorithm reconstructs neutral pions in single-prong τ_{had} decays. They account for 75% of the τ_{had} decays and 75% of them involve at least one neutral pion. The $\tau \to h^\pm\nu$ and $\tau \to h^\pm\pi^0\nu$ decays are among the most sensitive to tau spin effects.

Energy that originates from neutral pions is almost exclusively deposited in the presampler, strip, or Ecal2 layers of the calorimeter system, which are collectively referred to as *Ecal* in the following. Charged-hadron energy deposits in the *Ecal* are subtracted on calorimeter-cell level using averaged charged-pion shower shapes.

The total amount of energy deposited by the charged hadron produced in the tau decay in the *Ecal* is estimated using the Ecal3 and all Hcal layers, which are collectively referred to as *Hcal* in the following. The energy in the *Hcal* within the tau core region, $E^\pm_{Hcal}$, is assumed to originate exclusively from the charged hadron. This is valid for most τ_{had} decays apart from minor contributions from the underlying event, pile-up, or noise. An exception are the 2% of τ_{had} decays that involve neutral kaons, and no attempts are made to reconstruct neutral kaons. For noise suppression, only clustered energy is considered when computing $E^\pm_{Hcal}$. If a cluster is distributed among the *Ecal* and *Hcal*, only energy in *Hcal* cells is considered. The total amount of energy deposited by the charged hadron in the *Ecal* is estimated as

$$E^\pm_{Ecal} = \max\left(p^{\text{track}} - E^\pm_{Hcal}, 0\right).$$

The cut-off at zero eliminates rare non-physical values, which result from resolution effects. The total of $E^\pm_{Ecal}$ is subtracted on calorimeter-cell level. The charged-hadron energy per *Ecal* layer is estimated using average layer weights, w_{l}:

$$E^\pm_{\text{layer}} = w_{\text{l}} \cdot E^\pm_{Ecal}.$$

The layer weights are obtained from artificial, simulated samples of events including a single charged pion each. Average differences between showers created by charged pions and kaons are much smaller than the statistical fluctuations per shower. The layer weights are binned in $p_{\text{T}}^{\text{track}}$, $|\eta^{\text{track}}|$, and $f_{Hcal} = E^\pm_{Hcal}/p^{\text{track}}$ (see Table 5.2). Examples are shown in Figure 5.3. High-momentum pions typically create elongated showers. The $|\eta^{\text{track}}|$ binning separates structurally different calorimeter regions. A low (high) f_{Hcal} value indicates that the shower started early (late) during the passage of the pion through the calorimeter system.

The amount of charged-hadron energy in each cell per *Ecal* layer is estimated using lateral shower shapes, which are also obtained from the single-charged-pion samples. For this, the core track is extrapolated to the surface of each *Ecal* layer. The point where it enters a layer is represented by the corresponding direction from the nominal interaction point, which is given by $\eta^{\text{track}}_{\text{layer}}$ and $\phi^{\text{track}}_{\text{layer}}$. The

Variable	bin 0	bin 1	bin 2	bin 3	bin 4
$p_{\mathrm{T}}^{\mathrm{track}}$	< 5 GeV	5–10 GeV	10–40 GeV	40–100 GeV	≥ 100 GeV
$\lvert\eta^{\mathrm{track}}\rvert$	< 0.6	0.6–1.3	1.3–1.6	≥ 1.6	
f_{Hcal}	< 0.6	≥ 0.6			

Table 5.2: Three-dimensional binning of charged-hadron shower shapes. Adapted from [119].

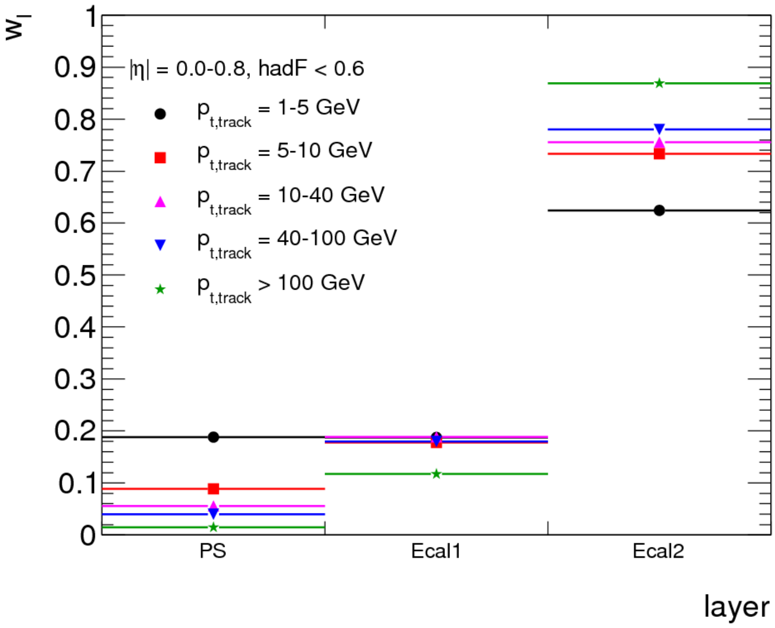

Figure 5.3: Longitudinal weights for $|\eta^{\mathrm{track}}| < 0.6$, $f_{Hcal} < 0.6$, and all $p_{\mathrm{T}}^{\mathrm{track}}$ bins (here labelled $p_{\mathrm{t,track}}$). The presampler and strip layers are labelled PS and Ecal1, respectively. Taken from [119].

average energy distribution is determined as a function of $\eta^{\mathrm{cell}} - \eta_{\mathrm{layer}}^{\mathrm{track}}$ and $\phi^{\mathrm{cell}} - \phi_{\mathrm{layer}}^{\mathrm{track}}$, where η^{cell} and ϕ^{cell} represent the lateral centre of a calorimeter cell. The energy distributions are normalised and parametrised as a function of $\Delta\eta = \eta - \eta_{\mathrm{layer}}^{\mathrm{track}}$ and $\Delta\phi = \phi - \phi_{\mathrm{layer}}^{\mathrm{track}}$, where η and ϕ represent a point on the surface of the calorimeter layer. The parametrisation is performed separately in the bins defined in Table 5.2. An example shower shape and parametrisation function are shown in Figure 5.4. In the reconstruction, the amount of energy deposited by the charged hadron in an *Ecal* cell is estimated via

$$E_{\mathrm{cell}}^{\pm} = E_{\mathrm{layer}}^{\pm} \int\limits_{\text{cell area}} F_{\mathrm{lat}}(\Delta\eta, \Delta\phi)\,\mathrm{d}A\,, \tag{5.1}$$

where F_{lat} is the parametrisation function. The respective $E_{\mathrm{cell}}^{\pm}$ amount is subtracted in each *Ecal* cell in the tau core and isolation regions.

After the charged-hadron shower subtraction, the topological energy clustering (see Section 3.2.6) is performed in the *Ecal* in the combined core and isolation regions. The resulting *Ecal* clusters are considered neutral-pion candidates. Candidates with $p_{\mathrm{T}} < 2.5$ GeV and those outside the core region are rejected to suppress charged-hadron shower remnants, pile-up, and noise. The remaining candidates

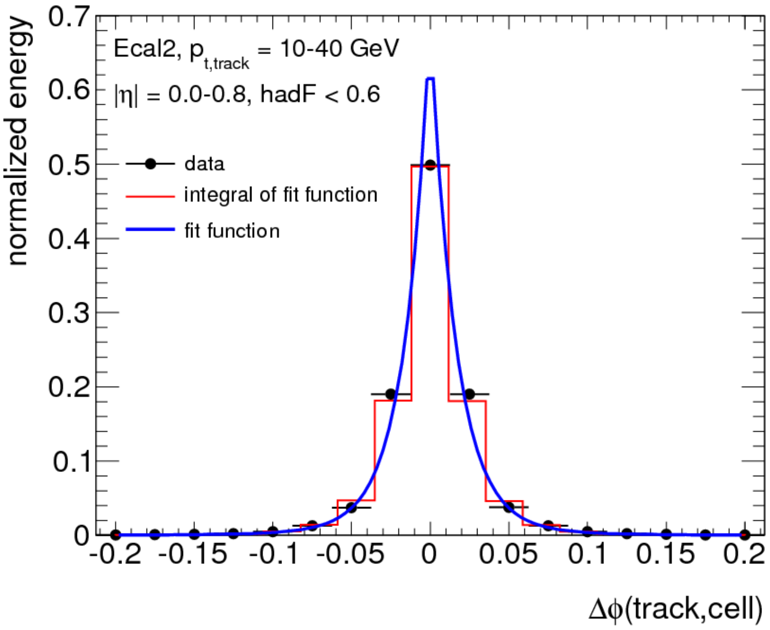

Figure 5.4: Projection in ϕ direction of the shower shape in the Ecal2 layer for $|\eta^{\text{track}}| < 0.6$, $f_{Hcal} < 0.6$, and $10 \leq p_{\mathrm{T}}^{\text{track}} < 40\,\text{GeV}$. The difference $\phi^{\text{cell}} - \phi_{\text{layer}}^{\text{track}}$ is labelled $\Delta\phi$(track,cell), and given in rad. The binned average energy distribution ("data"), the parametrisation function, and the integral of the parametrisation function are shown. Adapted from [119].

mostly originate from neutral pions or charged-hadron shower remnants left after the subtraction. Neutral pions are identified using a BDT classifier [87] that utilises 20 cluster-shape variables. The classifier is trained using simulated $Z/\gamma^* \to \tau\tau$ events. For the training, neutral-pion candidates that are geometrically matched to generated neutral pions are tagged as signal. The remaining candidates are tagged as background. In the reconstruction, neutral-pion candidates must pass an $|\eta|$-dependent requirement on the BDT response in order to be identified. The $|\eta|$ regions are those in Table 5.2 except that $1.6 \leq |\eta| < 2.0$ and $|\eta| \geq 2.0$ are separated. The signal and background efficiencies are around 75% and 25%, respectively.

The number of identified neutral-pion candidates is interpreted as neutral-pion multiplicity. Combined with the core-track multiplicity, which is interpreted as charged-hadron multiplicity and always equals one for τ_{had} candidates processed by the initial algorithm, it defines the decay topology in TauPi0Rec. The topologies in Table 2.5 are distinguished. The classification performance is shown in Figure 5.5. The chosen requirement on the BDT response maximises the diagonal fraction, defined as

$$\text{diagonal fraction} = \frac{\text{number of } \tau_{\text{had}} \text{ decays with correctly determined decay topology}}{\text{number of } \tau_{\text{had}} \text{ decays}}, \tag{5.2}$$

for τ_{had} decays from $Z/\gamma^* \to \tau\tau$ events after the selection in Table 5.3. Its features are discussed below. The neutral-pion four-momenta are reconstructed using the energy and direction of the identified candidates and a pion-mass hypothesis. The charged-hadron momentum is taken on from the core track assuming the pion mass. The $\tau_{\text{had-vis}}$ momentum is the sum of the charged-hadron and neutral-pion momenta.

Generated and reconstructed single- or three-prong (single-prong) τ_{had} decay with ΔR(generated, reconstructed) < 0.2
Absolute electric charge of one
Pass *medium* identification and *medium* electron veto (no identification requirements)
$\lvert\eta^{\tau_{\text{had}}}\rvert < 2.5$, $\lvert p_{\mathrm{T}}^{\tau_{\text{had}}}\rvert > 15\,\text{GeV}$ (20 GeV)

Table 5.3: Selection of τ_{had} decays considered to evaluate the performance of Tau Particle Flow. The requirements below the line are applied to the reconstructed τ_{had} decays. Requirements applied in Ref. [119] are given in parenthesis if they differ from those used subsequently and in Ref. [26].

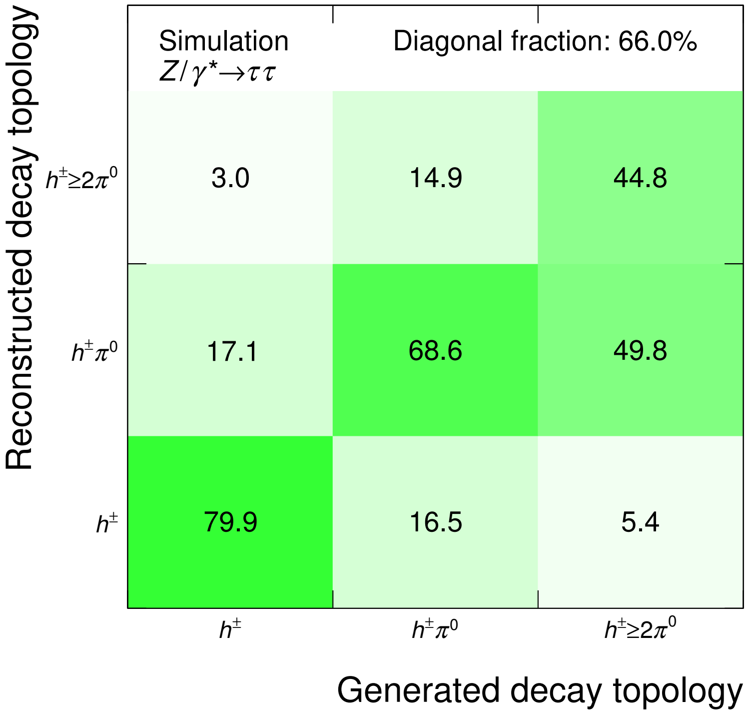

Figure 5.5: Decay topology classification performance in original TauPi0Rec algorithm. The probability for a given generated decay topology to be classified as a particular decay topology in simulated $Z/\gamma^* \rightarrow \tau\tau$ events is shown in percent. The decay topologies are labelled by the final state hadrons. Decays with neutral kaons are omitted. The τ_{had} decay selection in Table 5.3 is applied. The statistical uncertainties are $\lesssim 0.3\%$. Adapted from [119].

5.3 Development of TauPi0Rec Algorithm

This section documents the developments for TauPi0Rec in preparation for Run 2 performed as part of this thesis and in collaboration with Stephanie Yuen [120, 136]. The individual contributions are specified in Appendix A.2. The development focused on the following aspects:

- Extension to three-prong τ_{had} decays.
- Improvement of neutral-pion identification.
- Improvement of the algorithm's speed. Running the initial algorithm by default would have increased the τ_{had} reconstruction processing time significantly. The algorithm's processing time is dominated by the evaluation of the integral in Eq. (5.1) for each *Ecal* cell.
- Simplification of maintenance. The input parameters need to be updated when changes in preceding algorithms are made or major changes in the running conditions occur (e.g. pile-up levels or centre-of-mass energy). Specifically, the configuration of the clustering algorithms, the shower-shape parametrisation, and the neutral-pion identification need to be updated in the initial algorithm. The neutral-pion identification resembles other applications of multivariate methods, such as τ_{had} identification, and is comparably easy to update. Updating the shower-shape parametrisation or the clustering configuration requires expert knowledge. The shower subtraction and clustering are performed at low level and can only be changed, and potentially be fixed, in major data reprocessing campaigns.

New and altered features are discussed in the order in which they are used.

5.3.1 Extension to Three-Prong τ_{had} Decays

The main objective of reconstructing neutral pions in three-prong τ_{had} decays is to select high-purity samples of $\tau \to h^{\pm}h^{+}h^{-}\nu$ decays by suppressing decays with neutral pions. In $\tau \to h^{\pm}h^{+}h^{-}\nu$ decays, the momenta of the visible decay products and the $\tau_{\text{had-vis}}$ momentum can all be taken from the ID and reconstructed very accurately. Sensitivity to tau spin effects can be gained.

The key for the extension to three-prong candidates is to estimate an $E^{\pm}_{Hcal}$ value for each core track. For this, the full energy of a cluster in the *Hcal* is assigned to the core track closest to it. Specifically, the core tracks are extrapolated to the *Hcal* and the full cluster energy in *Hcal* cells is assigned to the track for which ΔR(track, cluster) is smallest. The cluster position is taken from the energy-weighted average of the cell positions in the *Hcal*. For each track, $E^{\pm}_{Hcal}$ is the total energy assigned to it, and the charged-hadron shower subtraction is performed. Subsequently, three-prong τ_{had} candidates are treated analogously to single-prong candidates.

This extension allows Tau Particle Flow to select an 85% pure sample of $\tau \to h^{\pm}h^{+}h^{-}\nu$ decays with an efficiency of 93% from $Z/\gamma^{*} \to \tau\tau$ decays. Minimal additional maintenance is needed. The processing times per single-prong and per three-prong τ_{had} candidate are similar after the changes discussed below.

5.3.2 Development of Cell-Level Charged-Hadron Shower Subtraction

This section documents the development of the cell-level subtraction of the charged-hadron shower from the *Ecal*. The algorithm performs best when doing the subtraction as described in this section. However, subsequently a simpler subtraction method was developed that operates on cluster level and performs almost as well. That method (see Section 5.3.3) is now the default because it is more versatile and easier

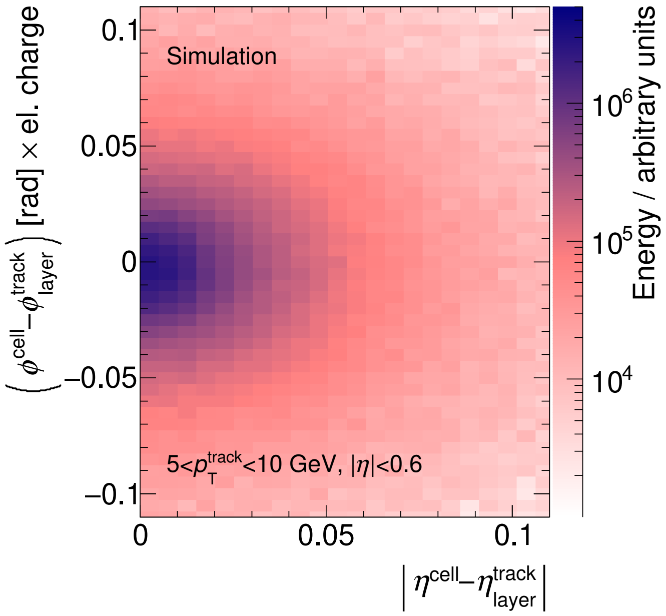

Figure 5.6: Example lateral shower shape used in the improved version of the cell-level subtraction.

to maintain. The concepts described in this section have been essential in the evolution of the algorithm and eventually triggered the development of the cluster-level subtraction. The performance reached with the latest cell-level subtraction and with the cluster-level subtraction are compared in Section 5.3.5.

The latest cell-level subtraction removes $E^{\pm}_{Ecal}$ fully from the Ecal2 layer, in which most energy is deposited (see Figure 5.3), instead of proportionally from all *Ecal* layers. The performance is almost unaffected. In particular, the neutral-pion identification does not benefit significantly if the charged-hadron energy in the individual *Ecal* layers is estimated accurately. This conclusion is supported by studies of another subtraction method designed specifically to identify and subtract charged-hadron energy deposits in the strip layer (see Appendix A.1). Although the latter method is more accurate than the initial and current ones, it improves the algorithm's performance only marginally when used. Subtracting $E^{\pm}_{Ecal}$ fully in the Ecal2 layer reduces the algorithm's complexity and processing time. The layer weights, and the lateral shower shapes in the presampler and strip layers are no longer needed.

The computation of the integral in Eq. (5.1) per cell, which dominates the processing time of the initial algorithm, is made obsolete by storing the average energy fraction deposited in a cell as a function of $\eta^{cell} - \eta^{track}_{layer}$ and $\phi^{cell} - \phi^{track}_{layer}$ in histograms (see example in Figure 5.6) that serve as lookup tables. The sign of $\phi^{cell} - \phi^{track}_{layer}$ is flipped if the particle has negative electric charge to account for the track bending due to the magnetic field. The statistical precision is improved by taking the absolute value of $\eta^{cell} - \eta^{track}_{layer}$. The histograms are obtained from the single-charged-pion samples in the p_T^{track} and $|\eta^{track}|$ bins shown in Table 5.2. The f_{Hcal} binning was primarily chosen to improve the accuracy of the layer weights, and is dropped. The performance is unaffected by this change. The processing time is reduced by about a factor of ten, and to an acceptable level.

5.3.3 Subtraction of Charged-Hadron Shower on Cluster Level

During its development, the algorithm's performance has been retained even though the charged-hadron shower subtraction has been simplified. Conversely, attempts to improve the accuracy of the subtraction have lead to marginal performance gains. This section describes a conceptually different subtraction method, which subtracts charged-hadron energy on cluster instead of cell level, and is now the default. No attempts are made to recover shapes of neutral-pion energy deposits that overlap or are merged with charged-hadron energy deposits. The algorithm now explicitly relies on mixtures of electromagnetic and hadronic showers to be recognised in neutral-pion identification.

Neutral-pion candidates are reconstructed by performing the topological clustering in the *Ecal* in the combined core and isolation regions.[3] The $E^{\pm}_{Ecal}$ estimation is unaltered. Each core track is extrapolated to the Ecal2 layer and the neutral-pion candidate closest to it is determined, i.e. that with smallest ΔR(track, candidate). If ΔR(track, candidate) < 0.04, the neutral-pion candidate's energy is reduced by $E^{\pm}_{Ecal}$. Its direction remains unaltered. The ΔR(track, candidate) < 0.04 requirement was optimised to maximise the diagonal fraction (see Eq. (5.2)). It prevents subtracting energy deposits other than from the charged hadron if a non-negligible $E^{\pm}_{Ecal}$ value is obtained due to resolution effects. The neutral-pion-identification and four-momentum-reconstruction procedures are unchanged. The identification is retrained to account for the altered cluster inputs.

The steps subsequent to the clustering can all be performed outside major data reprocessing campaigns. Necessary maintenance is reduced to updating the configuration of the clustering algorithms and the neutral-pion identification. The cluster-level subtraction does not assume a specific charged-hadron shower shape, and may hence be less affected by systematic uncertainties than the cell-level subtraction.

5.3.4 Neutral-Pion Identification

The neutral-pion identification is conceptually unchanged with respect to Section 5.2 but a number of adjustments have lead to significant performance gains overall. The neutral-pion identification was tuned separately for the neutral-pion candidates found after the cell-level and cluster-level subtraction. The figures and tables in this section show the results obtained with the cluster-level subtraction.

The BDT classifier that identifies neutral pions is trained using neutral-pion candidates that originate from single-prong τ_{had} decays subsequent to $Z/\gamma^* \to \tau\tau$ decays. The selection in Table 5.3 is applied. Background candidates are solely taken from $\tau \to h^{\pm}\nu$ decays, which creates a pure background sample by construction. Signal candidates are those matched to generated photons that originate from neutral-pion decays subsequent to single-prong τ_{had} decays. Specifically, a candidate is tagged as signal if the respective *Ecal* cluster contains one or more Ecal2 cells that are traversed by such a generated photon with $p_{\text{T}} > 500\,\text{MeV}$. This matching procedure takes into account that sizes of *Ecal* clusters vary. The p_{T} cut avoids tagging clusters with unrecognisably small photon contributions as signal.

The variables used to discriminate signal and background candidates are summarised in Table 5.4. The distributions can be found in Figures A.1–A.3. These variables are a subset of those used in Ref. [119], and the removed variables would contribute negligibly if used. The BDT classifier [87] now utilises gradient boosting instead of adaptive boosting (see Section 4.1). The BDT response for tagged signal and background is shown in Figure 5.7 and the discrimination is shown in Figure 5.8. Signal efficiencies above 80% can be reached while suppressing more than 80% of the background.

---

[3] Some of the variables used in neutral-pion identification are calculated by standard ATLAS tools in the clustering procedure. The clustering is performed to calculate these variables using *Ecal* cells, only. Otherwise it should be possible to use the common topological clusters found in the full calorimeter system after removing the *Hcal* cells.

Symbol	Description
$\lvert\eta^{\text{clus}}\rvert$	Magnitude of energy-weighted cluster η position
$\langle r^2\rangle^{\text{clus}}$	Second moment in distance to shower axis
$\langle\eta^2_{\text{strip}}\rangle^{\text{clus}}$	Second moment in η for strip layer
$\langle\eta^2_{\text{Ecal2}}\rangle^{\text{clus}}$	Second moment in η for Ecal2
$\lambda^{\text{clus}}_{\text{centre}}$	Distance of shower centre from calorimeter front face measured along shower axis
$f^{\text{clus}}_{\text{PS}}$	Energy fraction in presampler
$f^{\text{clus}}_{\text{core}}$	Sum of the highest cell energies in presampler, strip layer, and Ecal2 divided by total energy
$\log\langle\rho^2\rangle^{\text{clus}}$	Logarithm of second moment in energy density
$f^{\text{clus}}_{\text{core,strip}}$	Energy in three innermost strip layer cells divided by the total energy in strip layer
$\mathcal{A}^{\text{clus}}_{\text{track}}$	Asymmetry in η–ϕ space of energy distribution in strip layer with respect to extrapolated core-track position
$N^{\text{clus}}_{\text{strip}}$	Number of cells in strip layer with positive energy
$N^{\text{clus}}_{\text{Ecal2}}$	Number of cells in Ecal2 with positive energy

Table 5.4: Cluster-shape variables used to identify neutral pions. The variables $\lvert\eta^{\text{clus}}\rvert$, $\langle r^2\rangle^{\text{clus}}$, $\lambda^{\text{clus}}_{\text{centre}}$, $f^{\text{clus}}_{\text{core}}$, and $\log\langle\rho^2\rangle^{\text{clus}}$ are taken directly from the cluster reconstruction [72]. To avoid confusion with other variables, the superscript "clus" has been added to each variable. The set of variables is the same for both the cell-level and the cluster-level subtraction. Adapted from [26].

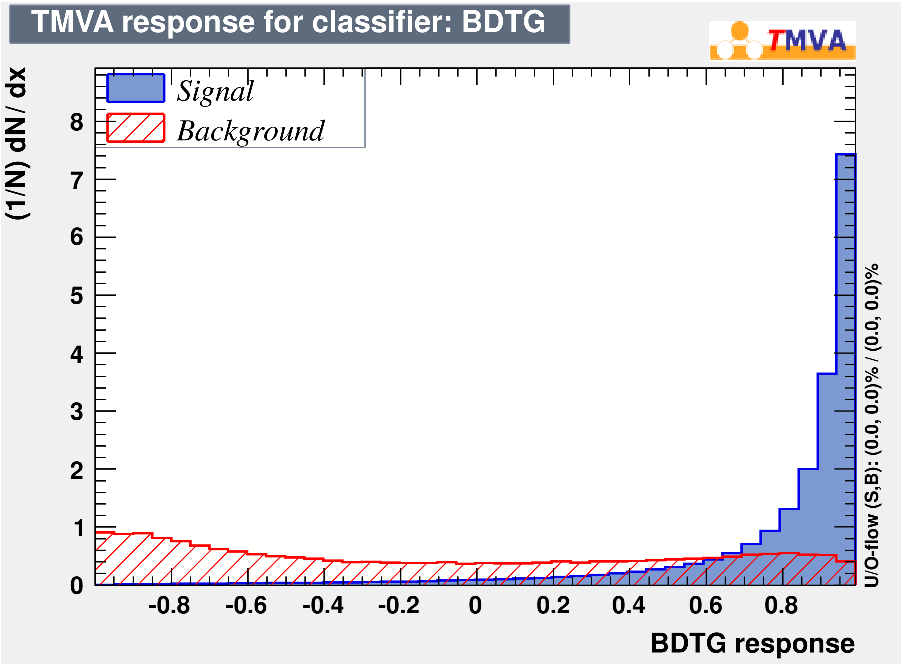

Figure 5.7: BDT response for tagged signal and background candidates. The shown signal (background) candidates are obtained from single-prong τ_{had} decays with neutral pions ($\tau \to h^{\pm}\nu$ decays) subsequent to $Z/\gamma^* \to \tau\tau$ decays. The ordinate is the number of candidates in an arbitrary unit. Taken from Ref. [137], the ATLAS internal documentation for Ref. [26].

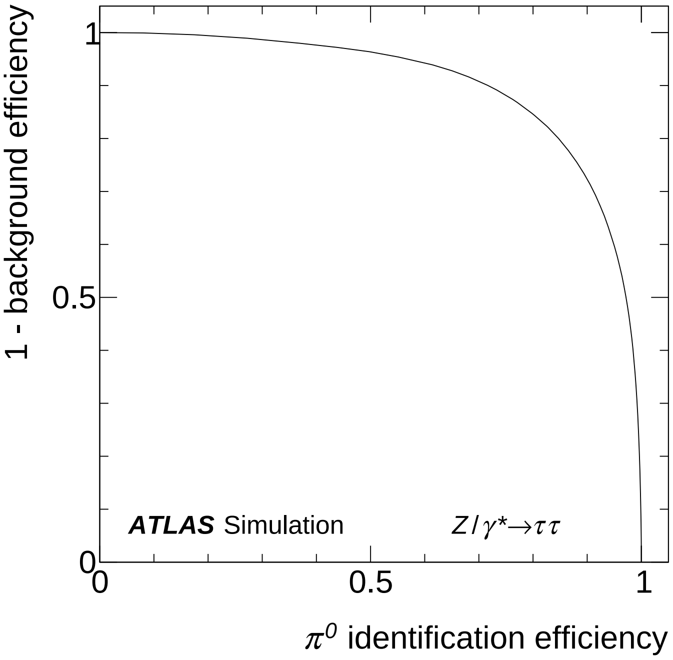

Figure 5.8: Efficiency for background vs. tagged signal neutral-pion candidates to pass the thresholds on the BDT response. Taken from [26].

	$\|\eta\| < 0.8$	$0.8 \leq \|\eta\| < 1.4$	$1.4 \leq \|\eta\| < 1.5$	$1.5 \leq \|\eta\| < 1.9$	$\|\eta\| \geq 1.9$
p_T [GeV]	2.1	2.5	2.7	2.5	2.2
BDT response (single-prong)	0.47	0.45	0.55	0.46	0.44
BDT response (three-prong)	0.61	0.60	0.71	0.69	0.52

Table 5.5: BDT-response and p_T thresholds in neutral-pion identification. Values above the thresholds are accepted.

BDT-response and p_T requirements are optimised simultaneously for single-prong τ_{had} decays to maximise the diagonal fraction. The BDT-response requirement is optimised separately for three-prong τ_{had} decays. It is tighter due to the larger backgrounds from charged-pion shower remnants. Additionally, $\tau \to h^{\pm}h^{+}h^{-}\nu$ decays are twice as common as $\tau \to h^{\pm}h^{+}h^{-} \geq 1\pi^{0}\nu$ decays, so it is beneficial to only accept high-quality neutral-pion candidates. The requirements are listed in Table 5.5. The $|\eta|$ bins correspond to detector regions in which the neutral-pion candidates have similar properties. Notably, the bin that corresponds to the Ecal transition regions, in which the performance is poorest, is now $1.4 \leq |\eta| < 1.5$ instead of $1.3 \leq |\eta| < 1.6$. The chosen neutral-pion identification requirements also provide the most accurate estimate of the $\tau_{had\text{-}vis}$ momentum.

5.3.5 Performance of TauPi0Rec Algorithm

The classification performance of the TauPi0Rec algorithm with the cluster-level subtraction is shown in Figure 5.9. Using the cell-level subtraction leads to an improvement of one percent point in terms of diagonal fraction. Generated single-prong decays are rarely reconstructed as three-prong decays

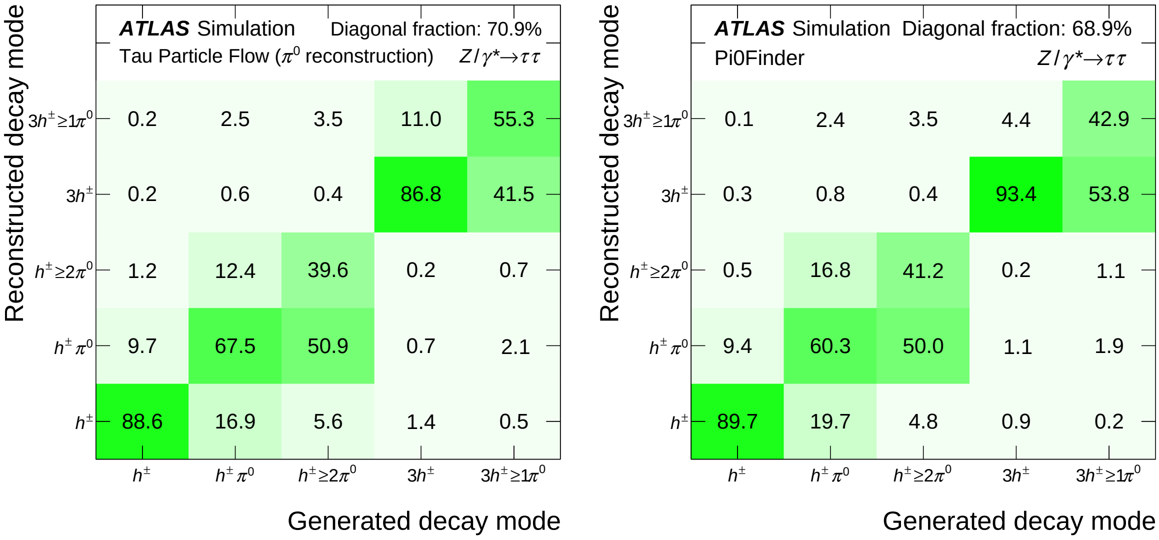

Figure 5.9: Decay topology classification performance of the TauPi0Rec (left, labelled “Tau Particle Flow (π^0 reconstruction)”) and Pi0Finder (right) algorithms. The probability for a given generated decay topology to be classified as a particular decay topology in simulated $Z/\gamma^* \to \tau\tau$ events is shown in percent. The topologies are labelled by the final state hadrons. Decays with neutral kaons are omitted. The τ_{had} decay selection in Table 5.3 is applied. The statistical uncertainties are negligible. Taken from [26].

and vice versa. Single-prong decays with and without neutral pions can also be distinguished reliably. The $\tau \to h^{\pm}\pi^0\nu$ and $\tau \to h^{\pm}\pi^0\pi^0\nu$ decay topologies are confused more frequently. Due to the tighter identification requirements most three-prong decays are reconstructed as $\tau \to h^{\pm}h^{+}h^{-}\nu$. Neutral pions are reconstructed for about half the τ_{had} decays involving neutral kaons. The stand-alone TauPi0Rec algorithm outperforms the Pi0Finder algorithm (see Section 3.2.6) in terms of diagonal fraction (see Figure 5.9) even though the latter exploits kinematic variables already.

Most misidentified neutral-pion candidates originate from remnants of charged-hadron showers. Other possible sources are the underlying event, pile-up, and noise. Real neutral-pion candidates may fail the identification requirements. Alternatively, neutral pions may remain unreconstructed, including cases in which they are removed in the shower subtraction. The two types of mistake are equally likely to occur in $Z/\gamma^* \to \tau\tau$ decays. The p_{T} and BDT-response requirements are failed with similar frequency by signal candidates. Neutral pions outside the core region are, by contrast, very rare. The $\tau \to h^{\pm}\pi^0\nu$ and $\tau \to h^{\pm} \geq 2\pi^0\nu$ topologies are particularly difficult to distinguish. In the decays with a single neutral pion, the two photons may be reconstructed separately and two neutral-pion candidates may be identified. Conversely, energy deposits from multiple neutral pions may be merged. Additionally, $\tau \to h^{\pm} \geq 2\pi^0\nu$ decays frequently involve a low-momentum neutral pion that is missed easily. The error frequency is reduced in the following steps (see Sections 5.4 and 5.5).

The energy reconstruction is evaluated using the relative residual $E_{\text{T}}/E_{\text{T}}^{\text{gen}}$, where E_{T} ($E_{\text{T}}^{\text{gen}}$) is the reconstructed (generated) transverse energy. The directional residuals are $\eta - \eta^{\text{gen}}$ and $\phi - \phi^{\text{gen}}$, where η and ϕ (η^{gen} and ϕ^{gen}) denote the reconstructed (generated) direction. The core and tail resolutions are defined as half of the 68% and 95% central intervals of the relative E_{T} or directional residuals. The neutral-pion energy residuals for the TauPi0Rec and Pi0Finder algorithms in correctly reconstructed $\tau \to \pi^{\pm}\pi^0\nu$ decays are shown in Figure 5.10. A slight bias is present when using the TauPi0Rec algorithm

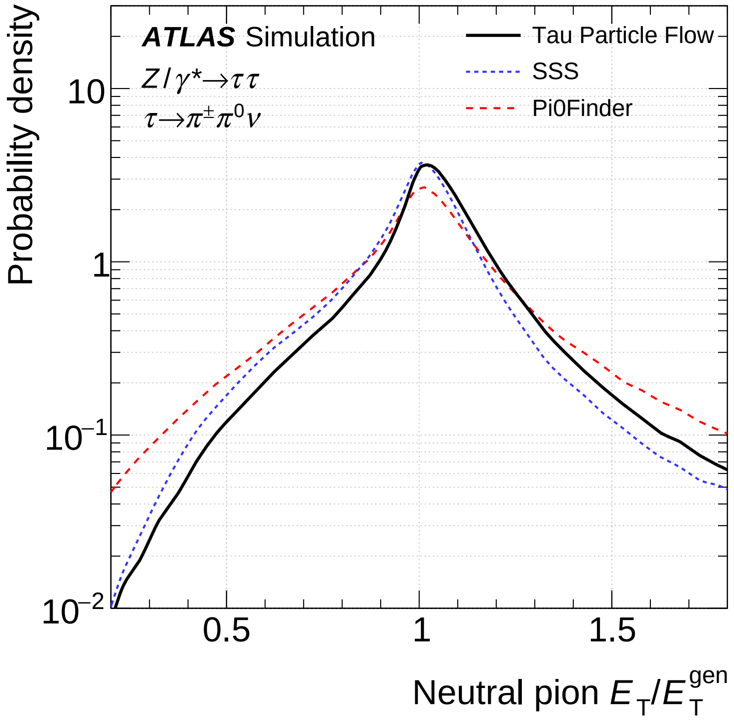

Figure 5.10: Distribution of the relative neutral-pion E_{T} residual for correctly reconstructed $\tau \to \pi^{\pm}\pi^{0}\nu$ decays in simulated $Z/\gamma^{*} \to \tau\tau$ events. “Tau Particle Flow” denotes the TauPi0Rec algorithm with the cluster-level subtraction. “SSS” (for “shower shape subtraction”) denotes the cell-level subtraction. The performance of the Pi0Finder algorithm is also shown. Taken from [26].

with the cluster-level subtraction. It originates from leakage of charged-hadron energy to the identified *Ecal* cluster, and is fixed in a later step. The widths of the residual distributions match for both subtraction methods. The core resolution is 16% (23%) for the TauPi0Rec (Pi0Finder) algorithm. The directional residuals are shown in Figure 5.11. The η (ϕ) core resolutions are 0.0056 (0.012 rad) for the TauPi0Rec algorithm and 0.0086 (0.016 rad) for the Pi0Finder algorithm. The η reconstruction benefits from the fine granularity of the strip layer. The performance of the $\tau_{\text{had-vis}}$ momentum reconstruction is discussed in Section 5.5.

5.4 Reconstruction of Energy Deposits in the Strip Layer

The results presented in this section have been obtained by Stephanie Yuen [120]. Photons typically leave around 30% of their energy in the strip layer. Its fine granularity is used to recover $\tau \to h^{\pm} \geq 2\pi^{0}\nu$ decays that are misclassified as $\tau \to h^{\pm}\pi^{0}\nu$ decays because the subshowers of the photons originating from the neutral pions are merged on cluster level. This is increasingly likely for high $\tau_{\text{had-vis}}$ momenta and accounts for about half of the $\tau \to h^{\pm} \geq 2\pi^{0}\nu$ decays that are misclassified as $\tau \to h^{\pm}\pi^{0}\nu$ decays in $Z/\gamma^{*} \to \tau\tau$ events. Reconstructed energy deposits in the strip layer are also utilised by the PanTau algorithm (see Section 5.5). Typical photon shower widths in the strip layer are comparable with the baseline cell width in η direction (0.003), and much smaller than the cell width in ϕ direction (0.10 rad). An example energy distribution in the strip layer is shown in Figure 5.12.

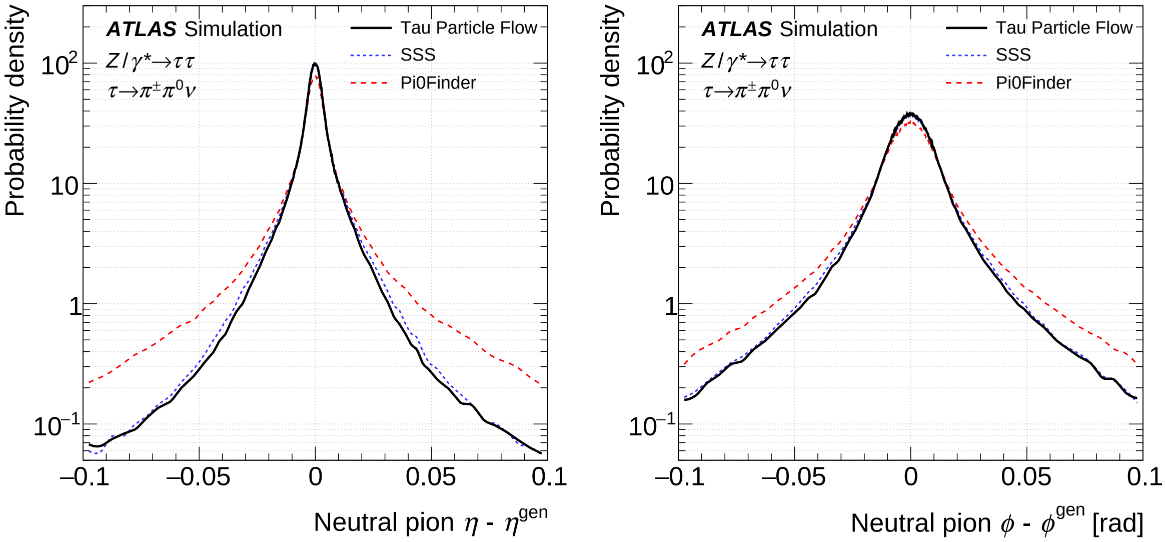

Figure 5.11: Distribution of the neutral-pion η (left) and ϕ (right) residuals for correctly reconstructed $\tau \rightarrow \pi^{\pm}\pi^{0}\nu$ decays in simulated $Z/\gamma^{*} \rightarrow \tau\tau$ events. “Tau Particle Flow” denotes the TauPi0Rec algorithm with the cluster-level subtraction. “SSS” (for “shower shape subtraction”) denotes the cell-level subtraction. The performance of the Pi0Finder algorithm is also shown. Taken from [26].

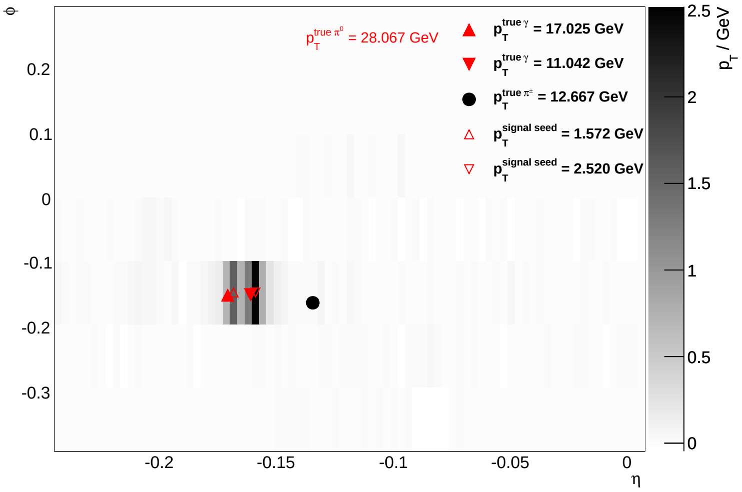

Figure 5.12: The p_T (=E_T) distribution in the strip layer for an example simulated $\tau \rightarrow \pi^{\pm}\pi^{0}\nu$ decay. The positions of the generated final-state particles are overlaid and their p_T values are shown. Two maxima are found. The position and p_T values of the seed cells are indicated. The ϕ values are given in rad. Taken from [120].

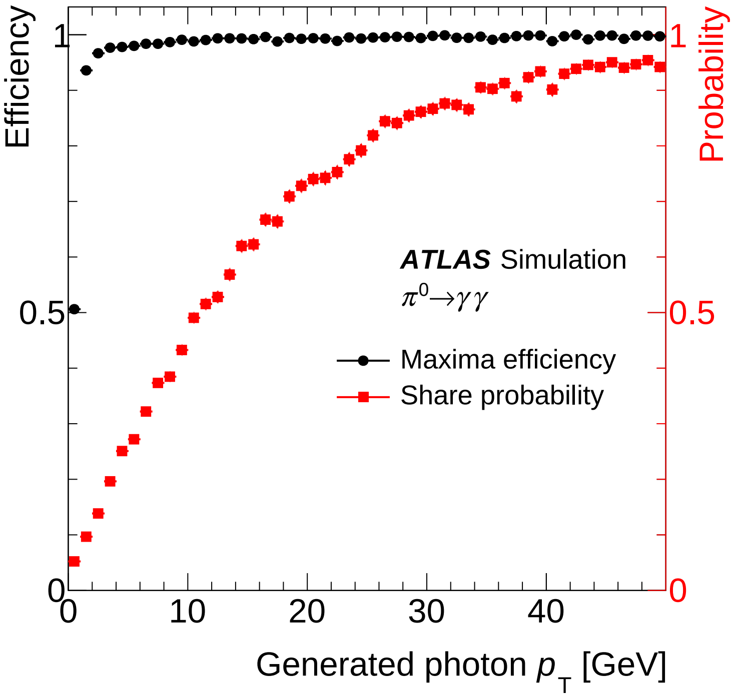

Figure 5.13: Efficiency for a photon to create a maximum in the strip layer in an artificial sample of simulated single $\pi^0 \rightarrow \gamma\gamma$ decays and the corresponding probability to create a maximum that is shared with the other photon. The photons are required to not interact with the material in the tracking system. Taken from [26].

Energy deposits in the strip layer are reconstructed by identifying local maxima in the energy distribution:

- Reconstructed maxima are seeded by cells with $E_\mathrm{T}^\mathrm{seed} > 100\,\mathrm{MeV}$ and larger than E_T measured in the two direct neighbour cells in η direction (see Figure 5.12).
- To avoid reconstructing two maxima if a photon traverses the strip layer close to the border of two cells in ϕ direction, maxima seeded by cells that are direct neighbours in ϕ direction are combined. Maxima are combined in order of decreasing $E_\mathrm{T}^\mathrm{seed}$ and preferentially with the neighbour with higher $E_\mathrm{T}^\mathrm{seed}$. Each maximum is combined with at most one neighbour, in which case the $E_\mathrm{T}^\mathrm{seed}$ values are summed.

The efficiency for photons to create maxima is shown in Figure 5.13. Photons with $p_\mathrm{T} \lesssim 300\,\mathrm{MeV}$ rarely deposit enough energy in the strip layer to do so.

Maxima with $E_\mathrm{T}^\mathrm{seed}$ above an η^seed-dependent threshold in the range 300–430 MeV are called “strip layer hits”. Lower-energy maxima often originate from background sources such as noise or fluctuations in a photon shower. The threshold maximises the diagonal fraction after recovering $\tau \rightarrow h^\pm \geq 2\pi^0\nu$ decays as follows:

- Hits with $E_\mathrm{T}^\mathrm{seed} \leq 10\,\mathrm{GeV}$ are counted as single reconstructed photons.
- Hits with higher $E_\mathrm{T}^\mathrm{seed}$ values contain the merged energy deposits of both photons from a neutral-pion decay with a probability above 95% (see Figure 5.13), so they are counted as two reconstructed photons each.

- Hits are assigned to a neutral-pion candidate if the seed cell belongs to the respective *Ecal* cluster.

- Identified neutral-pion candidates that contain three or more reconstructed photons are assumed to contain the merged energy deposits of two neutral pions. They are counted as two neutral pions and their mass is set to twice the pion mass. In particular, single-prong τ_{had} candidates with one identified neutral-pion candidate are classified as $\tau \to h^{\pm} \geq 2\pi^{0}\nu$ decays if the neutral-pion candidate contains three or more reconstructed photons.

In $Z/\gamma^{*} \to \tau\tau$ decays, 16% of the formally misclassified $\tau \to h^{\pm} \geq 2\pi^{0}\nu$ decays are recovered at a cost of misclassifying 2.5% of $\tau \to h^{\pm}\pi^{0}\nu$ decays.

5.5 The PanTau Algorithm and Final Calibration

The PanTau algorithm performs the final decay topology classification. In particular, it improves the difficult reconstruction of the neutral-pion multiplicity with respect to the preliminary classification made by the TauPi0Rec algorithm. The final neutral-pion four-momenta are determined and summed with the core-track momenta. The obtained $\tau_{\text{had-vis}}$ momentum is calibrated and combined with that found using the calorimeter only. The result is the final Tau Particle Flow four-momentum. Results are only shown for the combination of TauPi0Rec with the cluster-level subtraction and PanTau. The improvements are similar when the cell-level subtraction is used. The developments for the PanTau algorithm for Run 2 were performed by Christian Limbach [121].

Kinematic variables computed from the neutral-pion candidates and core tracks provide valuable information about the decay topology. Charged-hadron shower remnants are typically close to a core track and contain a small fraction of the charged hadron's energy. The four-momenta of τ_{had} decay products, and therefore those of the real neutral-pion candidates and tracks, are correlated. Additionally, the number of reconstructed photons in the strip layer is typically larger for τ_{had} candidates with neutral pions. This information is to a large extend orthogonal to that exploited in neutral-pion identification. PanTau combines the available information to correct mistakes made in the previous decay topology classification.

In the following, neutral-pion candidates within the core region and with $p_{\text{T}} \gtrsim 1.5\,\text{GeV}$ ($|\eta|$ dependent cut) are considered. They are called π^{0}_{cand}, while previously identified neutral-pion candidates are called π^{0}_{ID}, and are a subset of the π^{0}_{cand}. Reconstructed τ_{had} decays without π^{0}_{cand} are left unaltered by PanTau and remain $\tau \to h^{\pm}\nu$ or $\tau \to h^{\pm}h^{+}h^{-}\nu$. Similarly, single-prong τ_{had} that include a π^{0}_{ID} with at least three reconstructed photons remain $\tau \to h^{\pm} \geq 2\pi^{0}\nu$. The remaining τ_{had} candidates undergo a decay topology test that distinguishes the two likeliest decay topologies for a given candidate. The procedure is depicted in Figures 5.14 and 5.15. The $h^{\pm}\,\{0,1\}\pi^{0}$, $h^{\pm}\,\{1,\geq 2\}\pi^{0}$, and $3h^{\pm}\,\{0,\geq 1\}\pi^{0}$ tests defined in Figures 5.14 and 5.15 are each performed using a BDT classifier [87] that is trained to distinguish the respective decay topologies.

The variables used as input to the BDT are defined in Table 5.6 and the variables used in each test are specified in Table 5.7. The level of separation reached is shown in Figure 5.16. BDT response requirements are made to reach the maximal possible diagonal fraction. They are optimised separately for the two types of τ_{had} candidates, defined by the number of π^{0}_{ID}, that enter each test. The respective decay topology efficiencies are marked in Figure 5.16. The resulting decay topologies are the final ones reconstructed by Tau Particle Flow.

The performance of the topology classification is shown in Figure 5.17. The diagonal fraction is 75%, and increased by four percent points. The fraction of misclassified decays is decreased by 13%. The

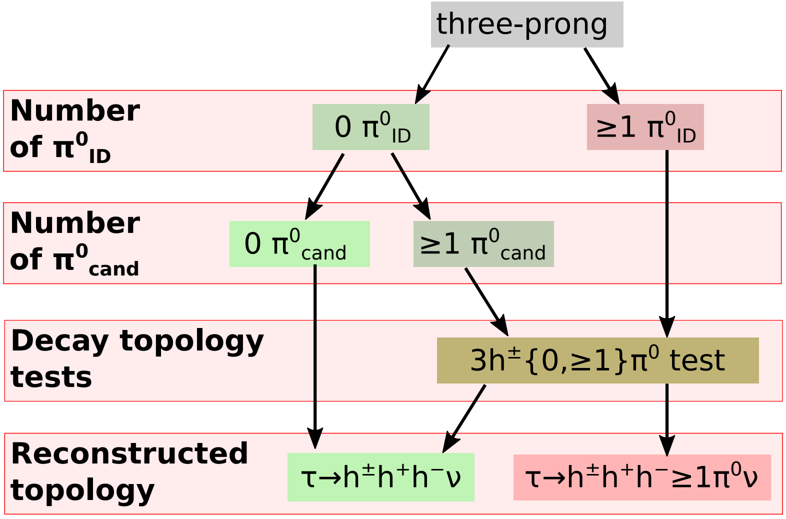

Figure 5.14: Decay topology classification with PanTau for three-prong τ_{had} candidates. Candidates without π^0_{cand} are immediately classified as $\tau \to h^\pm h^+ h^- \nu$. The remaining candidates undergo the so-called $3h^\pm\,\{0, \geq 1\}\pi^0$ test, which distinguishes $\tau \to h^\pm h^+ h^- \nu$ and $\tau \to h^\pm h^+ h^- \geq 1\pi^0 \nu$ decays.

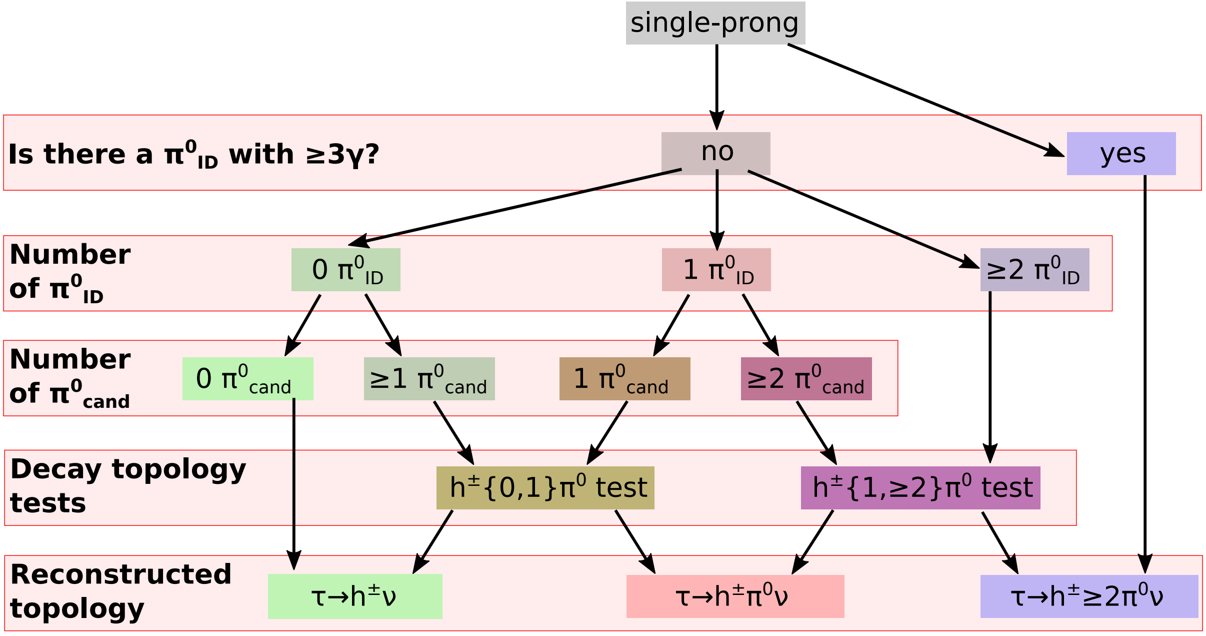

Figure 5.15: Decay topology classification with PanTau for single-prong τ_{had} candidates. Candidates that contain a π^0_{ID} with at least three reconstructed photons (without a π^0_{cand}) are immediately classified as $\tau \to h^\pm \geq 2\pi^0 \nu$ ($\tau \to h^\pm \nu$) decays. The remaining candidates undergo a decay topology test, the type of which is determined from the number of π^0_{ID} and π^0_{cand}. The so-called $h^\pm\,\{0, 1\}\pi^0$ ($h^\pm\,\{1, \geq 2\}\pi^0$) test distinguishes $\tau \to h^\pm \nu$ and $\tau \to h^\pm \pi^0 \nu$ ($\tau \to h^\pm \pi^0 \nu$ and $\tau \to h^\pm \geq 2\pi^0 \nu$) decays.

Symbol	Description
R_1^{BDT}	Highest identification response of a $\pi^0{}_{\mathrm{cand}}$
$f_{\pi^0,1}$	E_{T} of $\pi^0{}_{\mathrm{cand}}$ with highest identification response, divided by E_{T}-sum of all $\pi^0{}_{\mathrm{cand}}$ and core tracks
$\Delta R(h^{\pm},\pi^0)$	ΔR between the core track and the $\pi^0{}_{\mathrm{cand}}$ with the highest identification response
$D_{h^{\pm}}$	E_{T}-weighted ΔR between the core tracks and the four-momentum-sum of all $\pi^0{}_{\mathrm{cand}}$ and core tracks
N_{γ}	Number of reconstructed photons in the strip layer
R_2^{BDT}	Second-highest identification response of a $\pi^0{}_{\mathrm{cand}}$
f_{π^0}	E_{T}-sum of all $\pi^0{}_{\mathrm{cand}}$, divided by E_{T}-sum of all $\pi^0{}_{\mathrm{cand}}$ and core tracks
m_{π^0}	Invariant mass calculated from the sum of the $\pi^0{}_{\mathrm{cand}}$ four-momenta
N_{π^0}	Number of $\pi^0{}_{\mathrm{cand}}$
$\sigma_{E_{\mathrm{T}},h^{\pm}}$	Standard deviation, calculated from the p_{T} values of the core tracks for three-prong τ_{had} candidates
$m_{h^{\pm}}$	Invariant mass calculated from the sum of the core-track four-momenta

Table 5.6: Variables used in PanTau. Adapted from [26].

Decay topology test	Number of $\pi^0{}_{\mathrm{cand}}$	Number of $\pi^0{}_{\mathrm{ID}}$	Variables used in BDT
$h^{\pm}\,\{0,1\}\pi^0$	≥ 1	0	R_1^{BDT}, $f_{\pi^0,1}$, $\Delta R(h^{\pm},\pi^0)$, $D_{h^{\pm}}$, N_{γ}
	1	1	
$h^{\pm}\,\{1,\geq 2\}\pi^0$	≥ 2	1	R_2^{BDT}, f_{π^0}, m_{π^0}, N_{π^0}, N_{γ}
	≥ 2	≥ 2	
$3h^{\pm}\,\{0,\geq 1\}\pi^0$	≥ 1	0	R_1^{BDT}, f_{π^0}, $\sigma_{E_{\mathrm{T}},h^{\pm}}$, $m_{h^{\pm}}$, N_{γ}
	≥ 1	≥ 1	

Table 5.7: Compilation of variables used in each PanTau BDT classifier. Adapted from [26].

$\tau \to h^{\pm}\nu$, $\tau \to h^{\pm}\pi^0\nu$, and $\tau \to h^{\pm}h^{+}h^{-}\nu$ topologies, which represent 73% of the τ_{had} decays and provide access to tau spin effects, are reconstructed with high efficiency and purity.

The topology classification is robust against pile-up even through no dedicated correction is applied (see Figure 5.18). The diagonal fraction and the reconstruction efficiencies for $\tau \to h^{\pm}\nu$, $\tau \to h^{\pm}\pi^0\nu$, and $\tau \to h^{\pm}h^{+}h^{-}\nu$ decays are almost constant versus $E_{\mathrm{T}}^{\tau_{\text{had-vis}}}$ for the full range shown in Figure 5.18. The reconstruction efficiencies for $\tau \to h^{\pm} \geq 2\pi^0\nu$ and $\tau \to h^{\pm}h^{+}h^{-} \geq 1\pi^0\nu$ decays rise up to $E_{\mathrm{T}}^{\tau_{\text{had-vis}}} \approx 40\,\mathrm{GeV}$ because the signal neutral-pion candidates are more likely to pass the p_{T} requirements and to be identified. Generally, the performance is best in the barrel region of the Ecal and poorest in the transition regions between the barrel and endcaps. The η dependence of the efficiencies can be found in Figure A.4. For comparison, the CMS collaboration distinguishes single- and three-prong τ_{had} decays and single-prong decays with and without neutral pions with an accuracy similar to that of Tau Particle Flow. The $\tau \to h^{\pm}\pi^0\nu$ and $\tau \to h^{\pm} \geq 2\pi^0\nu$ topologies are analysed together in CMS and neutral pions are not identified in three-prong decays [117].

The final set of neutral-pion four-momenta is taken from the n neutral-pion candidates with the highest neutral-pion identification BDT response, where n is

- **zero** for reconstructed $\tau \to h^{\pm}\nu$ or $\tau \to h^{\pm}h^{+}h^{-}\nu$ decays,
- **one** for $\tau \to h^{\pm}\pi^0\nu$ and $\tau \to h^{\pm}h^{+}h^{-} \geq 1\pi^0\nu$ decays,
- **two** for $\tau \to h^{\pm} \geq 2\pi^0\nu$ decays.

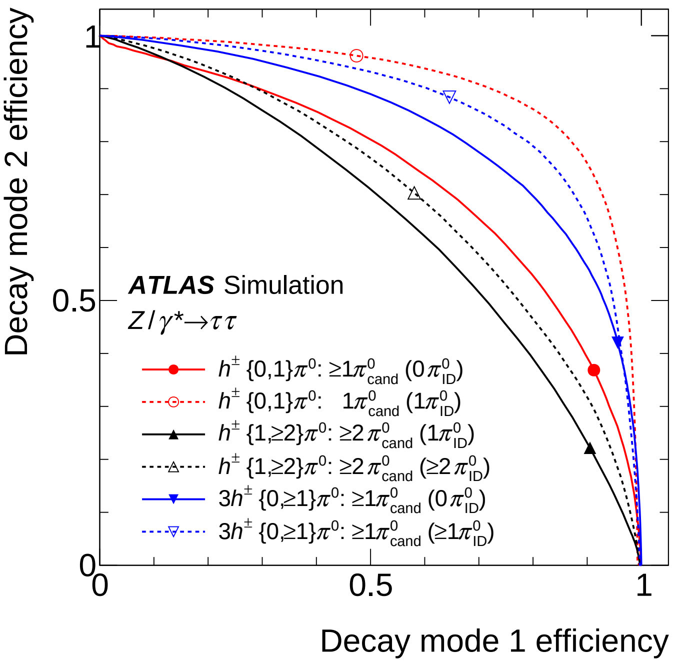

Figure 5.16: Decay topology classification efficiency for the $h^\pm\ \{0,1\}\pi^0$, $h^\pm\ \{1,\geq 2\}\pi^0$, and $3h^\pm\ \{0,\geq 1\}\pi^0$ tests. For each test, "decay mode 1" corresponds to the topology with fewer neutral pions. Working points corresponding to the optimal thresholds on the BDT response for each test are marked. Taken from [26].

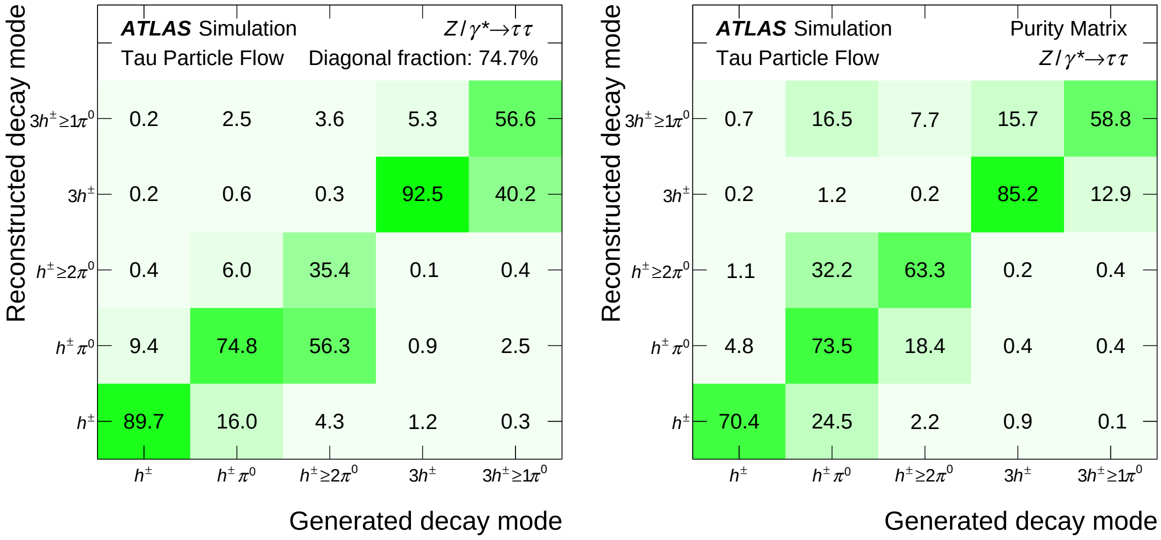

Reconstructed decay mode	$h^\pm$	$h^\pm\pi^0$	$h^\pm{\geq}2\pi^0$	$3h^\pm$	$3h^\pm{\geq}1\pi^0$
$3h^\pm{\geq}1\pi^0$	0.2	2.5	3.6	5.3	56.6
$3h^\pm$	0.2	0.6	0.3	92.5	40.2
$h^\pm{\geq}2\pi^0$	0.4	6.0	35.4	0.1	0.4
$h^\pm\pi^0$	9.4	74.8	56.3	0.9	2.5
$h^\pm$	89.7	16.0	4.3	1.2	0.3

Reconstructed decay mode	$h^\pm$	$h^\pm\pi^0$	$h^\pm{\geq}2\pi^0$	$3h^\pm$	$3h^\pm{\geq}1\pi^0$
$3h^\pm{\geq}1\pi^0$	0.7	16.5	7.7	15.7	58.8
$3h^\pm$	0.2	1.2	0.2	85.2	12.9
$h^\pm{\geq}2\pi^0$	1.1	32.2	63.3	0.2	0.4
$h^\pm\pi^0$	4.8	73.5	18.4	0.4	0.4
$h^\pm$	70.4	24.5	2.2	0.9	0.1

Figure 5.17: Performance of the final decay topology classification of Tau Particle Flow. The probability for a given generated decay topology to be classified as a particular decay topology in simulated $Z/\gamma^* \to \tau\tau$ events (left), and the fraction of τ_{had} candidates of a given classified topology that originated from a particular generated topology (right) are shown in percent. The topologies are labelled by the final state hadrons. Decays with neutral kaons are omitted. The τ_{had} decay selection in Table 5.3 is applied. The statistical uncertainties are negligible. Taken from [26].

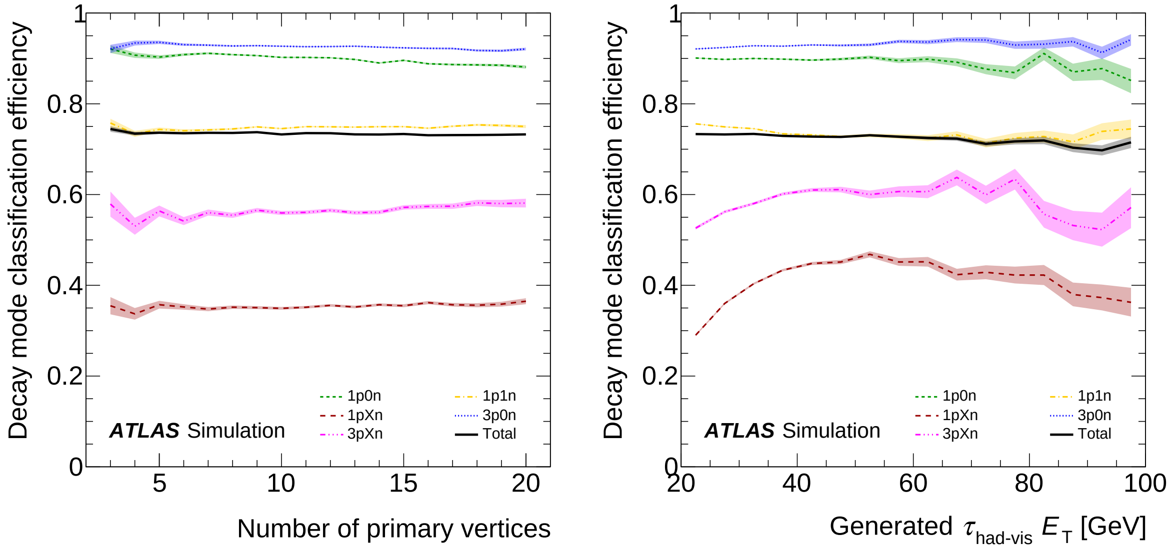

Figure 5.18: Stability of the decay topology classification vs. pile-up (left) and $E_T^{\tau_{\text{had-vis}}}$ (right). The $\tau \rightarrow h^{\pm}\nu$, $\tau \rightarrow h^{\pm}\pi^0\nu$, $\tau \rightarrow h^{\pm} \geq 2\pi^0\nu$, $\tau \rightarrow h^{\pm}h^{+}h^{-}\nu$, and $\tau \rightarrow h^{\pm}h^{+}h^{-} \geq 1\pi^0\nu$ decay topologies are labelled 1p0n, 1p1n, 1pXn, 3p0n, and 3pXn, respectively. The shown uncertainties are statistical. Taken from [26].

The pion mass is assumed. Exceptions are

- Single-prong candidates that include a π^0_{ID} with ≥ 3 reconstructed photons. Only the π^0_{ID} with ≥ 3 photons is considered and its mass is set to twice the pion mass.
- Reconstructed $\tau \rightarrow h^{\pm}\pi^0\nu$ decays with two π^0_{ID}. The π^0_{ID} likely originate from the two photons produced in a neutral-pion decay. A mass of zero is assigned to each and their momenta are summed.

The accuracy of the neutral-pion momentum reconstruction has been shown in Section 5.3.5.

The momenta of the reconstructed neutral pions and of the core tracks are summed. A decay topology dependent energy calibration is applied to compensate for the energy bias in the neutral-pion reconstruction. The result is the constituent-based $\tau_{\text{had-vis}}$ four-momentum. The performance of the $\tau_{\text{had-vis}}$ E_T reconstruction is shown in Figure 5.19. The constituent-based reconstruction is more accurate than the baseline for most τ_{had} decays. However, it significantly underestimates $E_T^{\tau_{\text{had-vis}}}$ if a high p_T neutral pion or kaon is missed, and it overestimates $E_T^{\tau_{\text{had-vis}}}$ if a neutral-pion candidate is misidentified. The final Tau Particle Flow $\tau_{\text{had-vis}}$ momentum, which provides the best performance, is obtained by weighting the baseline and constituent-based momenta by the inverse-square of their respective E_T dependent core resolutions. The baseline is used if the two E_T values differ by more than five times the sum of the core resolutions, because it has smaller residual tails.

The Tau Particle Flow momentum calculation provides a smooth transition between the low-E_T region, where the constituent-based momentum is superior, and the high-E_T region, where the baseline is competitive or better. All three methods are robust against pile-up although the constituent-based momentum does not include a pile-up correction (see Figure A.5). The E_T reconstruction performs best for correctly reconstructed $\tau \rightarrow h^{\pm}\nu$ and $\tau \rightarrow h^{\pm}h^{+}h^{-}\nu$ decays followed by correctly reconstructed decays with neutral pions. Decays with miscounted neutral pions have biases of up to 25%. The biases

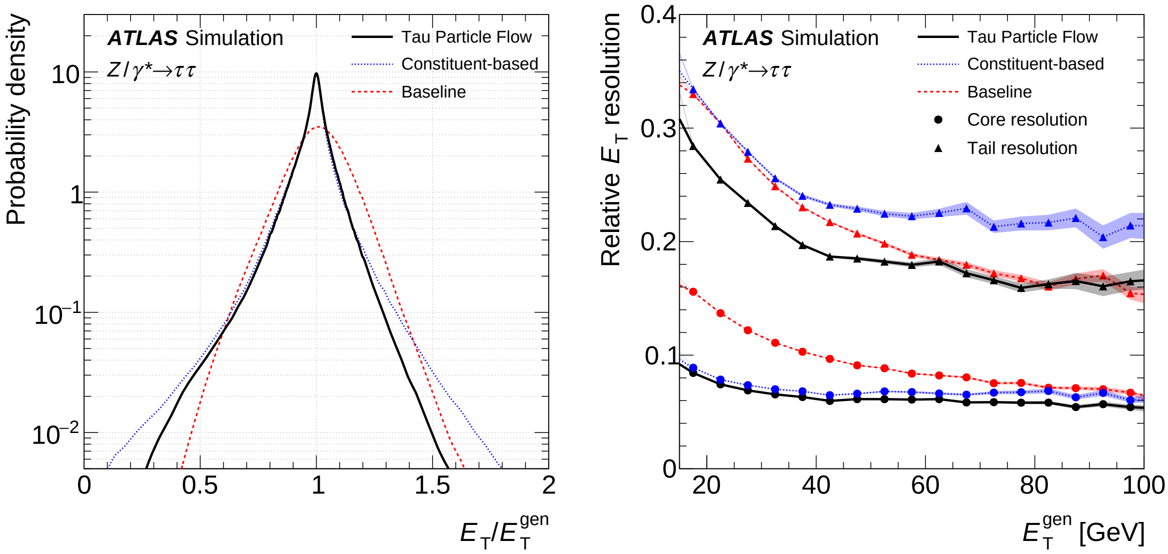

Figure 5.19: Relative $E_T^{\tau_{\text{had-vis}}}$ residuals (left) and the $E_T^{\tau_{\text{had-vis}}}$-dependent core and tail resolutions (right) for the baseline, constituent-based, and final Tau Particle Flow reconstruction. Taken from [26].

are smaller than average neutral-pion energy proportions because low-energy neutral pions are more easily missed and because most background candidates have low momenta. In contrast, neutral kaons are missed irrespective of the momentum fraction they carry, which results in larger low-energy biases. The E_T reconstruction performance for the individual reconstructed decay topologies can be found in Figure A.6.

The constituent-based $\tau_{\text{had-vis}}$ direction is much more accurate than the baseline and directly used in the Tau Particle Flow $\tau_{\text{had-vis}}$ momentum (see Figure 5.20). The abundance of events with very small residuals, in particular in ϕ, originate from correctly reconstructed $\tau \to h^{\pm}\nu$ and $\tau \to h^{\pm}h^{+}h^{-}\nu$ decays. The core resolutions are 0.002 (0.012) in η and 0.004 rad (0.02 rad) in ϕ for the Tau Particle Flow (baseline) momentum.

Overall, the directional $\tau_{\text{had-vis}}$ momentum resolution is improved by more than a factor of five and the energy resolution by up to a factor of two.

5.6 Validation

The modelling of the Tau Particle Flow reconstruction in the simulation for real and misidentified τ_{had} candidates is evaluated using data. The results shown in this section are taken from Ref. [26]. The estimation of systematic uncertainties is in progress and briefly discussed in Section 5.7. Events are selected by a single-muon trigger. Physics objects are reconstructed as described in Section 3.2.6 with the previously described additions in τ_{had} reconstruction.

A sample of **real τ_{had} candidates** is selected from $Z/\gamma^* \to \tau\tau$ data events with one $\tau \to \mu\nu\nu$ and one τ_{had} decay. The final-state muon is used to trigger and tag the event, and the modelling of the τ_{had} decays is studied. This is called a tag-and-probe analysis. The event selection is as follows.

- Exactly one isolated muon with $p_T > 26$ GeV and exactly one τ_{had} candidate with the properties in Table 5.8 are required. They must have opposite electric charges.

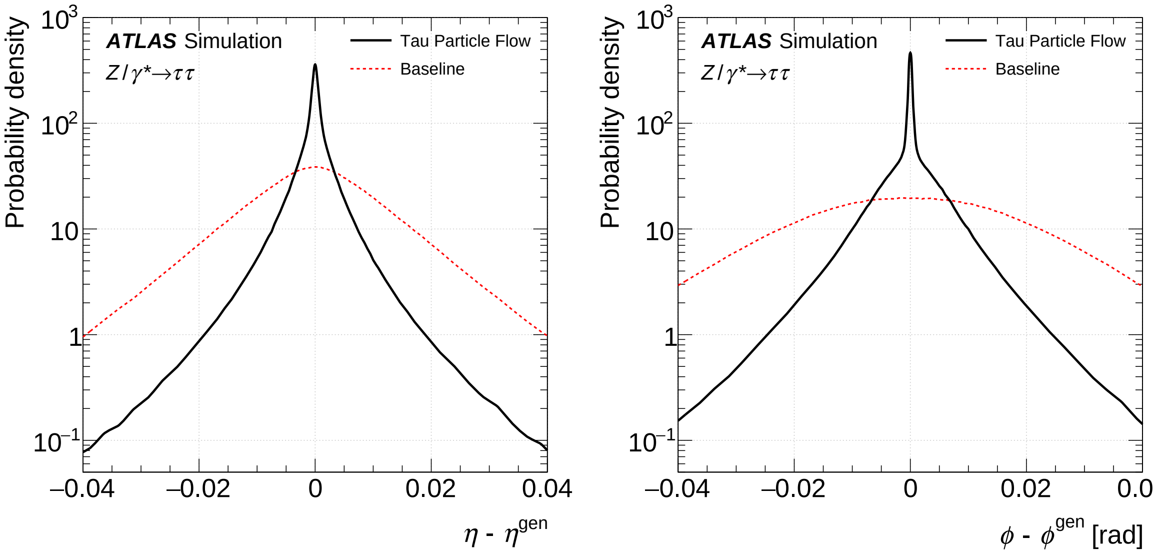

Figure 5.20: The $\tau_{\text{had-vis}}$ η (left) and ϕ (right) residuals for the baseline and the constituent-based (= final Tau Particle Flow) reconstruction. Taken from [26].

Reconstructed single- or three-prong τ_{had} decay
Absolute electric charge of one
Pass *medium* identification, *medium* electron veto, and muon veto
$\lvert\eta^{\tau_{\text{had}}}\rvert < 2.5$, $\lvert p_{\text{T}}^{\tau_{\text{had}}}\rvert > 20\,\text{GeV}$

Table 5.8: Selection of τ_{had} candidates in the validation of Tau Particle Flow. The baseline $\tau_{\text{had-vis}}$ four-momentum is used in the selection. The electron and muon vetoes are omitted in the validation with $Z \to \mu\mu$+jets data events.

- Kinematic requirements are applied:

$$\begin{aligned} m_{\text{T}} &= \sqrt{2 \cdot p_{\text{T}}^{\mu} \cdot E_{\text{T}}^{\text{miss}} \cdot \left(1 - \cos\Delta\phi\left(p_{\text{T}}^{\mu}, E_{\text{T}}^{\text{miss}}\right)\right)} \;<\; 50\,\text{GeV}, \\ \sum \cos\Delta\phi &= \cos\left(\Delta\phi\left(p_{\text{T}}^{\text{lepton}}, E_{\text{T}}^{\text{miss}}\right)\right) + \cos\left(\Delta\phi\left(p_{\text{T}}^{\tau_{\text{had-vis}}}, E_{\text{T}}^{\text{miss}}\right)\right) \;>\; -0.15, \text{ and} \\ 50\,\text{GeV} &< m(\mu, \tau_{\text{had-vis}}^{\text{baseline}}) \;<\; 85\,\text{GeV}, \end{aligned}$$

  where $m(\mu, \tau_{\text{had-vis}}^{\text{baseline}})$ is the invariant mass of the muon and baseline $\tau_{\text{had-vis}}$ four-momenta.

The m_{T} and $\sum\cos\Delta\phi$ requirements suppress the large $W \to \mu\nu$ + jets background. The $m(\mu, \tau_{\text{had-vis}}^{\text{baseline}})$ requirement suppresses all the relevant backgrounds: $W \to \mu\nu$ + jets, multijet, $Z/\gamma^* \to \ell\ell$, and top pair. Similar requirements are explained in Section 6.3.3. The backgrounds are estimated using the techniques from Ref. [98]. The W+jets background is estimated from simulation. Its normalisation is corrected using a W+jets control region, in which the m_{T} and $\sum\cos\Delta\phi$ requirements are modified, similar as in Section 6.4.2. The multijet background is estimated from control regions in which the opposite-electric-charges or muon-isolation requirements are modified, similar as in Section 6.4.3. The minor $Z/\gamma^* \to \ell\ell$ and top pair backgrounds are taken from simulation.

A sample of **background τ_{had} candidates** is selected from $Z \to \mu\mu$+jets data events that also include

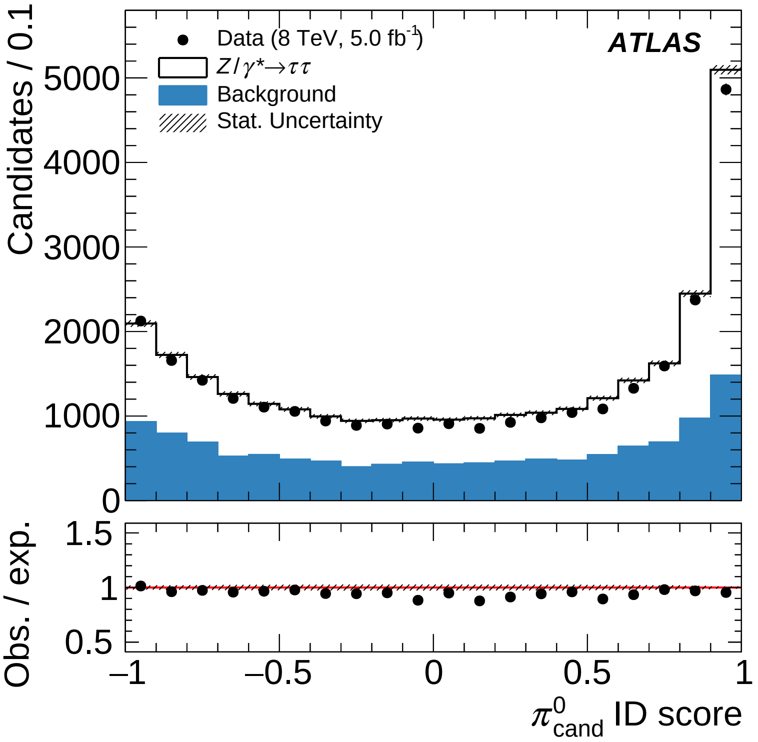

Figure 5.21: Distribution of the neutral-pion identification BDT response in the $Z/\gamma^* \rightarrow \tau\tau$ tag-and-probe analysis. The background (blue histogram) is dominated by multijet and $W \rightarrow \mu\nu$ + jets production. The shown uncertainties are statistical. Taken from [26].

an identified τ_{had} candidate. The selection is:

- Two isolated muons with $p_{\text{T}} > 26\,\text{GeV}$ are required. They must have opposite electric charges, and an invariant mass of 81–101 GeV.
- The highest-p_{T} jet must pass the τ_{had} selection in Table 5.8.

The muons serve as tags, and the probe τ_{had} candidates mostly originate from quark-initiated jets. The $Z/\gamma^* \rightarrow \mu\mu$ contribution is estimated from simulation and other contributions are negligible. Before the τ_{had} selection, the p_{T}^{Z} spectrum is reweighted to match the data. The p_{T}^{Z} distribution before that reweighting can be found in Figure A.7. After the τ_{had} selection, the estimate is scaled to the data.

The BDT response distribution in the $Z/\gamma^* \rightarrow \tau\tau$ tag-and-probe analysis is shown in Figure 5.21. The prediction is not perfect but still reasonable. The number of neutral-pion candidates is slightly overestimated overall and preferentially at high BDT response values. The reconstructed decay topology distributions are shown in Figure 5.22. The abundance of reconstructed $\tau \rightarrow h^{\pm}h^{+}h^{-}\nu$ decays is underestimated in both analyses and those of $\tau \rightarrow h^{\pm} \geq 2\pi^{0}\nu$ and $\tau \rightarrow h^{\pm}h^{+}h^{-} \geq 1\pi^{0}\nu$ decays are slightly overestimated. Overall, the modelling is reasonable. The decay topology distribution in misidentified τ_{had} decays resembles that in real τ_{had} decays, which indicates that the charged-hadron and neutral-pion multiplicity distributions of background and signal candidates are similar after τ_{had} identification.

The distribution of the visible mass obtained from the muon and the Tau Particle Flow τ_{had} four-momenta, $m(\mu, \tau_{\text{had-vis}})$, in the $Z/\gamma^* \rightarrow \tau\tau$ analysis before the $50 < m(\mu, \tau_{\text{had-vis}}^{\text{baseline}}) < 85\,\text{GeV}$ cut is

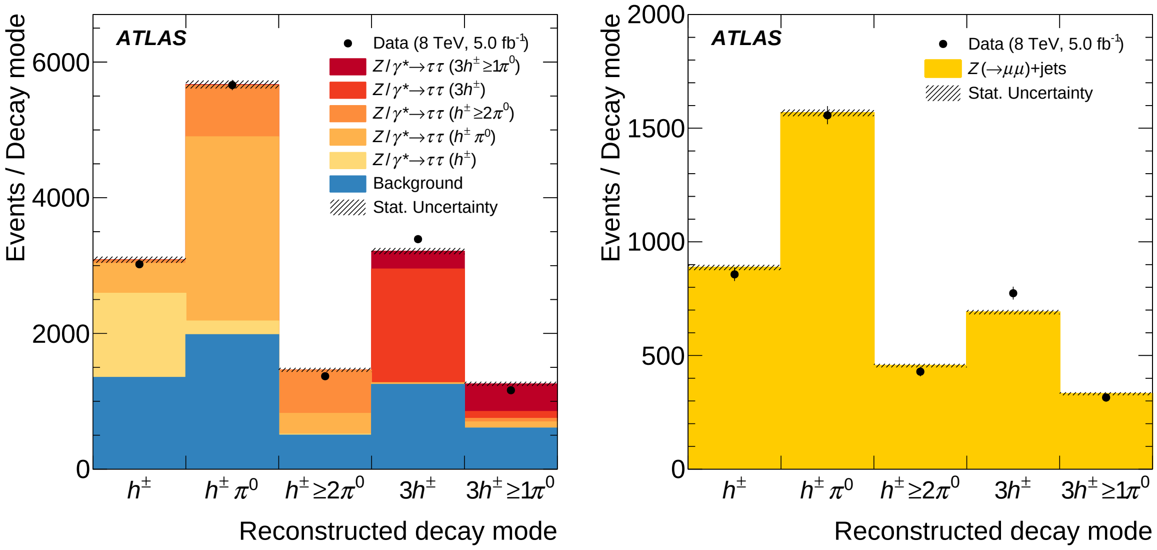

Figure 5.22: Number of $\tau_{\text{had-vis}}$ candidates for each classified decay topology in the $Z/\gamma^* \to \tau\tau$ (left) and $Z/\gamma^* \to \mu\mu$ (right) tag-and-probe analyses. The simulated $Z/\gamma^* \to \tau\tau$ sample is split into contributions from each generated tau decay topology. The background in the $Z/\gamma^* \to \tau\tau$ analysis (blue histogram) is dominated by multijet and $W \to \mu\nu$ + jets production. The shown uncertainties are statistical. Taken from [26].

shown in Figure 5.23. Within the statistical uncertainties, the prediction reproduces the data well in the signal-dominated region of 50–85 GeV. The modelling in the background-dominated tails is reasonable. The $m(\mu, \tau_{\text{had-vis}})$ variable depends linearly on the $\tau_{\text{had-vis}}$ E_{T} and can be used to judge its modelling. The $m(\mu, \tau_{\text{had-vis}}^{\text{baseline}})$ distribution has been used to calibrate $E_{\text{T}}^{\tau_{\text{had-vis}}}$ and to estimate systematic uncertainties [82, 138].

Figure 5.24 shows the $\tau_{\text{had-vis}}$ mass distributions in both analyses. The $\tau_{\text{had-vis}}$ mass was previously not reconstructed at ATLAS. The prediction agrees well with the data in the $Z/\gamma^* \to \tau\tau$ analysis, which indicates an accurate modelling of the reconstructed charged-hadron and neutral-pion four-momenta. The modelling is also reasonable in the $Z/\gamma^* \to \mu\mu$ analysis. The slightly larger discrepancies compared with those found for real τ_{had} decays may originate from inaccuracies in the parton-shower modelling. The events in the 100–200 MeV mass bin stem from reconstructed $\tau \to h^{\pm}\nu$ decays. The a_1 resonance in $\tau \to h^{\pm}h^{+}h^{-}\nu$ decays is reproduced with negligible experimental resolution because its decay products are reconstructed in the ID. Reconstructed $\tau \to h^{\pm}\pi^{0}\nu$ decays peak around the ρ mass of 775 MeV [27] but the reconstructed distribution is much wider than the intrinsic width of the ρ meson of 149 MeV. The a_1 resonance in $\tau \to h^{\pm} \geq 2\pi^{0}\nu$ decays is also visible. The reconstructed $\tau_{\text{had-vis}}$ mass distributions for generated $\tau \to h^{\pm}\nu$, $\tau \to h^{\pm}\pi^{0}\nu$, and $\tau \to h^{\pm}h^{+}h^{-}\nu$ decays can be found in Figure A.8.

5.7 Recent Developments and Outlook

This section documents studies directly related with the Tau Particle Flow reconstruction subsequent to Ref. [26], the ATLAS publication about Tau Particle Flow in which I was directly involved. The more recent studies have been performed using Run 2 samples of proton–proton collisions at a centre-of-mass energy of 13 TeV and with the upgraded ATLAS detector. The largest detector upgrades are related to the insertable B-layer [75] and the trigger system [76].

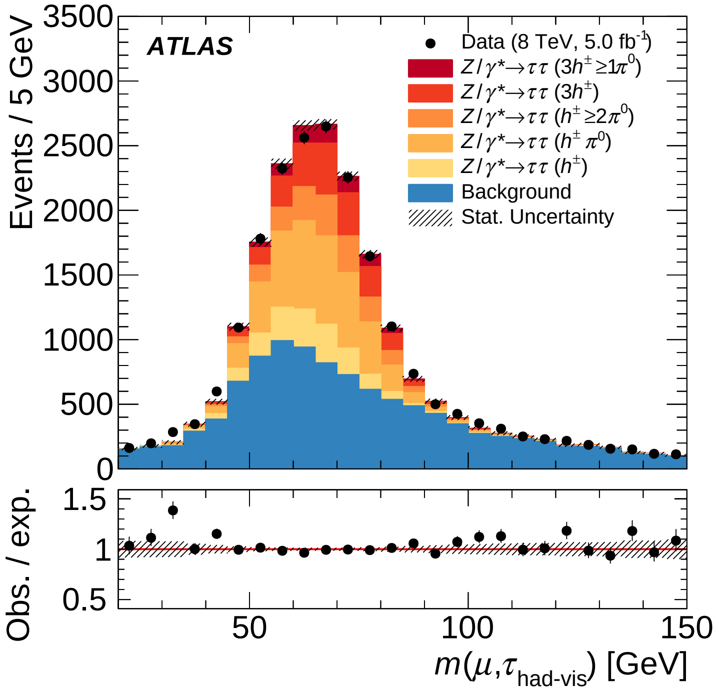

Figure 5.23: Distribution of the visible mass, which is the invariant mass of the muon and Tau Particle Flow $\tau_{\text{had-vis}}$, in the $Z/\gamma^* \rightarrow \tau\tau$ tag-and-probe analysis. The requirement $50 < m(\mu, \tau_{\text{had-vis}}^{\text{baseline}}) < 85$ GeV is dropped. The simulated $Z/\gamma^* \rightarrow \tau\tau$ sample is split into contributions from each generated tau decay topology. The background (blue histogram) is dominated by multijet and $W \rightarrow \mu\nu$ + jets production. The shown uncertainties are statistical. Taken from [26].

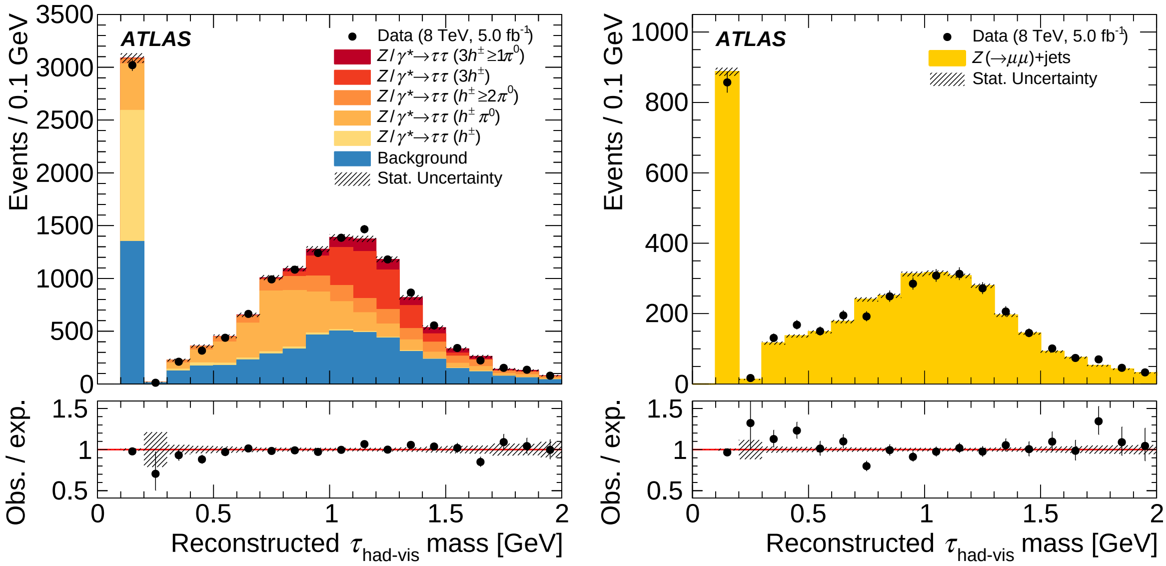

Figure 5.24: The Tau Particle Flow $\tau_{\text{had-vis}}$ mass distribution of τ_{had} candidates in the $Z/\gamma^* \rightarrow \tau\tau$ (left) and $Z/\gamma^* \rightarrow \mu\mu$ (right) tag-and-probe analyses. The simulated $Z/\gamma^* \rightarrow \tau\tau$ sample is split into contributions from each generated tau decay topology. The background in the $Z/\gamma^* \rightarrow \tau\tau$ analysis is dominated by multijet and $W \rightarrow \mu\nu$ + jets production. The shown uncertainties are statistical. Taken from [26].

The τ_{had} reconstruction and identification are being studied in simulated $Z/\gamma^* \to \tau\tau$ events as well as in a simulated sample of $\gamma^* \to \tau_{\text{had}}\tau_{\text{had}}$ decays without a Z boson component. In the latter sample, the mass spectrum is set to be smoothly decreasing over a large range without an abundance of events at the Z boson pole (see Figure A.9). This sample provides linearly unpolarised τ_{had} decays and covers a wide $p_{\text{T}}^{\tau_{\text{had-vis}}}$ spectrum (see Figure A.10). Further details about the samples can be found in Refs. [88, 138, 139].

The previously described Tau Particle Flow algorithms, with a cluster-level subtraction in TauPi0Rec, are part of the default τ_{had} reconstruction in Run 2 at ATLAS. The largest conceptual change with respect to Sections 5.3–5.5 is that neutral pions are now reconstructed in the presampler and all Ecal layers including Ecal3. This minimises leakage of photon showers at very high momenta. The τ_{had} identification input variables previously calculated by the Pi0Finder algorithm are replaced by other variables, specifically a subset of the previous inputs to the Pi0Finder algorithm. The τ_{had} identification performance is unaltered by this change. The updated set of variables used in τ_{had} identification can be found in Ref. [138].

The reconstruction of the $\tau_{\text{had-vis}}$ energy has been further improved. The baseline and constituent-based four-momenta are combined using multivariate techniques [138]. The $p_{\text{T}}^{\tau_{\text{had-vis}}}$ reconstruction performance is shown in Figure 5.25. At low momenta, the improvement in the p_{T} core resolution is similar as in Figure 5.19. However, the range in which the reconstruction is improved is extended significantly. The energy scale was measured with an accuracy of about 2% using the $m(\mu, \tau_{\text{had-vis}})$ distribution as in Run 1 [138]. The new $\tau_{\text{had-vis}}$ momentum reconstruction is being used in physics analyses. Due to observations made in the recent measurement of the tau polarisation in $Z/\gamma^* \to \tau\tau$ decays (see Chapter 6), the energy scale is measured using the Υ (see Eq. (2.21)) distribution. The results are expected to be more accurate.

A more advanced selection of charged-particle tracks using multivariate techniques has been used [139]. This method reconstructs the charged-hadron multiplicity and selects the correct set of charged-hadron tracks with significantly higher probability. In particular, the probability to reconstruct real τ_{had} candidates with an even number of tracks, which causes them to be lost in most analyses, is reduced. The new method also identifies electron tracks that stem from photon conversions, which may be utilised to further improve the reconstruction of neutral pions.

The performance of the decay topology classification in the $\gamma^* \to \tau_{\text{had}}\tau_{\text{had}}$ sample is shown in Figure 5.26. The τ_{had} decay selection is that used in Figures 5.9 and 5.17 except that the tau identification requirement and electron veto are dropped, the transition region $1.37 < |\eta| < 1.52$ is vetoed, and $20 < \tau_{\text{had-vis}} < 100\,\text{GeV}$ is required. The transition-region veto is a standard requirement in τ_{had} reconstruction in Run 2. The $\tau_{\text{had-vis}} < 100\,\text{GeV}$ requirement selects the kinematic region of primary interest for Tau Particle Flow. The advanced track selection is used. The neutral-pion counting performance is qualitatively similar to Run 1. Quantitative comparisons are very difficult due to various differences between the samples and selection requirements.

Systematic uncertainties in the decay topology classification are being estimated in a $Z/\gamma^* \to \tau\tau$ tag-and-probe analysis and an in-situ method. Specifically, a template fit to the Υ distribution is being performed. Accurate information about reconstructed τ_{had} decay topologies is essential for an ongoing measurement of the Higgs boson's CP properties in $H \to \tau\tau$ decays and may be valuable for further analyses of $H \to \tau\tau$, $Z/\gamma^* \to \tau\tau$, and other decays with tau leptons.

The performance of the decay topology classification can be improved further by utilising recurrent neural networks (RNN), as demonstrated in Ref. [88]. In the same sample and with the same selection as in Figure 5.26, RNN reach a diagonal fraction of 78% instead of 73% when using the same information as the PanTau algorithm. Larger improvements are possible when considering reconstructed photon-conversion tracks and further information [88]. An obtainable performance of the decay topology

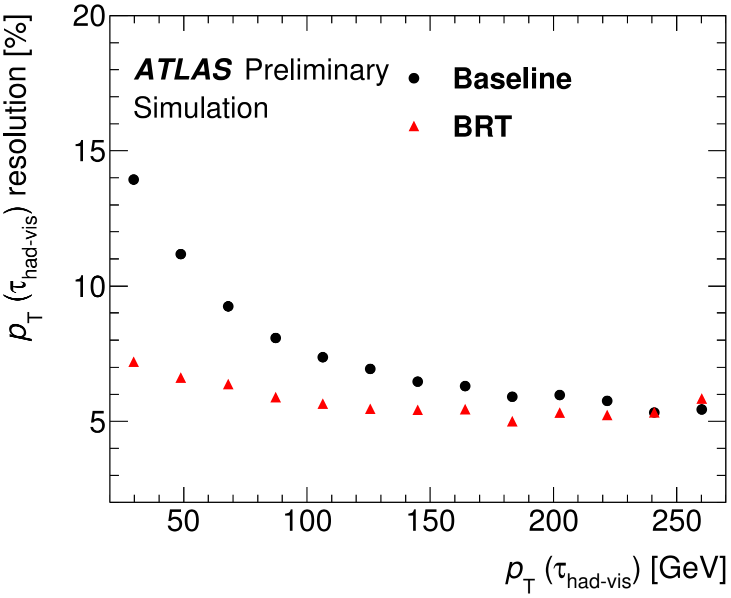

Figure 5.25: The $p_{\mathrm{T}}^{\tau_{\text{had-vis}}}$ core resolutions reached by the baseline reconstruction and with a multivariate regression method (“BRT”) in simulated $Z/\gamma^* \to \tau\tau$ decays in Run 2. The core resolution is shown as a function of the generated $p_{\mathrm{T}}^{\tau_{\text{had-vis}}}$. The p_{T} core resolution is analogous to the previously defined E_{T} core resolution, and $p_{\mathrm{T}} = E_{\mathrm{T}}$ for boosted $\tau_{\text{had-vis}}$ like those shown. Taken from [138].

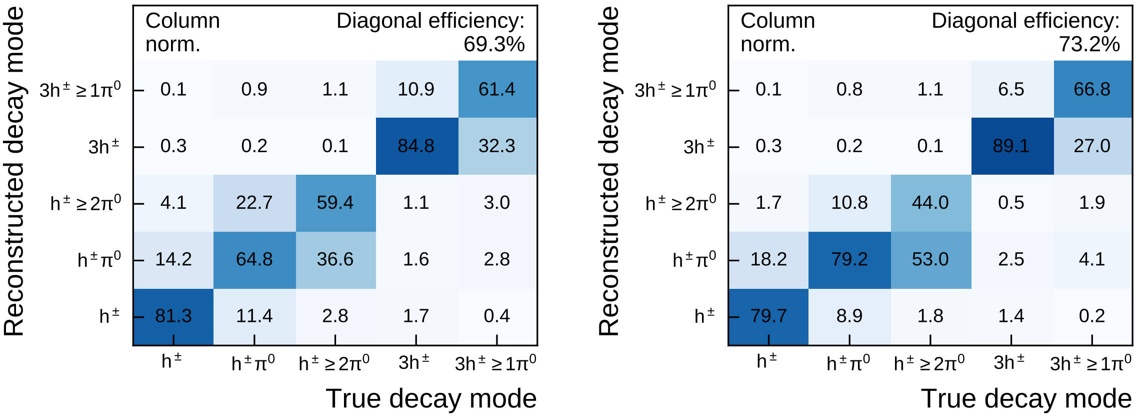

Reconstructed decay mode	$h^\pm$	$h^\pm\pi^0$	$h^\pm \geq 2\pi^0$	$3h^\pm$	$3h^\pm \geq 1\pi^0$
$3h^\pm \geq 1\pi^0$	0.1	0.9	1.1	10.9	61.4
$3h^\pm$	0.3	0.2	0.1	84.8	32.3
$h^\pm \geq 2\pi^0$	4.1	22.7	59.4	1.1	3.0
$h^\pm\pi^0$	14.2	64.8	36.6	1.6	2.8
$h^\pm$	81.3	11.4	2.8	1.7	0.4

Reconstructed decay mode	$h^\pm$	$h^\pm\pi^0$	$h^\pm \geq 2\pi^0$	$3h^\pm$	$3h^\pm \geq 1\pi^0$
$3h^\pm \geq 1\pi^0$	0.1	0.8	1.1	6.5	66.8
$3h^\pm$	0.3	0.2	0.1	89.1	27.0
$h^\pm \geq 2\pi^0$	1.7	10.8	44.0	0.5	1.9
$h^\pm\pi^0$	18.2	79.2	53.0	2.5	4.1
$h^\pm$	79.7	8.9	1.8	1.4	0.2

Figure 5.26: Decay topology classification performance of the TauPi0Rec algorithm (left) and full Tau Particle Flow (right) algorithms in Run 2. Strip layer hits are already used to recover $\tau \to h^\pm \geq 2\pi^0\nu$ decays in the left figure. The probability for a given generated decay topology to be classified as a particular decay topology in simulated $\gamma^* \to \tau_{\text{had}}\tau_{\text{had}}$ events is shown in percent. The topologies are labelled by the final state hadrons. Decays with neutral kaons are omitted. The τ_{had} decay selection is specified in the text. The statistical uncertainties are negligible. Taken from [88].

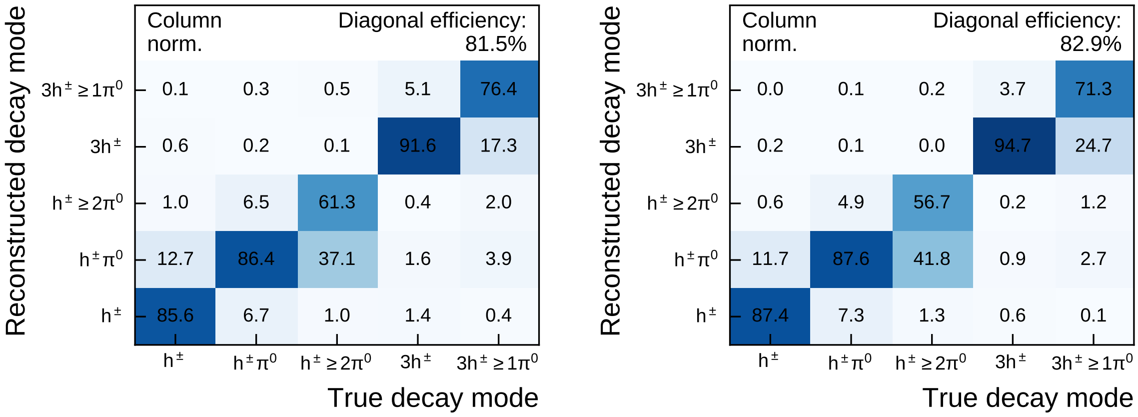

Figure 5.27: Decay topology classification performance possible with recurrent neural networks (text). The selection and sample is the same as in Figure 5.26 (left) except that τ_{had} identification is applied (right). The probability for a given generated decay topology to be classified as a particular decay topology in simulated $\gamma^* \to \tau_{\text{had}}\tau_{\text{had}}$ events is shown in percent. The topologies are labelled by the final state hadrons. Decays with neutral kaons are omitted. The τ_{had} decay selection is specified in the text. The statistical uncertainties are negligible. Taken from [88].

classification is shown in Figure 5.27. The fraction of misreconstructed decay topologies is reduced by 31% for the selection in Figure 5.26. After τ_{had} identification, which is nearly always applied in physics analyses, the $\tau \to h^{\pm}\nu$, $\tau \to h^{\pm}\pi^{0}\nu$, and $\tau \to h^{\pm}h^{+}h^{-}\nu$ decays can all be reconstructed with an efficiency of $\geq 87\%$ and a purity of $\geq 80\%$ (see Figure A.11). The method has not yet been validated with data.

While it is very difficult to improve the $\tau_{\text{had-vis}}$ momentum reconstruction substantially at high momenta using particle-flow techniques, information about reconstructed τ_{had} decay topologies and neutral pions may be useful to some analyses such as measurements of the tau polarisation in $\tau\tau$ or $\tau\nu_{\tau}$ final states with large invariant mass. A diagonal fraction of 78% can be reached for the τ_{had} candidates in the $\gamma^* \to \tau_{\text{had}}\tau_{\text{had}}$ sample with $p_{\text{T}}^{\tau_{\text{had-vis}}} > 100\,\text{GeV}$ when extending the previously mentioned RNN to these candidates [88].

CHAPTER 6

Measurement of Tau Polarisation in $Z/\gamma^* \rightarrow \tau\tau$ Decays

This chapter presents a measurement of the average tau polarisation in $Z/\gamma^* \rightarrow \tau\tau$ decays in proton–proton collisions at ATLAS [25]. The $20.2\,\mathrm{fb}^{-1}$ dataset recorded at a centre-of-mass energy of $\sqrt{s} = 8\,\mathrm{TeV}$ in 2012 is utilised.

The most precise tau polarisation measurement in $Z/\gamma^* \rightarrow \tau\tau$ decays has been performed by the experiments at the Large Electron–Positron Collider (LEP) [23]. An asymmetry in the $Z\tau\tau$ coupling of $A_\tau = 0.1439 \pm 0.0043$ was found. Combined with the corresponding result for the Zee coupling from the same measurement, $A_e = 0.1498 \pm 0.0049$, it corresponds to an effective weak mixing angle of $\sin^2\theta_\mathrm{W}^\mathrm{eff} = 0.23159 \pm 0.00041$ (using Eq. (2.24) and corrections for radiative effects, the $\gamma^* \rightarrow \tau\tau$ contribution, and the Z–γ interference [23]).

The presented measurement is complementary to the LEP measurement. The Z bosons are produced via a qqZ vertex instead of an eeZ vertex, and there might be unknown ditau production processes specific to hadron colliders. A signal region enhanced with $Z/\gamma^* \rightarrow \tau\tau$ events with one τ_lep decay and one single-prong τ_had decay is selected. The lepton is used to trigger the event, and helps in suppressing backgrounds. The τ_had decay is unbiased by the trigger and serves as a spin analyser. The major W+jets and multijet backgrounds are estimated using data-driven methods. The signal contribution as well as the minor backgrounds from $Z/\gamma^* \rightarrow \ell\ell$ and top pair events are estimated from the simulation. Binned maximum-likelihood fits to the Υ distribution (see Eq. (2.21)) are performed to determine the tau polarisation.

The polarisation is measured for two kinematic regions that are defined using generator-level quantities: a fiducial region that closely resembles the signal region, and the full phase space within the mass-selected region of $66\,\mathrm{GeV} < m_{Z/\gamma^*} < 116\,\mathrm{GeV}$. The results are compared with predictions obtained from the ALPGEN [128] event generator, which is interfaced with the PYTHIA6 [140] parton shower and underlying event modelling as well as with the TAUOLA [122] tau decay library. An approximate $\sin^2\theta_\mathrm{W}^\mathrm{eff}$ value is determined from the tau polarisation in the mass-selected region by using Eq. (2.24) without performing corrections for the photon contribution.

The first and so far only other tau polarisation measurement at a hadron collider was performed in $W \rightarrow \tau\nu$ decays at ATLAS [24]. It is based on $24\,\mathrm{pb}^{-1}$ of proton–proton–collision data recorded at $\sqrt{s} = 7\,\mathrm{TeV}$ in 2010 and has confirmed that parity is maximally violated in $W \rightarrow \tau\nu$ decays. The methodology to determine the tau polarisation with template fits to the observable Υ is retained from that measurement. In the analysis on hand, refined experimental techniques for tau polarisation measurements at hadron colliders are pioneered. Uncertainties in the modelling of the Υ observable for signal events and the background contributions are estimated more accurately. These techniques make it possible to benefit from the large ($20.2\,\text{fb}^{-1}$) dataset and account for the presence of significant backgrounds in ditau final states. In the future, they may be used to study properties of the Higgs boson in $H \to \tau\tau$ decays [6] or to measure the tau polarisation in ditau or tau–$E_{\text{T}}^{\text{miss}}$ final states at higher masses. Furthermore, tau polarisation can be used to select signals that share a final state involving taus with a large SM background but have a different helicity configuration [10]. Possible examples are decays of neutral and charged Higgs bosons to the final states of $Z/\gamma^* \to \tau\tau$ and $W \to \tau\nu$ decays, respectively.

This chapter is structured as follows. The data and simulated samples are introduced in the first section. The physics objects are defined in Section 6.2. In the next section the selection of events is presented and its effect on the signal is discussed. The background estimates and the related systematic uncertainties are covered in Section 6.4. The estimates are compared with the data in the signal region and other kinematic regions. Section 6.5 documents the estimation of the systematic uncertainties in the simulated samples. The fit models used to determine the tau polarisation are introduced and validated in Section 6.6. The results are presented in the final section.

This measurement is the result of a team effort by postdoctoral researchers and (post-)graduate students as customary at ATLAS. The analysis team consisted of about 15 people overall, including supervisors. Typically two to four people contributed actively at a time. I was a key analyser from an early stage of the analysis to its completion. I made major contributions to the estimation of the systematic uncertainties, the fit models, the event selection and evaluating its effect on the signal, and to background estimates. I was an editor of the ATLAS publication of the results of the tau polarisation analysis [25]. Additionally, I wrote or maintained and ran the computer code required to process the data starting from a standard ATLAS format to the results presented in the publication and in this chapter.

6.1 Data and Simulated Samples

The measurement is based on the ATLAS dataset of proton–proton collisions collected at a centre-of-mass energy of $\sqrt{s} = 8\,\text{TeV}$, which corresponds to $20.2\,\text{fb}^{-1}$. Events were selected by triggers that require an isolated electron or muon with $p_{\text{T}} > 24\,\text{GeV}$ [74]. Alternative triggers require an electron with $p_{\text{T}} > 60\,\text{GeV}$ or a muon with $p_{\text{T}} > 36\,\text{GeV}$ without isolation requirements. Events are categorised into the τ_e–τ_{had} and τ_μ–τ_{had} channels based on whether they were selected by an electron or a muon trigger. An event may appear in both channels at this stage. Double counting of events is avoided subsequently.

Samples of simulated events are used to model the signal and some background contributions. The nominal signal sample consists of $Z/\gamma^* \to \tau\tau$ decays with $m_{Z/\gamma^*} > 60\,\text{GeV}$ and was created with the matrix-element-based Alpgen [128] event generator with default electroweak parameters (see Table 6.1). Complying with the LO relations between the parameters ensures gauge invariance and avoids unphysical corrections in the calculations [128]. In particular, the effective weak mixing angle cannot be used in the LO matrix element. The matrix elements were computed for up to six additional partons.

The Alpgen event generator was interfaced with the Pythia6 [140] parton shower and underlying event (UE) modelling with the Perugia2011C tune [129]. The CTEQ6L1 PDF set [126] was used. Electromagnetic radiation was modelled with the Photos [123] algorithm. The tau helicity states were not stored in the generation of the $Z/\gamma^* \to \tau\tau$ production process. Hence, the helicity states and spin correlations were simulated with the Tauola Universal Interface [141] assuming the effective weak mixing angle, $\sin^2\theta_{\text{W}}^{\text{eff}} = 0.23147$, in the LO matrix element. Tau decays were modelled with the Tauola [122] decay library. The systematic uncertainty resulting from the inconsistency between the weak mixing angles assumed in the generation of the $Z/\gamma^* \to \tau\tau$ production process and in the modelling of the tau decays is evaluated in following sections. It has a minor effect on the measurement.

Parameter	Value	Calculated from
W boson mass	$m_W = 80.41\,\text{GeV}$	(input)
Z boson mass	$m_Z = 91.188\,\text{GeV}$	(input)
Fermi coupling constant	$G_\text{F} = 1.16639 \times 10^{-5}\,\text{GeV}^{-2}$	(input)
Weak mixing angle	$\sin^2\theta_\text{W} = 0.2224$	$\sin^2\theta_\text{W} = 1 - m_W^2/m_Z^2$
SU(2) gauge coupling constant	$g = 0.653$	$g^2 = 4\sqrt{2}G_\text{F}m_W^2$
Fine-structure constant	$\alpha_\text{EM} = 1/132.42$	$\alpha_\text{EM} = g^2\sin^2\theta_\text{W}/(4\pi)$

Table 6.1: Electroweak parameters assumed in the Alpgen event generator (`ievopt=3`) [128]. The first three values are taken as inputs. The latter three are calculated from the shown LO gauge relationships.

Process	Event generator	PDF	UE tune
$(Z/\gamma^* \to \tau\tau)$ + jets	Alpgen 2.14 [128] + Pythia6.427 [140]	CTEQ6L1 [126]	Perugia2011C [129]
$(Z/\gamma^* \to \tau\tau)$ + jets	Pythia 8.160 [118]	CTEQ6L1	AU2 [127]
$(Z/\gamma^* \to \tau\tau)$ + jets	Powheg r1556 [142–144] + Pythia 8.160	CT10 [135]	AUET2 [145]
$(Z/\gamma^* \to \tau\tau)$ + jets	Alpgen 2.14 + Herwig 6.5/Jimmy 4.3 [133, 134]	CTEQ6L1	Perugia2011C
Top pairs + jets	Powheg r2129 + Pythia 6.426	CT10	AUET2
$(W \to e\nu$ + jets) + jets	Alpgen 2.14 + Pythia 6.427	CTEQ6L1	Perugia2011C
$(W \to \mu\nu$ + jets) + jets	Alpgen 2.14 + Pythia 6.427	CTEQ6L1	Perugia2011C
$(W \to \tau\nu$ + jets) + jets	Alpgen 2.14 + Pythia 6.427	CTEQ6L1	Perugia2011C
$(Z/\gamma^* \to ee)$ + jets	Alpgen 2.14 + Pythia 6.427	CTEQ6L1	Perugia2011C
$(Z/\gamma^* \to \mu\mu)$ + jets	Alpgen 2.14 + Pythia 6.427	CTEQ6L1	Perugia2011C

Table 6.2: List of simulated event samples. The processes, event generators, PDF sets, and underlying-event tunes are shown. Adapted from [25].

An auxiliary signal sample was created using the Alpgen event generator interfaced with the Herwig/Jimmy [133, 134] parton shower and UE modelling. The tau helicity states, spin correlations, and tau decays were modelled as in the nominal signal sample. The sample is used to evaluate the uncertainties in the parton shower and UE modelling and referred to as the Alpgen+Jimmy sample. Further auxiliary signal samples were created using the Pythia8 [118] event generator and using the Powheg [142–144] event generator interfaced with the Pythia8 parton shower, UE, and tau decay modelling. They are referred to as Pythia8 sample and Powheg+Pythia8 sample, respectively, and are used to evaluate the uncertainties in the modelling of the $Z/\gamma^* \to \tau\tau$ production process. The PDF sets and UE tunes are listed in Table 6.2.

The simulated tau helicity states were not stored. Hence, each signal sample is split into a subsample with left-handed taus and another with right-handed taus outside the event generation procedure. Left-handed and right-handed refer to the respective chiral states that the helicity states agree with in the ultra-relativistic limit. Explicitly, τ^- particles with helicity $\lambda = -1/2$ ($\lambda = +1/2$) are called left-handed (right-handed), and vice versa for τ^+ antiparticles. The splitting into subsamples is performed using the TauSpinner [146] algorithm associated with the Tauola library. It assigns the tau helicities randomly based on probabilities computed from the kinematic configuration of the tau decays. The spin correlations are assumed to match the predictions for $Z/\gamma^* \to \tau\tau$ decays. While the Tauola library utilises the stable-particle-level information about the incoming partons, the TauSpinner algorithm averages over all possible incoming quark combinations weighted using the MRSTMCal [147] PDF set. The TauSpinner algorithm has been validated extensively [146, 148, 149] and used in measurements [109, 150].

Samples of $Z/\gamma^* \to ee$, $Z/\gamma^* \to \mu\mu$, $W \to e\nu$ + jets, $W \to \mu\nu$ + jets, and $W \to \tau\nu$ + jets events were created using the Alpgen event generator interfaced with the Pythia6 parton shower and UE modelling. Electromagnetic radiation and tau decays were modelled as in the nominal signal sample and the same UE event tune and PDF set were used. A sample of top pair events was created using the Powheg event generator interfaced with the Pythia6 parton shower and UE modelling. Only events with at least one $W \to e\nu$, $W \to \mu\nu$, or $W \to \tau\nu$ decay subsequent to a top quark decay were accepted. The CT10 [135] PDF set and AUET2 [145] UE tune were used. Tau decays were modelled as in the nominal signal sample.

The response of the ATLAS detector was simulated [124] using the Geant4 toolkit [125]. The simulated events were overlaid with additional minimum-bias events created with the Pythia8 event generator, which account for in-time and out-of-time pile-up interactions. Each sample is reweighted such that the spectrum of the average number of pile-up interactions per bunch crossing matches that found in data. This procedure is referred to as pile-up reweighting. The data and simulated samples are processed through the same reconstruction algorithms. Corrections are applied that account for known differences between the reconstruction and identification of physics objects in simulated and data events following ATLAS recommendations.

The samples with Z or W boson decays, including the signal sample, are scaled such that the total cross-sections match the respective inclusive next-to-next-to-leading-order (NNLO) predictions [151]. The top pair sample is scaled to the next-to-next-to-leading-logarithm (NNLO+NNLL) cross-section predictions [143]. The cross-sections can be found in Table B.1 along with the sample sizes. The samples with Z boson decays are reweighted such that the simulated p_{T}^{Z} spectra match those found in $Z/\gamma^* \to \mu\mu$ data events using Figure A.7 as in the $Z/\gamma^* \to \mu\mu$ tag-and-probe analysis in Section 5.6.

6.2 Definition of Physics Objects

The definitions of the electron, muon, τ_{had} decay, jet, and $E_{\mathrm{T}}^{\mathrm{miss}}$ objects ensue from the output of the reconstruction algorithms described in Section 3.2.6.

Electron candidates must be within the acceptance of the ID ($|\eta^e| < 2.47$)[1] and have $p_{\mathrm{T}}^{e} > 15\,\mathrm{GeV}$. Candidates outside (inside) the Ecal transition regions, $1.37 < |\eta| < 1.52$, are required to pass the *loose* (*medium*) identification criteria [81]. Muon candidates must be within the acceptance of the ID ($|\eta^\mu| < 2.50$), pass the *loose* identification criteria [73], and have $p_{\mathrm{T}}^{\mu} > 10\,\mathrm{GeV}$.

Candidates for τ_{had} decays must have one or three core tracks and unit absolute electric charge. The ID acceptance requirement $|\eta^{\tau_{\text{had-vis}}}| < 2.47$ ($|\eta^{\tau_{\text{had-vis}}}| < 2.50$) is applied to single-prong (three-prong) candidates. For single-prong candidates, the core track must satisfy $|\eta^{\mathrm{track}}| < 2.47$. All τ_{had} candidates must pass the *medium* τ_{had} identification [82] and $p_{\mathrm{T}}^{\tau_{\text{had-vis}}} > 20\,\mathrm{GeV}$ criteria. The *loose* electron veto is applied to τ_{had} candidates in the τ_e–τ_{had} channel.

Jets with $p_{\mathrm{T}}^{\mathrm{jet}} > 20\,\mathrm{GeV}$ and within the range $|\eta| < 4.50$ are considered. For reconstructed jets within the acceptance of the ID ($|\eta^{\mathrm{jet}}| < 2.40$) and with $p_{\mathrm{T}}^{\mathrm{jet}} < 50\,\mathrm{GeV}$, tracks originating from the primary vertex must contribute at least 50% of the transverse momentum carried by all tracks associated with the candidate [152]. This criterion suppresses candidates that originate from in-time pile-up and is axiomatically passed by candidates without any associated tracks. No specific selection is made on the number or transverse momenta of jets but they contribute to $E_{\mathrm{T}}^{\mathrm{miss}}$.

---

[1] The acceptance of the ID is $|\eta| < 2.50$. However, tighter requirements may be chosen to ensure that the charged particles associated with or nearby the physics object can be reconstructed.

If two types of the previously defined objects are reconstructed in the same detector region, specifically if $\Delta R < 0.2$, one type of object is selected in the following order of decreasing priority: muon, electron, τ_{had} decay, and jet. The remaining objects are removed, which is called overlap removal. For the purpose of removing τ_{had} candidates that overlap with muon candidates, the muon selection criteria are loosened to suppress τ_{had} candidates that are mimicked by muons. The p_{T}^{μ} requirement is loosened to 2 GeV and the requirements on the number of hits in the ID are dropped.

The reconstructed $E_{\mathrm{T}}^{\mathrm{miss}}$ is based on the previously defined physics objects after overlap removal, and the energy remaining after pile-up suppression that is not associated with these objects.

6.3 Event Selection

The event selection is similar to previous analyses of $Z/\gamma^* \to \tau\tau$ and $H \to \tau\tau$ decays at ATLAS and CMS, such as those described in Refs. [98, 99, 153, 154]. It is divided into a loose preselection and the selection that defines the signal region. In the preselection, events with one electron or muon (lepton) candidate and one τ_{had} candidate are selected for subsequent investigation. The signal region selection contains additional criteria designed to suppress background processes that can mimic the signature of the signal.

The Υ distribution for the data in the signal region was kept unknown (“blinded”) before the estimates of the backgrounds and experimental systematic uncertainties were finalised. The theory uncertainties were estimated after unblinding using predefined methods. The p_{T} of charged-particle tracks in the core region of τ_{had} candidates is an input for Υ (see Eq. (2.21)). Its distribution is very sensitive to the polarisation, so it was blinded as well.

In the following the relevant background processes are introduced. The preselection and the signal region selection are defined. Afterwards the expected properties of the signal in the signal region are discussed in detail.

6.3.1 Background Processes

The relevant background processes are multijet, W+jets $\left(W \to \ell_\tau \nu + \text{jets}, \ell_\tau \in \{e, \mu, \tau\}\right)$, $Z/\gamma^* \to \ell\ell$ ($\ell \in \{e, \mu\}$), and top pair production. In multijet events, both the lepton and τ_{had} candidates originate from quark- or gluon-initiated jets. The W+jets background events involve a real lepton candidate, which for $W \to \tau\nu + \text{jets}$ events originates from a τ_{lep} decay, and a quark- or gluon-initiated jet that is misidentified as a τ_{had} decay. The $Z/\gamma^* \to \ell\ell$ background consists of two components. The first are events in which one of the leptons is missed and a quark- or gluon-initiated jet is misidentified as a τ_{had} decay. The second are events in which one of the leptons is misidentified as a τ_{had} decay. They are called $Z/\gamma^* \to \ell\ell$ (jet $\to \tau_{\mathrm{had}}$) and $Z/\gamma^* \to \ell\ell$ ($\ell \to \tau_{\mathrm{had}}$), respectively. The latter is rare in the τ_μ–τ_{had} channel but substantial in the τ_e–τ_{had} channel because electrons are much more likely to mimic τ_{had} decays than muons. Top pair background events involve a real lepton candidate and a τ_{had} candidate that may be real or originate from a quark- or gluon-initiated jet. The leptons and taus stem from W decays subsequent to the top decays.

The major backgrounds are multijet and W+jets events. The $Z/\gamma^* \to \ell\ell$ and top pair backgrounds are often combined and referred to as other backgrounds. Further properties of the backgrounds and their estimation are presented in Section 6.4.

6.3.2 Preselection

An event cleaning is performed as recommended by ATLAS, which ensures that the analysed data events were recorded while the detector was functioning normally. The remaining selection is applied identically to data and simulated events. A primary vertex with four or more associated tracks is required. Exactly one τ_{had} candidate must pass the criteria described in Section 6.2.

In events for the τ_e–τ_{had} (τ_μ–τ_{had}) channel, exactly one electron (muon) and no muon (electron) candidate must pass the requirements given in Section 6.2. Hence, events cannot be counted in both channels. An event is preselected if the lepton candidate has $p_{\mathrm{T}}^{\mathrm{lepton}} > 26\,\mathrm{GeV}$ and passes the following requirements. Electron candidates must be outside the Ecal transition regions ($1.37 < |\eta| < 1.52$) and pass the *tight* identification criteria. Muon candidates must have a common track in the ID and the muon system.

The data and expected signal and background event yields after the preselection are shown in Table 6.3. The expected $Z/\gamma^* \to \tau\tau$ contribution accounts for about 10% of the data events.

6.3.3 Signal Region Selection

The signal purity is increased by suppressing misidentified lepton and τ_{had} candidates via further object selection criteria. Complementary requirements select event topologies that are common in signal and rare in background processes. The combined preselection and selection criteria are compiled in Table 6.4. An overview of the signal region selection is shown in Table 6.3.

Misidentified lepton candidates from quark- or gluon-initiated jets are suppressed using the isolation variables defined in Eq. (3.3). Specifically $f_{p_{\mathrm{T}},\mathrm{iso}} < 0.06$ and $f_{E_{\mathrm{T}},\mathrm{iso}} < 0.06$ are required. Candidates for τ_{had} decays that originate from leptons are suppressed by the *medium* electron veto and by the muon veto. Three-prong τ_{had} candidates are rejected because the polarisation observable, Υ, is targeted at single-prong τ_{had} decays.

The first requirement on the event topology is that the electric charges of the lepton and τ_{had} candidates must be opposite as expected in $Z/\gamma^* \to \tau\tau$ decays. Two dedicated kinematic requirements are employed to reduce the large W+jets background. First, the transverse mass of the lepton candidate and $E_{\mathrm{T}}^{\mathrm{miss}}$ must fulfil

$$m_{\mathrm{T}} = \sqrt{2 \cdot p_{\mathrm{T}}^{\mathrm{lepton}} \cdot E_{\mathrm{T}}^{\mathrm{miss}} \cdot \left(1 - \cos\Delta\phi\left(p_{\mathrm{T}}^{\mathrm{lepton}}, E_{\mathrm{T}}^{\mathrm{miss}}\right)\right)} < 30\,\mathrm{GeV}.$$

The m_{T} distributions before this requirement are shown in Figure 6.1. In W+jets events the m_{T} value is often close to the W boson mass even though the longitudinal components of the lepton and neutrino momenta are not considered. In signal events it is typically much smaller than the Z boson mass. The τ_{had} candidate is not considered in the m_{T} calculation although it emerges from the Z decay. The neutrinos from the τ_{lep} decay are nearly collinear with the lepton, which can make the $1 - \cos\Delta\phi\left(p_{\mathrm{T}}^{\mathrm{lepton}}, E_{\mathrm{T}}^{\mathrm{miss}}\right)$ factor small (see Figure 6.2). The neutrinos from the τ_{lep} and τ_{had} decays are preferentially emitted in opposite directions, which reduces the $E_{\mathrm{T}}^{\mathrm{miss}}$ magnitude.

The second requirement that primarily targets W+jets events is

$$\sum\Delta\phi = \left|\Delta\phi\left(p_{\mathrm{T}}^{\mathrm{lepton}}, E_{\mathrm{T}}^{\mathrm{miss}}\right)\right| + \left|\Delta\phi\left(p_{\mathrm{T}}^{\tau_{\mathrm{had\text{-}vis}}}, E_{\mathrm{T}}^{\mathrm{miss}}\right)\right| < 3.5\,\mathrm{rad}.$$

It exploits another difference between $Z/\gamma^* \to \tau\tau$ and W+jets events that is visible in Figure 6.2. In signal events the $E_{\mathrm{T}}^{\mathrm{miss}}$ vector is preferentially collinear with the lepton or τ_{had} transverse momenta or lies in the sector between them. In W+jets events it is preferentially outside this sector. The $\sum\Delta\phi$ distributions before the $\sum\Delta\phi$ requirement are shown in Figure 6.3. The m_{T} and $\sum\Delta\phi$ variables are correlated. The discrimination power of the $\sum\Delta\phi$ variable is strongly reduced after the m_{T} cut but the $\sum\Delta\phi$ requirement

τ_e–τ_{had} channel								
Requirement	Data	Total expected	$Z/\gamma^* \to \tau\tau$	$Z/\gamma^* \to \ell\ell$ (jet $\to \tau_{\text{had}}$)	$Z/\gamma^* \to \ell\ell$ ($\ell \to \tau_{\text{had}}$)	Top pair	W+jets	Multijet
Preselection	736030		74340 ± 190	21890 ± 180	35440 ± 350	15290 ± 60	246000 ± 4000	
Lepton isolation	461537 (63%)		65380 ± 180 (88%)	19920 ± 170 (91%)	32010 ± 340 (90%)	13230 ± 60 (87%)	220800 ± 3400 (90%)	
Lepton vetoes for τ_{had} decay	392954 (85%)		58900 ± 170 (90%)	15930 ± 140 (80%)	7020 ± 160 (22%)	11970 ± 60 (90%)	201600 ± 3100 (91%)	
Single-prong τ_{had} decay	272529 (69%)		42460 ± 140 (72%)	11640 ± 120 (73%)	6780 ± 160 (97%)	8130 ± 50 (68%)	141600 ± 2200 (70%)	
Opposite e and τ_{had} charges	194088 (71%)	191400 ± 3400	41590 ± 140 (98%)	5970 ± 90 (51%)	6490 ± 150 (96%)	7080 ± 40 (87%)	99800 ± 1600 (70%)	30000 ± 3000
$m_{\text{T}} < 30\,\text{GeV}$	51260 (26%)	50300 ± 1200 (26%)	25620 ± 110 (62%)	2180 ± 60 (37%)	3470 ± 120 (54%)	975 ± 16 (14%)	5860 ± 160 (6%)	12200 ± 1200 (40%)
$\sum \Delta\phi < 3.5\,\text{rad}$	46194 (90%)	45300 ± 1000 (90%)	24070 ± 110 (94%)	1760 ± 50 (81%)	3230 ± 120 (93%)	918 ± 15 (94%)	4770 ± 140 (81%)	10600 ± 1000 (87%)
$40 < m_{\text{vis}} < 85\,\text{GeV}$	32721 (71%)	32400 ± 600 (71%)	22180 ± 100 (92%)	888 ± 32 (50%)	340 ± 40 (11%)	370 ± 10 (40%)	2260 ± 90 (47%)	6300 ± 600 (60%)

τ_μ–τ_{had} channel								
Requirement	Data	Total expected	$Z/\gamma^* \to \tau\tau$	$Z/\gamma^* \to \ell\ell$ (jet $\to \tau_{\text{had}}$)	$Z/\gamma^* \to \ell\ell$ ($\ell \to \tau_{\text{had}}$)	Top pair	W+jets	Multijet
Preselection	804777		92550 ± 210	17690 ± 160	2990 ± 100	18770 ± 70	286000 ± 4000	
Lepton isolation	427174 (53%)		85990 ± 210 (93%)	16560 ± 150 (94%)	2840 ± 100 (95%)	15150 ± 60 (81%)	266000 ± 4000 (93%)	
Lepton vetoes for τ_{had} decay	369305 (68%)		74160 ± 190 (86%)	13750 ± 130 (83%)	1220 ± 60 (43%)	12390 ± 60 (82%)	233300 ± 3400 (88%)	
Single-prong τ_{had} decay	255331 (69%)		53620 ± 160 (72%)	10030 ± 110 (73%)	1200 ± 60 (99%)	8410 ± 50 (68%)	164300 ± 2400 (70%)	
Opposite μ and τ_{had} charges	192973 (76%)	189000 ± 2000	52800 ± 160 (98%)	5060 ± 80 (50%)	1200 ± 60 (100%)	7350 ± 40 (87%)	115400 ± 1800 (70%)	7000 ± 1000
$m_{\text{T}} < 30\,\text{GeV}$	44788 (23%)	44800 ± 500 (24%)	31620 ± 120 (60%)	772 ± 32 (15%)	400 ± 40 (34%)	1026 ± 17 (14%)	6350 ± 170 (6%)	4600 ± 400 (64%)
$\sum \Delta\phi < 3.5\,\text{rad}$	40824 (91%)	40700 ± 400 (91%)	29640 ± 120 (94%)	596 ± 27 (77%)	380 ± 40 (93%)	965 ± 16 (94%)	5210 ± 150 (82%)	3900 ± 400 (82%)
$40 < m_{\text{vis}} < 85\,\text{GeV}$	32805 (80%)	33230 ± 280 (82%)	27390 ± 120 (92%)	307 ± 18 (52%)	94 ± 18 (25%)	394 ± 10 (41%)	2630 ± 110 (50%)	2420 ± 230 (62%)

Table 6.3: Overview of the selection for the τ_e–τ_{had} (top) and τ_μ–τ_{had} (bottom) channels. The requirements are applied sequentially from top to bottom. The $Z/\gamma^* \to \tau\tau$, $Z/\gamma^* \to \ell\ell$, and top pair event yields are estimated from the simulation. The uncertainties are statistical. The W+jets and multijet event yields are estimated as described in Sections 6.4.2 and 6.4.3. The quoted uncertainties include statistical uncertainties as well as the k_W (see Table 6.9) and r_{QCD} (see Table 6.12) scaling uncertainties. The multijet estimate can only be performed after requiring that the lepton and τ_{had} candidate charges are opposite. Hence, the multijet and total expected event yields are shown from that stage of the selection on. The efficiency of each requirement is given in percent.

		τ_e–τ_{had} channel	τ_μ–τ_{had} channel
Single lepton trigger	p_{T} quality	$p_{\text{T}} > 24\,\text{GeV}$ (isolated) or $p_{\text{T}} > 60\,\text{GeV}$ *medium* identification	$p_{\text{T}} > 24\,\text{GeV}$ (isolated) or $p_{\text{T}} > 36\,\text{GeV}$ *tight* identification
Lepton	p_{T} $\lvert\eta\rvert$ quality isolation	$p_{\text{T}} > 26\,\text{GeV}$ $\lvert\eta\rvert < 1.37$ or $1.52 < \lvert\eta\rvert < 2.47$ *tight* identification $f_{p_{\text{T}},\text{iso}} < 0.06$, $f_{E_{\text{T}},\text{iso}} < 0.06$	$p_{\text{T}} > 26\,\text{GeV}$ $\lvert\eta\rvert < 2.5$ *loose* identification, combined $f_{p_{\text{T}},\text{iso}} < 0.06$, $f_{E_{\text{T}},\text{iso}} < 0.06$
τ_{had} decay	p_{T} quality $\lvert\eta\rvert$	$> 20\,\text{GeV}$ *medium* identification, *medium* electron veto, muon veto, single-prong $\lvert\eta\rvert < 2.47$ (both τ_{had} and core track)	
Event topology	charges m_{T} $\sum\Delta\phi$ m_{vis}	Lepton and τ_{had} candidate have opposite electric charges $m_{\text{T}} < 30\,\text{GeV}$ $\sum\Delta\phi < 3.5\,\text{rad}$ $40 < m_{\text{vis}} < 85\,\text{GeV}$	

Table 6.4: Compilation of the selection criteria that define the signal region.

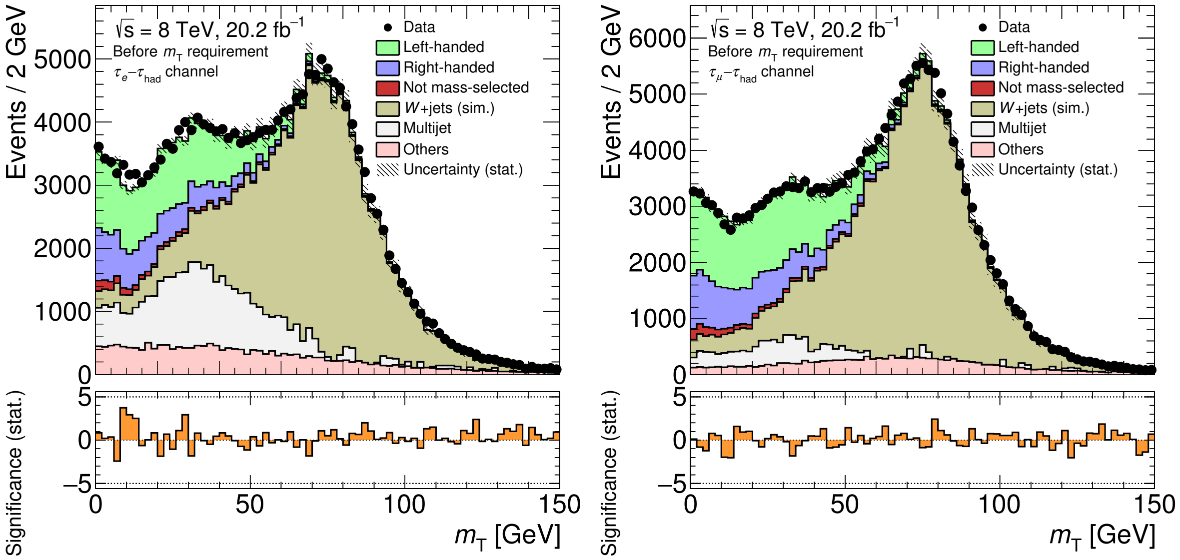

Figure 6.1: The m_{T} distributions in the τ_e–τ_{had} (left) and τ_μ–τ_{had} (right) channels before the m_{T}, $\sum\Delta\phi$ and m_{vis} requirements are applied. The remaining requirements are applied (see Table 6.3). The tau polarisation in $Z/\gamma^* \to \tau\tau$ events is taken from the simulation. The $Z/\gamma^* \to \tau\tau$ contributions with left- and right-handed taus inside the mass-selected region ($66\,\text{GeV} < m_{Z/\gamma^*} < 116\,\text{GeV}$) and the $Z/\gamma^* \to \tau\tau$ contribution outside the mass-selected region are shown separately. The backgrounds are estimated as described in Section 6.4. The uncertainties are statistical. The significance of the difference of the predicted and data event yields, which is calculated considering only statistical uncertainties, is shown as well. Adapted from Ref. [25].

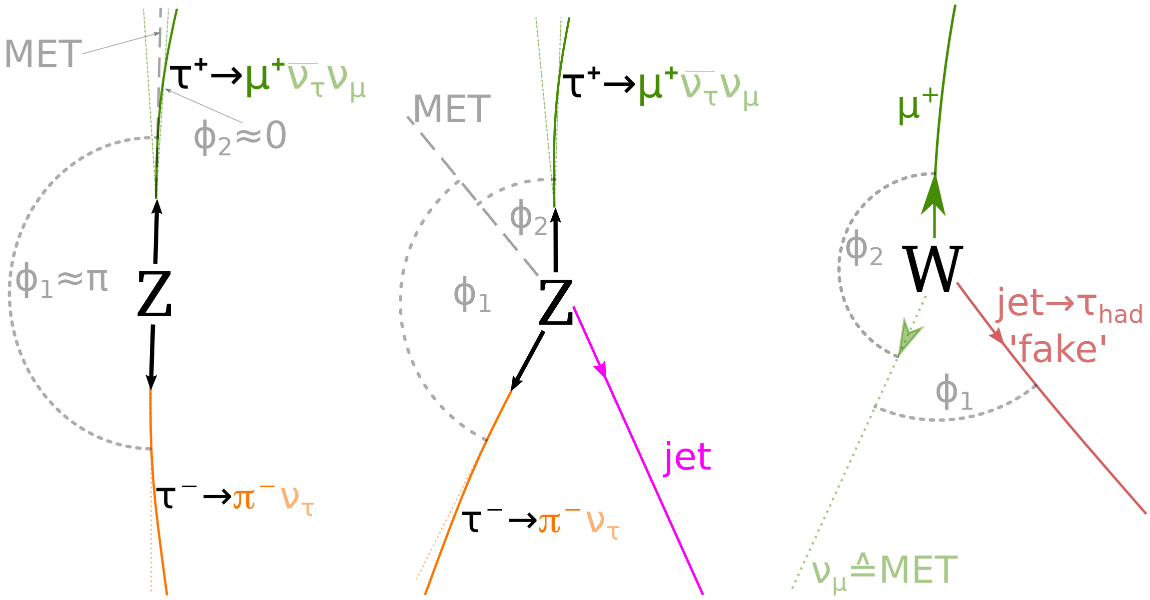

Figure 6.2: Representative topologies of signal events without jets (left), signal events with one jet (centre), and W background events with one jet (right) in the plane transverse to the beam axis. The trajectories of the Z or W decay products, the direction of $E_{\text{T}}^{\text{miss}}$ (MET), and the direction of the jet are indicated. The jet mimics the τ_{had} candidate in W background events. The angles $\phi_1 = \Delta\phi(p_{\text{T}}^{\tau_{\text{had-vis}}}, E_{\text{T}}^{\text{miss}})$ and $\phi_2 = \Delta\phi(p_{\text{T}}^{\text{lepton}}, E_{\text{T}}^{\text{miss}})$ are indicated.

still decreases the impact of the backgrounds on the measurement. The $\sum \Delta\phi$ distribution before the m_{T} cut is also shown in Figure 6.3 for comparison. The m_{T} and $\sum \Delta\phi$ cuts are taken on from the zero-jet category in the cut-based $H \to \tau\tau$ analysis [155] performed with the same dataset. The m_{T} and $\sum \Delta\phi$ variables are not particularly sensitive to the kinematic differences between $H \to \tau\tau$ and $Z/\gamma^* \to \tau\tau$ decays, the largest of which result from the Z and H boson masses and spins (see Table 2.3). The accuracy of the tau polarisation measurement is limited by uncertainties other than background modelling and statistical uncertainties, which might be reduced after a reoptimisation of the m_{T} and $\sum \Delta\phi$ cuts.

A further requirement utilises the visible mass

$$m_{\text{vis}} = \sqrt{\left(p^{\text{lepton}} + p^{\tau_{\text{had-vis}}}\right)^2},$$

where p^{lepton} and $p^{\tau_{\text{had-vis}}}$ are the lepton and $\tau_{\text{had-vis}}$ four-momenta. The m_{vis} distributions after the previous cuts are shown in Figure 6.4. Because tau decays involve neutrinos, most m_{vis} values lie below the Z boson mass in signal events. Signal events with high m_{vis} values are favoured by the $p_{\text{T}}^{\text{lepton}}$ and $p_{\text{T}}^{\tau_{\text{had-vis}}}$ requirements. The m_{vis} values in $Z/\gamma^* \to \ell\ell$ $(\ell \to \tau_{\text{had}})$ events are typically close to the Z boson mass because the lepton and τ_{had} candidates correspond to the Z/γ^* decay products. The m_{vis} distributions of the other backgrounds are wider than those of the signal, because the lepton and τ_{had} candidates do not originate from the same Z or W boson decays. The chosen cut, $40 < m_{\text{vis}} < 85\,\text{GeV}$, minimises the statistical uncertainties in the measured tau polarisation in both channels.

One large benefit from the m_{vis} cut is the reduction of the $Z/\gamma^* \to \ell\ell$ $(\ell \to \tau_{\text{had}})$ background. It represents the only relevant contributions with τ_{had} candidates that originate from leptons and has dedicated modelling uncertainties. The m_{vis} cut makes the impact of these uncertainties on the measurement negligible.

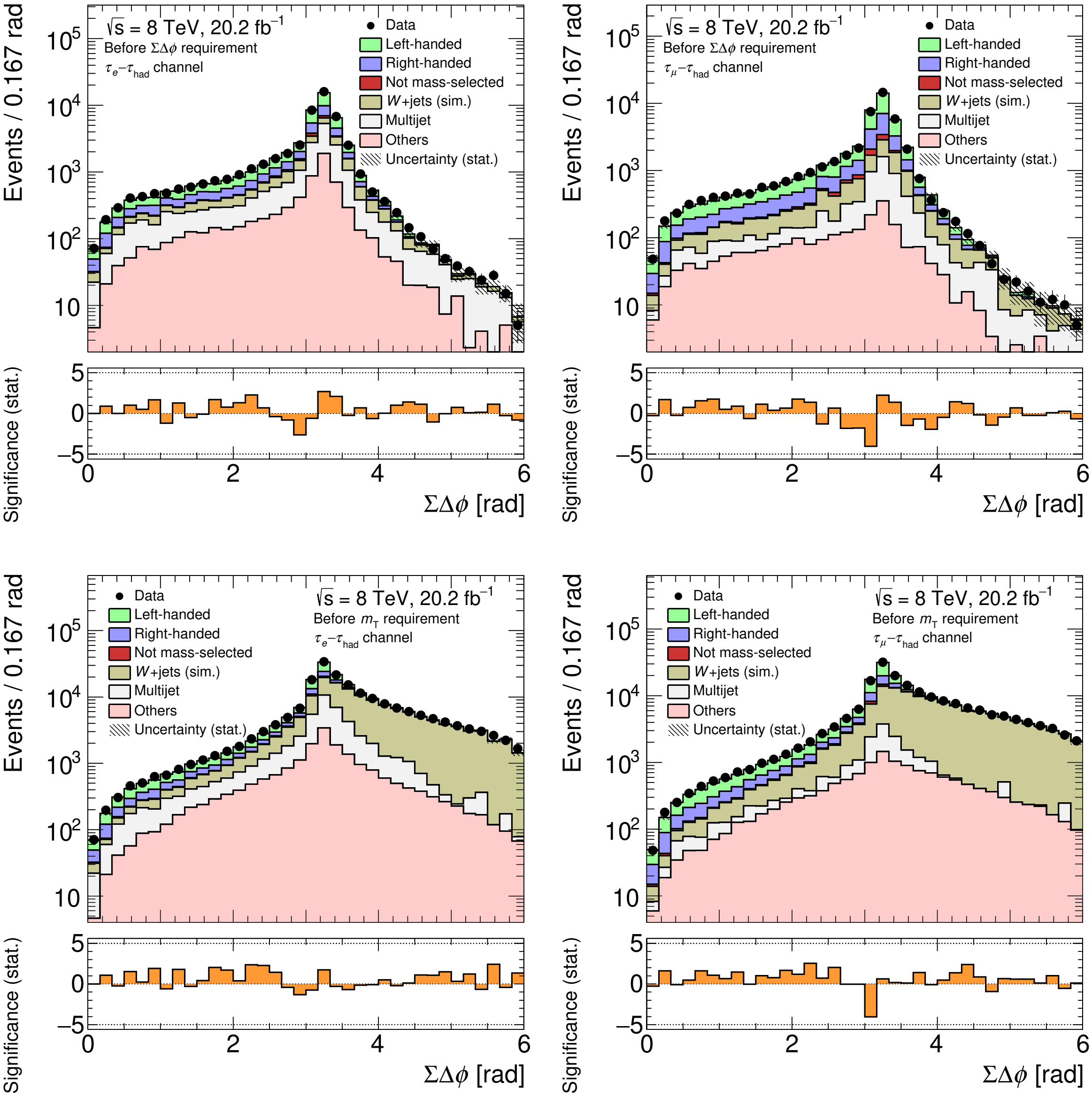

Figure 6.3: The $\sum\Delta\phi$ distributions in the τ_e–$\tau_{\rm had}$ (left) and τ_μ–$\tau_{\rm had}$ (right) channels before the $\sum\Delta\phi$ and $m_{\rm vis}$ requirements are applied (top), and before the $m_{\rm T}$, $\sum\Delta\phi$, and $m_{\rm vis}$ requirements are applied (bottom). The remaining requirements are applied (see Table 6.3). The tau polarisation in $Z/\gamma^* \to \tau\tau$ events is taken from the simulation. The $Z/\gamma^* \to \tau\tau$ contributions with left- and right-handed taus inside the mass-selected region ($66\,\text{GeV} < m_{Z/\gamma^*} < 116\,\text{GeV}$) and the $Z/\gamma^* \to \tau\tau$ contribution outside the mass-selected region are shown separately. The backgrounds are estimated as described in Section 6.4. The uncertainties are statistical. The significance of the difference of the predicted and data event yields, which is calculated considering only statistical uncertainties, is shown as well. Top adapted from Ref. [25].

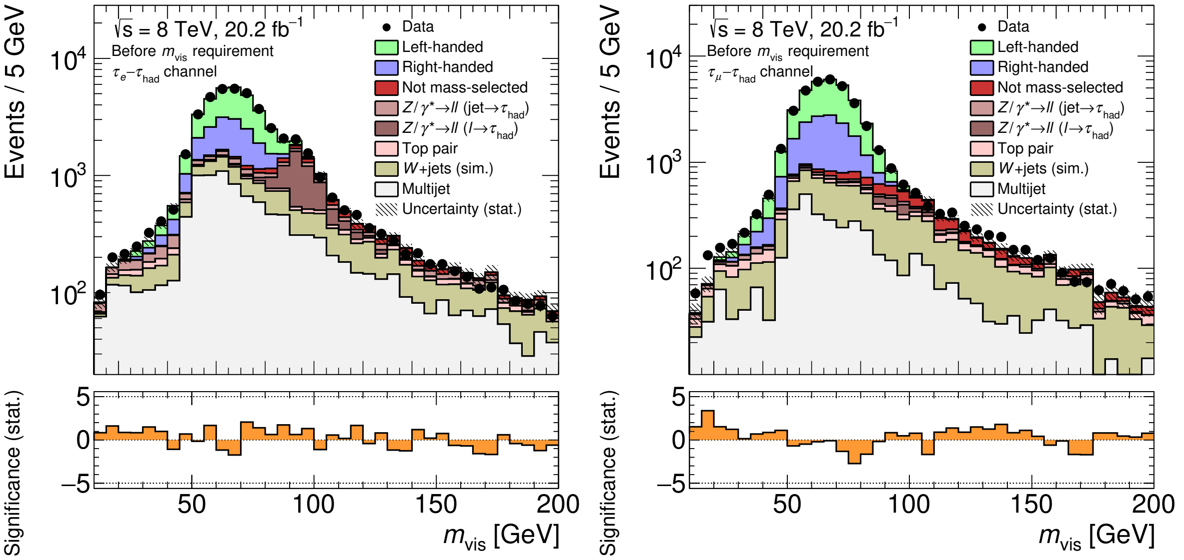

Figure 6.4: The m_{vis} distributions in the τ_e–τ_{had} (left) and τ_μ–τ_{had} (right) channels before the m_{vis} requirement is applied. The remaining requirements are applied (see Table 6.3). The tau polarisation in $Z/\gamma^* \to \tau\tau$ events is taken from the simulation. The backgrounds are estimated as described in Section 6.4. The uncertainties are statistical. The significance of the difference of the predicted and data event yields, which is calculated considering only statistical uncertainties, is shown as well.

6.3.4 Properties of the Expected Signal in the Signal Region

The selection requirements affect the properties of the signal. The effect of the kinematic requirements is studied on stable-particle (event-generator) level (see Table 6.5). Events with left-handed taus are strongly preferred by the $p_{\text{T}}^{\text{lepton}}$ cuts as suggested by Eq. (2.22) and Figure 2.7. The $p_{\text{T}}^{\tau_{\text{had-vis}}}$ cut preferentially selects events with right-handed taus as suggested by Eqs. (2.17) and (2.19) as well as by Figure 2.7. Events with left-handed taus are more likely to fail the m_{T} requirement because the $E_{\text{T}}^{\text{miss}}$ direction is more likely to be opposite to the lepton momentum than in events with right-handed taus. The remaining requirements have little effect on the tau polarisation.

The cuts shown in Table 6.5 define the fiducial region. It is very similar to the signal region and it is one of the kinematic regions in which the tau polarisation is measured. The overall efficiency of the fiducial region selection is about 0.60% (0.45%) for events with left-handed (right-handed) taus. The losses of events predominantly result from experimental acceptance requirements. The overall efficiency is about 6% larger in the τ_μ–τ_{had} channel than in the τ_e–τ_{had} channel due to the looser lepton pseudorapidity requirement. Otherwise there are only minor differences between the channels. Three cuts are omitted for brevity in Table 6.5 and in the fiducial region selection: the $p_{\text{T}}^{h^\pm} > 1\,\text{GeV}$ cut, which is implied in the assignment of tracks to reconstructed τ_{had} decays, the $|\eta^{h^\pm}| < 2.47$ cut, and the $\sum \Delta\phi$ cut. The first two are $\geq 99\%$ efficient on stable-particle level after the $p_{\text{T}}^{\tau_{\text{had}}}$ and $\eta^{\tau_{\text{had}}}$ cuts, and the third is passed by all simulated signal events left after the m_{T} cut.

The selection also alters the m_{Z/γ^*} spectra. The requirements on the lepton and τ_{had} decay suppress low-mass events (see Figure 6.5), which is mainly due to the $p_{\text{T}}^{\text{lepton}}$ and $p_{\text{T}}^{\tau_{\text{had-vis}}}$ cuts. Signal contributions with $m_{Z/\gamma^*} < 60\,\text{GeV}$, which are not included in the simulated signal samples, are negligible after these cuts. The m_{T} cut and in particular the m_{vis} cut suppress high-mass events. This does not affect the tau polarisation to a large extend because the m_{Z/γ^*} spectrum is peaked strongly at the Z boson pole.

τ_e–τ_{had} channel			
Requirement	Left-handed	Right-handed	P_τ [1/100]
All $Z/\gamma^* \to \tau\tau$ events	13287100 ± 2500	9989400 ± 2200	-14.17 ± 0.01
τ_e–τ_{had} channel	3094400 ± 1200 (23%)	2326500 ± 1000 (23%)	-14.17 ± 0.03
$p_{\text{T}}^{e} > 26\,\text{GeV}$	475400 ± 500 (15%)	164540 ± 270 (7%)	-48.58 ± 0.11
$\lvert\eta^{e}\rvert < 1.37$ or $1.52 < \lvert\eta^{e}\rvert < 2.47$	337200 ± 400 (71%)	118580 ± 230 (72%)	-47.97 ± 0.13
Single-prong τ_{had} decay	262210 ± 350 (78%)	91850 ± 200 (77%)	-48.12 ± 0.15
$p_{\text{T}}^{\tau_{\text{had-vis}}} > 20\,\text{GeV}$	127580 ± 240 (49%)	60050 ± 170 (65%)	-35.99 ± 0.18
$\lvert\eta^{\tau_{\text{had-vis}}}\rvert < 2.47$	111670 ± 230 (88%)	53040 ± 160 (88%)	-35.60 ± 0.20
$m_{\text{T}} < 30\,\text{GeV}$	84140 ± 200 (75%)	47320 ± 150 (89%)	-28.01 ± 0.21
$40 < m_{\text{vis}} < 85\,\text{GeV}$	78880 ± 190 (94%)	45260 ± 140 (96%)	-27.08 ± 0.21

τ_μ–τ_{had} channel			
Requirement	Left-handed	Right-handed	P_τ [1/100]
All $Z/\gamma^* \to \tau\tau$ events	13287100 ± 2500	9989400 ± 2200	-14.17 ± 0.01
τ_μ–τ_{had} channel	3009100 ± 1200 (23%)	2262200 ± 1000 (23%)	-14.17 ± 0.03
$p_{\text{T}}^{\mu} > 26\,\text{GeV}$	470100 ± 500 (16%)	163620 ± 270 (7%)	-48.36 ± 0.11
$\lvert\eta^{\mu}\rvert < 2.50$	358800 ± 400 (76%)	126770 ± 240 (77%)	-47.79 ± 0.13
Single-prong τ_{had} decay	279080 ± 360 (78%)	98170 ± 210 (77%)	-47.95 ± 0.14
$p_{\text{T}}^{\tau_{\text{had-vis}}} > 20\,\text{GeV}$	135810 ± 250 (49%)	63970 ± 170 (65%)	-35.96 ± 0.18
$\lvert\eta^{\tau_{\text{had-vis}}}\rvert < 2.47$	118550 ± 230 (87%)	56350 ± 160 (88%)	-35.57 ± 0.19
$m_{\text{T}} < 30\,\text{GeV}$	89130 ± 200 (75%)	50310 ± 150 (89%)	-27.84 ± 0.20
$40 < m_{\text{vis}} < 85\,\text{GeV}$	83570 ± 200 (94%)	48120 ± 150 (96%)	-26.92 ± 0.21

Table 6.5: Overview of the selection criteria for signal events on stable-particle level. The effect on the event yields and on the tau polarisation is shown for the τ_e–τ_{had} (top) and τ_μ–τ_{had} (bottom) channels. The requirements are applied sequentially from top to bottom. The distributions are normalised according to their respective cross-sections. Here, the polarisation is taken from the simulation. The statistical uncertainties and the efficiency of each requirement in percent are given. The listed cuts define the fiducial region.

However, possible contributions of possible unknown ditau production processes with high ditau masses may be removed. In practice, this analysis would not be sensitive to such contributions even if a dedicated high-m_{vis} category was introduced as the relative background contributions are very large above the Z boson pole (see Figure 6.4). Additionally, events with ditau masses $\lesssim 150\,\text{GeV}$ are not separated effectively from the many signal events at the Z boson pole. Events with even higher ditau masses are expected to be rare, which was confirmed in dedicated searches [9, 103, 109, 156, 157]. A measurement of the tau polarisation in events with high ditau masses may be possible with Run 2 data.

The tau polarisation is measured using the Υ spectrum of the τ_{had} decays. In the form given in Eq. (2.21), the Υ observable does not rely on reconstruction-level information about neutral hadrons (e.g. multiplicity or four-momenta), which is not available in the utilised dataset.[2] The charged-hadron

---

[2] The Pi0Finder algorithm is used to identify τ_{had} decays in data taken in Run 1 of the LHC but it has not been validated for other purposes. A dedicated validation is beyond the scope of this analysis. The new algorithms presented in Chapter 5 are being validated for use in analyses of Run 2 data.

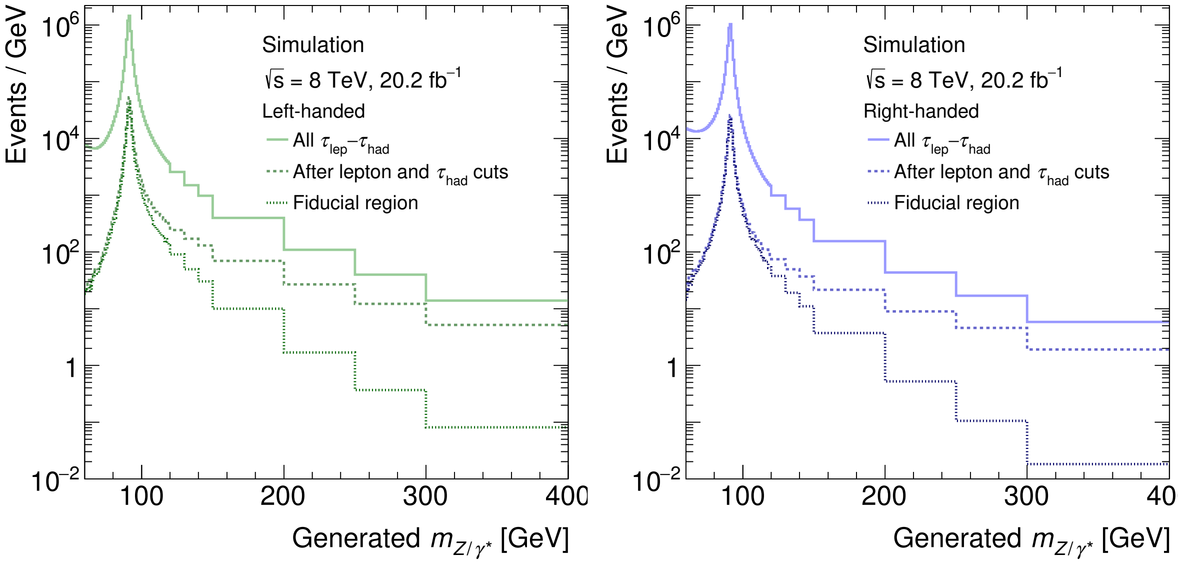

Figure 6.5: Generated m_{Z/γ^*} spectra in events with left-handed (left) and right-handed (right) taus. The spectra are shown for all events in the τ_e–τ_{had} and τ_μ–τ_{had} channels, the events remaining after the stable-particle level lepton and τ_{had} momenta cuts (all except the m_{T} and m_{vis} cuts in Table 6.5), and after the fiducial region selection. The distributions are normalised according to their respective cross-sections. Here, the polarisation is taken from the simulation.

momentum is taken from the charged-particle track:

$$\Upsilon = 2\frac{p_{\text{T}}^{h^\pm}}{p_{\text{T}}^{\tau_{\text{had-vis}}}} - 1 = 2\frac{p_{\text{T}}^{\text{track}}}{p_{\text{T}}^{\tau_{\text{had-vis}}}} - 1. \tag{6.1}$$

The Υ spectra of the selected signal events in the τ_μ–τ_{had} channel are shown in Figure 6.6. They are very similar for the τ_e–τ_{had} channel as well. The stable-particle level spectra of $\tau \to h^\pm\nu$ decays are peaked at one due to the absence of neutral hadrons. They are broader on reconstruction level due to resolution effects. The $p_{\text{T}}^{\tau_{\text{had-vis}}}$ requirement is preferentially passed by $\tau \to h^\pm\nu$ decays of right-handed taus because the pion typically carries a larger fraction of the tau momentum than in $\tau \to h^\pm\nu$ decays of left-handed taus. The typical momentum fraction carried by the visible decay products is more different between left- and right-handed taus than for the other τ_{had} decay topologies (see Section 2.3.1). Therefore, the fraction of $\tau \to h^\pm\nu$ decays in the selected τ_{had} sample, which is reflected in the fraction of measured τ_{had} decays with $\Upsilon \approx 1$, provides sensitivity to the tau polarisation.

The stable-particle level Υ spectra of the selected $\tau \to h^\pm\pi^0\nu$ decays are not symmetric as in Figure 2.9 because candidates with high-$p_{\text{T}}^{\text{track}}$ values are identified more efficiently. The reconstruction preserves most of the shape differences between left- and right-handed taus. This is also the case for the other τ_{had} decays.

The correlation of the reconstructed and stable-particle level Υ values for the selected τ_{had} decays in the τ_μ–τ_{had} channel is shown in Figure 6.7. It agrees with that in the τ_e–τ_{had} channel. The tau polarisation sensitivity predominantly results from $\tau \to h^\pm\pi^0\nu$ decays. Individually, the $\tau \to h^\pm\nu$ and the other τ_{had} decays provide similar sensitivities and they contribute noticeably to the overall sensitivity.

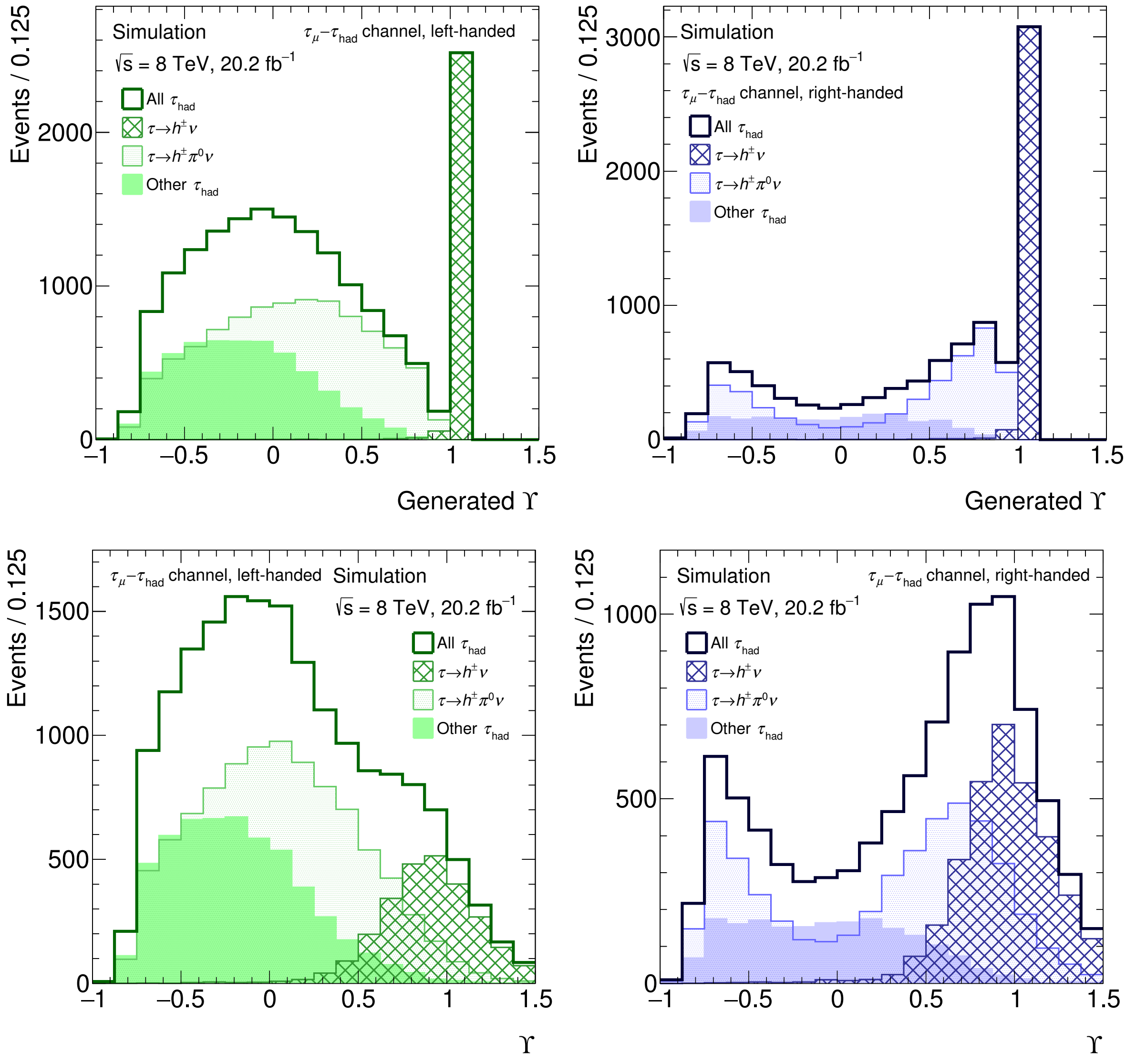

Figure 6.6: Expected ϒ distributions as defined in Eq. (6.1) for decays of left-handed (left) and right-handed (right) single-prong reconstructed $\tau_{\rm had}$ decays in simulated $Z/\gamma^* \to \tau\tau$ decays in the signal region for the τ_μ–$\tau_{\rm had}$ channel. The ϒ value is calculated from stable-particle level (top) and reconstruction level (bottom) quantities. In addition to the inclusive distributions, the constituent distributions corresponding to generated $\tau \to h^\pm \nu$ and $\tau \to h^\pm \pi^0 \nu$ ($h^\pm$ denotes $\pi^\pm$ or $K^\pm$) topologies are overlaid, as well as that of the remaining decays. The latter mainly consist of $\tau \to h^\pm \geq 2\pi^0 \nu$ decays. The analysis does not, however, distinguish between the decay topologies. The distributions are normalised according to their respective cross-sections. Here, the polarisation is taken from the simulation. Adapted from Ref. [25].

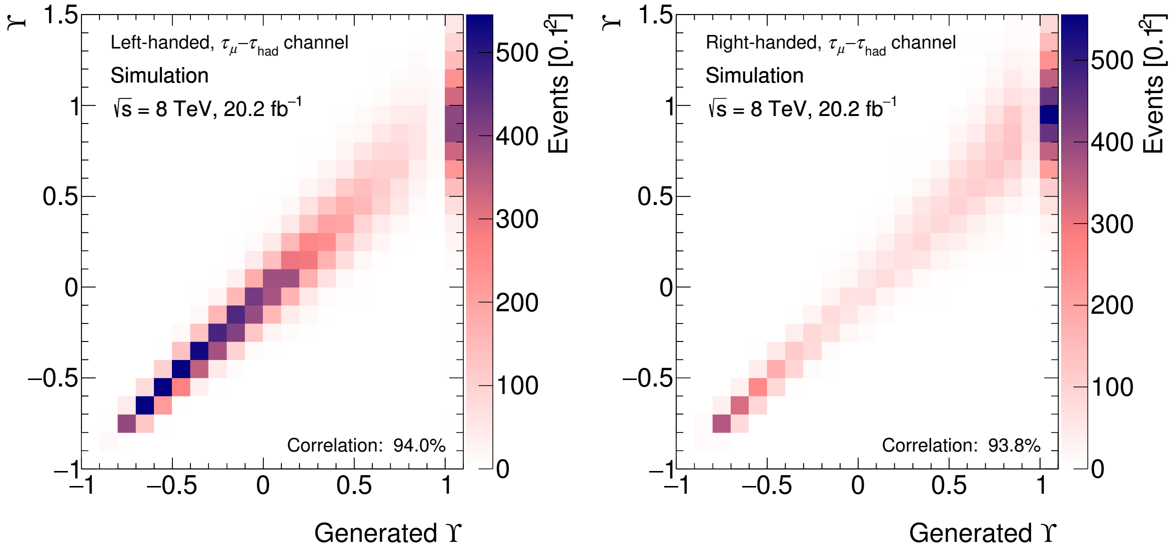

Figure 6.7: Reconstruction level versus stable-particle level Υ distributions in signal decays for the τ_μ–τ_{had} channel for τ_{had} decays with left-handed (left) and right-handed (right) taus. The linear correlations are given in the plots. The distributions are normalised according to their respective cross-sections. Here, the polarisation is taken from the simulation.

The tau polarisation is measured in the fiducial region defined in Table 6.5 and in the mass-selected region, in which only $66\,\text{GeV} < m_{Z/\gamma^*} < 116\,\text{GeV}$ is required. The polarisation measured in the fiducial region resembles that directly observed in the signal region. The polarisation measured in the mass-selected region approximately equals that at the Z boson pole and can be used to obtain an approximate $\sin^2\theta_{\text{W}}^{\text{eff}}$ value via Eq. (2.24). Both results can be utilised by physicists outside ATLAS because only stable-particle-level requirements are needed to select the fiducial and mass-selected regions.

To measure the tau polarisation in the **fiducial region**, the nominal signal sample is split into the following components:

- Events in the left-handed subsample that are inside the fiducial region (50% of the total expected signal in the signal region),
- Events in the right-handed subsample that are inside the fiducial region (30%),
- Events outside the fiducial region (20%).

The events outside the fiducial region fail a requirement at stable-particle level but pass it at reconstruction level in order to be selected for the signal region. This is most likely for the m_{T} (9% of the total expected signal in the signal region), $p_{\text{T}}^{\tau_{\text{had-vis}}}$ (5%), and $p_{\text{T}}^{\tau_{\text{lep}}}$ (3%) requirements.

To measure the tau polarisation in the **mass-selected region**, the nominal signal sample is instead split into the following three components:

- Events in the left-handed subsample that are inside the mass-selected region (63% of the expected signal in the signal region),
- Events in the right-handed subsample that are inside the mass-selected region (36%),
- Events outside the mass-selected region (2%).

The tau polarisation values in the mass-selected and fiducial regions are predicted using the nominal signal sample. These values are mostly determined by the weak mixing angle set for the Tauola Universal Interface [141] and for the TAUOLA [122] decay library ($\sin^2\theta_{\mathrm{W}}^{\mathrm{eff}} = 0.23147$). The polarisation in the mass-selected region is predicted from the normalised x_{vis} distribution in $\tau \to \pi^\pm\nu$ decays, which is

$$f(x_{\mathrm{vis}}) = 1 + P_\tau(2x_{\mathrm{vis}} - 1) \tag{6.2}$$

because of Eqs. (2.2) and (2.17). The x_{vis} distribution is shown in Figure 6.8. The fit function matches the distribution within the statistical uncertainties in the fit range in Figure 6.8. The slope is stable against changes of the fit range as long as values $\lesssim 0.05$ are excluded. The drop close to zero is due to a kinematic boundary that results from the non-zero pion mass. The prediction for the tau polarisation in the **mass-selected region** is $P_\tau = -0.1536 \pm 0.0006$ (stat) $\pm\ 0.0013$ (syst). Systematic uncertainties in the shower modelling and in the choice of the PDF set are considered. The former are estimated with the ALPGEN+JIMMY sample. The latter are determined using the LHAPDF package [158]. The nominal PDF set, CTEQ6L1 [126], is reweighted to the following alternative leading-order PDF sets: NNPDF30_LO_AS_0118 [159], MMHT2014LO68CL [160], and CT14LO [161]. The predicted tau polarisation in the mass-selected region is that simulated by the Tauola Universal Interface and the TAUOLA library.

The tau polarisation in the fiducial region cannot be obtained from the x_{vis} distribution because the $p_{\mathrm{T}}^{\tau_{\text{had-vis}}}$ spectrum is altered in a complex way. Instead, it is computed from the number of events in the left- and right-handed subsamples that pass the fiducial region selection. The prediction for the tau polarisation in the **fiducial region** is $P_\tau = -0.270 \pm 0.006$. The uncertainties in the signal sample splitting are dominant and estimated with the methods documented in Section 6.5.2.

The measurements in the mass-selected and fiducial regions are performed analogously. The expected signal contributions are identical except for the splitting into components. The figures and tables in this thesis preferentially show the components used in the measurement in the mass-selected region. The backgrounds are identical in both measurements.

The prediction of the spin correlations of the two taus is of minor importance for the measurement in the fiducial region. The largest exception is that the signal contributions outside the fiducial region are directly taken from the simulation. In order to determine the polarisation in the mass-selected region an extrapolation from the signal region to the full phase space is performed assuming that the two taus originate from a mediator with unit spin. The interpretation in the mass-selected region relies severely on this assumption. For example, the large selection bias introduced by the $p_{\mathrm{T}}^{\tau_{\mathrm{lep}}}$ requirement (see Figure 2.7 and Table 6.5) can only be corrected if the spin correlations are predicted correctly. An anomalous measured tau polarisation would indicate that unknown ditau contributions are present. This would undermine the foundation of the interpretation in the mass-selected region.

The effect of the selection criteria on the three signal components in the measurement in the mass-selected region is documented in Table 6.6. The m_{T} requirement is less efficient than at stable-particle level (compare Table 6.5) due to resolution effects but its effect on the tau polarisation is similar. For the same reasons the $\sum\Delta\phi$ requirement is not fully efficient for signal events on reconstruction level. The m_{vis} requirement is as efficient as on stable-particle level. The overall signal efficiencies are about 0.10% (0.13%) for events with left-handed taus and 0.08% (0.10%) for events with right-handed taus in the τ_e–τ_{had} (τ_μ–τ_{had}) channel. They are noticeably smaller than for the fiducial region selection due to losses at the trigger stage, in τ_{had} and lepton reconstruction and identification, and resolution effects. For example, real single-prong τ_{had} decays are reconstructed as single-prong τ_{had} decays and pass the *medium* τ_{had} identification with a combined efficiency of ~45%. The efficiencies are larger in the τ_μ–τ_{had} channel because muons are selected more efficiently than electrons.

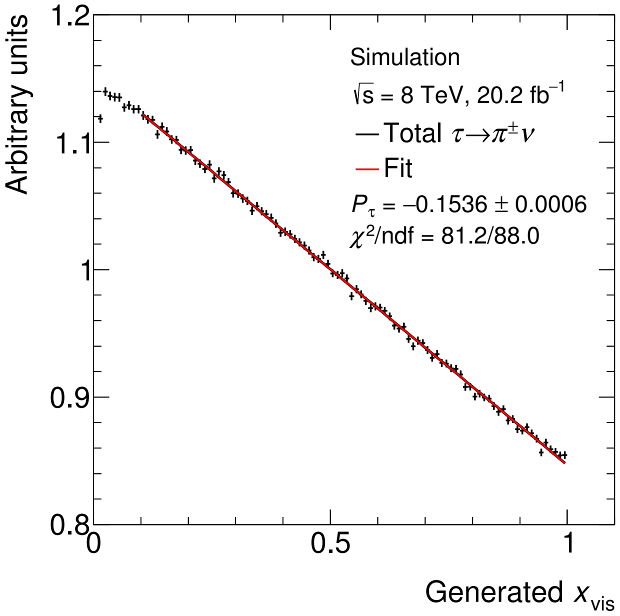

Figure 6.8: Visible-energy fraction on stable-particle level in $\tau \to \pi^{\pm}\nu$ decays for signal events within the mass-selected region. The visible-energy fraction is calculated in the rest frame of the Z/γ^* boson. Only tau decays without initial-state or final-state radiation are considered. The tau polarisation is extracted using a linear fit in the range $0.10 < x_{\mathrm{vis}} < 1.0$ using the fit function from Eq. (6.2). The polarisation and χ^2 per number of degrees of freedom are indicated.

6.4 Background Estimation

In this section the estimation of the backgrounds and their properties are presented. The minor $Z/\gamma^* \to \ell\ell$ and top pair backgrounds are estimated from the simulation and discussed first. The major W+jets and multijet backgrounds are estimated using data and discussed in Sections 6.4.2 and 6.4.3. The background estimates are validated using data, and the shapes of the predicted Υ distributions are compared to each other in Section 6.4.4. In the final section, various kinematic distributions in the signal region are shown and the modelling of the data is discussed.

6.4.1 The $Z/\gamma^* \to \ell\ell$ and Top Pair Backgrounds

Events with $Z/\gamma^* \to \ell\ell$ decays or top pairs have been studied in detail, and are well understood from precision measurements such as Refs. [94, 162–173]. They were also studied as backgrounds in analyses of ditau final states prior to this analysis, for example in Refs. [98, 99, 153, 154]. However, the reconstructed Υ distributions at ATLAS were only studied once in a 24 pb^{-1} dataset collected in 2010 [24]. In the analysis on hand, the $Z/\gamma^* \to \ell\ell$ and top pair backgrounds are estimated from the simulation. The p_{T}^{Z} reweighting is applied to the $Z/\gamma^* \to \ell\ell$ samples. The predicted Υ distributions are shown in Figure 6.9. The properties of the small $Z/\gamma^* \to \ell\ell$ (jet $\to \tau_{\mathrm{had}}$), $Z/\gamma^* \to \ell\ell$ ($\ell \to \tau_{\mathrm{had}}$), and top pair backgrounds are of minor importance for this analysis. They are discussed in Appendix C.1.

τ_e–τ_{had} channel				
Requirement	Left-handed	Right-handed	Not mass-selected	P_τ [1/100]
Preselection	48670 ± 150	21600 ± 100	4060 ± 40	-38.52 ± 0.24
Lepton isolation	42880 ± 140 (88%)	18840 ± 90 (87%)	3660 ± 40 (90%)	-38.94 ± 0.25
Lepton vetoes for τ_{had} decay	39030 ± 140 (91%)	16610 ± 90 (88%)	3260 ± 40 (89%)	-40.30 ± 0.27
Single-prong τ_{had} decay	27400 ± 110 (70%)	12690 ± 80 (76%)	2362 ± 33 (72%)	-36.69 ± 0.32
Opposite e and τ_{had} charges	26830 ± 110 (98%)	12430 ± 80 (98%)	2327 ± 33 (99%)	-36.67 ± 0.32
$m_{\text{T}} < 30\,\text{GeV}$	15570 ± 90 (58%)	8750 ± 60 (70%)	1299 ± 25 (56%)	-28.10 ± 0.40
$\sum \Delta\phi < 3.5\,\text{rad}$	14630 ± 80 (94%)	8180 ± 60 (93%)	1260 ± 24 (97%)	-28.30 ± 0.40
$40 < m_{\text{vis}} < 85\,\text{GeV}$	13860 ± 80 (95%)	7880 ± 60 (96%)	431 ± 14 (34%)	-27.50 ± 0.50

τ_μ–τ_{had} channel				
Requirement	Left-handed	Right-handed	Not mass-selected	P_τ [1/100]
Preselection	61050 ± 170	26750 ± 110	4750 ± 50	-39.07 ± 0.22
Lepton isolation	56770 ± 170 (93%)	24800 ± 110 (93%)	4420 ± 50 (93%)	-39.19 ± 0.23
Lepton vetoes for τ_{had} decay	49300 ± 160 (87%)	21050 ± 100 (85%)	3810 ± 40 (86%)	-40.15 ± 0.24
Single-prong τ_{had} decay	34800 ± 130 (71%)	16040 ± 90 (76%)	2780 ± 40 (73%)	-36.89 ± 0.29
Opposite μ and τ_{had} charges	34270 ± 130 (98%)	15780 ± 90 (98%)	2750 ± 40 (99%)	-36.94 ± 0.29
$m_{\text{T}} < 30\,\text{GeV}$	19290 ± 100 (56%)	10800 ± 70 (68%)	1532 ± 27 (56%)	-28.20 ± 0.40
$\sum \Delta\phi < 3.5\,\text{rad}$	18050 ± 90 (94%)	10110 ± 70 (94%)	1479 ± 27 (97%)	-28.20 ± 0.40
$40 < m_{\text{vis}} < 85\,\text{GeV}$	17110 ± 90 (95%)	9720 ± 70 (96%)	560 ± 16 (38%)	-27.50 ± 0.40

Table 6.6: Overview of the selection for signal events in the τ_e–τ_{had} (top) and τ_μ–τ_{had} (bottom) channels. The requirements are applied sequentially from top to bottom. The exclusive contributions of $Z/\gamma^* \to \tau\tau$ decays with left-handed and right-handed taus inside the mass-selected region and of $Z/\gamma^* \to \tau\tau$ decays outside the mass-selected region are listed. The efficiency of each requirement is given in percent. Additionally, the tau polarisation inside the mass-selected region predicted by simulation is shown. The event yields are estimated from the simulation and the uncertainties are statistical.

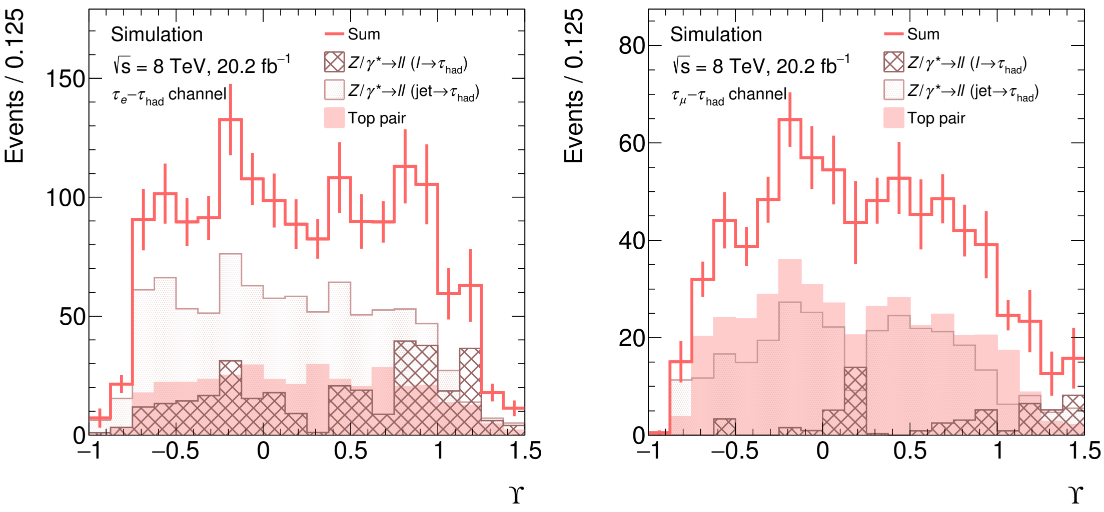

Figure 6.9: Simulated Υ distributions for minor backgrounds in the signal region for the τ_e–τ_{had} (left) and τ_μ–τ_{had} (right) channels. The $Z/\gamma^* \to \ell\ell$ (jet $\to \tau_{\text{had}}$), $Z/\gamma^* \to \ell\ell$ ($\ell \to \tau_{\text{had}}$), and top pair contributions are shown separately and summed. The statistical uncertainties in the sum are indicated.

6.4.2 The W+jets Background

The estimate of the major W+jets background utilises data and simulated events. It was developed in Ref. [174], and is presented in the following. Thereafter, key properties of W+jets background events are discussed.

Many properties of W+jets events relevant for this analysis are described adequately by the simulation. Data-driven techniques are employed to rectify the shortcomings. Because of inaccuracies in the modelling of τ_{had} identification for quark- or gluon-initiated jets, the event yields are overestimated in the simulation. More accurate yield predictions are obtained by correcting the simulated yields using data. The W+jets production cross-sections are so large that it is not feasible to simulate a number of events that is comparable with the yield in the dataset. Additionally, it is very difficult to model the shape of the Υ distribution precisely. The Υ observable is sensitive to the number of hadrons from a τ_{had} candidate and to the energy fractions carried by the individual hadrons, so its modelling relies on the description of parton showers. Consequently, both the statistical precision and the robustness of the estimated Υ shapes can be improved with data-driven techniques.

The data-driven corrections of the simulated W+jets event yields are estimated in a kinematic region that is enriched in W+jets decays. An opposite-sign W+jets control region is found by modifying the requirements that suppress W+jets events in the signal region selection. Specifically, the m_{T} requirement is modified to $m_{\text{T}} > 70\,\text{GeV}$ and the $\sum \Delta\phi$ requirement is inverted. Additionally, there is a same-sign W+jets control region for which the requirement of opposite lepton and τ_{had} charges is also inverted. It is used in the multijet background estimate (see Section 6.4.3). All control and validation regions in the analysis are listed in Table 6.7.

The data-driven estimation of the W+jets event yields in the W+jets control regions and the differences between the estimated and simulated yields are documented in Table 6.8. The multijet contributions can be neglected due to the strict m_{T} requirement. The W+jets control regions are of high purity ($>$ 90%) and the opposite-sign control region contains about nine times more W+jets events than the signal region for both channels.

The W+jets yields are estimated using one correction factor, k_W, per W+jets control region

$$k_W = \frac{N_{\text{data}}^{\text{WCR}} - N_{\text{non-}W}^{\text{WCR}}}{N_{\text{sim}}^{\text{WCR}}}, \tag{6.3}$$

where $N_{\text{data}}^{\text{WCR}}$ is the number of data events, $N_{\text{non-}W}^{\text{WCR}}$ is the number of events expected from processes other than W+jets, and $N_{\text{sim}}^{\text{WCR}}$ is the number of simulated W+jets event yields in the control region. The k_W values are shown in Table 6.9. The W+jets event yield in a given kinematic region and channel is estimated via

$$N_{\text{est}}^{\text{region}} = k_W \cdot N_{\text{sim}}^{\text{region}} = \left(N_{\text{data}}^{\text{WCR}} - N_{\text{non-}W}^{\text{WCR}}\right) \cdot \frac{N_{\text{sim}}^{\text{region}}}{N_{\text{sim}}^{\text{WCR}}}, \tag{6.4}$$

where $N_{\text{sim}}^{\text{region}}$ is the simulated W+jets yield in that region and the appropriate k_W factor (dependent on the channel and the lepton and τ_{had} charge requirement) is used. The systematic uncertainties in the subtraction of the non-W contributions from the data are very small thanks to the high purity of the control regions. The statistical uncertainties in the relative simulated W+jets event yields in the signal and opposite-sign W+jets control regions (ratio on the right-hand side of Eq. (6.4)) are 3% in both channels. The systematic uncertainties in the ratio are covered in Section 6.5.

The shape of the Υ distribution in W+jets events is estimated as described in the following. The shapes of other distributions are taken from the simulation. The Υ shapes in the signal region are estimated using

Region	Altered requirements	Requirements in signal region
W+jets control	$\sum \Delta\phi \geq 3.5$ rad and $m_\mathrm{T} > 70$ GeV	$\sum \Delta\phi < 3.5$ rad and $m_\mathrm{T} < 30$ GeV
W+jets validation 1	$\sum \Delta\phi \geq 3.5$ rad and $30 < m_\mathrm{T} < 70$ GeV	$\sum \Delta\phi < 3.5$ rad and $m_\mathrm{T} < 30$ GeV
W+jets validation 2	$30 < m_\mathrm{T} < 70$ GeV	$m_\mathrm{T} < 30$ GeV
Same-sign	Same lepton and τ_had charges	Opposite charges
Multijet control	$f_{p_\mathrm{T},\mathrm{iso}} \geq 0.06$ or $f_{E_\mathrm{T},\mathrm{iso}} \geq 0.06$	$f_{p_\mathrm{T},\mathrm{iso}} < 0.06$ and $f_{E_\mathrm{T},\mathrm{iso}} < 0.06$
$Z/\gamma^* \to \ell\ell$ ($\ell \to \tau_\mathrm{had}$) validation	$85 < m_\mathrm{vis} < 97$ GeV	$40 < m_\mathrm{vis} < 85$ GeV
Top pair validation	Various, see Section 6.4.4	

Table 6.7: Summary of the kinematic regions that are utilised to perform and validate background estimates. All regions have versions in which the lepton and τ_had charges are required to be opposite or the same, respectively. They are referred to as opposite-sign W+jets control region, same-sign W+jets control region, etc. The opposite of the same-sign region is the signal region. The τ_e–τ_had and τ_μ–τ_had channels are separated for all regions.

Opposite-sign W+jets control regions

Channel	Data	Data−non-W	W+jets (sim)	$Z/\gamma^* \to \tau\tau$	$Z/\gamma^* \to \ell\ell$	Top pair
τ_e–τ_had	21534	20360 ± 150	25770 ± 330	194 ± 9	231 ± 15	745 ± 14
τ_μ–τ_had	25913	24130 ± 160	31200 ± 400	287 ± 11	699 ± 31	796 ± 15

Same-sign W+jets control regions

Channel	Data	Data−non-W	W+jets (sim)	$Z/\gamma^* \to \tau\tau$	$Z/\gamma^* \to \ell\ell$	Top pair
τ_e–τ_had	8877	8530 ± 90	8860 ± 270	24.1 ± 3.2	229 ± 15	96 ± 5
τ_μ–τ_had	10060	9390 ± 100	9790 ± 280	22.3 ± 3.1	669 ± 27	121 ± 6

Table 6.8: Event yields in the opposite-sign (top) and same-sign (bottom) W+jets control regions. The estimated W+jets yields are data−non-W. The non-W yields are those of simulated $Z/\gamma^* \to \tau\tau$, $Z/\gamma^* \to \ell\ell$, and top pair events. The simulated (sim) W+jets yields are shown for comparison. The uncertainties are statistical.

Channel	Opposite-sign	Same-sign
τ_e–τ_had	0.790 ± 0.012	0.963 ± 0.031
τ_μ–τ_had	0.774 ± 0.011	0.959 ± 0.030

Table 6.9: Correction factors, k_W, as defined in Eq. (6.3), which are used to normalise W+jets contributions via Eq. (6.4). The statistical uncertainties are considered in this table. The systematic uncertainties in the normalisation of the W+jets background are evaluated separately (see text).

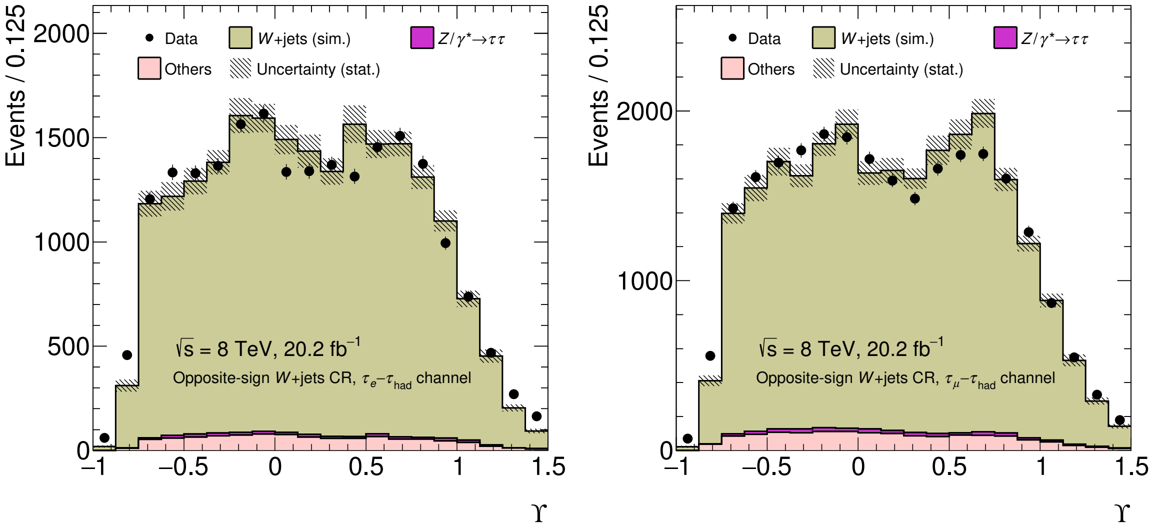

Figure 6.10: The Υ distribution in the opposite-sign W+jets control region for the τ_e–τ_{had} (left) and τ_μ–τ_{had} (right) channel. The contributions of $Z/\gamma^* \to \tau\tau$ and of $Z/\gamma^* \to \ell\ell$ and top pair (other) events are estimated from the simulation. The estimated W+jets contribution corresponds to the difference of the data and the aforementioned contributions. The W+jets distribution obtained from simulation is shown for comparison. It is normalised using Eq. (6.4), i.e. such that the total estimated event yield matches the observed yield. The uncertainties are statistical. Adapted from Ref. [25].

the data in the opposite-sign W+jets control region. The shapes of the W+jets contributions in the control region are obtained by subtracting the $Z/\gamma^* \to \tau\tau$, $Z/\gamma^* \to \ell\ell$, and top pair contributions from the data (see Figure 6.10). The shapes simulated for W+jets events are found to be reasonable even though they are not fully consistent with the data. Hence, the simulation is judged adequate to estimate the shape differences between the opposite-sign W+jets control and signal regions. The following procedure is applied analogously in the τ_e–τ_{had} and τ_μ–τ_{had} channels and similar results are obtained as illustrated for the τ_μ–τ_{had} channel:

- The normalised, simulated distributions in the W+jets control and signal regions are compared to each other in Figure 6.11. A linear function is fit to the ratio (see Figure 6.12). The parameters obtained from this fit and from similar fits described in the following can be found in Table C.2.

- Figure 6.13 shows the ratio after the Υ distribution in the control region is corrected with the linear function from Figure 6.12. An additional linear fit is performed and the fitted slope is very close to zero as expected.

- The final estimated shape in the signal region is obtained by applying the linear correction from Figure 6.12 to that found in the data in the control region. The correction is only dependent on the slope of the linear function. The event yields are left unchanged. The effect of the correction is shown in Figure 6.14.

The statistical uncertainties in the slope from Figure 6.13 are taken on as preliminary uncertainties in the shape correction. The correction is applied even though the slopes are consistent with zero in both channels in order to keep the uncertainties symmetric.

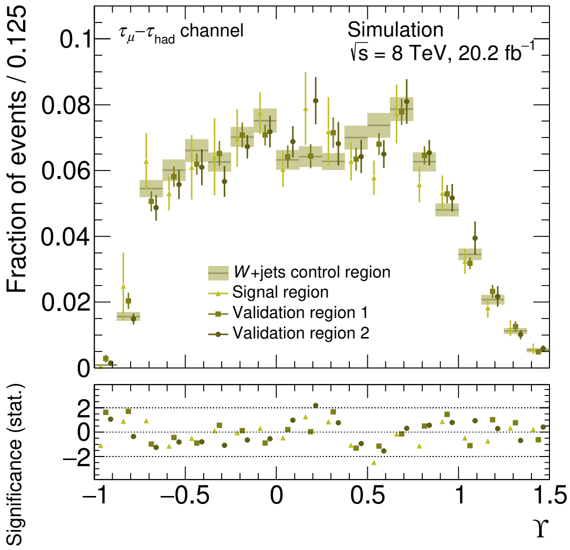

Figure 6.11: Normalised, simulated ϒ distributions for W+jets events in the opposite-sign W+jets control, signal, and opposite-sign W+jets validation regions for the τ_μ–τ_{had} channel. The control and validation regions are defined in Table 6.7. The uncertainties are statistical. The significances, calculated from the statistical uncertainties, of the differences between the shapes in the W+jets control region and those in the signal and validation regions are shown as well.

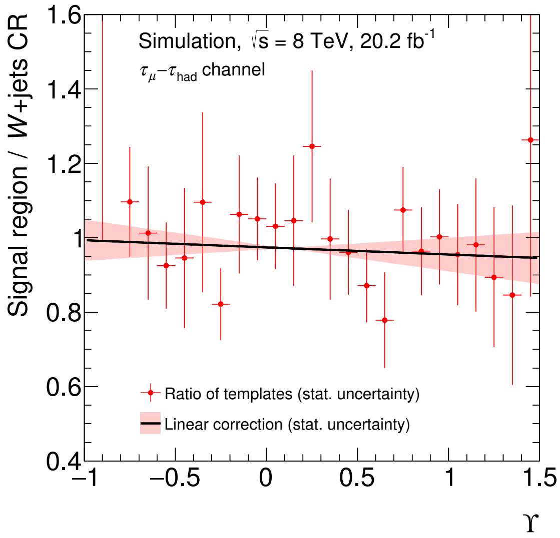

Figure 6.12: Ratio of normalised, simulated ϒ distributions for W+jets events in the signal region and in the opposite-sign W+jets control region for the τ_μ–τ_{had} channel. A linear function is fit to the ratio. The fitted function and the statistical uncertainties in its slope are indicated. Adapted from [25].

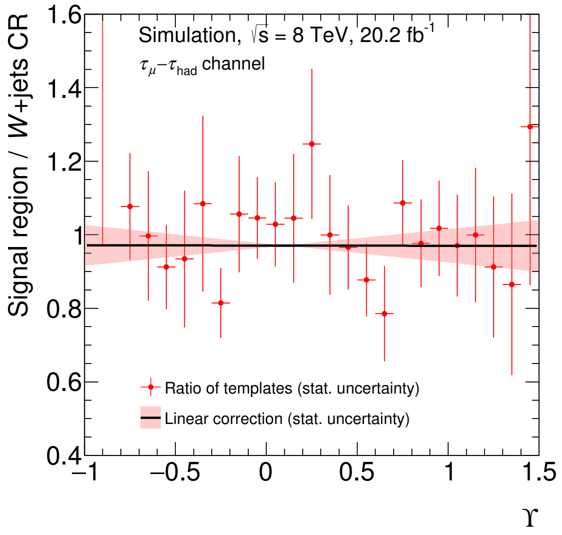

Figure 6.13: Ratio of normalised, simulated Υ distributions in W+jets events in the signal region and in the opposite-sign W+jets control region for the τ_μ–τ_{had} channel. The distribution in the W+jets control region is corrected using the linear function obtained in Figure 6.12. A linear function is fit to the ratio. The fitted function and the statistical uncertainties in its slope are indicated.

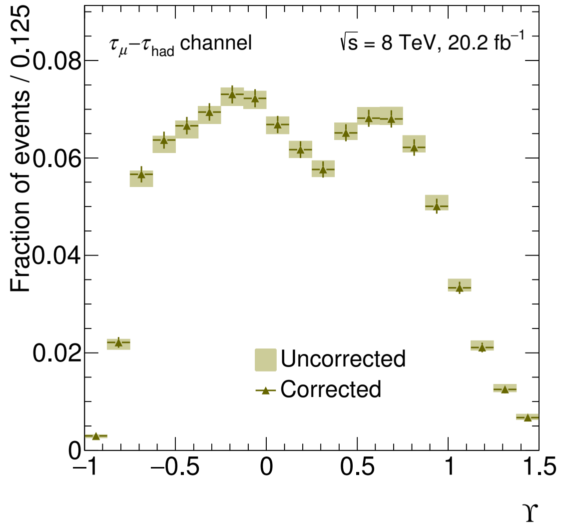

Figure 6.14: Corrected and uncorrected W+jets distributions obtained from the opposite-sign W+jets control region for the τ_μ–τ_{had} channel. The uncertainties are statistical.

Channel	Opposite-sign	Same-sign
τ_e–τ_{had}	0.03 ± 0.05	-0.15 ± 0.10
τ_μ–τ_{had}	-0.02 ± 0.06	0.07 ± 0.13

Table 6.10: Slopes and final uncertainties in the linear correction for the W+jets background estimate. The values are obtained from Table C.2, following the methodology described in the text.

The impact of the different m_{T} and $\sum \Delta\phi$ requirements in the signal and control regions on the Υ shapes is additionally studied in two dedicated W+jets validation regions. This way the final uncertainties in the shape correction are estimated. In the first of these regions, W+jets VR1, the m_{T} and $\sum \Delta\phi$ requirements are $30 < m_{\text{T}} < 70\,\text{GeV}$ and $\sum \Delta\phi \geq 3.5\,\text{rad}$. In the second validation region, W+jets VR2, they are $30 < m_{\text{T}} < 70\,\text{GeV}$ and $\sum \Delta\phi < 3.5\,\text{rad}$. The remaining requirements are the same as in the W+jets control and signal region selections (see Table 6.7). The validation regions cover the phase space between the control and signal regions.

The shapes of the simulated Υ distributions in the control and validation regions are compared to each other in Figure 6.11. Additional linear fits are performed. In each channel it is checked whether the preliminary uncertainty covers the absolute slopes in the additional fits. Otherwise the uncertainty is increased to the larger absolute slope in the additional fits. Following this procedure, the preliminary uncertainty of 0.05 is increased to 0.06 in the τ_μ–τ_{had} channel. The uncertainty in the τ_e–τ_{had} channel remains unchanged. The nominal slopes used in the shape correction and their final uncertainties are listed in Table 6.10.

Additional systematic uncertainties result from the subtraction of the $Z/\gamma^* \to \tau\tau$ contribution from the data in the W+jets control region because the tau polarisation is taken from the simulation. To evaluate these uncertainties it is tested how the measured tau polarisation changes if it is assumed to be $+1$ or -1 in signal events in the W+jets control region. As the signal contamination is small in the control region, the changes are negligible.

In the estimation of the multijet background, which is described in Section 6.4.3, the so-called same-sign region is utilised. It matches the signal region except that the lepton and τ_{had} charges are required to be the same instead of opposite. The large W+jets contribution in the same-sign region is estimated analogously to that in the signal region (details can be found in Appendix C.2). The slopes for the linear corrections and their final uncertainties are included in Table 6.10.

In the following the primary properties of W+jets background events are reviewed. They are about as common and pass the signal region selection criteria with similar efficiencies in both channels (see Table 6.3), because no failed reconstruction or misidentification of leptons are needed to mimic the signal topology. The W+jets contribution is strongly reduced by the m_{T} cut and it is also suppressed noticeably by the m_{vis} and $\sum \Delta\phi$ cuts as discussed in Section 6.3.3.

Due to contributions of t-channel diagrams like that in Figure 2.4 the lepton and τ_{had} candidate charges are preferentially opposite. The identified τ_{had} candidates in W+jets events in the signal region mostly originate from up, down, or strange quarks. The differences between the k_W factors in events with opposite and same lepton and τ_{had} candidate charges may result from differences between the τ_{had} candidate's quark–gluon composition. The t-channel diagrams mostly contribute events in which the τ_{had} candidate stems from the final-state quark (see Figure 2.4), and carries the opposite of the W boson, and therefore lepton, charge. Other diagrams contribute events in which the τ_{had} candidate may originate from a quark or a gluon and carry the same or opposite of the lepton charge.

6.4.3 The Multijet Background

The multijet background is estimated using data-driven techniques. The estimate is presented in the following. Its validation and the estimation of systematic uncertainties are also described.

In multijet background events both the lepton and τ_{had} candidates originate from quark- or gluon-initiated jets. The selected lepton candidate may either originate from a decay of a charm or bottom quark or from a misidentified hadron. Most lepton candidates of either source are accompanied by additional particles. In contrast, the leptons in the signal and previously discussed background processes are mostly isolated because they originate from decays of much heavier particles, specifically W and Z bosons. The τ_{had} candidates originate from misidentified quark- or gluon-initiated jets as in most background events. It was shown in previous analyses [98, 153, 154, 175] that there are only small differences between the kinematic distributions in multijet events with opposite and same electric charges of lepton and τ_{had} candidate, and that events with opposite and same charges are about as common. These properties are verified for the Υ distribution where necessary and utilised in the multijet background estimate.

The multijet contribution in the signal region is estimated from the data in the same-sign region, which matches the signal region except that the requirement of opposite lepton and τ_{had} charges is inverted. Differences between events with opposite and same lepton and τ_{had} candidate charges are studied in dedicated opposite-sign and same-sign multijet control regions, which match the signal and same-sign regions, respectively, except that the lepton isolation requirements are inverted (see Table 6.7). The multijet contributions in the same-sign region and in the multijet control regions are estimated by subtracting the $Z/\gamma^* \to \tau\tau$, $Z/\gamma^* \to \ell\ell$, top pair, and W+jets contributions from the data (see Figures 6.15 and 6.16). The Υ distribution in the multijet control region for the τ_e–τ_{had} channel is similar to that for the τ_μ–τ_{had} channel and can be found in Figure C.6. The event yields are summarised in Table 6.11.

The ratio of the multijet event yields in the opposite-sign and same-sign multijet control regions (see Table 6.12),

$$r_{\text{QCD}} = \frac{N^{\text{opposite}}_{\text{multijet}}}{N^{\text{same}}_{\text{multijet}}}, \tag{6.5}$$

is assumed to be the same in events with isolated and non-isolated leptons. Thus the estimated multijet event yield in the signal region for a given channel is

$$N^{\text{SR}}_{\text{multijet}} = r_{\text{QCD}} \cdot N^{\text{SSR}}_{\text{multijet}}, \tag{6.6}$$

where $N^{\text{SSR}}_{\text{multijet}}$ is the estimated multijet event yield in the same-sign region and the r_{QCD} value for the respective channel is used.

The accuracy of Eq. (6.6) is evaluated by studying the dependency of the r_{QCD} factors on the isolation variables. The $f_{p_{\text{T}},\text{iso}}$ and $f_{E_{\text{T}},\text{iso}}$ distributions in the multijet control regions can be found in Figures C.7 and C.8. The r_{QCD} dependencies on $f_{p_{\text{T}},\text{iso}}$ and $f_{E_{\text{T}},\text{iso}}$ are shown in Figure 6.17. The r_{QCD} values are mostly consistent with the average within the statistical uncertainties. The deviations right above $f_{E_{\text{T}},\text{iso}} = 0.06$ may originate from an inaccurate subtraction of the non-multijet contributions or from the multijet contributions themselves. They reach up to about 0.1. The r_{QCD} dependencies on $f_{p_{\text{T}},\text{iso}}$ are additionally studied in a region for which the $f_{p_{\text{T}},\text{iso}}$ requirement is dropped but $f_{E_{\text{T}},\text{iso}} < 0.06$ is required as in the signal region. An analogous study is performed for the $f_{E_{\text{T}},\text{iso}}$ variable. The observed deviations are similar to those in Figure 6.17. Consequently, a systematic uncertainty of 0.1 is assigned to r_{QCD}.

The systematic uncertainties in the subtraction of the non-multijet contributions from the multijet control regions are negligible due to their high multijet purities. This includes uncertainties in the tau polarisation assumed for $Z/\gamma^* \to \tau\tau$ events.

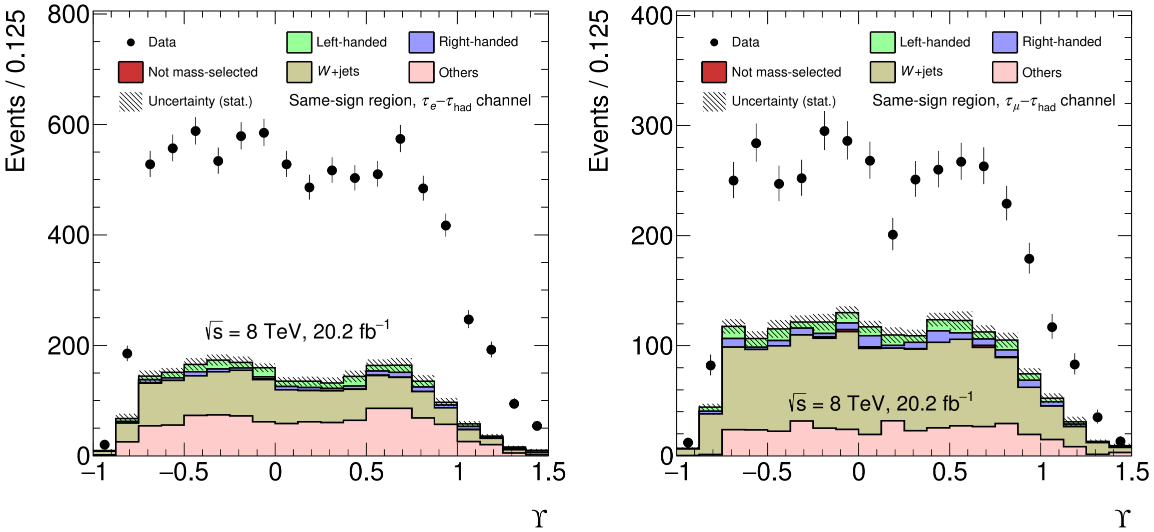

Figure 6.15: The ϒ distribution in the same-sign region for the τ_e–τ_{had} (left) and τ_μ–τ_{had} (right) channel. The contributions of $Z/\gamma^* \to \tau\tau$ and of $Z/\gamma^* \to \ell\ell$ and top pair (other) events are estimated from the simulation. The W+jets contribution is estimated as described in Section 6.4.2. The estimated multijet contribution corresponds to the difference of the data and the aforementioned contributions. The uncertainties are statistical. Adapted from Ref. [25].

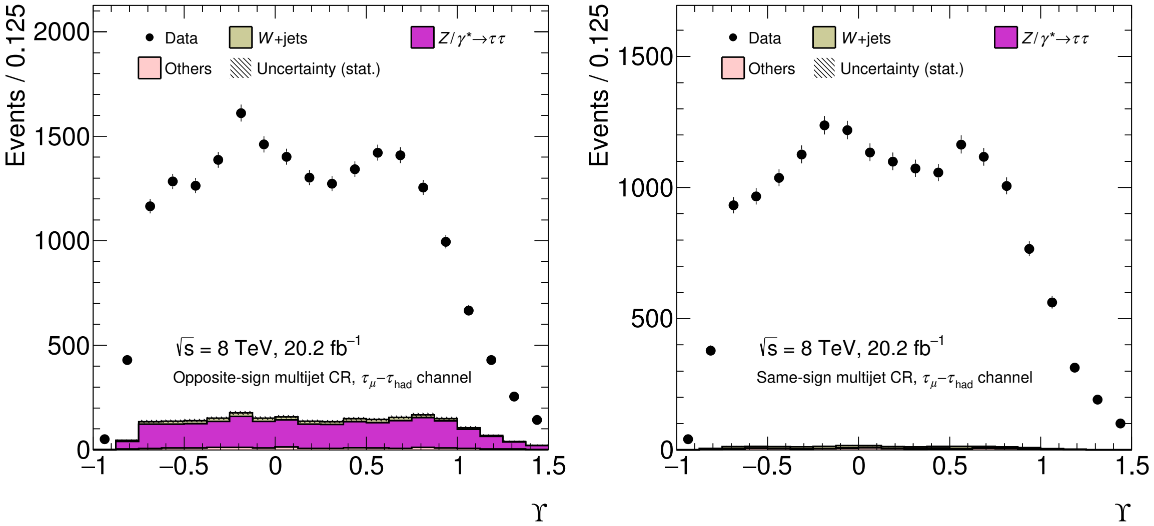

Figure 6.16: The ϒ distribution in the opposite-sign multijet control region (left) and the same-sign multijet control region (right) for the τ_μ–τ_{had} channel. The contributions of $Z/\gamma^* \to \tau\tau$ and of $Z/\gamma^* \to \ell\ell$ and top pair (other) events are estimated from the simulation. The W+jets contribution is estimated as described in Section 6.4.2. The estimated multijet contribution corresponds to the difference of the data and the aforementioned contributions. The uncertainties are statistical. Adapted from Ref. [25].

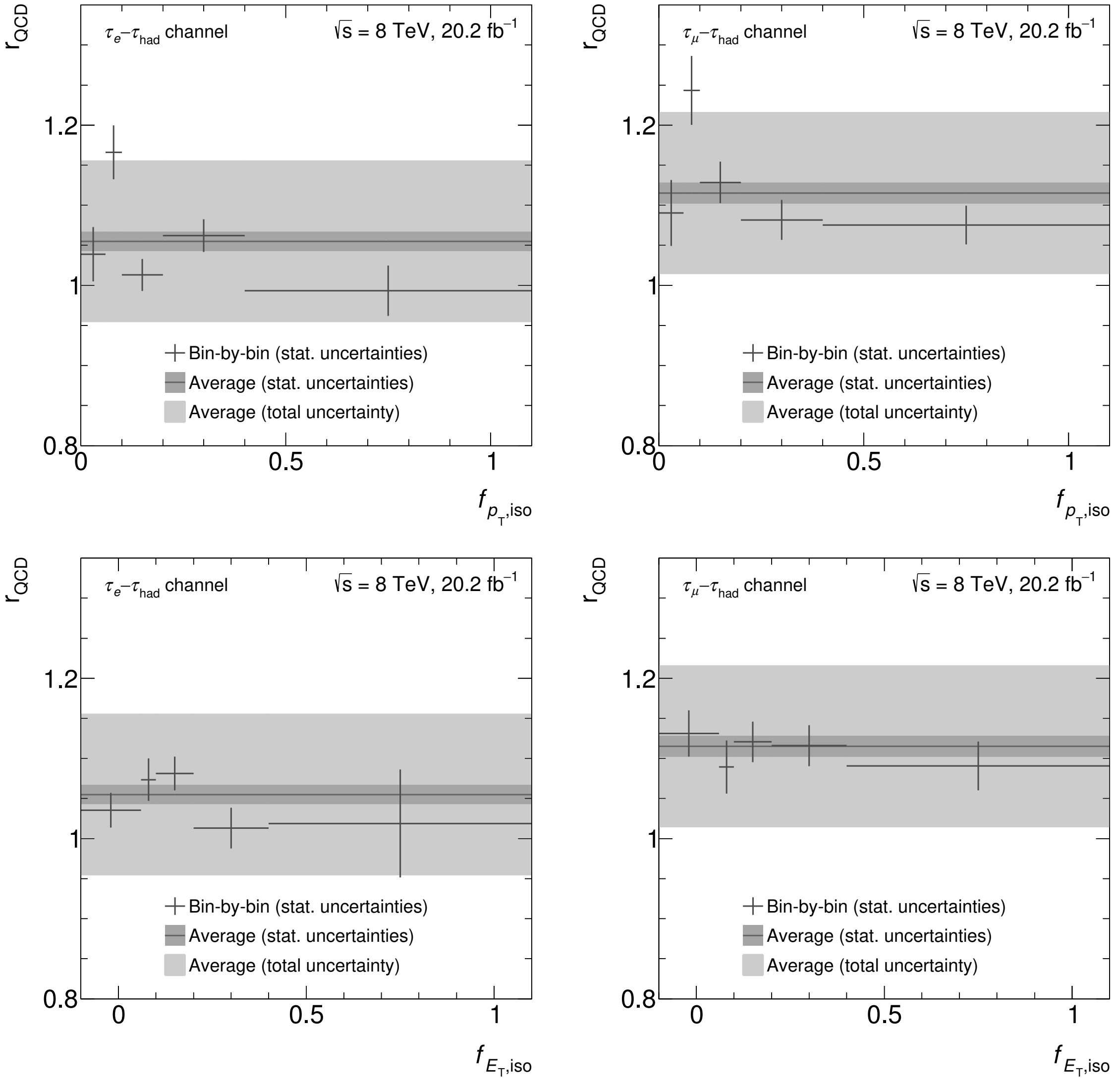

Figure 6.17: Dependence of r_{QCD} on $f_{p_{\mathrm{T}},\mathrm{iso}}$ (top) and $f_{E_{\mathrm{T}},\mathrm{iso}}$ (bottom) in the multijet control region for the τ_e–τ_{had} (left) and τ_μ–τ_{had} (right) channels. The average r_{QCD} value in the multijet control region and the statistical uncertainties are indicated. The total r_{QCD} uncertainties are shown as well. They include the systematic uncertainty of 0.10 in both channels, which is estimated from these distributions.

	τ_e–τ_{had} channel					
	Data	Data−non-multijet	$Z/\gamma^* \to \tau\tau$	$Z/\gamma^* \to \ell\ell$	Top pair	W+jets
Same-sign region	8303	6000 ± 120	298 ± 11	955 ± 35	64 ± 4	990 ± 70
Opposite-sign CR	23787	19960 ± 160	3210 ± 40	184 ± 19	76 ± 4	356 ± 28
Same-sign CR	19283	18910 ± 140	90 ± 6	124 ± 11	16.6 ± 2.0	141 ± 27

	τ_μ–τ_{had} channel					
	Data	Data−non-multijet	$Z/\gamma^* \to \tau\tau$	$Z/\gamma^* \to \ell\ell$	Top pair	W+jets
Same-sign region	3945	2170 ± 110	252 ± 11	309 ± 19	73 ± 4	1140 ± 80
Opposite-sign CR	20843	18450 ± 150	2019 ± 31	33 ± 7	110 ± 5	230 ± 40
Same-sign CR	16740	16540 ± 130	22.6 ± 3.1	27 ± 5	41.1 ± 3.3	108 ± 26

Table 6.11: Event yields in the same-sign region and the opposite-sign and same-sign multijet control regions in the τ_e–τ_{had} (top) and τ_μ–τ_{had} (bottom) channels. The $Z/\gamma^* \to \tau\tau$, $Z/\gamma^* \to \ell\ell$, and top pair contributions are taken from the simulation. The W+jets event yields are obtained by scaling the simulated yields with the k_W factors given in Table 6.9. The multijet contributions are estimated by subtracting the aforementioned contributions from the data. The uncertainties are statistical. For the W+jets contributions the uncertainties in the k_W scaling are also considered.

Channel	τ_e–τ_{had}	τ_μ–τ_{had}
r_{QCD}	$1.05 \pm 0.01\,(\text{stat}) \pm 0.10\,(\text{syst})$	$1.12 \pm 0.01\,(\text{stat}) \pm 0.10\,(\text{syst})$

Table 6.12: Relative multijet event yields with opposite and same lepton and τ_{had} candidate charges, r_{QCD}, as defined in Eq. (6.5). The values are determined in the multijet control regions and used in Eq. (6.6).

The shapes of the estimated Υ distributions in multijet events in the same-sign region are directly used in the signal region. This procedure is validated by comparing the estimated shapes in the multijet control and same-sign regions (see Figure 6.18). The differences between the shapes in the opposite-sign and same-sign multijet control regions are fully covered by the statistical uncertainties in the same-sign region. Additionally, there are no large differences between the shapes in the multijet control regions and those in the same-sign region. It is concluded that there are only minor differences between the τ_{had} candidates, from which the Υ observable is calculated, in multijet events with isolated and non-isolated leptons. Therefore, the shape differences between the Υ distributions in the signal and same-sign regions are similar to those between the opposite-sign and same-sign multijet control regions and covered by the statistical uncertainties in the same-sign region.

The same-sign region is well suited for use in the multijet estimate because it is very similar to the signal region. In particular, the systematic uncertainties are relatively small and can be studied without simulated multijet events. However, the multijet event yields in the same-sign region are slightly smaller than those in the signal region. This leads to significant statistical uncertainties in the multijet contributions in the signal region. Additional statistical uncertainties arise from the subtraction of the significant non-multijet contributions in the same-sign region. The template fits that determine the tau polarisation are designed to estimate these uncertainties accurately (see Section 6.6).

In the distributions of the Υ or other observables shown for the signal region or other regions in which

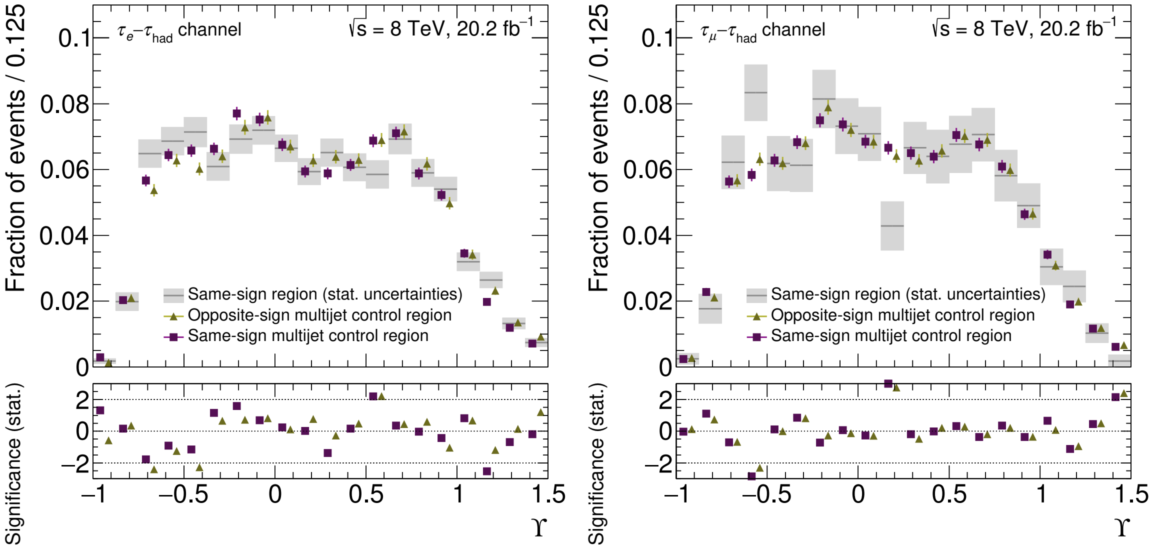

Figure 6.18: Normalised multijet distributions obtained in the same-sign region and in the opposite-sign and same-sign multijet control regions in the τ_e–$\tau_{\rm had}$ (left) and τ_μ–$\tau_{\rm had}$ (right) channel. The uncertainties are statistical. The significances, calculated from the statistical uncertainties, of the differences between the shapes in the same-sign region and those in the multijet control regions are shown as well. Adapted from Ref. [25].

the opposite-sign requirement is applied, the shape of the multijet contributions are estimated in the respective same-sign region. The resulting distributions are scaled using the $r_{\rm QCD}$ values.

Further studies of the properties of multijet background events are beyond the scope of this analysis. Studies in previous analyses such as in Ref. [176] show that identified muons which do not stem from decays of heavy bosons mostly originate from (semi-)leptonic decays of hadrons that involve charm or bottom quarks. In contrast, identified electrons may also originate from misidentifed quark- or gluon-initiated jets. Therefore, multijet background events are more common in the τ_e–$\tau_{\rm had}$ channel than in the τ_μ–$\tau_{\rm had}$ channel. The differences between the processes involved in events with identified electrons and muons may cause further differences between the channels, such as those between the measured $r_{\rm QCD}$ values.

6.4.4 Validation of Background Estimates and Comparison of ϒ Distributions

The top pair, $Z/\gamma^* \rightarrow \ell\ell$ ($\ell \rightarrow \tau_{\rm had}$), and W+jets background estimates are validated using data. Thereafter, the ϒ distributions for the backgrounds for which the $\tau_{\rm had}$ candidate stems from a quark- or gluon-initiated jet are compared to each other.

The modelling of the top pair background is validated in a dedicated kinematic region, which is defined as follows:

- Only preselected events are considered (see Section 6.3.2).
- The same requirements on the lepton and $\tau_{\rm had}$ candidates are made as in the signal region selection (see Section 6.3.3). Additionally, the $\tau_{\rm had}$ candidate must have $p_{\rm T}^{\tau_{\text{had-vis}}} < 100\,\text{GeV}$.
- At least two jets with $|\eta^{\rm jet}| < 2.5$ and $p_{\rm T}^{\rm jet} > 30\,\text{GeV}$ are required.

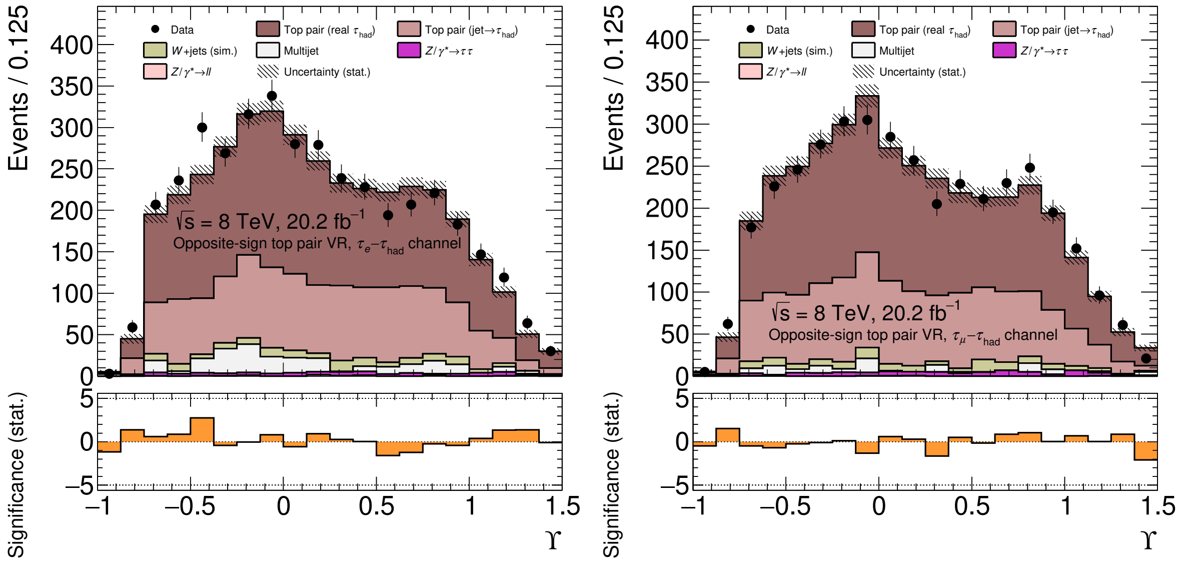

Figure 6.19: The Υ distribution in the top pair validation region for the τ_e–τ_{had} (left) and τ_μ–τ_{had} (right) channels. The shape of the W+jets contribution is estimated from the simulation. The uncertainties are statistical. The significance of the difference of the predicted and data event yields, which is calculated considering only statistical uncertainties, is shown as well. Top pair contributions in which the τ_{had} candidate is mimicked by a lepton are negligible.

- One jet with $p_{\text{T}}^{\text{jet}} > 30\,\text{GeV}$ must be tagged [177] as a bottom quark jet.
- $E_{\text{T}}^{\text{miss}}$ must exceed 30 GeV.
- The sum of the absolute p_{T} values of the lepton, τ_{had} candidate, and jets must exceed 170 GeV.

The Υ distributions in the opposite-sign top pair validation region are shown in Figure 6.19. The differences between the estimate and data are of the order of the statistical uncertainties. No additional uncertainties have to be assigned to the top pair background. In addition to verifying the top pair background estimate, this test gives a first indication that real τ_{had} decays are modelled well by the simulation. The tau decays in the top pair sample are modelled by the Tauola algorithm as in the signal sample. However, there are about ten times fewer real τ_{had} decays in the top pair validation region than in the signal region and the taus in this region are exclusively left-handed because they originate from W boson decays. Hence, it cannot be judged whether the modelling is sufficiently accurate for the signal events in the signal region.

The modelling of the Υ distributions in $Z/\gamma^* \to \ell\ell$ ($\ell \to \tau_{\text{had}}$) events is studied in a validation region, in which the m_{vis} requirement is altered to $85 < m_{\text{vis}} < 97\,\text{GeV}$ (see Figure 6.20). The distribution in the τ_e–τ_{had} channel shows that the $Z/\gamma^* \to ee$ ($e \to \tau_{\text{had}}$) contribution is described adequately by the simulation. As in Figure 6.9, the $Z/\gamma^* \to ee$ ($e \to \tau_{\text{had}}$) contribution is not peaked at one as could be expected for τ_{had} candidates mimicked by electrons. It can be assumed that electrons are more likely to be misidentifed as τ_{had} decays if they lose a significant fraction of their energy via bremsstrahlung. The reconstructed Υ value of such a τ_{had} candidate is smaller than one if the bremsstrahlung photon is included in the reconstructed $\tau_{\text{had-vis}}$ momentum but only the remaining electron momentum is measured in the ID. In the τ_μ–τ_{had} channel, the $Z/\gamma^* \to \mu\mu$ ($\mu \to \tau_{\text{had}}$) fraction is below 10% in the validation region. Nevertheless, the validation region contains about twice as many $Z/\gamma^* \to \mu\mu$ ($\mu \to \tau_{\text{had}}$) events

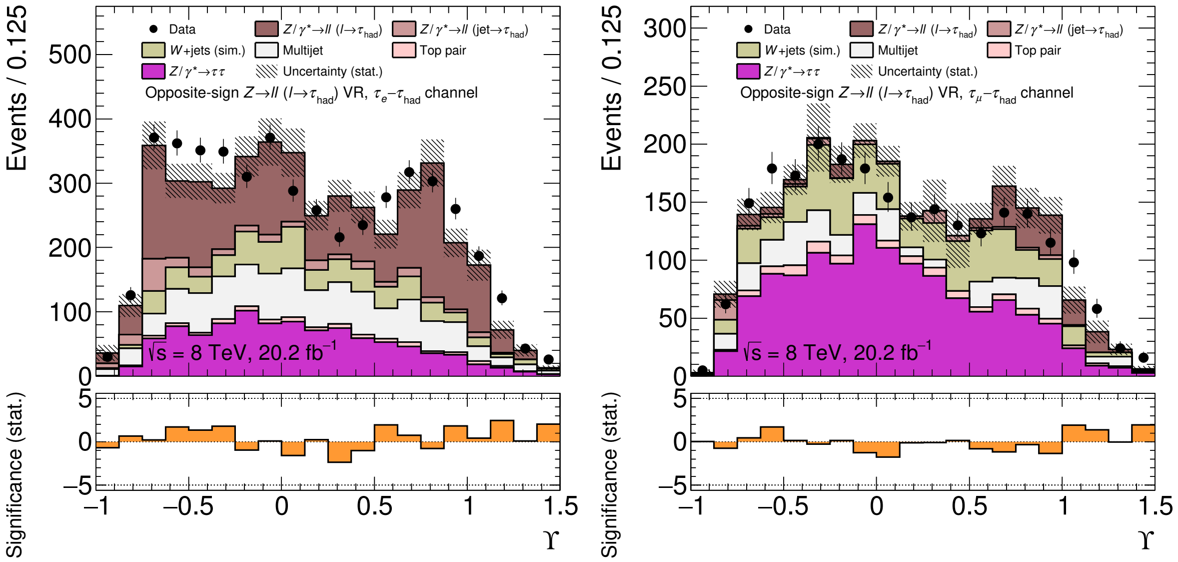

Figure 6.20: The Υ distributions in the $Z/\gamma^* \to \ell\ell$ ($\ell \to \tau_{\text{had}}$) validation region for the τ_e–τ_{had} (left) and τ_μ–τ_{had} (right) channels. The shape of the W+jets contribution is estimated from the simulation. The uncertainties are statistical. The significance of the difference of the predicted and data event yields, which is calculated considering only statistical uncertainties, is shown as well.

as the signal region and the fraction is about 28 times larger. Therefore, the lack of unexpected features alone shows that these events are modelled adequately for this analysis.

The data-driven W+jets background estimate is tested in the opposite-sign and same-sign W+jets VR1 (see Table 6.7). The purities of these regions are 60–80% dependent on the channel and the lepton and τ_{had} charge requirement. The W+jets event yields in the opposite-sign (same-sign) W+jets VR1 are about seven times larger than those in the signal (same-sign) region for both channels. Additionally, the W+jets VR1 lies between the W+jets control and signal regions. It is thus suitable for a validation of the W+jets estimate. While the studies on the W+jets background which are summarised in Section 6.4.2 and utilised in Ref. [25] were developed in Ref. [174], this test is performed specifically for this thesis. The W+jets contributions estimated from the data in the W+jets control regions are scaled using Eq. (6.4). The linear shape corrections for the transfer from the W+jets control regions to W+jets VR1 are applied.

The distributions in the same-sign VR1 are shown in Figure 6.21. In the τ_μ–τ_{had} channel, the data are described well by the W+jets, signal, $Z/\gamma^* \to \ell\ell$, and top pair contributions and no indications for a noticeable multijet contribution are found. In the τ_e–τ_{had} channel a substantial multijet contribution is estimated. The Υ distributions in the opposite-sign VR1 are shown in Figure 6.22. In the τ_μ–τ_{had} channel, the data are described well by the estimate. The data distribution in the τ_e–τ_{had} channel is also described well over most of the Υ range. The slight overestimation around $0.2 \leq \Upsilon \leq 0.7$ may result from inaccuracies in the multijet background estimate, which was not validated for use in this region. Alternatively, the deviations may be in the W+jets contribution. Irrespective of this, the deviations are of the order of the statistical uncertainties in the W+jets data events in the signal region and much smaller than the overall statistical uncertainties in the signal region.

The W+jets VR2 contains significant signal and multijet contributions in both channels. The W+jets fraction in the opposite-sign W+jets VR2 is only about 30%. Therefore, no conclusions about the modelling of W+jets events can be drawn from W+jets VR2.

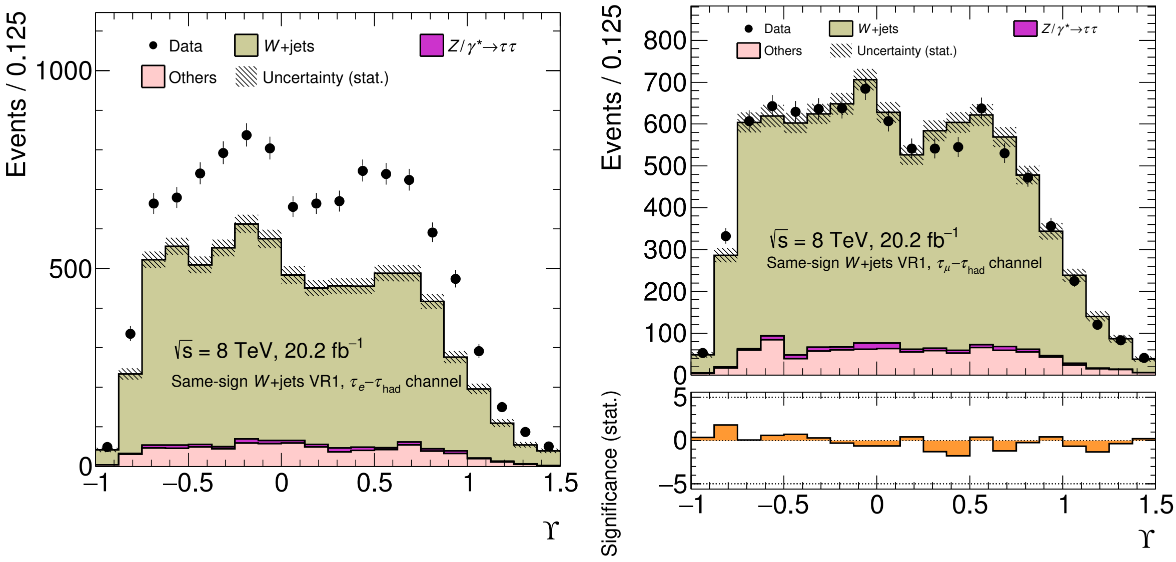

Figure 6.21: The Υ distributions in the same-sign W+jets VR1 for the τ_e–τ_{had} (left) and τ_μ–τ_{had} (right) channels. The W+jets background is estimated analogously to the signal region. In the τ_e–τ_{had} channel, the multijet contribution is estimated from the difference between the data and the estimate of the remaining contributions. In the τ_μ–τ_{had} channel the difference is consistent with zero (-100 ± 400 over the full Υ range), so no multijet contribution is estimated. The uncertainties are statistical. In the τ_μ–τ_{had} channel the significance of the difference of the predicted and data event yields, which is calculated considering only statistical uncertainties, is also shown.

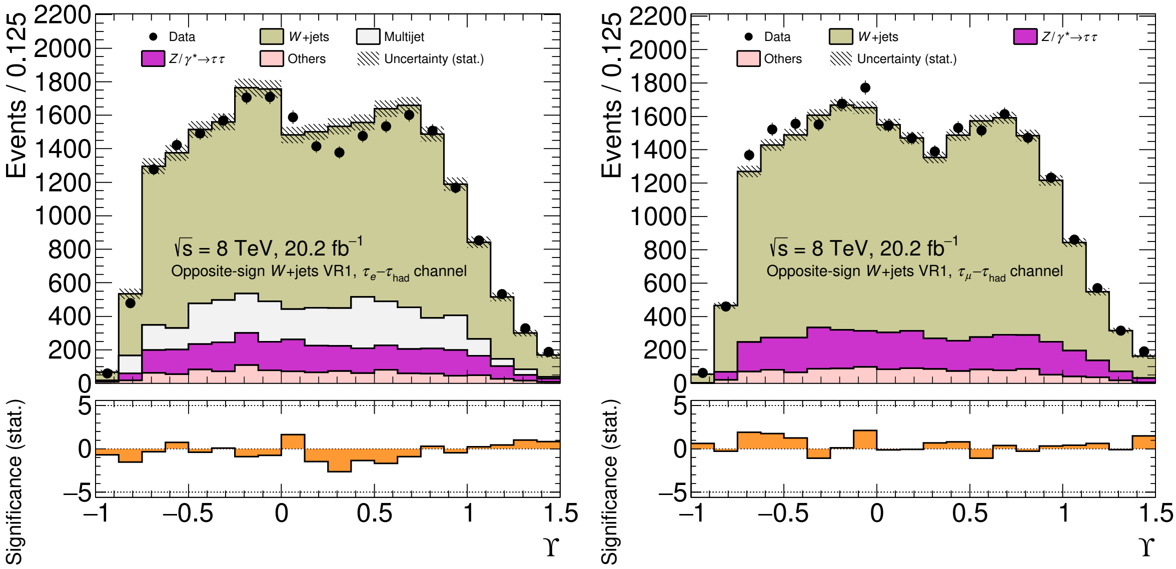

Figure 6.22: The Υ distributions in the opposite-sign W+jets VR1 for the τ_e–τ_{had} (left) and τ_μ–τ_{had} (right) channels. The W+jets background is estimated analogously to the signal region. In the τ_e–τ_{had} channel, the multijet contribution is estimated from the same-sign W+jets VR1 analogously to the signal region. In the τ_μ–τ_{had} channel it is found negligible (see Figure 6.21) and it is therefore omitted. The uncertainties are statistical. The significance of the difference of the predicted and data event yields, which is calculated considering only statistical uncertainties, is also shown.

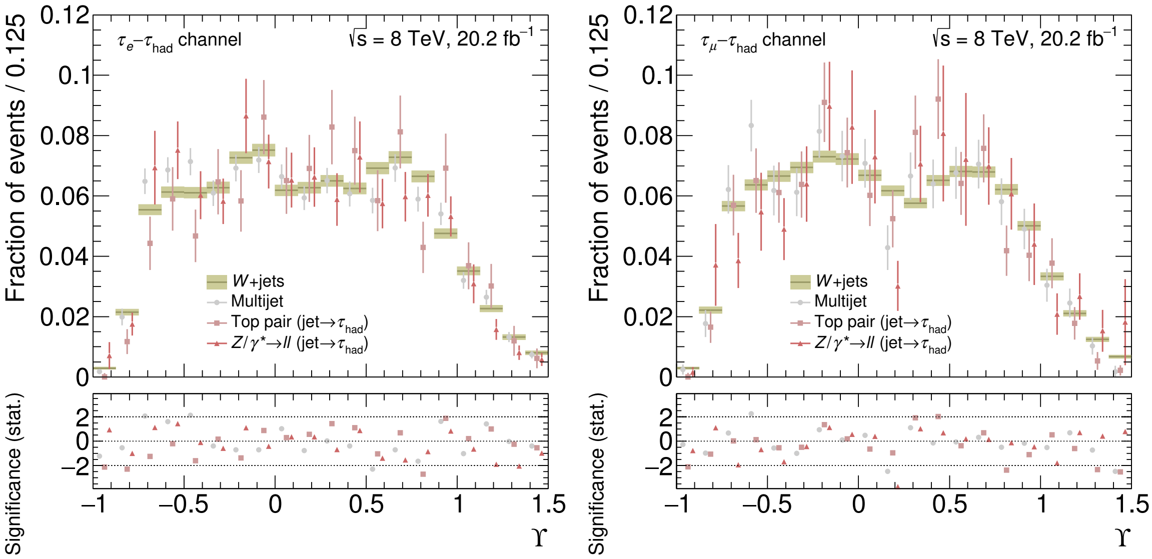

Figure 6.23: Normalised, estimated Υ distributions in W+jets, multijet, top pair (jet→ τ_{had}), and $Z/\gamma^* \to \ell\ell$ (jet → τ_{had}) events in the signal region. The uncertainties are statistical.

In most background events the τ_{had} candidates originate from quark- or gluon-initiated jets. The shapes of the Υ distributions in W+jets, top pair (jet→ τ_{had}), and $Z/\gamma^* \to \ell\ell$ (jet → τ_{had}) events are expected to be similar, because there are only small differences between the quark–gluon composition of the τ_{had} candidates. Minor differences may result from differences between the p_{T} and other kinematic distributions. The shapes are compared to each other in Figure 6.23. Because the W+jets contribution is estimated using data, this comparison can be used to verify that the modelling of top pair (jet→ τ_{had}) and $Z/\gamma^* \to \ell\ell$ (jet → τ_{had}) events is adequate. The observed differences are of the order of the statistical uncertainties. In particular, it can be concluded that specific systematic uncertainties in the shape of the small $Z/\gamma^* \to \ell\ell$ (jet → τ_{had}) background, which is not studied in a dedicated validation region, are negligible. The shape of the Υ distribution in multijet events is similar to those of the remaining backgrounds with quark- or gluon-initiated jets that are misidentified as τ_{had} decays.

6.4.5 Distributions of Kinematic Variables in the Signal Region

The distributions of various kinematic variables in the signal region are shown in Figures 6.24 and 6.25. The differences between the estimates and the data are mostly of the order of the statistical uncertainties. There are no indications for modelling issues that may affect the measurement. A similar level of agreement has already been observed at earlier stages of the event selection (see Figures 6.1 and 6.3). In the τ_μ–τ_{had} channel, the overall estimated event yield in the signal region is 1.3% larger than the data yield (see also Table 6.3). The event yields are consistent within 1.5σ when considering the statistical, r_{QCD} scaling, and k_W scaling uncertainties, as done in Table 6.3. The difference is also covered by the systematic uncertainties in the muon trigger efficiency and other systematic uncertainties (see Section 6.5).

The $p_{\text{T}}^{\text{track}}$ and Υ distributions are shown in Figures 6.26 and 6.27. The data in these distributions were blinded during the development of the analysis (see Section 6.3). The $p_{\text{T}}^{\text{track}}$ distributions are described well by the estimate. The estimated and data Υ distributions differ around $\Upsilon = 1$ (mainly in the τ_μ–τ_{had} channel) and in particular close to $\Upsilon = 1.5$. These effects are explained in the following sections.

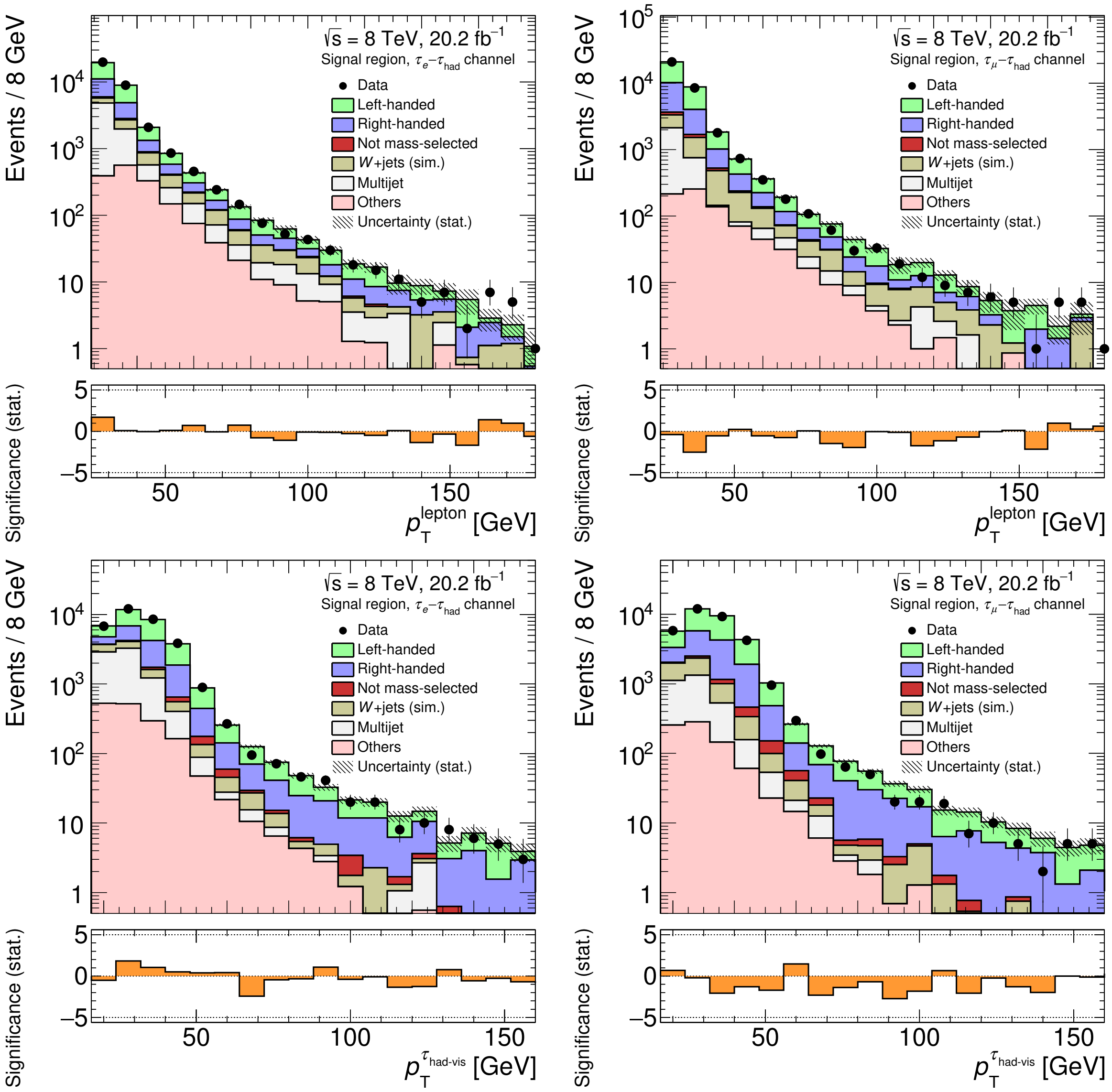

Figure 6.24: Distributions of $p_{\mathrm{T}}^{\mathrm{lepton}}$ (top) and $p_{\mathrm{T}}^{\tau_{\text{had-vis}}}$ (bottom) in the signal region for the τ_e–τ_{had} (left) and τ_μ–τ_{had} (right) channels. The shape of the W+jets contribution is estimated from the simulation. The remaining contributions are estimated as for the Υ distribution. The uncertainties are statistical. The significance of the difference of the predicted and data event yields, which is calculated considering only statistical uncertainties, is also shown.

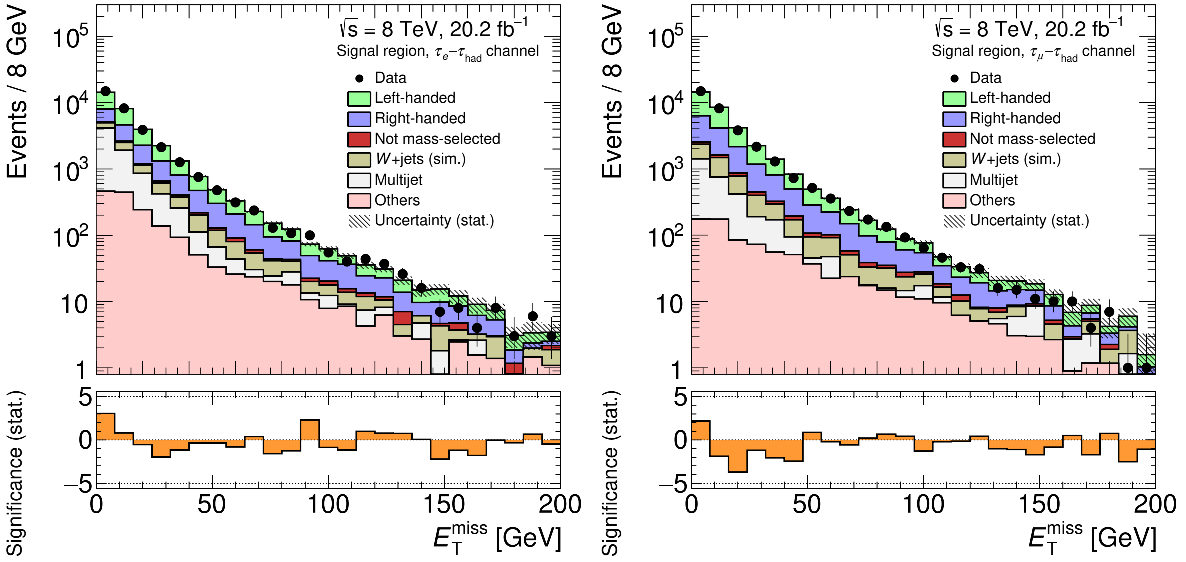

Figure 6.25: Distribution of $E_{\mathrm{T}}^{\mathrm{miss}}$ in the signal region for the τ_e–τ_{had} (left) and τ_μ–τ_{had} (right) channels. The shape of the W+jets contribution is estimated from the simulation. The remaining contributions are estimated as for the Υ distribution. The uncertainties are statistical. The significance of the difference of the predicted and data event yields, which is calculated considering only statistical uncertainties, is also shown.

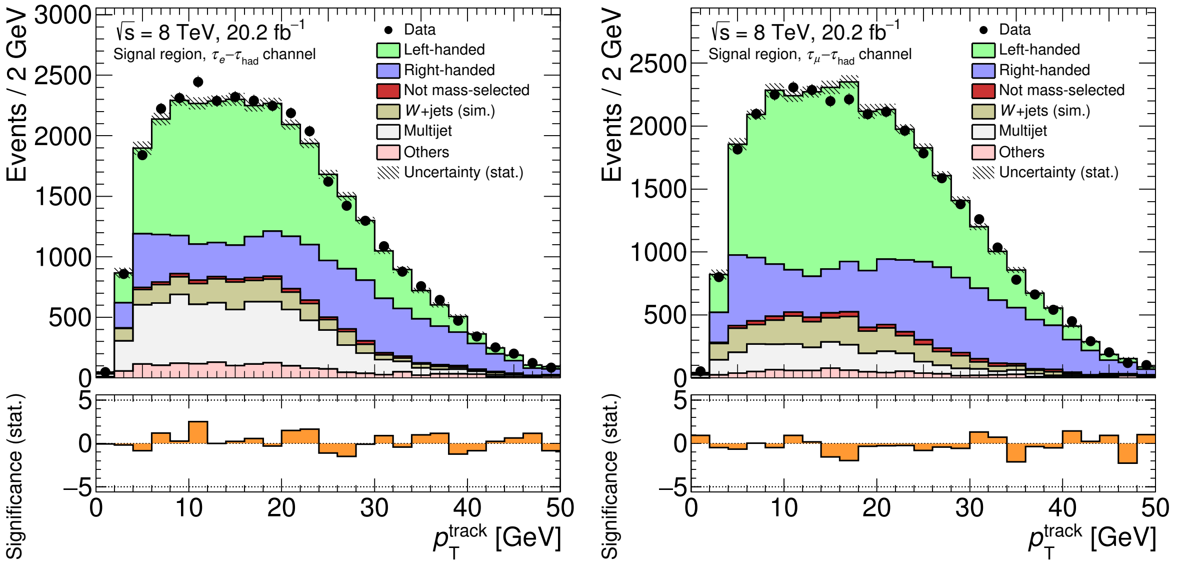

Figure 6.26: Distribution of $p_{\mathrm{T}}^{\mathrm{track}}$ in the signal region for the τ_e–τ_{had} (left) and τ_μ–τ_{had} channel. The uncertainties are statistical. The significance of the difference of the predicted and data event yields, which is calculated considering only statistical uncertainties, is also shown.

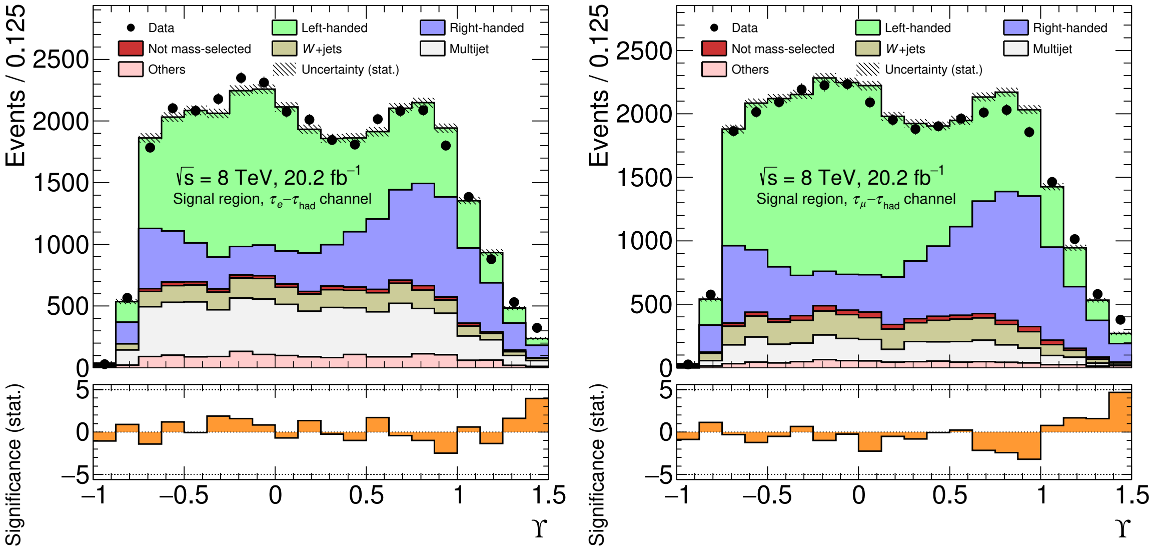

Figure 6.27: Distribution of Υ in the signal region for the τ_e–$\tau_{\rm had}$ (left) and τ_μ–$\tau_{\rm had}$ channel. The signal contribution is estimated from the simulation, in particular the tau polarisation is as predicted. The uncertainties are statistical. The significance of the difference of the predicted and data event yields, which is calculated considering only statistical uncertainties, is also shown. Adapted from Ref. [25].

6.5 Systematic Uncertainties

The determination of the tau polarisation using template fits relies on the accuracy of the shapes and of the normalisation of the templates. About 70% (80%) of the events in the signal region for the τ_e–$\tau_{\rm had}$ (τ_μ–$\tau_{\rm had}$) channel are signal events. The largest backgrounds are estimated using data-driven techniques. Therefore, uncertainties in the signal templates are dominant among the uncertainties in the simulated samples. Specifically, uncertainties that can affect the shapes of the signal templates or alter the acceptance differently for events with left- and right-handed taus lead to uncertainties in the tau polarisation.

In the following, the systematic uncertainties in the simulated signal and background samples are discussed. They are grouped into experimental and theory uncertainties. The uncertainties in the template shapes are shown. Most normalisation uncertainties are negligible, exceptions are noted. The section concludes with compilations of the shape and normalisation uncertainties.

The uncertainties in the data-driven estimates of the W+jets and multijet contributions have mostly been covered in Sections 6.4.2 and 6.4.3, respectively. Only the uncertainties resulting from the use of simulated samples in their estimates remain to be evaluated in this section. This is done by propagating the uncertainties in the simulated samples through to the data-driven estimates. The largest of these uncertainties in the W+jets contribution are in the ratio $N_{\rm sim}^{\rm signal\ region}/N_{\rm sim}^{\rm WCR}$ of simulated W+jets events in Eq. (6.4). The largest uncertainties in the multijet estimate are the analogous uncertainties in the normalisation of the W+jets contribution in the same-sign region.

6.5.1 Experimental Uncertainties

The largest experimental uncertainties are in the modelling of $\tau_{\rm had}$ identification and of the energy response to $\tau_{\rm had}$ decays in signal events. Both can effect the shapes of the signal Υ distributions. The uncertainties in the Υ distribution are specific to this analysis and estimated using new techniques, which are documented in detail. The remaining experimental uncertainties are estimated using standard techniques, which are recommended by ATLAS. They are small and thus only described briefly.

Tau Identification Uncertainties

The dominant τ_{had} identification uncertainties are related to the effect of the τ_{had} identification on the shapes of the left- and right-handed signal templates. Real τ_{had} decays are more likely to be identified if their signature is particularly rare for quark- or gluon-initiated jets. This is for example the case for decays that involve few neutral pions. The shapes of the Υ distributions for the individual τ_{had} decay topologies (see Table 2.5) differ significantly. Hence, the inclusive left- and right-handed distributions depend on the decay topology composition and are altered by the τ_{had} identification (see Figure 6.28).

The shapes of the distributions for the individual decay topologies are altered by the τ_{had} identification as well. The underlying effects cannot be modelled analytically and they may be mismodelled in the simulation. The related uncertainties are estimated from observed inaccuracies in the modelling of the τ_{had} identification input variables. The input variables of τ_{had} identification are defined in Table 3.2 and simply referred to as input variables in the following.

The distributions of some input variables are noticeably different for left- and right-handed taus (see the example in Figure 6.29). This makes it very difficult to evaluate the relevant uncertainties, which are those in the modelling of the detector response, by studying the input variable distributions in the signal region: the related discrepancies between the data and estimated distributions would have to be disentangled from possible discrepancies caused by an incorrectly assumed tau polarisation.

Instead, the quality of the modelling is evaluated in the opposite-sign W+jets control region and, complementarily, in the opposite-sign top pair validation region. The τ_{had} candidates in the W+jets control region originate from quark- or gluon-initiated jets. They are, however, similar to real τ_{had} decays because they pass τ_{had} identification. In particular, the shape of the Υ distribution resembles that in simulated $Z/\gamma^* \rightarrow \tau\tau$ decays in the signal region. This indicates that the neutral-hadron multiplicities are similar to real τ_{had} decays. The simulated $Z/\gamma^* \rightarrow \tau\tau$ contributions contain a mixture of events with left- and right-handed taus. Hence, the τ_{had} candidates in the W+jets control region can represent decays of left- and right-handed taus.

In addition to modelling inaccuracies present for real τ_{had} decays, the simulated quark- and gluon-initiated jets may be affected by inaccuracies in the modelling of parton showers. These may increase or coincidentally decrease the differences between the data and estimated input variable distributions. In contrast, the majority of the τ_{had} candidates in the top pair validation region originate from real τ_{had} decays of left-handed taus. Inaccuracies in the modelling that mainly affect right-handed taus may be underrepresented in this region.

The input variable distributions in the W+jets control region for the τ_μ–τ_{had} channel are shown in Figures 6.30 and 6.31. The distributions in the top pair validation region can be found in Figures D.1 and D.2. The quality of the modelling is similar in the τ_e–τ_{had} channel. The modelling is evaluated using the estimated, CDF_{est}, and data, CDF_{data}, cumulative distribution functions. An example is shown in Figure 6.32.

For the continuous variables, which are all used variables except for $N_{\text{track}}^{\text{iso}}$ and N_{π^0}, the variations

$$\text{CDF}_{\text{data}}(x') = \text{CDF}_{\text{est}}(x) \qquad \Rightarrow \qquad \text{var}(x) = x' - x \tag{6.7}$$

are computed, where x and x' are input variable values (see Figure 6.32). If the variables in the estimate are varied by $\text{var}(x)$, the resulting cumulative distribution function and the shape of the input variable

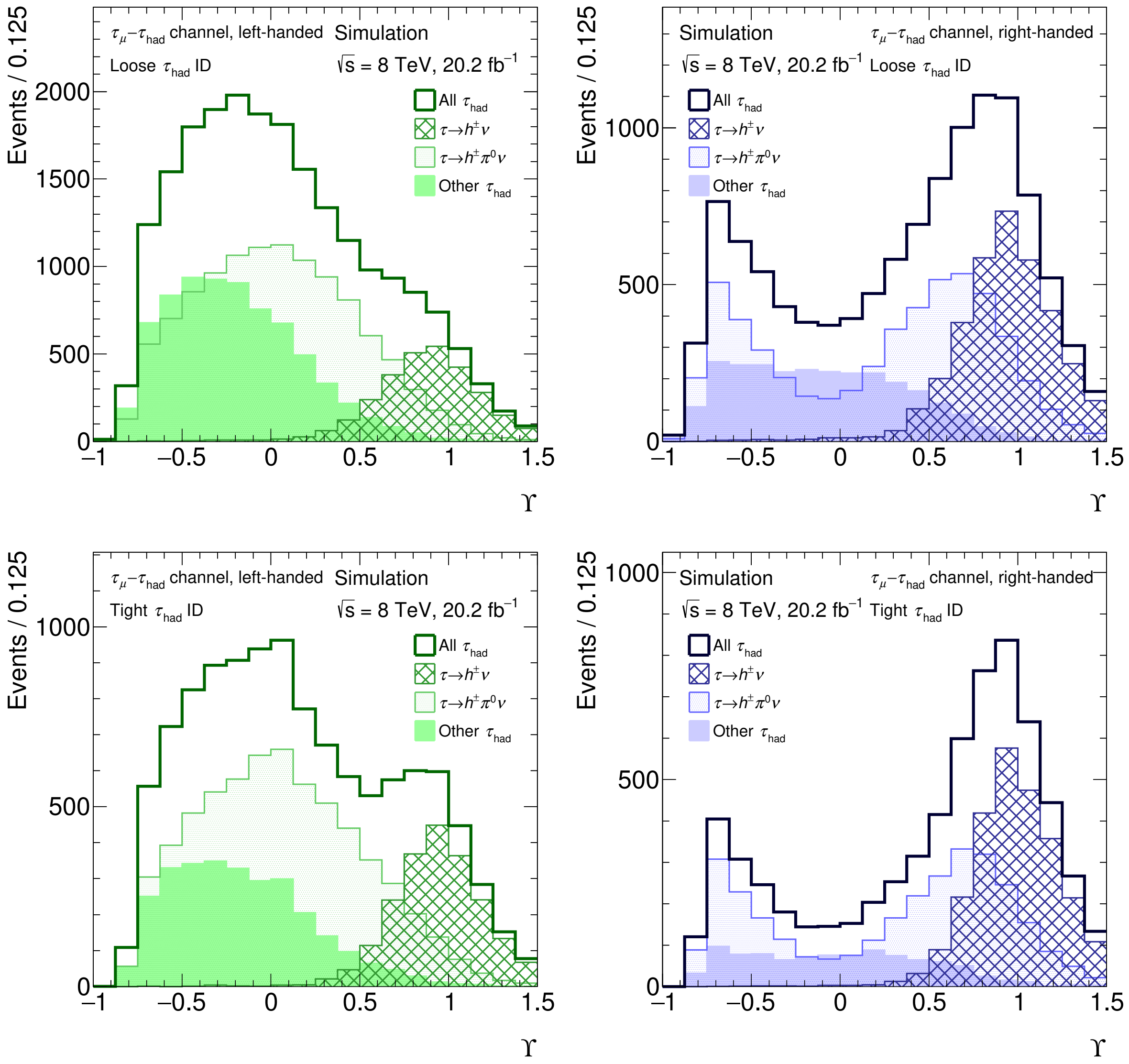

Figure 6.28: The Υ distributions for events with left-handed (left) and right-handed (right) taus in simulated signal events in the τ_μ–τ_{had} channel. The *loose* (top) or *tight* (bottom) level of τ_{had} identification is applied. The remaining selection is as in the signal region. In addition to the inclusive distributions, the constituent distributions corresponding to generated taus that decay in the $\tau \to h^\pm\nu$ and $\tau \to h^\pm\pi^0\nu$ ($h^\pm$ denotes $\pi^\pm$ or $K^\pm$) topologies are overlaid, as well as that of the remaining decays. The latter mainly consist of $\tau \to h^\pm \geq 2\pi^0\nu$ decays. The distributions are normalised according to their respective cross-sections. Here, the polarisation is taken from the simulation.

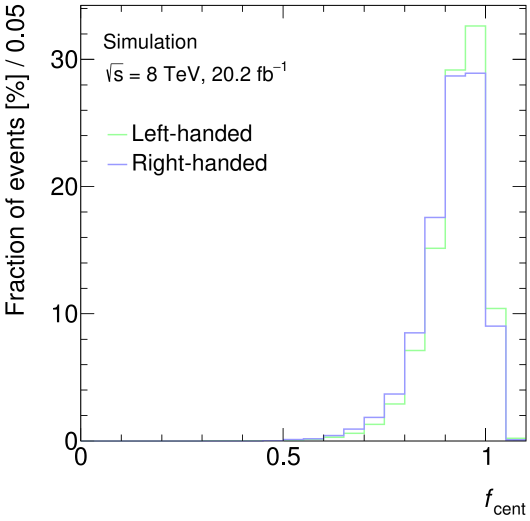

Figure 6.29: Normalised, simulated f_cent distributions in signal events with left- and right-handed taus in the signal region for the τ_μ–τ_had channel.

distribution match those in data. The variations are computed separately in the τ_e–τ_had and τ_μ–τ_had channels and found to be similar. For the integer input variables the methodology is adapted to discrete input variable values as documented in Appendix D.1. The variations are interpreted as uncertainties in the modelling of the input variables. Their impact on the signal in the signal region is evaluated by varying one input variable at a time by var(x) for all signal events. Thereafter, the *medium* τ_had identification criteria and the remaining selection are applied as usual. The differences between the resulting and the nominal Υ distributions are considered $+1\sigma$ variations. The -1σ variations are computed by varying the input variable values by $-$var(x) and proceeding analogously.

The impact of the uncertainties in a specific input variable on the measurement depends on its importance in τ_had identification, its correlation with the Υ observable, and the quality of the modelling. The largest uncertainties are related to f_cent and further noticeable contributions are due to S_track and f_track. The effect of the uncertainties in these variables from the W+jets control region on the signal inside the mass-selected region for the τ_μ–τ_had channel is shown in Figures 6.33 and 6.34. The impact on the signal in the τ_e–τ_had channel and on the signal inside the fiducial region is similar as shown in Appendix D.1. The variations of the signal contributions outside the mass-selected or fiducial regions have a negligible effect on the measurement. The uncertainties in the other input variables are also negligible. The uncertainties estimated from the top pair validation region are smaller than those from the W+jets control region.

The impact of the input variable variations on the signal normalisation is documented in Table 6.13. The combined effect of the uncertainties in the input variables is compared with the total τ_had identification efficiency uncertainties from Ref. [82]. They were obtained in $Z/\gamma^* \to \tau\tau$ decays using an orthogonal method and are the recommended τ_had identification efficiency uncertainties in ATLAS. For the signal in the signal region, the total uncertainty is 2.9%; it is composed of a 2.5% systematic uncertainty and a 1.5% statistical uncertainty. The input variable variations obtained from the W+jets control region have a similar combined effect on the signal normalisation, which indicates that they are reasonable. The variations from the top pair control region are smaller, which is also the case for the related Υ shape variations. Hence, the variations from the W+jets control region are chosen.

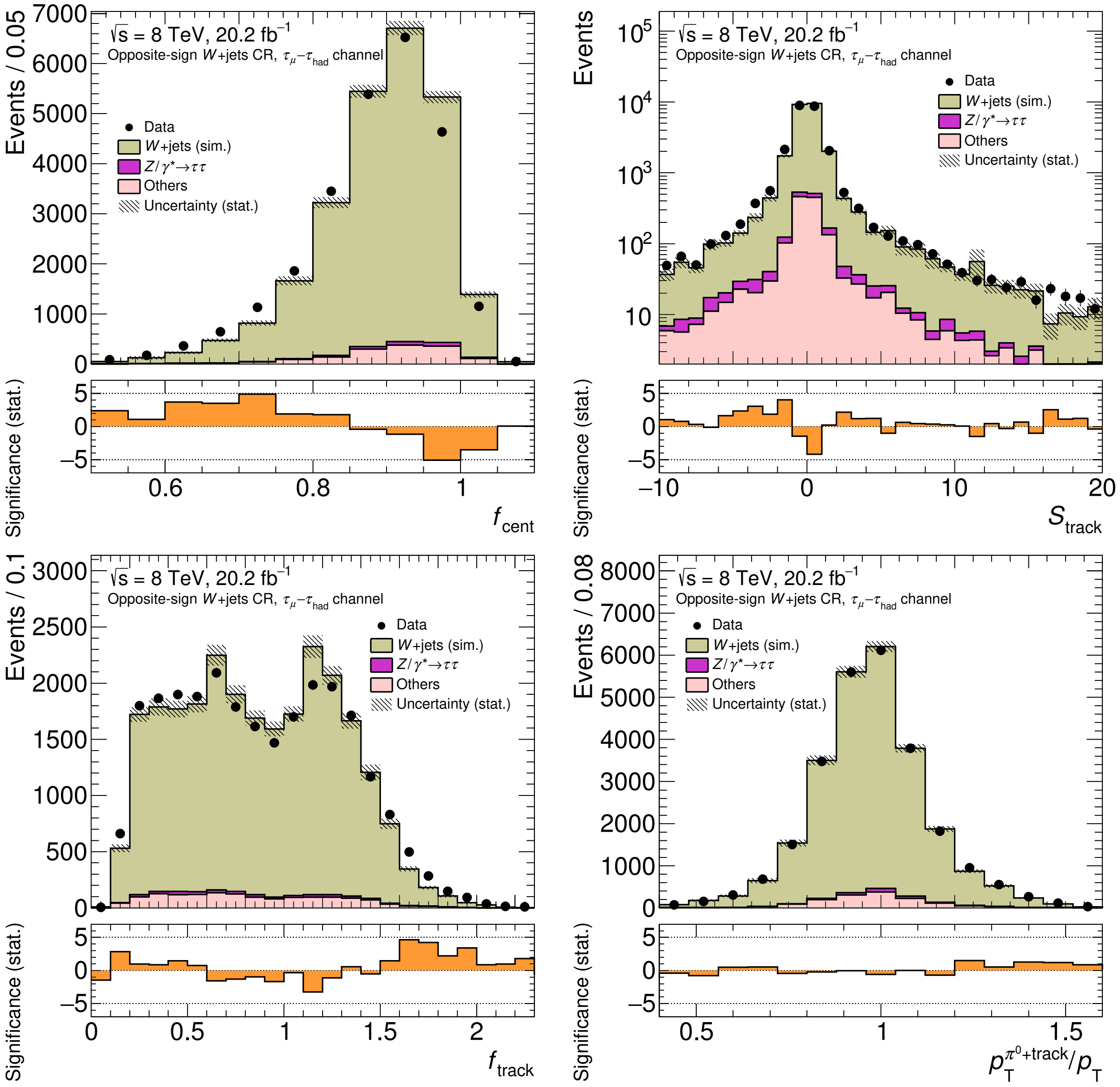

Figure 6.30: Distributions of τ_{had} identification input variables in the W+jets control region for the τ_μ–τ_{had} channel. The shape of the distributions in W+jets events is estimated from the simulation.

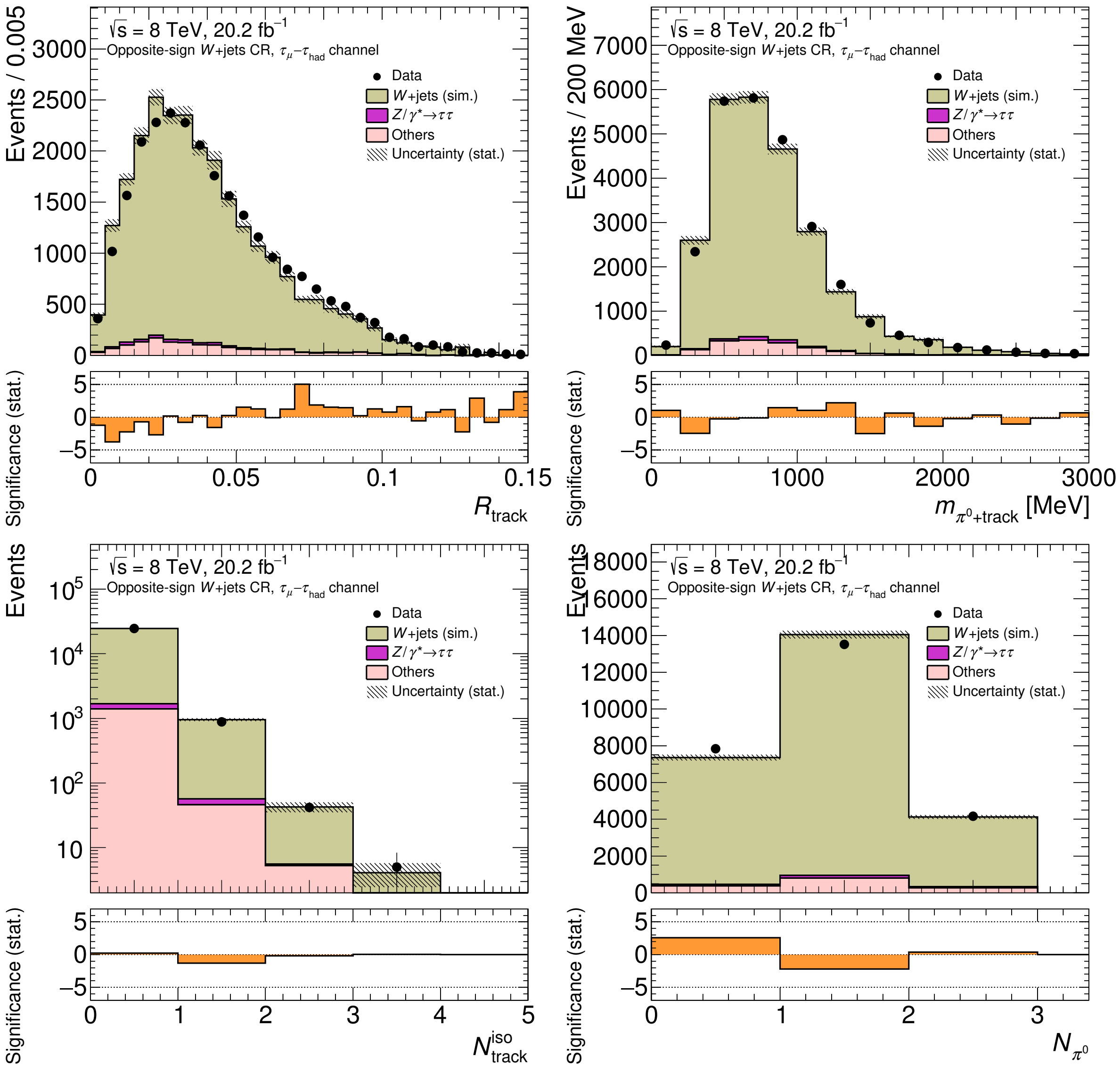

Figure 6.31: Distributions of τ_{had} identification input variables in the W+jets control region for the τ_{μ}–τ_{had} channel. The shape of the distributions in W+jets events is estimated from the simulation.

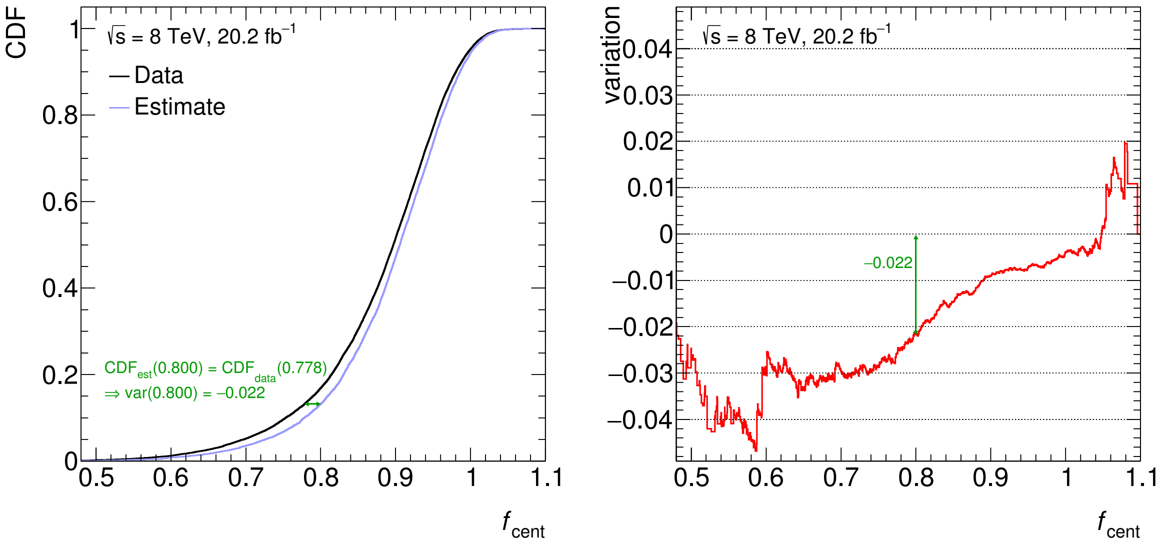

Figure 6.32: Estimation of the uncertainty in the modelling of the input variable f_{cent} for the τ_μ–τ_{had} channel. The left plot shows the cumulative distribution function in data and the one estimated using simulation for the W+jets control region. The right plot shows the variation that is applied to the f_{cent} values for signal events in order to determine the uncertainty. The variation is a function of f_{cent}, and its estimation via Eq. (6.7) is demonstrated for $f_{\mathrm{cent}} = 0.800$ in green.

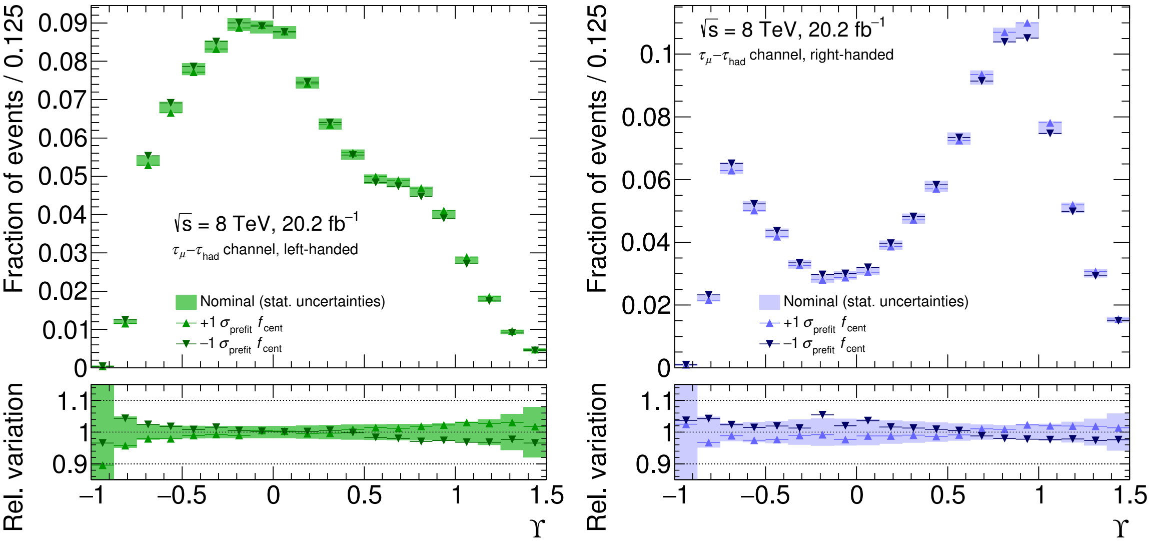

Figure 6.33: Impact of the uncertainties in f_{cent} on the signal in the signal region for the τ_μ–τ_{had} channel. The impact on the shape of the ϒ distribution for events inside the mass-selected region with left-handed (left) and right-handed (right) taus is shown. The uncertainties from the W+jets control region are used. Adapted from Ref. [25].

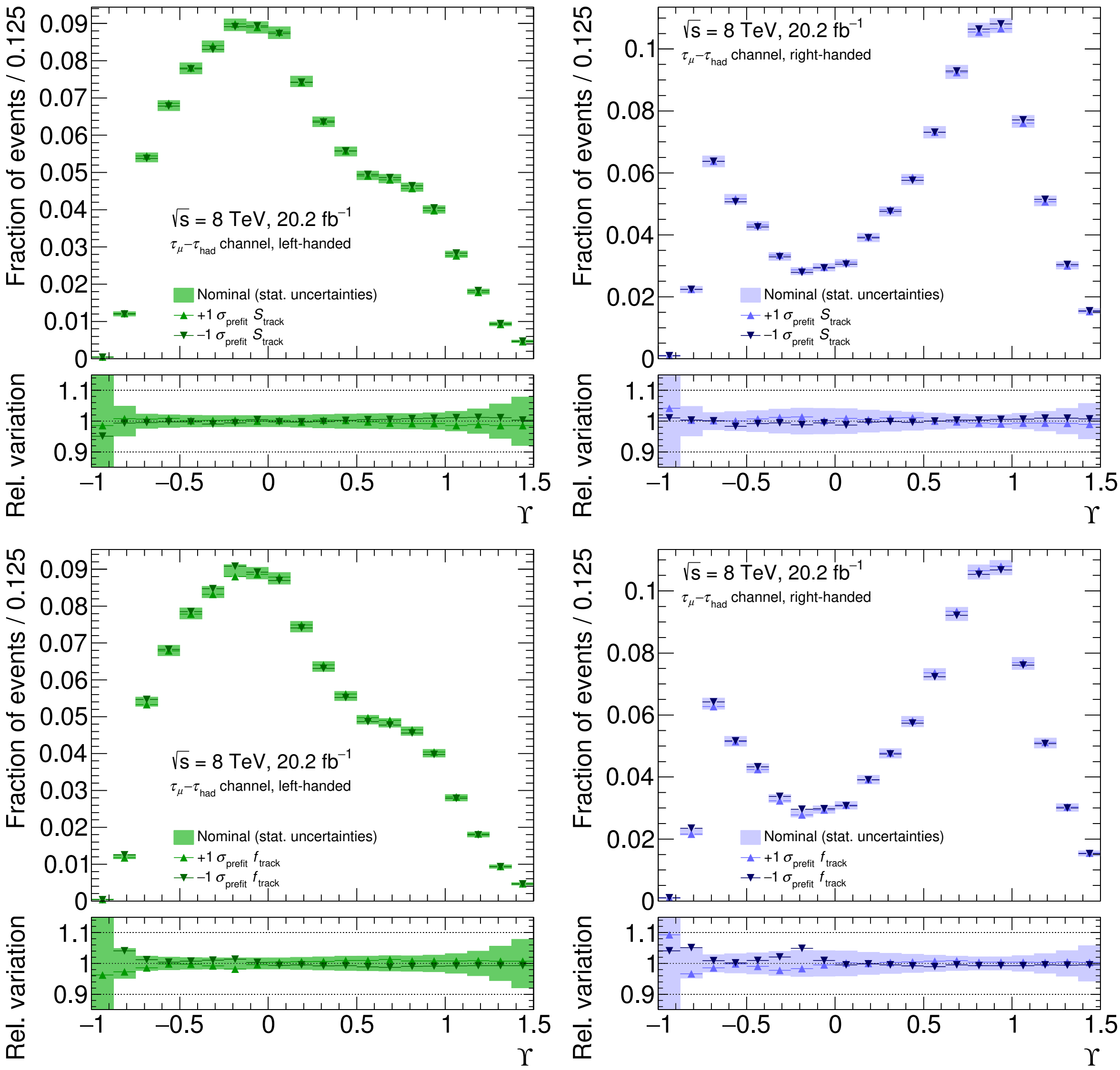

Figure 6.34: Impact of the uncertainties in $S_{\rm track}$ (top) and $f_{\rm track}$ (bottom) on the signal in the signal region for the τ_μ–$\tau_{\rm had}$ channel. The impact on the shape of the ϒ distribution for events inside the mass-selected region with left-handed (left) and right-handed (right) taus is shown. The uncertainties from the W+jets control region are used.

Uncertainties obtained from W+jets control region

Signal contribution	channel	f_{cent}	S_{track}	f_{track}	$p_{\text{T}}^{\pi^0\text{+track}}/p_{\text{T}}$	R_{track}	$m_{\pi^0\text{+track}}$	$N_{\text{track}}^{\text{iso}}$	N_{π^0}	combined
Left-handed	τ_e–τ_{had}	3.9	1.4	0.6	0.0	0.3	0.1	0.2	0.5	4.2
Left-handed	τ_μ–τ_{had}	3.6	1.4	0.7	0.0	0.2	0.3	0.3	0.4	4.0
Right-handed	τ_e–τ_{had}	2.8	1.1	0.1	0.0	0.3	0.1	0.2	0.3	3.0
Right-handed	τ_μ–τ_{had}	2.8	1.1	0.5	0.0	0.3	0.2	0.3	0.2	3.1
Not mass-selected	τ_e–τ_{had}	2.1	1.0	0.7	0.1	0.4	0.0	0.1	0.2	2.5
Not mass-selected	τ_μ–τ_{had}	2.3	1.0	0.1	0.0	0.1	0.2	0.4	0.2	2.6

Uncertainties obtained from top pair validation region

Signal contribution	channel	f_{cent}	S_{track}	f_{track}	$p_{\text{T}}^{\pi^0\text{+track}}/p_{\text{T}}$	R_{track}	$m_{\pi^0\text{+track}}$	$N_{\text{track}}^{\text{iso}}$	N_{π^0}	combined
Left-handed	τ_e–τ_{had}	0.3	0.6	0.8	0.7	0.1	0.4	0.1	0.1	1.3
Left-handed	τ_μ–τ_{had}	0.7	0.5	0.4	0.7	0.2	0.2	0.2	0.2	1.2
Right-handed	τ_e–τ_{had}	0.3	0.3	0.8	0.5	0.0	0.3	0.1	0.1	1.1
Right-handed	τ_μ–τ_{had}	0.5	0.4	0.6	0.5	0.2	0.1	0.1	0.1	1.0
Not mass-selected	τ_e–τ_{had}	0.2	0.2	0.8	0.4	0.0	0.5	0.1	0.1	1.1
Not mass-selected	τ_μ–τ_{had}	0.3	0.1	0.4	0.3	0.1	0.1	0.3	0.2	0.7

Table 6.13: Relative signal normalisation variations resulting from a variation of the τ_{had} identification input variables within their uncertainties. The variations in the input variables that are obtained from the opposite-sign W+jets control region (top) and top pair validation region (bottom) are used. The normalisation change is shown separately for the signal contributions inside the mass-selected region with left-handed and right-handed taus and for the contribution outside the mass-selected region. The combined effect of the uncertainties in all variables is estimated by summing the individual contributions in quadrature. All values are given in %.

The uncertainties in the τ_{had} identification input variables are only considered as uncertainties in the shapes of the Υ distribution. Instead of the values in Table 6.13, the recommended τ_{had} identification efficiency uncertainties are considered to evaluate the normalisation uncertainties. This has the advantage that the recommended τ_{had} identification efficiency correction factors, which are also estimated in Ref. [82], can be utilised even though their correlations with the uncertainties in the input variables are unknown. The systematic and statistical components of the recommended uncertainty are considered separately. They have the same effect on events with left- and right-handed taus and are fully correlated between them. Thus the normalisation uncertainties have no effect on the polarisation measurement. For testing purposes, the uncertainties from Table 6.13 can be considered instead. The normalisation and shape uncertainties in each input variable are treated as fully correlated. The τ_{had} identification component of the tau polarisation uncertainty is 5% larger than nominal when using this treatment. The change in the total tau polarisation uncertainty is negligible.

To cross check the newly developed method, the estimated uncertainties in the shape of the signal Υ templates are compared with those obtained using a simpler method. The τ_{had} identification requirement is varied such that its efficiency is altered by the total identification efficiency uncertainty of 2.9%. The differences between the resulting and nominal template shapes are considered as systematic uncertainties. The impact on the polarisation uncertainty is 13% smaller than for the nominal τ_{had} identification uncertainties. In particular, the nominal shape uncertainties cover the shape uncertainties that correspond to a variation of the τ_{had} identification efficiency by its uncertainty.

A similar method is used to obtain a rough estimate of the uncertainties in the simulated Υ distributions in $Z/\gamma^* \to \ell\ell$ and top pair background events. The uncertainties are found negligible as expected for these small backgrounds. The uncertainties in the modelling of the electron veto in simulated signal and $Z/\gamma^* \to \ell\ell$ and top pair background events are also estimated like this and are found to be negligible. The fraction of selected signal events with a misidentified τ_{had} candidate is around 5 permille. Quark- or gluon-initiated jets are modelled adequately in the $Z/\gamma^* \to \ell\ell$ and W+jets samples, which were created with the same event generators as the signal sample. Hence, no dedicated uncertainties are assigned to this contribution.

Tau Energy Uncertainties

The $E_{\text{T}}^{\tau_{\text{had-vis}}}$ value measured in the calorimeter is directly used to calculate the Υ observable. The other used quantity, $p_{\text{T}}^{\text{track}}$, is measured much more accurately in the range of $\lesssim 50\,\text{GeV}$, which is of interest for this analysis. Hence, the dominant uncertainties in the Υ determination lie in the energy response to τ_{had} candidates.

The $\tau_{\text{had-vis}}$ energy scale (TES) and its uncertainties were determined in Ref. [82]. The most precise results with an uncertainty of about 2% were obtained with an in-situ method from the m_{vis} spectrum in $Z/\gamma^* \to \tau\tau$ decays in the τ_μ–τ_{had} channel. Because the m_{vis} spectra are different for events with left- and right-handed taus, however, that measurement relies on the assumption that the tau polarisation is as predicted by the SM. Therefore, the TES calibration and uncertainties determined with the so-called deconvolution method [82] are used here. The taus were decomposed into their decay products. The uncertainties in the energy response to the individual visible decay products were propagated to the reconstructed τ_{had} decays using pseudo experiments. Gaussian distributions were fit to the distribution of shifts of the TES in the pseudo experiments to determine the TES uncertainties. They are 2–3% for single-prong τ_{had} decays.

The charged decay products in real τ_{had} decays, $\pi^\pm$ or $K^\pm$ mesons, leave hadronic showers in the calorimeter system. The neutral, visible decay products are mostly neutral pions. They immediately decay into photon pairs, which leave electromagnetic showers in the Ecal. Because different processes are involved, the uncertainties in the modelling of electromagnetic and hadronic showers are not strongly correlated. Inaccuracies in the modelling of the two types of showers can affect the Υ distributions differently and may be distinguishable. Real τ_{had} decays in which a large fraction of the $\tau_{\text{had-vis}}$ momentum is carried by $\pi^\pm$ or $K^\pm$, such as $\tau \to h^\pm \nu$ decays, have large Υ values. A mismodelling of hadronic showers would predominantly affect this part of the signal Υ distributions. A mismodelling of electromagnetic showers would instead mainly affect τ_{had} decays with low Υ values.

To account for this difference, the TES uncertainty estimated with the deconvolution method, σ_{TES}, is split into two components. The splitting is based on the stable-particle level fraction of the visible E_{T} carried by neutral pions, f_{EM}, and performed individually for each τ_{had} decay:

$$
\begin{aligned}
\sigma_{\text{TES,EM}} &= \frac{f_{\text{EM}} \cdot \sigma_{\text{TES}}}{\sqrt{f_{\text{EM}}^2 + (1 - f_{\text{EM}})^2}} \\
\sigma_{\text{TES,HAD}} &= \frac{(1 - f_{\text{EM}}) \cdot \sigma_{\text{TES}}}{\sqrt{f_{\text{EM}}^2 + (1 - f_{\text{EM}})^2}} \,.
\end{aligned}
$$

The denominator ensures that the combined electromagnetic and hadronic uncertainty components equal the original TES uncertainty. The two components are treated as uncorrelated. Their effect on the signal templates in the τ_μ–τ_{had} channel for events inside the mass-selected region can be seen in Figure 6.35. The effect is similar in the τ_e–τ_{had} channel and in the measurement in the fiducial region. The TES uncertainties in events outside the mass-selected region are small.

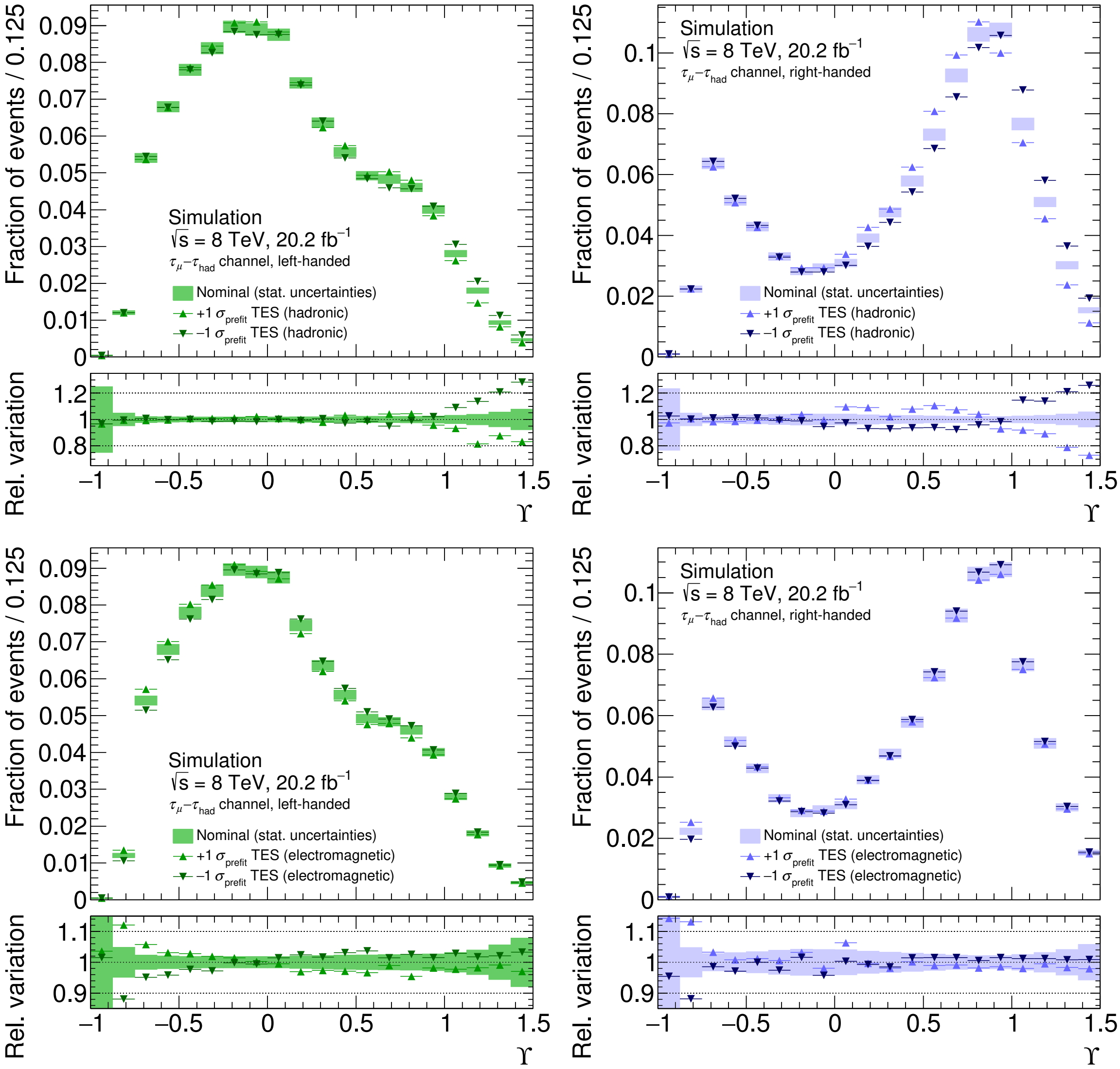

Figure 6.35: Impact of the hadronic (top) and electromagnetic (bottom) components of the TES uncertainty on the signal in the signal region for the τ_μ–τ_{had} channel. The impact on the shape of the Υ distributions for events inside the mass-selected region with left-handed (left) and right-handed (right) taus is shown. Adapted from Ref. [25].

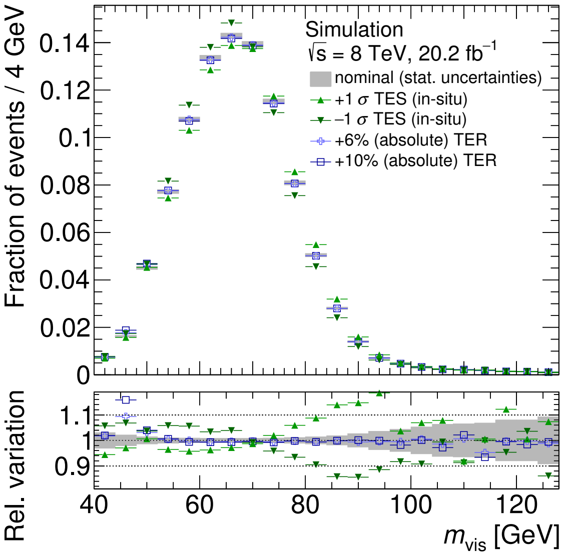

Figure 6.36: The m_{vis} distribution in $Z/\gamma^* \to \tau\tau$ events in the τ_e–τ_{had} and τ_μ–τ_{had} channels. The signal region selection is applied except that the m_{vis} requirement is dropped. Events with left- and right-handed taus and inside and outside the mass-selected region are accepted. The effect of varying the TES by the uncertainties determined using the in-situ method [82], i.e. using the m_{vis} distribution, is indicated. The effect of an increased TER is also shown. Both for the TES and TER the hadronic and electromagnetic components are varied simultaneously.

The Υ distribution is also sensitive to the τ_{had} energy resolution (TER). At stable-particle level the maximum value is $\Upsilon = 1$ and reached by $\tau \to h^\pm \nu$ decays. Reconstructed values above one can occur if $E_{\text{T}}^{\tau_{\text{had-vis}}}$ is exclusively or mostly carried by a $\pi^\pm$ or $K^\pm$ meson and underestimated. This part of the Υ distribution is therefore sensitive to the hadronic component of the TER. The part of the distribution with low Υ values is sensitive to the electromagnetic component. The Υ observable exclusively utilises visible particles, so its reconstruction is unaffected by the $E_{\text{T}}^{\text{miss}}$ resolution. It also utilises the products of only one τ_{had} decay, so kinematic constraints are not weakened by the presence of undetected neutrinos. These two properties make the Υ observable more sensitive to the TER than other observables used in ATLAS analyses so far. The shape of the m_{vis} distribution, for example, is significantly affected by the presence of unaccounted for neutrinos. It therefore only has a small sensitivity to alterations of the TER (see Figure 6.36). Consequently, this is the first ATLAS analysis in which TER uncertainties are noticeable and considered.[3]

The quality of the TER modelling and the related uncertainties are determined in the same template fits in which the tau polarisation is measured. For this, alternative signal templates with varied TER are needed. The templates with an increased, i.e. degraded, TER are obtained by varying $E_{\text{T}}^{\tau_{\text{had-vis}}}$ by

$$\Delta_{\text{TER,EM}} = s \cdot f_{\text{EM}} \cdot E_{\text{T}}^{\tau_{\text{had-vis}}} \qquad \text{or}$$
$$\Delta_{\text{TER,HAD}} = s \cdot (1 - f_{\text{EM}}) \cdot E_{\text{T}}^{\tau_{\text{had-vis}}} ,$$

where s is a pseudo-random number that is determined separately for the electromagnetic and hadronic components and for each event. The s values are drawn from Gaussian distributions. Nominally, a mean of $m_s = 0$ and a width of $\sigma_s = 0.025$ are used both for the electromagnetic and hadronic components of

---

[3] In the tau polarisation measurement in $W \to \tau\nu$ events [24] the TER uncertainties are covered by the statistical uncertainties.

the TER, which means that the TER is implicitly assumed to agree with the simulation within 2.5%. If larger σ_s values are chosen weaker assumptions about the TER modelling are made but the template fits become less stable. The nominal σ_s values are chosen such that the TER parameters are constrained to half their initial uncertainty in the fit that extracts the tau polarisation (see Section 6.6). This way the post-fit TER uncertainties are determined from the data to a large extend and the validity of the assumptions on the TER modelling can be judged from the pulls of the TER parameter. Alternative assumptions are tested where necessary, as discussed in Section 6.7.

The effect of a reduced TER is estimated by a reverse variation in each bin b of a signal template F:

$$F_{\mathrm{b}}^{-1\sigma\ \mathrm{TER}} = F_{\mathrm{b}}^{\mathrm{nominal}} - \left(F_{\mathrm{b}}^{+1\sigma\ \mathrm{TER}} - F_{\mathrm{b}}^{\mathrm{nominal}}\right) = 2 \cdot F_{\mathrm{b}}^{\mathrm{nominal}} - F_{\mathrm{b}}^{+1\sigma\ \mathrm{TER}}. \tag{6.8}$$

The template variations of the signal in the mass-selected region are shown in Figure 6.37.

The uncertainties in the energy response to τ_{had} decays are dominated by the uncertainty in the hadronic component of the TES, which is among the largest single uncertainties in the analysis. The uncertainty in the hadronic component of the TER is among the larger single uncertainties but it contributes little to the overall tau polarisation uncertainty. The uncertainties in the electromagnetic components of the TES and TER are smaller than those in the hadronic components.

The TES uncertainties in the backgrounds are also estimated using the results from the deconvolution method. It is implicitly assumed that the magnitude of the uncertainties is the same for misidentified and real τ_{had} candidates. The splitting into electromagnetic and hadronic components is omitted. The TES uncertainties in the shapes of the $Z/\gamma^* \to \ell\ell$ ($\ell \to \tau_{\mathrm{had}}$), $Z/\gamma^* \to \ell\ell$ (jet $\to \tau_{\mathrm{had}}$), top pair, and W+jets templates in the τ_e–τ_{had} channel are shown in Figure 6.38. The background TES uncertainties are considered uncorrelated from those in the signal. The uncertainties in the $Z/\gamma^* \to ee$ ($e \to \tau_{\mathrm{had}}$) background are considered uncorrelated from those in the remaining backgrounds, in which the tau candidates originate from quark- or gluon-initiated jets or are real. The background TES uncertainties have only a small effect on the measurement. The TER uncertainties would be even smaller and are neglected.

Other Experimental Uncertainties

The remaining experimental uncertainties have only a minor effect on the final result. The following list is taken from Ref. [25]:

- Trigger, reconstruction and identification of electrons and muons: The efficiencies for triggering, reconstructing, and identifying electrons and muons are measured in data using tag-and-probe techniques. Electron energy and muon momentum corrections and their uncertainties are evaluated by comparing the response in data and in the simulation [73, 81]. The simulated event samples are corrected for the differences.

- Electron misidentification as τ_{had}: Tag-and-probe studies of $Z/\gamma^* \to ee$ events are used to derive the correction factors on the rate of electrons to be misidentified as τ_{had} decays, as well as their uncertainties [82].

- Uncertainties that affect the $E_{\mathrm{T}}^{\mathrm{miss}}$ estimation: In this analysis, uncertainties in the jet energy scale (JES) and resolution (JER) are only relevant due to their effect on the $E_{\mathrm{T}}^{\mathrm{miss}}$ reconstruction. Various sources of JES and JER uncertainty are considered [80]. Along with the TES, TER, electron energy, and muon momentum uncertainties, they are propagated to the $E_{\mathrm{T}}^{\mathrm{miss}}$ calculation. Additional uncertainties in the $E_{\mathrm{T}}^{\mathrm{miss}}$ scale and resolution due to energy clusters in the calorimeter that do not belong to any reconstructed object are considered as well [85].

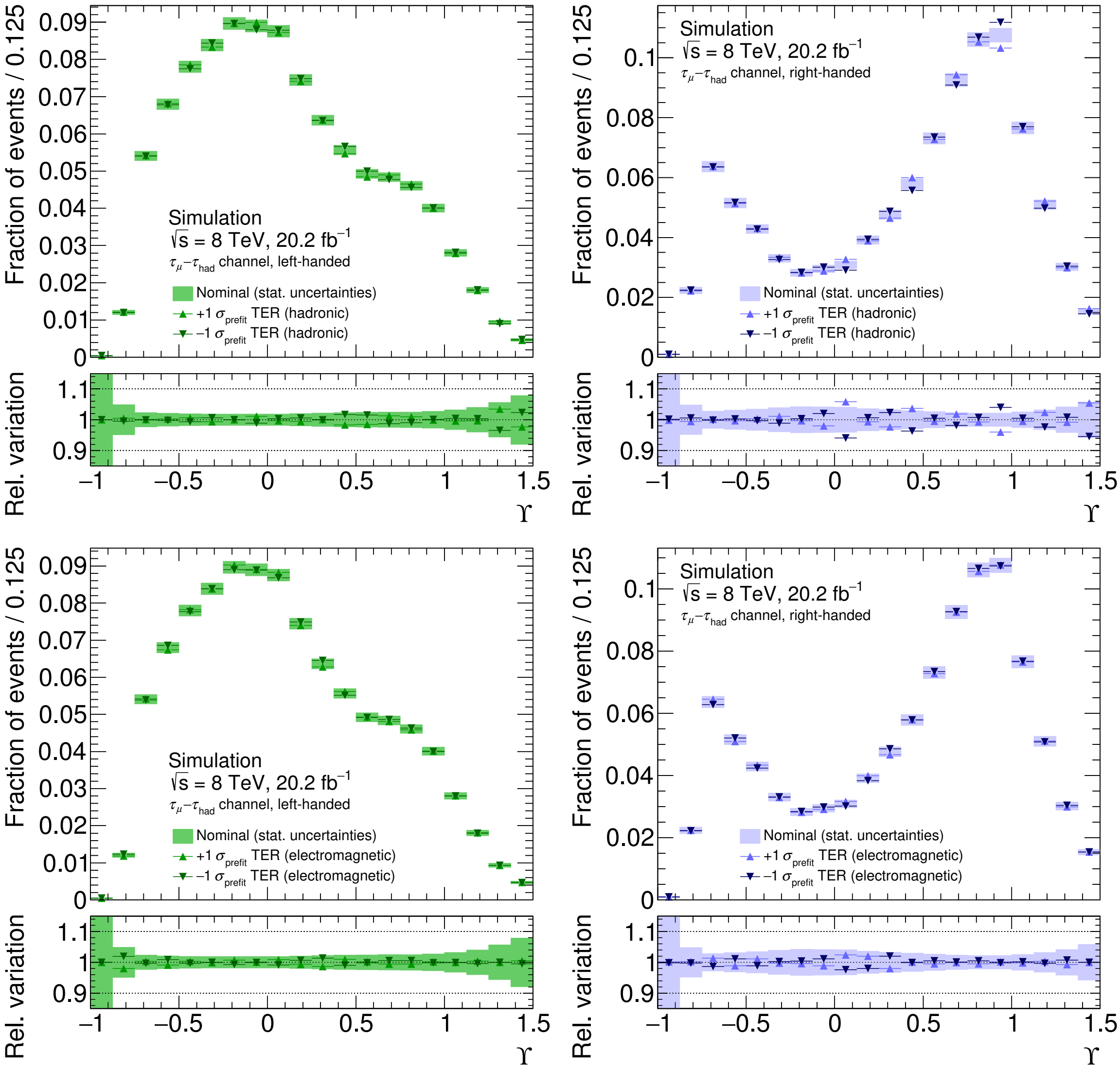

Figure 6.37: Impact of the hadronic (top) and electromagnetic (bottom) components of the TER uncertainty on the signal in the signal region for the τ_μ–τ_{had} channel. The impact on the shape of the Υ distributions for events inside the mass-selected region with left-handed (left) and right-handed (right) taus is shown. Adapted from Ref. [25].

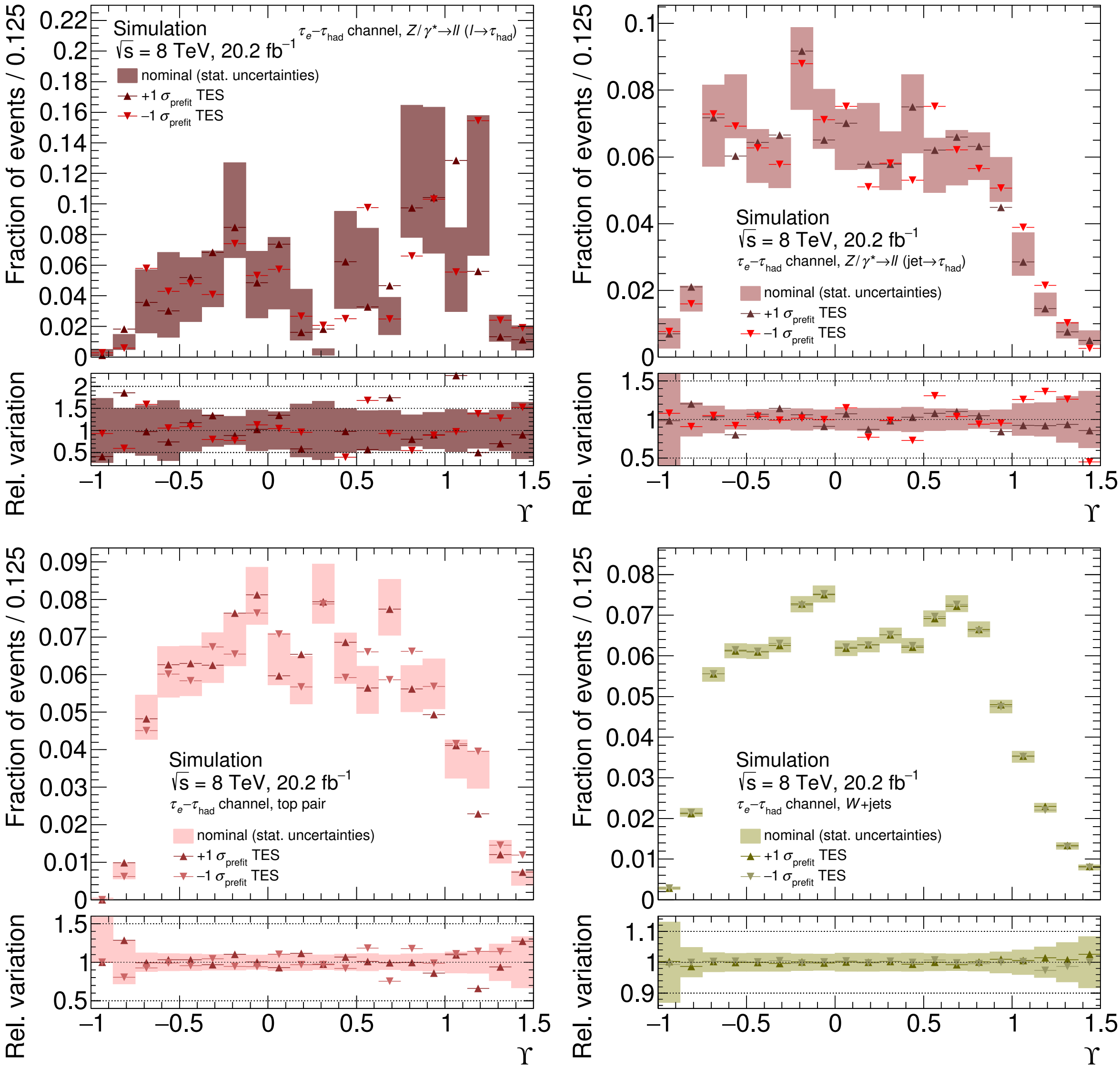

Figure 6.38: TES uncertainties in the shapes of the $Z/\gamma^{*} \rightarrow \ell\ell$ ($\ell \rightarrow \tau_{\text{had}}$) (top left), $Z/\gamma^{*} \rightarrow \ell\ell$ (jet $\rightarrow \tau_{\text{had}}$) (top right), top pair (bottom left), and W+jets (bottom right) background templates for the τ_e–τ_{had} channel.

- Luminosity: The absolute luminosity scale is derived from beam-separation scans performed in November 2012. The uncertainty in the integrated luminosity is 1.9% [178].

The uncertainties described above are propagated through the analysis.

For the tau tracks in this analysis, uncertainties in the $p_{\mathrm{T}}^{\mathrm{track}}$ reconstruction are dominated by the ID alignment. Specifically, the largest uncertainties originate from so-called weak modes, to which the χ^2 function that is used to evaluate the alignment is insensitive. The uncertainties resulting from potential biases are documented in Ref. [71]. They scale approximately linearly with the momentum and are below 1% for tracks with $p_{\mathrm{T}}^{\mathrm{track}} = 50\,\mathrm{GeV}$ in almost the entire ID. In particular, they are smaller than the TES uncertainties and can be neglected. Uncertainties in the track reconstruction efficiency are included in the tau identification uncertainties.

6.5.2 Theory Uncertainties

Uncertainties in Modelling of Signal Process

The uncertainties in the modelling of the signal process are estimated by comparing the nominal and auxiliary signal samples (see Section 6.1). Due to the limited size of the auxiliary samples direct comparisons in the signal region would be affected by statistical fluctuations to a large extend. Instead, kinematic distributions are compared at stable-particle level in $Z/\gamma^* \to \tau\tau$ decays with one τ_{lep} decay and one τ_{had} decay without further event selection. Differences are propagated to the signal in the signal region with reweighting techniques and considered as systematic uncertainties.

Prior to the comparison, the auxiliary samples are reweighted such that the tau polarisation matches that in the nominal sample. Specifically, the tau polarisation in the mass-selected region is equalised when the uncertainties in the measurement of the polarisation in the mass-selected region are evaluated. The analogous is done for the measurement in the fiducial region. The reasoning is as follows: the template fits determine the tau polarisation from the relative normalisation of the left- and right-handed signal contributions taking the pre-fit relative normalisation as a reference (see Section 6.6). Equalising the tau polarisation in the signal samples ensures that the reference is the same in the nominal and varied signal templates. The relevant uncertainties are retained including those in the relative acceptance of events with left- and right-handed taus.

Uncertainties in the modelling of the hard $qq \to Z \to \tau\tau$ process and of the tau decays are evaluated from the differences between the nominal and the Pythia8 and Powheg+Pythia8 signal samples. The nominal and Pythia8 samples were generated using the CTEQ6L1 PDF set [126]. The Powheg+Pythia8 sample, which was generated with the CT10 PDF set [135], is reweighted to the CTEQ6L1 PDF set using the LHAPDF package [158] to avoid double-counting of uncertainties.

The differences between the p_{T}^{Z} and η^{Z} distributions in the nominal and auxiliary signal samples are shown in Figure 6.39. After a two-dimensional reweighting of these distributions the $p_{\mathrm{T}}^{\tau_{\mathrm{had}}}$ and $\eta^{\tau_{\mathrm{had}}}$ distributions are still different. This may be due to differences between the predicted m_{Z/γ^*} distributions. The development of a higher-dimensional reweighting is beyond the scope of this analysis. Instead the uncertainties in the kinematic distributions of Z bosons and taus are estimated separately.

For this, one of the following distributions in the nominal signal samples at a time is reweighted to match the respective distribution in the Pythia8 or Powheg+Pythia8 signal sample:

- p_{T}^{Z},
- η^{Z},
- $p_{\mathrm{T}}^{\tau_{\mathrm{lep}}}$ vs. $p_{\mathrm{T}}^{\tau_{\mathrm{had}}}$,

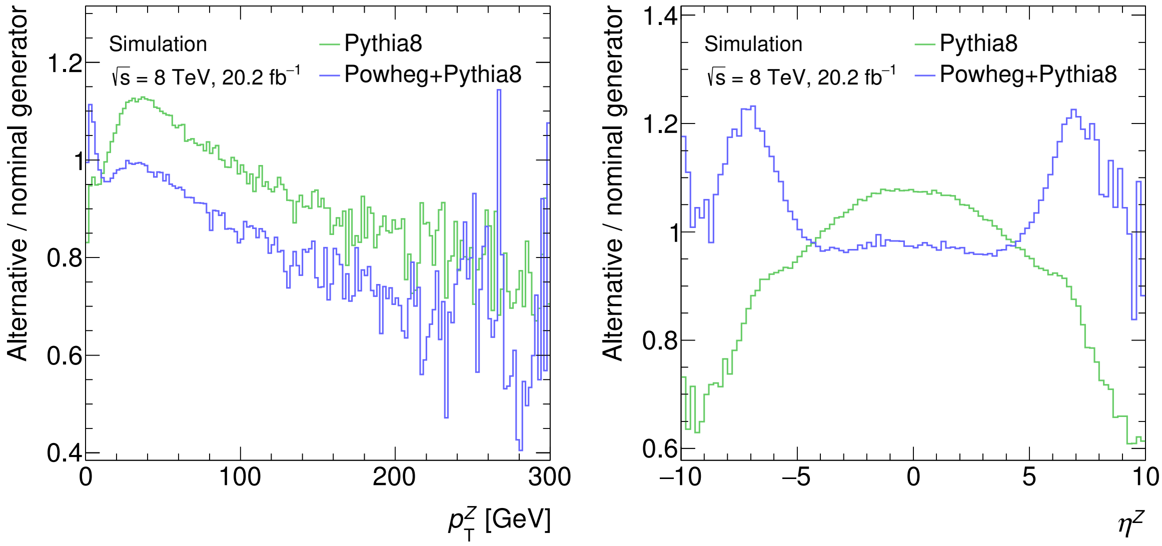

Figure 6.39: Differences between the p_{T}^{Z} (left) and η^{Z} (right) spectra in the nominal and alternative signal samples. The ratios of the distributions, which are used in the reweighting, are shown.

- $\eta^{\tau_{\mathrm{lep}}}$ vs. $\eta^{\tau_{\mathrm{had}}}$.

For the last two items, p_{T} and η are the full tau transverse momentum and pseudorapidity, not the visible ones. The tau distributions are reweighted separately in events with left- and right-handed taus.

The differences between these distributions in the nominal and PYTHIA8 samples are shown in Figure 6.40. The effect of each reweighting is propagated to the signal templates and through the analysis. Of the reweightings to the PYTHIA8 and POWHEG+PYTHIA8 samples for each distribution, the one that gives the larger tau polarisation uncertainty is chosen. The kinematic distributions of the Z boson and the taus are correlated. To avoid double-counting of uncertainties, only the larger of the uncertainties in the p_{T}^{Z} and $p_{\mathrm{T}}^{\tau_{\mathrm{lep}}}$ vs. $p_{\mathrm{T}}^{\tau_{\mathrm{had}}}$ modelling and the larger of the uncertainties in the η^{Z} and $\eta^{\tau_{\mathrm{lep}}}$ vs. $\eta^{\tau_{\mathrm{had}}}$ modelling are considered. They are denoted as generator p_{T} and generator η uncertainties, respectively. The considered uncertainties in the p_{T}^{Z} modelling cover those in the p_{T}^{Z} reweighting described in Section 6.1.

Following this methodology, the p_{T}^{Z} uncertainties estimated from the POWHEG+PYTHIA8 sample and the $\eta^{\tau_{\mathrm{lep}}}$ vs. $\eta^{\tau_{\mathrm{had}}}$ uncertainties estimated from the PYTHIA8 sample are considered as generator p_{T} and generator η uncertainties in the measurement of the tau polarisation in the mass-selected region. Both have a minor effect on the shapes of the signal templates. However, the normalisation variations caused by the generator η uncertainty differ by three percent points between events with left- and right-handed taus, which makes it one of the largest single uncertainties in the polarisation within the mass-selected region. The generator p_{T} uncertainty is much smaller.

For the measurement in the fiducial region, the p_{T}^{Z} and $\eta^{\tau_{\mathrm{lep}}}$ vs. $\eta^{\tau_{\mathrm{had}}}$ uncertainties estimated from the POWHEG+PYTHIA8 sample are considered as generator p_{T} and generator η uncertainties, respectively. They are small because no extrapolation to outside the η and p_{T} acceptance is performed.

Further differences are observed between the generated Υ distributions in $\tau \to h^{\pm}\pi^{0}\nu$ and $\tau \to h^{\pm}\pi^{0}\pi^{0}\nu$ decays (see Figure 6.41). The related uncertainties are called generator Υ ($\tau \to h^{\pm}\pi^{0}\nu$) and generator Υ ($\tau \to h^{\pm}\pi^{0}\pi^{0}\nu$) uncertainties and estimated in analogy to those in the tau momenta. The uncertainties estimated using the POWHEG+PYTHIA8 sample are considered for both of these tau decay

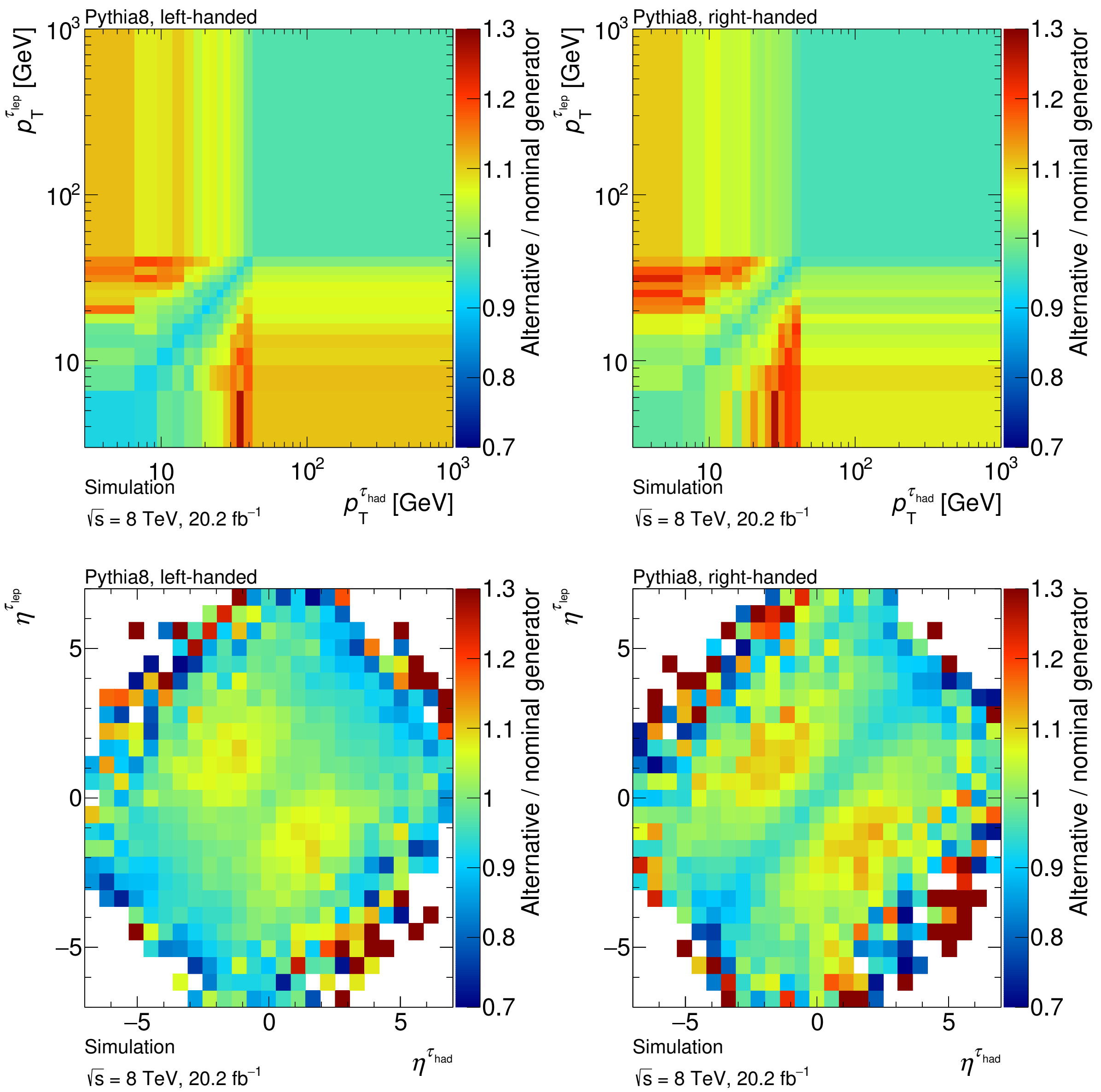

Figure 6.40: Differences between the $p_T^{\tau_{lep}}$ vs. $p_T^{\tau_{had}}$ spectra (top) and between the $\eta^{\tau_{lep}}$ vs. $\eta^{\tau_{had}}$ spectra (bottom) in events with left-handed (left) and right-handed (right) taus in the nominal and Pythia8 signal samples. The ratios of the distributions, which are used in the reweighting, are shown.

topologies and in both polarisation measurements. The variations of the left- and right-handed signal templates inside the mass-selected region are shown in Figures 6.42 and 6.43. The variations in the corresponding templates for the measurement in the fiducial region can be found in Figure D.9. The uncertainties in the templates for events outside the mass-selected or fiducial region are negligible.

The generator Υ ($\tau \to h^\pm\pi^0\nu$) uncertainty is the largest (second largest) single uncertainty in the measurement of the tau polarisation in the mass-selected (fiducial) region. In studies of simulated $Z/\gamma^* \to \tau\tau$ samples for ATLAS analyses in Run 2 of the LHC, much smaller differences between the Υ distributions predicted by Tauola and Pythia8 were found. Hence, this uncertainty may be reduced in future analyses. The Run 2 samples were generated using version 8.212 instead of version 8.160 of the Pythia generator.

The uncertainties in the parton shower modelling are estimated in analogy to those in the modelling of the hard process. The nominal and Alpgen+Jimmy signal samples are compared to each other.

Uncertainties in Splitting of Signal Sample

The uncertainties in the splitting of the signal sample into subsamples with left- and right-handed taus originate from the uncertainties in the tau polarisation determined by the TauSpinner [146] algorithm (P_τ^{TS}). These uncertainties are estimated, propagated to the signal templates, and through the analysis.

The uncertainties in P_τ^{TS} that are related to the input parameters of the TauSpinner algorithm are estimated using the same methods as in Ref. [149]. Samples of $pp \to \tau\tau + 2$ jets events were created with the MadGraph [179] event generator interfaced with the Pythia8 [118] parton shower, UE, and tau decay modelling. The effect of varying the input was evaluated in three different mass-selected regions: 66–116 GeV, 81–101 GeV, and 88–92 GeV. The findings in the 66–116 GeV region, which coincides with that used in this analysis, are utilised. The absolute uncertainties in the QCD factorisation and renormalisation scales, the α_{s} coupling, and the PDF are 0.004, 0.0011, and 0.0022, respectively. The splitting may also be affected by the inconsistency between the weak mixing angles set in the Alpgen event generator ($\sin^2\theta_{\mathrm{W}}^{\mathrm{eff}} = 0.2224$) and the Tauola and TauSpinner algorithms (0.23147). The P_τ^{TS} value differs by 0.006 from the tau polarisation obtained in the fit to the x_{vis} distribution in $\tau \to \pi^\pm\nu$ decays (see Figure 6.8). This difference is considered as an uncertainty. The total uncertainty in P_τ^{TS} is 0.007.

Differences between the real tau polarisation in the signal sample and P_τ^{TS} would be accompanied by a net migration between the left- and right-handed subsamples. The uncertainties in the relative net migration from the left-handed subsample to the right-handed subsample, σ_{LR}, and those in the relative net migration in the opposite direction, σ_{RL}, are assumed to be uncorrelated. Values of $\sigma_{\mathrm{LR}} = \sigma_{\mathrm{RL}} = 0.007$ are found by requiring that they each cover the total uncertainty in P_τ^{TS} (see Appendix D.3.1).

The uncertainties in P_τ^{TS} are related to the evaluation of information about the Z boson production in the TauSpinner algorithm. Therefore, it is assumed that the net migration is independent of the tau decays and, in particular, of the Υ values. One possible type of net migration from the left-handed to the right-handed subsamples is that events with kinematic configurations that are more common for events with **left-handed** taus are **classified** as **right-handed** too **often**. This type of migration could be mimicked by transferring 0.7% ($=\sigma_{\mathrm{LR}}$) of the events randomly from the left-handed to the right-handed subsample. However, it is more practical to calculate the resulting variations of the left- and right-handed signal templates analytically.

For the fit (see Section 6.6), the left- and right-handed signal templates are normalised to the full $Z/\gamma^* \to \tau\tau$ cross-section within the mass-selected or fiducial region using the P_τ^{TS} value for the respective region. This must be considered when calculating the varied templates. For example, the discussed type of migration has two effects on the normalisation of a left-handed template:

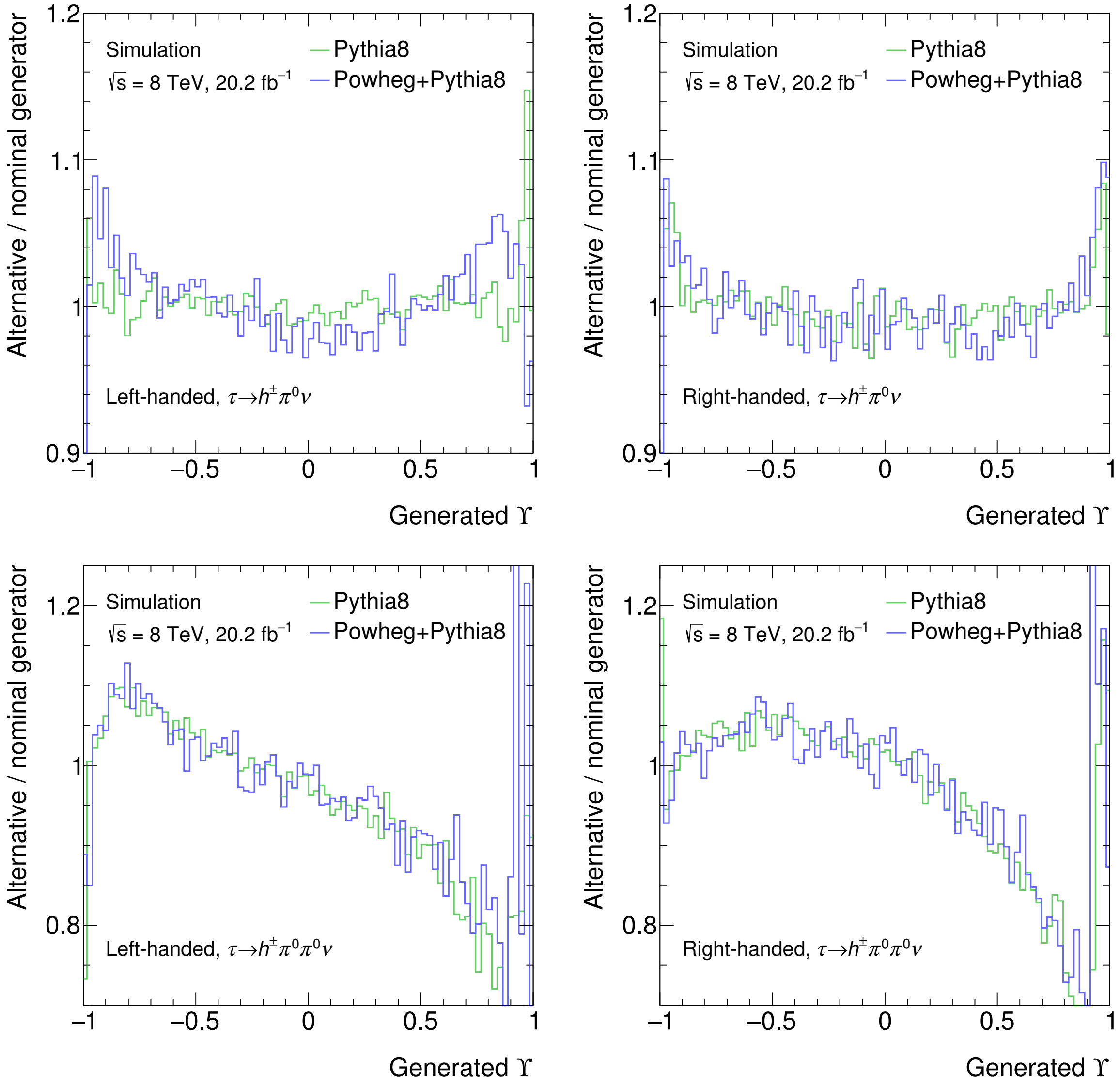

Figure 6.41: Differences between the Υ spectra in $\tau \to h^{\pm}\pi^{0}\nu$ (top) and $\tau \to h^{\pm}\pi^{0}\pi^{0}\nu$ (bottom) decays of left-handed (left) and right-handed (right) taus in the nominal and alternative signal samples. The ratios of the distributions, which are used in the reweighting, are shown.

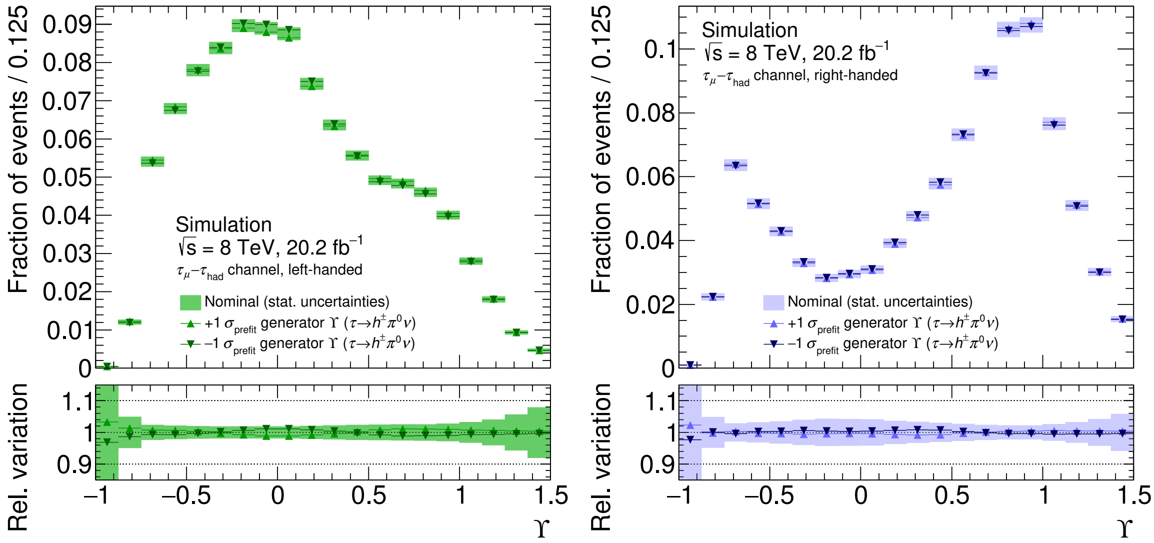

Figure 6.42: Impact of the generator Υ ($\tau \to h^{\pm}\pi^{0}\nu$) uncertainties in the signal region for the τ_{μ}–τ_{had} channel. The impact on the shape of the Υ distributions for signal events inside the mass-selected region with left-handed (left) and right-handed (right) taus is shown. Adapted from Ref. [25].

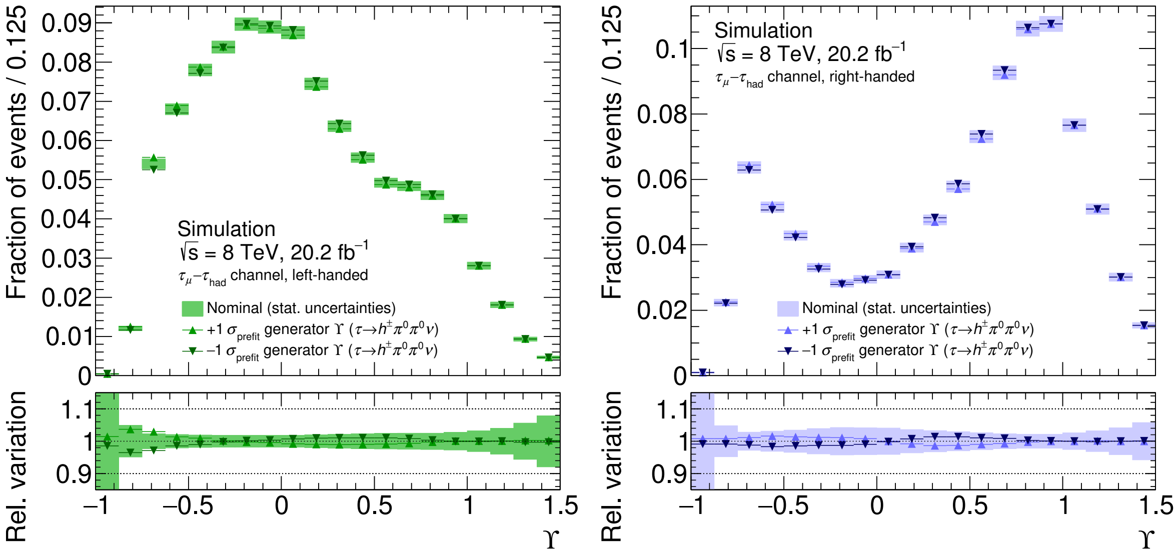

Figure 6.43: Impact of the generator Υ ($\tau \to h^{\pm}\pi^{0}\pi^{0}\nu$) uncertainties in the signal region for the τ_{μ}–τ_{had} channel. The impact on the shape of the Υ distributions for signal events inside the mass-selected region with left-handed (left) and right-handed (right) taus is shown.

- It is reduced by a factor of $(1 - \sigma_{\mathrm{LR}})$, because events are transferred to the respective right-handed template.
- The P_τ^{TS} value is increased. Therefore, the left-handed template is scaled up more when being normalised to the full $Z/\gamma^* \to \tau\tau$ cross-section.

The two effects cancel each other (see Appendix D.3.2). Because the shapes of left-handed templates are also unaltered by this type of migration, they remain fully unchanged. The discussed type of migration has the following effect on a right-handed template (see Appendix D.3.2):

$$F'_{\mathrm{right}} = F^{\mathrm{nominal}}_{\mathrm{right}} + \frac{\sigma_{\mathrm{LR}}\left(1 - f^{\mathrm{rep}}_{\mathrm{R}}\right)}{f^{\mathrm{rep}}_{\mathrm{R}} + \sigma_{\mathrm{LR}}\left(1 - f^{\mathrm{rep}}_{\mathrm{R}}\right)}\left(F^{\mathrm{nominal}}_{\mathrm{left}} - F^{\mathrm{nominal}}_{\mathrm{right}}\right), \tag{6.9}$$

where $F^{\mathrm{nominal}}_{\mathrm{left}}$ and $F^{\mathrm{nominal}}_{\mathrm{right}}$ are the nominal left- and right-handed templates, respectively, and $f^{\mathrm{rep}}_{\mathrm{R}}$ is the fraction of events in the right-handed template prior to the migration. The templates are scaled and summed bin by bin as in Eq. (6.8).

The other possible types of net migration are

- Events with kinematic configurations that are more common for events with **left-handed** taus are **classified** as **right-handed** too **rarely**.
- Events with kinematic configurations that are more common for events with **right-handed** taus are **classified** as **left-handed** too **often**.
- Events with kinematic configurations that are more common for events with **right-handed** taus are **classified** as **left-handed** too **rarely**.

The first of these types of migration leads to the opposite change for right-handed templates with respect to Eq. (6.9), and left-handed templates remain unchanged. The uncertainties that affect right-handed templates are called splitting (LH→RH) uncertainties. The second type of migration in the list leaves right-handed templates unaltered but changes left-handed templates as follows:

$$F''_{\mathrm{left}} = F^{\mathrm{nominal}}_{\mathrm{left}} + \frac{\sigma_{\mathrm{RL}} f^{\mathrm{rep}}_{\mathrm{R}}}{1 + f^{\mathrm{rep}}_{\mathrm{R}}\left(\sigma_{\mathrm{RL}} - 1\right)}\left(F^{\mathrm{nominal}}_{\mathrm{right}} - F^{\mathrm{nominal}}_{\mathrm{left}}\right).$$

The third type in the list leads to the opposite change for left-handed templates. The uncertainties related to these types of migration are called splitting (RH→LH) uncertainties. The varied templates for events in the mass-selected region are shown in Figure 6.44. The signal contribution outside the mass-selected or fiducial region is not split into left-handed and right-handed components, so it is not affected by the splitting uncertainties.

Uncertainties in Parton Distribution Functions

The PDF uncertainties in the signal modelling are evaluated using the LHAPDF package [158]. The signal sample, which was generated using the CTEQ6L1 [126] PDF set, is reweighted to the following alternative leading order PDF sets: NNPDF30_LO_AS_0118 [159], MMHT2014LO68CL [160], and CT14LO [161]. The effect of the reweightings is propagated to the signal templates and through the analysis. Reweighting to the CT14LO PDF set causes the largest variations in the templates (see Figure 6.45) and the largest tau polarisation uncertainty. It is hence used for the measurement. The

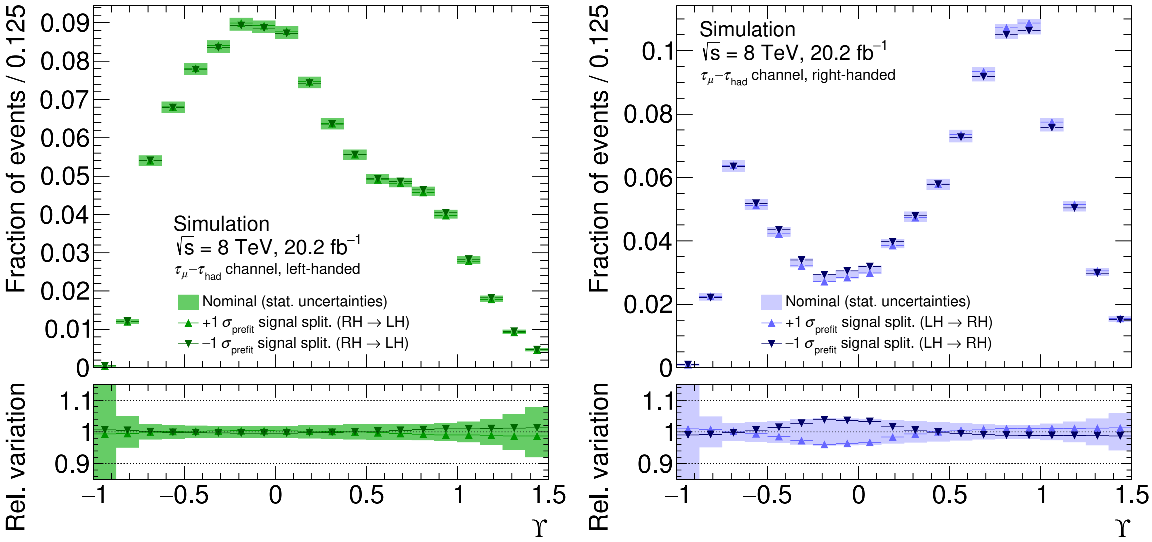

Figure 6.44: Impact of the signal sample splitting uncertainties on the Υ distribution for mass-selected signal events in the signal region for the τ_μ–τ_{had} channel. The (RH→LH) uncertainties affect the template for events with left-handed taus (left) and the (LH→RH) affect the template for events with right-handed taus (right). Adapted from Ref. [25].

effect of the PDF uncertainties on the measurement is small. The effect of the PDF uncertainties in the modelling of the backgrounds are much smaller than those in the signal and are neglected.

6.5.3 Overall Systematic Uncertainties

The various systematic uncertainties in the signal and background templates are evaluated in order to identify the relevant ones to be considered in the statistical interpretation of the analysis. In the following, only events in the Υ range $[-1.0, 1.5]$, in which the template fits are performed, are considered. About 99% of the signal and background events in the signal region are in this Υ range.

The relevant uncertainties in the shapes of the Υ templates are identified using the template fits directly (see Section 6.6), and they are listed in Table 6.14. The relevant normalisation uncertainties are selected as follows. For each template the largest normalisation uncertainties are considered until 95% of its total normalisation uncertainty is accounted for. The total uncertainty is the combination of the statistical and all systematic uncertainties. The remaining normalisation uncertainties are omitted in the following and in the fit except those for which the shape component is considered (see Table 6.14). The omitted uncertainties would be negligible if considered. The uncertainties that are selected for at least one template are listed in Table 6.15.

The signal normalisation uncertainties in the measurement of the tau polarisation in the mass-selected region are listed in Tables 6.16 and 6.17. The uncertainties in the measurement for the fiducial region can be found in Tables D.1 and D.2. The dependence of the signal selection efficiency on m_{Z/γ^*} and the total uncertainties are shown in Figures 6.46 and 6.47. These figures can be used to evaluate whether a model other than the SM is consistent with this measurement. The overall efficiency is in the permille level, as discussed in Section 6.3.4. Because the systematic uncertainties in the acceptance of events with left- and right-handed taus are strongly and positively correlated, the systematic uncertainties in the relative acceptance of the two are small.

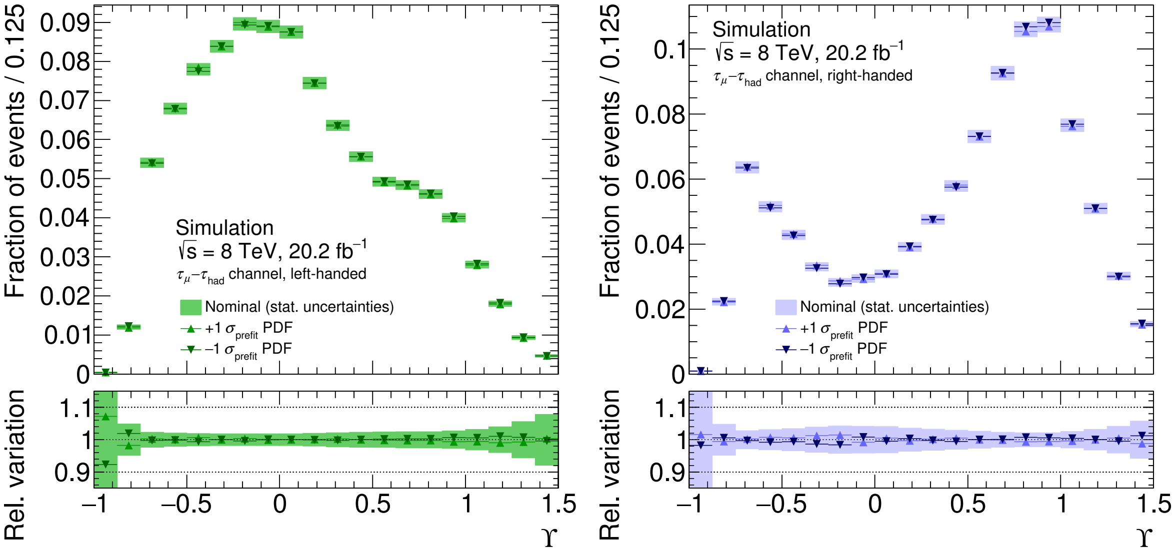

Figure 6.45: Impact of the PDF uncertainties on the signal in the signal region for the τ_μ–τ_{had} channel. The PDF uncertainties are evaluated by reweighting the CTEQ6L1 PDF set to the CT14LO PDF set. The impact on the shape of the Υ distributions for events inside the mass-selected region with left-handed (left) and right-handed (right) taus is shown.

Category	Uncertainty	Description
τ_{had} identification	Tau ID f_{cent} Tau ID S_{track} Tau ID f_{track}	f_{cent} modelling S_{track} modelling f_{track} modelling
TES and TER	TES (hadronic) TES (electromagnetic) TER (hadronic) TER (electromagnetic) TES ($e \to \tau_{\text{had}}$) TES (background)	Hadronic TES component in signal decays Electromagnetic TES component in signal decays Hadronic TER component in signal decays Electromagnetic TER component in signal decays TES modelling in $Z/\gamma^* \to ee$ ($e \to \tau_{\text{had}}$) events TES modelling in other background events
Modelling of signal process	generator Υ ($\tau \to h^\pm\pi^0\nu$) generator Υ ($\tau \to h^\pm\pi^0\pi^0\nu$) generator η	Υ modelling in $\tau \to h^\pm\pi^0\nu$ decays Υ modelling in $\tau \to h^\pm\pi^0\pi^0\nu$ decays $\eta^{\tau_{\text{lep}}}$ vs. $\eta^{\tau_{\text{had}}}$ modelling
Signal sample splitting	Splitting (LH→RH)	Events with kinematic configurations that are more common for events with left-handed taus may be classified as right-handed too often or too rarely
	Splitting (RH→LH)	(Swap left-handed and right-handed above)
PDF	PDF	Parton distribution functions
W+jets shape	W+jets shape (τ_e–τ_{had}) W+jets shape (τ_μ–τ_{had})	Shape correction in τ_e–τ_{had} channel Shape correction in τ_μ–τ_{had} channel

Table 6.14: List of shape uncertainties in the signal and background templates.

Uncertainty	Description
Luminosity	Integrated luminosity
Tau ID (stat)	Identification efficiency for real τ_{had} decays (statistical unc.)
Tau ID (syst)	Identification efficiency for real τ_{had} decays (systematic unc.)
$e \to \tau_{\text{had}}$ ID	$e \to \tau_{\text{had}}$ misidentification probability
Electron ID	Electron identification efficiency
Electron isolation	Electron isolation efficiency
Electron trigger	Electron trigger efficiency
Electron scale (1–4)	Electron energy scale (4 sources)
Electron resolution	Electron energy resolution
Muon isolation	Muon isolation
Muon trigger	Muon trigger efficiency
Muon scale	Muon momentum scale
Muon resolution	Muon momentum resolution
Jet scale (1–12)	Jet energy scale (12 sources)
Jet resolution	Jet energy resolution
JVF	Jet vertex fraction
$E_{\text{T}}^{\text{miss}}$ scale	Scale of $E_{\text{T}}^{\text{miss}}$ part not associated with other objects
$E_{\text{T}}^{\text{miss}}$ resolution	Resolution of $E_{\text{T}}^{\text{miss}}$ part not associated with other objects
Pile-up	Pile-up reweighting
Generator p_{T}	p_{T}^{Z} modelling
Parton shower η, parton shower p_{T}	Parton shower modelling in signal events
W+jets MC norm (τ_e–τ_{had})	MC statistical uncertainties in W+jets normalisation for τ_e–τ_{had} channel
W+jets MC norm (τ_μ–τ_{had})	MC statistical uncertainties in W+jets normalisation for τ_μ–τ_{had} channel
W+jets data norm (τ_μ–τ_{had})	Data statistical uncertainties in W+jets normalisation for τ_μ–τ_{had} channel
r_{QCD} (τ_e–τ_{had})	r_{QCD} uncertainty for τ_e–τ_{had} channel
r_{QCD} (τ_μ–τ_{had})	r_{QCD} uncertainty for τ_μ–τ_{had} channel

Table 6.15: List of uncertainties that affect the normalisation of signal or background templates but not their shape. There are multiple sources of electron scale and jet scale uncertainties which are considered separately.

Left-handed	Right-handed	Not mass-selected
$^{+4.2}_{-4.2}$ PDF	$^{+3.7}_{-3.7}$ PDF	$^{+4.0}_{-4.0}$ PDF
$^{+3.2}_{-2.4}$ TES (hadronic)	$^{+2.6}_{-2.4}$ TES (hadronic)	$^{-0.1}_{-0.5}$ TES (hadronic)
$^{+1.7}_{-1.3}$ TES (electromagnetic)	$^{+0.9}_{-0.9}$ TES (electromagnetic)	$^{-0.1}_{+0.7}$ TES (electromagnetic)
$^{+0.4}_{-0.4}$ TER (hadronic)	$^{0.0}_{0.0}$ TER (hadronic)	$^{-0.4}_{+0.4}$ TER (hadronic)
$^{+0.1}_{-0.1}$ TER (electromagnetic)	$^{0.0}_{0.0}$ TER (electromagnetic)	$^{+0.5}_{-0.5}$ TER (electromagnetic)
$^{+1.3}_{-1.3}$ generator η	$^{-1.8}_{+1.8}$ generator η	$^{+0.6}_{-0.6}$ generator η
$^{+0.2}_{-0.2}$ splitting (RH→LH)	$^{-0.5}_{+0.5}$ splitting (LH→RH)	
$^{+2.5}_{-2.5}$ tau ID (syst)	$^{+2.5}_{-2.5}$ tau ID (syst)	$^{+2.5}_{-2.5}$ tau ID (syst)
$^{+1.9}_{-1.9}$ luminosity	$^{+1.9}_{-1.9}$ luminosity	$^{+1.9}_{-1.9}$ luminosity
$^{+1.0}_{-1.8}$ parton shower η	$^{+1.2}_{-1.9}$ parton shower η	$^{+1.2}_{-1.9}$ parton shower η
$^{+1.4}_{-1.4}$ tau ID (stat)	$^{+1.4}_{-1.4}$ tau ID (stat)	$^{+1.4}_{-1.4}$ tau ID (stat)
$^{+0.5}_{-1.4}$ parton shower p_{T}	$^{+1.0}_{-1.0}$ electron ID	$^{+1.3}_{+1.3}$ electron scale (2)
$^{+1.0}_{-1.0}$ electron ID	$^{+0.9}_{-0.9}$ electron trigger	$^{+1.2}_{+1.1}$ electron scale (4)
$^{+0.9}_{-0.9}$ electron trigger	$^{+0.8}_{-1.0}$ pile-up	$^{+0.6}_{+1.5}$ electron scale (3)
$^{-0.2}_{+0.7}$ generator p_{T}	$^{-1.4}_{+2.0}$ generator p_{T}	$^{-1.1}_{+1.1}$ jet scale (12)
		$^{+0.9}_{+1.3}$ electron scale (1)
		$^{+0.7}_{-1.2}$ parton shower p_{T}
		$^{+0.9}_{-0.9}$ electron ID
		$^{-1.9}_{+2.3}$ generator p_{T}

Table 6.16: Relative signal normalisation uncertainties in the signal region for the τ_e–τ_{had} channel for the fit that extracts the tau polarisation in the mass-selected region. All numbers are given in %. The upper (lower) number for each uncertainty corresponds to a variation by $+1\sigma$ (-1σ). The uncertainties listed above the line affect the shape and the normalisation of the respective template. The ones below the line only affect the normalisation.

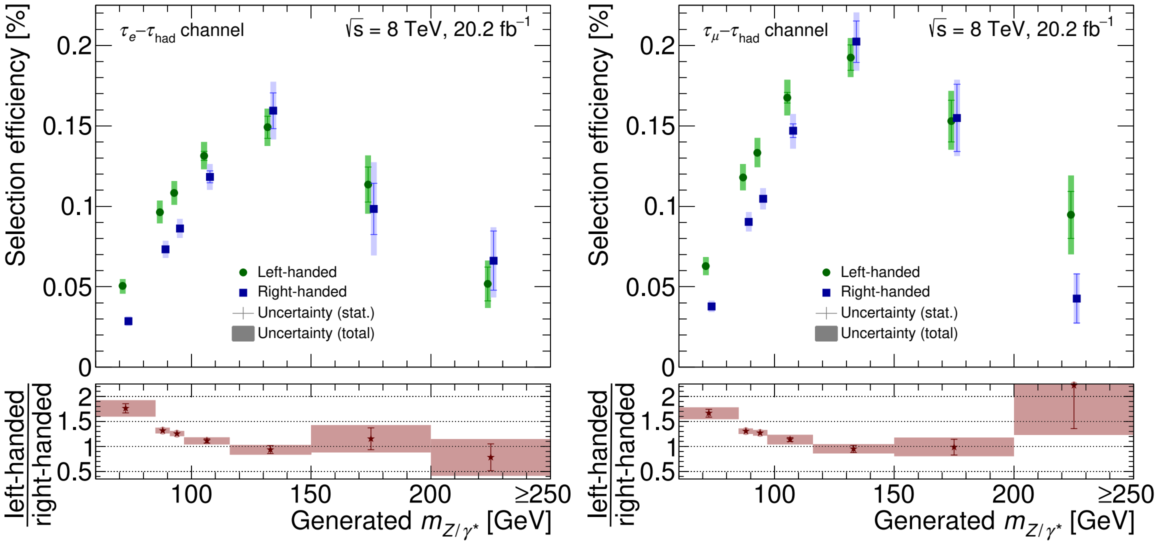

Figure 6.46: Selection efficiency for signal events in the τ_e–τ_{had} (left) and τ_μ–τ_{had} (right) channels as a function of m_{Z/γ^*}. No requirement is placed on the tau decay modes at stable-particle level. The statistical and total uncertainties are indicated. The statistical and total uncertainties in the efficiency ratio are shown. The last bin includes overflow events. Adapted from [25].

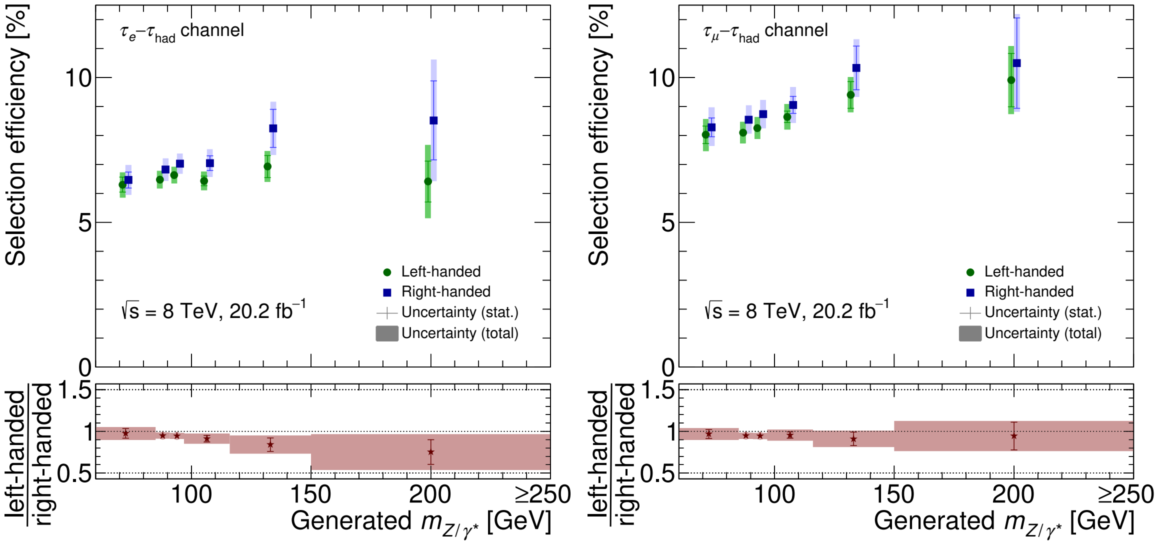

Figure 6.47: Selection efficiency for signal events in the τ_e–τ_{had} (left) and τ_μ–τ_{had} (right) channels as a function of m_{Z/γ^*}. Only events inside the fiducial region are considered. The statistical and total uncertainties are indicated. The statistical and total uncertainties in the selection efficiency ratio are shown. The last bin includes overflow events. Adapted from [25].

Left-handed	Right-handed	Not mass-selected
$^{+3.5}_{-3.5}$ PDF	$^{+2.9}_{-2.9}$ PDF	$^{+3.1}_{-3.1}$ PDF
$^{+3.4}_{-2.7}$ TES (hadronic)	$^{+2.6}_{-2.6}$ TES (hadronic)	$^{+0.6}_{+0.1}$ TES (hadronic)
$^{+1.8}_{-1.5}$ TES (electromagnetic)	$^{+1.0}_{-0.8}$ TES (electromagnetic)	$^{-0.1}_{+0.9}$ TES (electromagnetic)
$^{0.0}_{0.0}$ TER (hadronic)	$^{+0.1}_{-0.1}$ TER (hadronic)	$^{+0.2}_{-0.2}$ TER (hadronic)
$^{0.0}_{0.0}$ TER (electromagnetic)	$^{+0.1}_{-0.1}$ TER (electromagnetic)	$^{0.0}_{0.0}$ TER (electromagnetic)
$^{+1.1}_{-1.2}$ generator η	$^{-2.0}_{+2.0}$ generator η	$^{+0.4}_{-0.4}$ generator η
$^{+0.2}_{-0.2}$ splitting (RH→LH)	$^{-0.5}_{+0.5}$ splitting (LH→RH)	
$^{+2.5}_{-2.5}$ tau ID (syst)	$^{+2.5}_{-2.5}$ tau ID (syst)	$^{+2.5}_{-2.5}$ tau ID (syst)
$^{+1.9}_{-1.9}$ luminosity	$^{+1.9}_{-1.9}$ luminosity	$^{+1.9}_{-1.9}$ luminosity
$^{+1.8}_{-1.8}$ muon trigger	$^{+1.8}_{-1.8}$ muon trigger	$^{+1.8}_{-1.8}$ muon trigger
$^{+1.0}_{-1.8}$ parton shower η	$^{+1.2}_{-1.9}$ parton shower η	$^{+1.1}_{-1.9}$ parton shower η
$^{+1.5}_{-1.5}$ tau ID (stat)	$^{+1.5}_{-1.5}$ tau ID (stat)	$^{+1.5}_{-1.5}$ tau ID (stat)
$^{+1.1}_{-1.1}$ muon isolation	$^{+1.1}_{-1.1}$ muon isolation	$^{-1.2}_{+1.2}$ jet scale (12)
$^{+0.5}_{-1.4}$ parton shower p_{T}	$^{-0.9}_{+1.5}$ generator p_{T}	$^{-1.3}_{+1.9}$ generator p_{T}
$^{0.0}_{-0.4}$ generator p_{T}		

Table 6.17: Relative signal normalisation uncertainties in the signal region for the τ_μ–τ_{had} channel for the fit that extracts the tau polarisation in the mass-selected region. All numbers are given in %. The upper (lower) number for each uncertainty corresponds to a variation by $+1\sigma$ (-1σ). The uncertainties listed above the line affect the shape and the normalisation of the respective template. The ones below the line only affect the normalisation.

The background normalisation uncertainties, including the ones previously discussed in Section 6.4, are listed in Tables 6.18 and 6.19. The event yields expected for the signal region and their total uncertainties are compiled in Table 6.20.

6.6 Template Fits

In this section, the template fits used to determine the tau polarisation are described, validated, and studied.

6.6.1 Fit Models

Extended binned maximum-likelihood fits to the Υ distribution are performed. The probability density functions are built using the histogram-based HistFactory tool [90] within the RooFit/RooStats framework [91, 92] (see Section 4.2). The Υ distributions in the signal and same-sign regions are fit in 20 equally spaced bins in the range $[-1.0, 1.5]$. Two slightly different fit models determine the tau polarisation in the mass-selected and fiducial regions. Separate fits in the τ_e–τ_{had} and τ_μ–τ_{had} channels

$Z/\gamma^* \to \ell\ell$ ($\ell \to \tau_{\text{had}}$)	$Z/\gamma^* \to \ell\ell$ (jet $\to \tau_{\text{had}}$)	Top pair	W+jets	Multijet
±10 TES ($e \to \tau_{\text{had}}$)	±8 TES (background)	±2.8 TES (background)	±2.2 TES (background)	
±27 $e \to \tau_{\text{had}}$ ID	±3.2 jet scale (12)	±7 jet scale (12)	±7 jet scale (12)	±10 r_{QCD} (τ_e–τ_{had})
± 1.9 luminosity	±2.6 jet scale (5)	±1.9 luminosity	±3.3 W+jets MC norm (τ_e–τ_{had})	± 1.9 jet scale (12)
	±2.3 jet scale (1)	±1.8 electron scale (3)	±3.1 jet scale (5)	± 1.9 TES (background)
	±2.2 jet scale (6)	±1.5 tau ID (syst)	±2.9 electron scale (1)	
	±1.9 luminosity	±1.5 electron scale (4)	±2.9 jet scale (1)	
	±1.8 electron resolution		±2.6 jet scale (6)	
	±1.4 electron scale (1)		±2.4 jet scale (9)	
	±1.1 $E_{\text{T}}^{\text{miss}}$ scale		±2.1 jet scale (10)	
			±2.0 jet scale (11)	
			±1.6 jet scale (8)	
			±1.6 jet scale (2)	
			±1.4 jet scale (4)	
			±1.3 jet scale (3)	
			±1.3 jet scale (7)	
			±1.3 muon resolution	
			±1.3 muon scale	
			±1.3 JVF	

Table 6.18: Relative background normalisation uncertainties in the signal region for the τ_e–τ_{had} channel. All numbers are given in %. The uncertainties listed above the line affect the shape and the normalisation of the respective template. The ones below the line only affect the normalisation.

$Z/\gamma^* \to \ell\ell$ ($\ell \to \tau_{\text{had}}$)	$Z/\gamma^* \to \ell\ell$ (jet $\to \tau_{\text{had}}$)	Top pair	W+jets	Multijet
±14 TES (background)	±12 TES (background)	±2.4 TES (background)	±2.8 TES (background)	
± 9 JER	± 2.8 jet scale (12)	±7 jet scale (12)	±5 jet scale (12)	±10 r_{QCD} (τ_μ–τ_{had})
± 5 jet scale (12)	± 2.8 jet scale (1)	±1.9 luminosity	±3.4 W+jets MC norm (τ_μ–τ_{had})	± 5 jet scale (12)
± 4 $E_{\text{T}}^{\text{miss}}$ resolution	± 1.9 luminosity	±1.8 muon trigger	±1.9 jet scale (1)	± 5 TES (background)
± 1.9 luminosity	± 1.8 muon trigger		±1.9 jet scale (5)	
	± 1.6 JER		±1.7 JER	
			±1.5 jet scale (6)	
			±1.3 jet scale (9)	
			±0.9 jet scale (10)	
			±0.7 jet scale (11)	
			±0.7 W+jets data norm (τ_μ–τ_{had})	
			±0.7 jet scale (3)	
			±0.6 jet scale (7)	
			±0.6 JVF	

Table 6.19: Relative background normalisation uncertainties in the signal region for the τ_μ–τ_{had} channel. All numbers are given in %. The uncertainties listed above the line affect the shape and the normalisation of the respective template. The ones below the line only affect the normalisation.

Process	τ_e–τ_{had} channel	τ_μ–τ_{had} channel
Data	32243	32347
Total expected	$32000\,^{+1600}_{-1600}$	$33000\,^{+1800}_{-1800}$
Left-handed	$13800\,^{+1100}_{-1100}$	$17000\,^{+1400}_{-1300}$
Right-handed	$7800\,^{+600}_{-600}$	$9600\,^{+700}_{-700}$
Not mass-selected	$430\,^{+40}_{-40}$	$550\,^{+40}_{-40}$
W+jets	$2240\,^{+260}_{-240}$	$2600\,^{+210}_{-220}$
Multijet	$6200\,^{+600}_{-600}$	$2400\,^{+270}_{-300}$
Top pair	$360\,^{+40}_{-40}$	$390\,^{+40}_{-40}$
$(Z/\gamma^* \to \ell\ell)$+jets	$1210\,^{+140}_{-140}$	$360\,^{+50}_{-40}$

Table 6.20: Event yields expected in the selected signal region for both channels. The signal contribution is shown separately for the three components used when extracting the polarisation in the mass-selected region. The tau polarisation is taken from the simulation for signal events. Total uncertainties are shown. Adapted from [25].

Category	Parameters	Description
Tau polarisation	P_τ^{POI}	Parameter of interest (unconstrained)
Signal normalisation	α_{signal}	Overall signal normalisation (unconstrained)
Multijet estimate	$t_{\text{b}}^{\text{multijet}}$	20 unconstrained parameters per channel, each determines the multijet contributions in the corresponding bins in the signal and same-sign regions
MC statistical	$\gamma_{\text{b}}^{\text{MC stat}}$	20 Poissonian constrained parameters per channel, each controls variations of total simulated event yield in one bin
Shape uncertainties		One Gaussian constrained parameter per uncertainty in Table 6.14
Other uncertainties		One Gaussian constrained parameter per uncertainty in Table 6.15

Table 6.21: Parameters in the template fits.

as well as combined fits are performed. Table 6.21 provides an overview of the fit parameters, which are discussed further in the following.

The fit model that determines the tau polarisation in the mass-selected region includes three signal templates for each signal and same-sign region and for each channel. They are obtained from the simulated $Z/\gamma^* \to \tau\tau$ events with left-handed taus in the mass-selected region, with right-handed taus in the mass-selected region, and outside the mass-selected region, respectively, that pass the corresponding selection requirements. The left- and right-handed templates are each normalised to the full $Z/\gamma^* \to \tau\tau$

cross-section within the mass-selected region:

$$\begin{aligned} N_{\text{template}}^{\text{left-handed}} &= \frac{2}{1 - P_\tau^{\text{TS}}} \cdot N_{\text{expected}}^{\text{left-handed}} \qquad \text{and} \\ N_{\text{template}}^{\text{right-handed}} &= \frac{2}{1 + P_\tau^{\text{TS}}} \cdot N_{\text{expected}}^{\text{right-handed}}. \end{aligned} \tag{6.10}$$

Here, $N_{\text{expected}}^{\text{left-handed}}$ and $N_{\text{expected}}^{\text{right-handed}}$ are the expected yields of mass-selected events with left-handed and right-handed taus, respectively, for the signal or same-sign region, and P_τ^{TS} is the tau polarisation in the mass-selected region determined by the TauSpinner [146] algorithm. Before the scaling in Eq. (6.10) the summed left- and right-handed templates account for the $Z/\gamma^* \to \tau\tau$ cross-section within the mass-selected region.

The relative normalisation of the left-handed and right-handed templates is bound to the parameter of interest, P_τ^{POI}, which represents the tau polarisation in the fit:

$$\begin{aligned} N_{\text{fit}}^{\text{left-handed}} &\propto \frac{1 - P_\tau^{\text{POI}}}{2} \cdot N_{\text{template}}^{\text{left-handed}} \qquad \text{and} \\ N_{\text{fit}}^{\text{right-handed}} &\propto \frac{1 + P_\tau^{\text{POI}}}{2} \cdot N_{\text{template}}^{\text{right-handed}}. \end{aligned} \tag{6.11}$$

The parameter P_τ^{POI} is constrained to the physically sensible range $[-1, 1]$ in the fit, but not further constrained. The templates for signal events outside the mass-selected region are unaffected by P_τ^{POI} . By construction P_τ^{POI} determines the tau polarisation that corresponds to the observed relative abundance of signal events with left- and right-handed taus. Specifically, it determines the tau polarisation in the mass-selected region before any other selection because differences between the relative acceptance of events with left- and right-handed taus are considered when normalising the templates. For example the P_τ^{POI} and P_τ^{TS} values are equal if the relative abundance is as predicted. Effects that could cause a deviation of the tau polarisation in the data from the prediction may also affect the prediction of the $Z/\gamma^* \to \tau\tau$ cross-section. Hence, all signal templates are scaled proportionally to an unconstrained nuisance parameter, α_{signal}, with a nominal value of one. The P_τ^{POI} and α_{signal} parameters are common to the signal and same-sign regions and to the channels.

Analogously, the fit model that determines the tau polarisation in the fiducial region includes templates for signal events with left- and right-handed taus inside the fiducial region and templates for events outside the fiducial region each in the signal and same-sign regions and per channel. The left- and right-handed templates are scaled to the full $Z/\gamma^* \to \tau\tau$ cross-section in the fiducial region as in Eq. (6.10). Their relative normalisation is bound to a P_τ^{POI} parameter as in Eq. (6.11), so the P_τ^{POI} parameter measures the tau polarisation in the fiducial region. All signal templates are scaled proportionally to an α_{signal} parameter. The data and the background templates are identical in both fit models and the two models are described in parallel in the following.

The $Z/\gamma^* \to \ell\ell$ ($\ell \to \tau_{\text{had}}$), $Z/\gamma^* \to \ell\ell$ (jet $\to \tau_{\text{had}}$), and top pair templates are taken from the simulation. There are separate templates for the signal and same-sign regions and per channel as for the signal. In each channel the W+jets template in the signal (same-sign) region is taken from the opposite-sign (same-sign) W+jets control region, the small simulation-based linear shape correction is applied, and the template is scaled as presented in Section 6.4.2.

The multijet background is estimated in the fits. For this, 20 unconstrained nuisance parameters, $t_{\text{b}}^{\text{multijet}}$, per channel are introduced. They are common to the corresponding Υ bins, b, in the signal and same-sign regions in a channel. In the same-sign region the multijet contribution in a bin equals the value of the $t_\mathrm{b}^\mathrm{multijet}$ parameter. In the signal region the $t_\mathrm{b}^\mathrm{multijet}$ value is multiplied with the respective r_QCD value from Table 6.12. The post-fit $t_\mathrm{b}^\mathrm{multijet}$ values minimise the differences between the data and the remaining templates simultaneously in the signal and same-sign regions. In practice, they are mostly determined from the same-sign region for which the multijet fraction is much larger. The statistical uncertainties in the multijet estimate are evaluated accurately with this method. The W+jets and multijet control regions are not included in the fit models because the statistical uncertainties are negligible in these regions.

Overall, the fitted event yield in a bin in the signal region of a given channel without systematic uncertainties in the templates is

$$\begin{aligned} F_\mathrm{b}^\text{signal region} &= \alpha_\mathrm{signal}\left(\frac{1-P_\tau^\mathrm{POI}}{2}F_\mathrm{b}^\text{left-handed}+\frac{1+P_\tau^\mathrm{POI}}{2}F_\mathrm{b}^\text{right-handed}+F_\mathrm{b}^\text{not mass-selected/fiducial}\right)\\ &\quad + F_\mathrm{b}^{Z/\gamma^*\to\ell\ell\ (\ell\to\tau_\mathrm{had})}+F_\mathrm{b}^{Z/\gamma^*\to\ell\ell\ (\mathrm{jet}\to\tau_\mathrm{had})}+F_\mathrm{b}^\text{top pair}+F_\mathrm{b}^{W\text{+jets}}+r_\mathrm{QCD}\cdot t_\mathrm{b}^\mathrm{multijet}, \end{aligned}$$

where $F_\mathrm{b}^\mathrm{contribution}$ stands for the bin content of the nominal template of the respective contribution. The fitted yield in the same-sign region is analogous except that the r_QCD factor is dropped.

Nuisance parameters are included to model the remaining systematic uncertainties. They only alter the templates in the signal region. Common uncertainties are treated as fully correlated between the templates and channels. Instead of including uncertainties in the non-multijet templates in the same-sign region, they are propagated to the multijet contribution in the signal region (see multijet normalisation uncertainties in Tables 6.18 and 6.19). This improves the stability of the fit and simplifies it. For testing purposes the uncertainties in the same-sign region can be considered as in the signal region. The test results agree with those in the nominal fit.

The statistical uncertainties in the simulated samples[4] (MC statistical uncertainties) are accounted for with a variation of the Barlow–Beeston method [93] that is provided by the HistFactory tool. One nuisance parameter per bin and channel in the signal region with a Poissonian constraint is introduced. Each parameter controls variations of the total simulated event yield in one bin by its statistical uncertainty. The MC statistical uncertainties are dominated by the uncertainties in the signal sample.

Uncertainties in the shapes of templates are modelled using nuisance parameters with Gaussian constraints. Piecewise-linear interpolations [90] between the nominal template shapes and those obtained after $\pm1\sigma$ variations as well as linear extrapolations are performed, which is the default for shape uncertainties in HistFactory. All uncertainties discussed in Section 6.5 and the uncertainties in the shape corrections of the W+jets template (see Section 6.4.2) were evaluated as shape uncertainties. In the final fit models an uncertainty is included as a shape uncertainty in all templates in the signal region to which it applies if doing so increases the tau polarisation uncertainty by at least 1%. Following this methodology, the shape uncertainty parameters compiled in Table 6.14 are implemented. If any of the remaining uncertainties are included as shape uncertainties, the post-fit uncertainties of the related parameters are $\geq 90\%$ of their pre-fit uncertainties, and the constraints of all other fit parameters are altered by $< 10\%$.

Uncertainties in the normalisation of templates are also modelled by nuisance parameters with Gaussian constraints. Piecewise-exponential interpolations [90] between the nominal and varied normalisations are performed as well as exponential extrapolations, which is the default for normalisation uncertainties in HistFactory. If an uncertainty affects the shape and the normalisation of a template a piecewise-linear (piecewise-exponential) interpolation and extrapolation is used for the shape (normalisation) variation and the two are controlled by the same nuisance parameter. All uncertainties that exclusively alter the normalisation of templates have a negligible impact on the final result. They are collectively referred to as other uncertainties and listed in Table 6.15.

---

[4] Statistical uncertainties in simulated samples are classified as systematic uncertainties by convention.

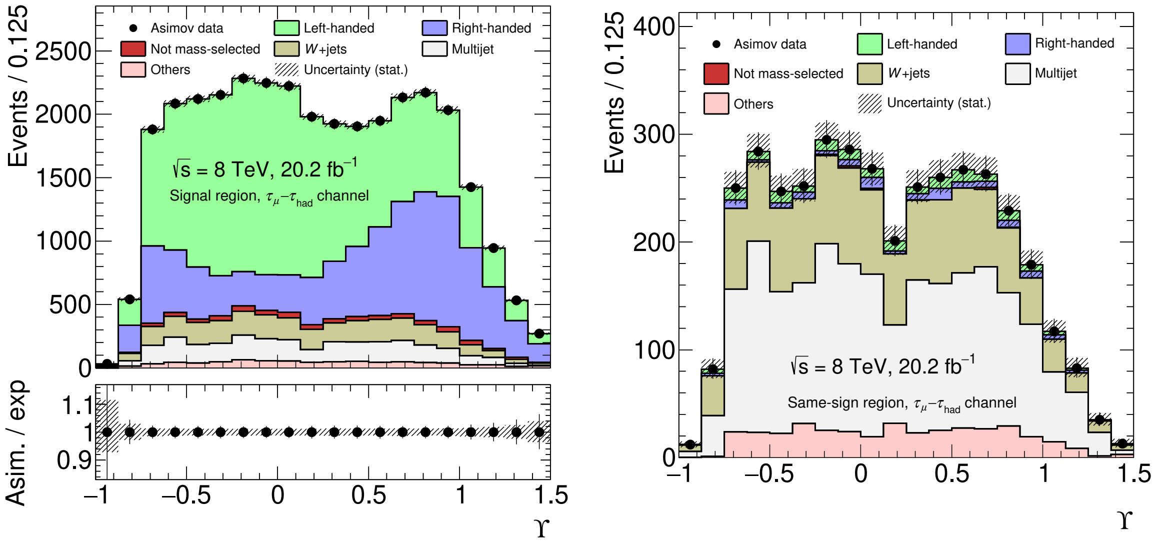

Figure 6.48: Distribution of Υ in the signal (left) and same-sign (right) region for the τ_μ–τ_{had} channel with Asimov data. The signal contribution is estimated from the simulation, in particular the tau polarisation is as predicted. The uncertainties are statistical.

6.6.2 Fits to Asimov Data and Expected Accuracy of the Measurement

The fit models are tested with pseudo data. The pseudo data for the same-sign region correspond to the real data, and those for the signal region correspond to the total estimate (see Figure 6.48). The total post-fit estimates match the pseudo data. All parameters are fit to their nominal values, so the pseudo data are Asimov data.

In particular, the post-fit P_τ^{POI} values match the tau polarisation values determined by TauSpinner [146], which are the assumed values in the Asimov data (see Table 6.22). The P_τ^{POI} uncertainties are obtained from the likelihood profiles in Figure 6.49. The profiles are approximately parabolic, so the P_τ^{POI} probability density functions are approximately Gaussian. The 1σ uncertainties are read off from the values at which $2 \cdot \Delta\text{NLL} = 1$ (see Eq. (4.3)). They agree within 1% with the P_τ^{POI} uncertainties estimated by the minos algorithm, which follows the same methodology and is provided by the RooStats package [92]. The statistical uncertainties are determined in fits in which P_τ^{POI} and α_{signal} are the only free parameters. Due to the larger signal fraction, the measurements in the τ_μ–τ_{had} channel are slightly more accurate than those in the τ_e–τ_{had} channel. Both channels contribute noticeably in the combined fits. The statistical uncertainties are a bit larger in the measurements in the fiducial region because the fractions of signal events outside the fiducial region are larger than those of signal events outside the mass-selected region.

Additional Asimov datasets are created assuming various tau polarisations for signal events in the mass-selected region. The assumed signal contributions outside the mass-selected region and the background contributions are the same as in the previously discussed Asimov data. The fits can determine the tau polarisation in these input data (see Figure 6.50).

In the following the post-fit nuisance parameter values, uncertainties, and correlations are discussed. The results are taken from the combined fits to Asimov data that include the tau polarisation predicted by the simulation. The post-fit uncertainties in the nuisance parameters are obtained from their likelihood profiles, which are approximately parabolic. The uncertainties agree within 2% with those estimated

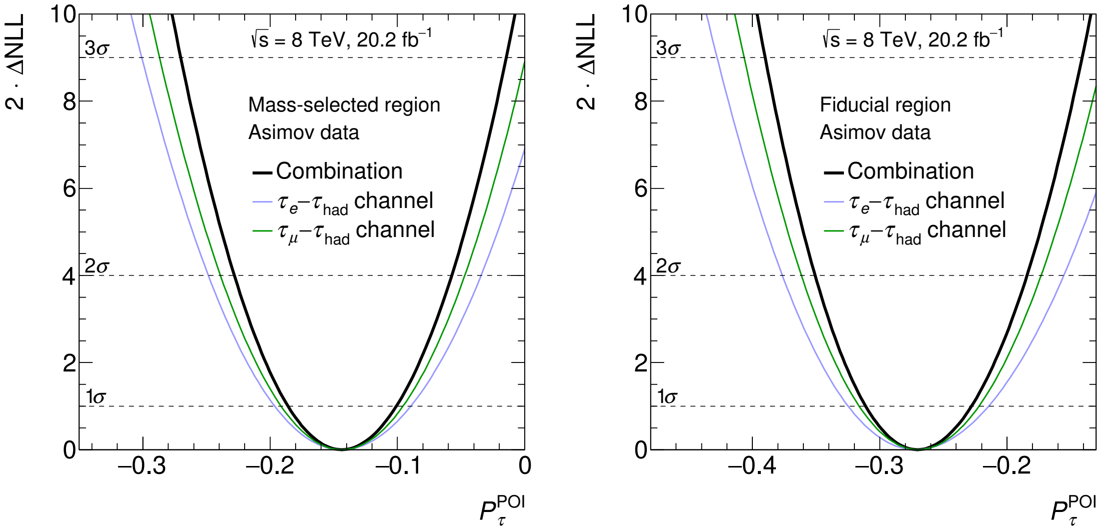

Figure 6.49: Likelihood profiles of the tau polarisation parameter, P_τ^{POI}, for the fits to Asimov data that determine the polarisation in the mass-selected (left) and fiducial (right) regions. The profiles are shown for the τ_e–τ_{had} and τ_μ–τ_{had} channels and for the combination.

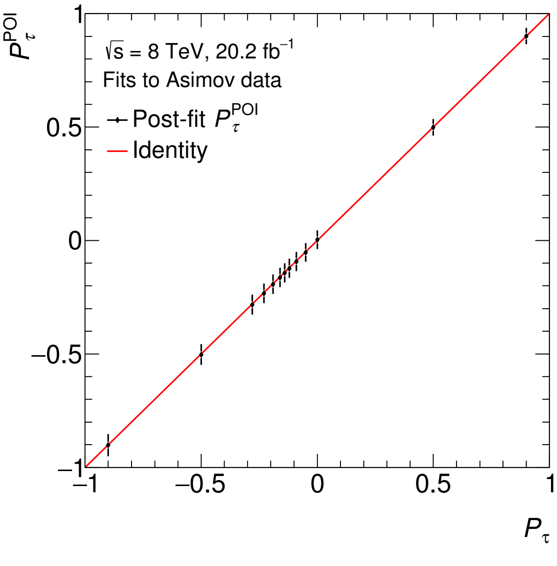

Figure 6.50: Post-fit P_τ^{POI} value in fits to Asimov data as a function of the assumed tau polarisation. The test results are shown for the fit model that is used to extract the tau polarisation in the mass-selected region. The identity function is overlaid.

Channel	P_τ^{POI} in mass-selected region	P_τ^{POI} in fiducial region
τ_e–τ_{had}	-0.144 ± 0.024 (stat) $\pm$ 0.051 (syst)	-0.271 ± 0.026 (stat) $\pm$ 0.050 (syst)
τ_μ–τ_{had}	-0.144 ± 0.020 (stat) $\pm$ 0.045 (syst)	-0.270 ± 0.021 (stat) $\pm$ 0.045 (syst)
Combination	-0.144 ± 0.015 (stat) $\pm$ 0.040 (syst)	-0.270 ± 0.016 (stat) $\pm$ 0.039 (syst)

Table 6.22: Post-fit values and uncertainties of P_τ^{POI} in the fits to Asimov data for the mass-selected and fiducial regions. The TauSpinner [146] algorithm determines $P_\tau^{\mathrm{TS}} = -0.144$ (-0.270) for the mass-selected (fiducial) region. The quoted systematic uncertainties are estimated from the total and statistical uncertainties.

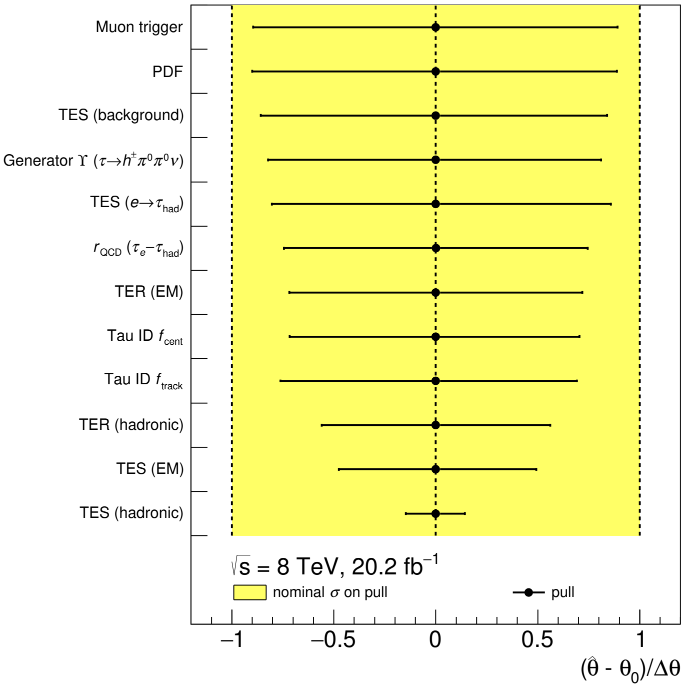

Figure 6.51: Values of Gaussian-constrained nuisance parameters and their uncertainties after the combined fits to Asimov data. The parameters have nominal values of 0 ± 1. Parameters with post-fit uncertainties below 0.9 are shown. The shown results are obtained from the fit that extracts the tau polarisation in the mass-selected region. They agree within 1% with those in the measurement in the fiducial region.

by the minos algorithm. Some of the Gaussian constrained nuisance parameters are constrained further (see Figure 6.51). Most of them model shape uncertainties and are constrained by the shapes of the Υ distributions. For example, the Υ distributions are very sensitive to the hadronic component of the TES (see Section 6.5.1), so the TES (hadronic) parameter can be constrained to about 14% of its initial uncertainty. The TES (electromagnetic) and TER parameters are constrained as well. Consequently, the Υ observable is being utilised in a dedicated measurement of the energy response to τ_{had} decays at ATLAS. The results may be the basis of future calibration and uncertainty recommendations. There are no unexpected parameter constraints that may lead to an underestimation of the related uncertainties.

The impact of an individual parameter on a measurement is estimated from the deviations of the P_τ^{POI} value from the nominal value in fits in which the parameter under study is varied by $\pm 1\sigma$. The

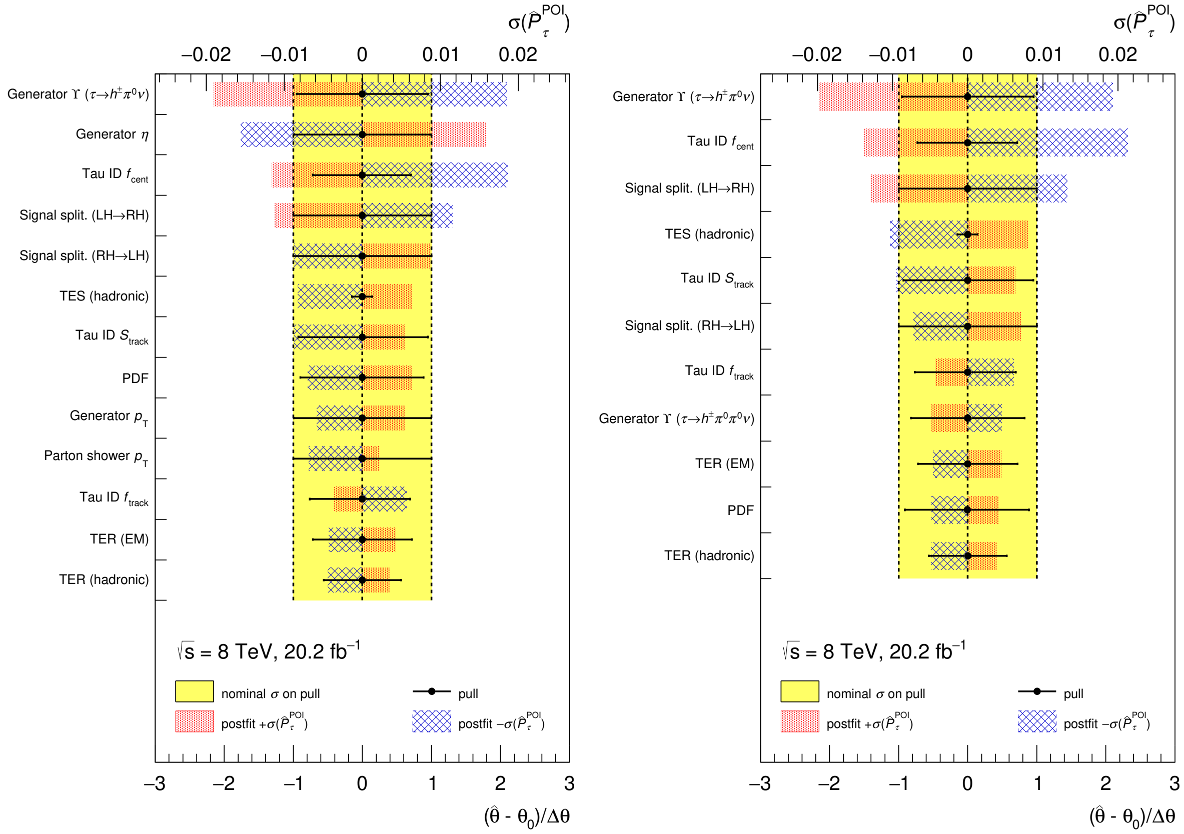

Figure 6.52: Values of Gaussian-constrained nuisance parameters and their uncertainties as well as their impact on the P_τ uncertainty in the fits to Asimov data. They are shown for the combined fits that extract P_τ in the mass-selected (left) and the fiducial (right) regions. The black markers show the post-fit nuisance parameter values and uncertainties (use bottom axis). The yellow areas indicate the range covered by the post-fit nuisance parameter values with pre-fit uncertainties (use bottom axis). The red (+1) and blue (−1) areas indicate the impact of varying the nuisance parameter value by one post-fit standard deviation on the fitted polarisation value (use top axis). The nuisance parameters shown cover 99% of the P_τ uncertainty in Gaussian constrained nuisance parameters.

results are shown in Figure 6.52. Most of the largest uncertainties are shape uncertainties and affect the measurements in the mass-selected and fiducial regions similarly. The generator η, generator p_T, and parton shower p_T uncertainties are much smaller in the measurement in the fiducial region (see Section 6.5.2). The MC statistical uncertainties and those in the multijet estimate cannot be judged intuitively on a parameter-by-parameter basis and be compared with other uncertainties. Instead the uncertainties in the categories defined in Table 6.14, the MC statistical uncertainties, the uncertainties in the multijet estimate, and the remaining uncertainties are combined per category (see Table 6.23). Several of these categories contribute noticeably to the overall tau polarisation uncertainty. The uncertainties in the individual channels can be found in Tables E.1 and E.2.

The post-fit signal normalisation is $\alpha_\mathrm{signal} = 1.00 \pm 0.01\,(\mathrm{stat}) \pm 0.06\,(\mathrm{syst}) \pm 0.02\,(\mathrm{lumi})$ in the combination. It is likely possible to measure the $Z/\gamma^* \to \tau\tau$ cross-section with a similar relative precision using this analysis as a basis, and it is instructive to discuss this potential briefly. The following aspects would have to be investigated, added, or changed for a cross-section measurement:

- The α_signal values do not correspond the signal cross-sections in the mass-selected or fiducial

Source of uncertainty	σ_{P_τ} in mass-selected region	σ_{P_τ} in fiducial region
Modelling of signal process	0.026	0.021
τ_{had} identification	0.020	0.023
MC statistical	0.015	0.017
Signal sample splitting	0.015	0.015
TES and TER	0.010	0.012
Multijet estimate	0.012	0.012
PDF	0.007	0.005
W+jets shape	0.002	0.003
Other	0.007	0.002
Total systematic uncertainty	0.040	0.039
Statistical uncertainty	0.015	0.016

Table 6.23: Impact of the individual sources of uncertainty on the polarisation uncertainty σ_{P_τ} in the fits to Asimov data. The values are shown for the combined fits that extract the tau polarisation in the mass-selected and fiducial regions. The total systematic uncertainty quoted is estimated from the total uncertainty and the statistical uncertainty.

regions because the α_{signal} parameter also scales the signal contributions outside these regions.

- The p_{T}^{Z} reweighting would have to be propagated to the measured cross-sections.
- The PDF uncertainties, which are among the largest in α_{signal}, include those in the cross-section. A cross-section measurement would only consider the acceptance uncertainties.
- The systematic uncertainties were primarily studied for their effect on the polarisation measurement. For example, other generator p_{T} and η uncertainties may be chosen for a cross-section measurement using the methodology described in Section 6.5.2.
- The implications of nuisance parameter constraints would have to be re-investigated. For example, the TES parameters are constrained from the Υ shape. It may be more appropriate to treat the related shape and normalisation variations as uncorrelated in a cross-section measurement.
- LHC beam energy uncertainties would have to be considered. They may be ~1% as in Ref. [180].

The relative systematic uncertainties in α_{signal} are similar to those in the dedicated $Z/\gamma^* \to \tau\tau$ cross-section measurements at ATLAS, in which events with two τ_{lep} decays are also considered [98, 180, 181]. Improvements with respect to the previous results in the τ_e–τ_{had} and τ_μ–τ_{had} channels would be possible thanks to the advanced understanding of τ_{had} reconstruction and identification, which is reflected in the reduced TES and τ_{had} identification uncertainties in Ref. [82].[5] Additionally, there are benefits from the reduced uncertainties in the modelling of electrons and muons. Because of the latter improvements a cross-section measurement in the τ_e–τ_μ channel would still be competitive.

The correlations between most fit parameters are small. The following absolute correlations are above 20% in the fit that extracts the polarisation in the mass-selected region:

---

[5] Even though the τ_{had} identification efficiency measurement was performed in $Z/\gamma^* \to \tau\tau$ decays it does not rely on the prediction of the signal cross-section. The efficiency was measured by comparing the signal yields before and after applying the identification requirements. Therefore, that measurement could be utilised in a $Z/\gamma^* \to \tau\tau$ cross-section measurement.

- The P_τ^{POI} parameter is anti-correlated with the generator Υ ($\tau \rightarrow h^\pm\pi^0\nu$) (44%) and f_{cent} (36%) parameters. Increasing the values of the nuisance parameters leads to increased (decreased) yields in Υ bins that are primarily populated in the right-handed (left-handed) templates (see Figures 6.42 and 6.33). The changes can be compensated partially by decreasing the P_τ^{POI} value.
- The P_τ^{POI} parameter is positively correlated with the generator η parameter (36%) because of the template normalisation variations in Tables 6.16 and 6.17.
- The P_τ^{POI} parameter is anti-correlated (30%) with the splitting (LH→RH) parameter. The original polarisation value must have been lower if a positive net migration from the left-handed to the right-handed template is present. Analogously, the P_τ^{POI} parameter is positively correlated with the splitting (RH→LH) parameter (20%).
- The α_{signal} parameter is anti-correlated with the PDF (64%), tau ID (syst) (51%), luminosity (40%), muon trigger (33%), tau ID (stat) (30%), and parton shower η (30%) parameters.
- The TES (electromagnetic) parameter is positively correlated with the f_{track} (54%) and f_{cent} (43%) parameters. It is also anti-correlated (44%) with the generator Υ ($\tau \rightarrow h^\pm\pi^0\pi^0\nu$) parameter. The TES (hadronic) and generator Υ ($\tau \rightarrow h^\pm\pi^0\pi^0\nu$) parameters are positively correlated (22%).
- The r_{QCD} (τ_e–τ_{had}) parameter is positively correlated with the muon trigger (41%) and muon isolation (22%) parameters. This may be the result of cross-correlations via the α_{signal} parameter and others.
- The two nuisance parameters in the same Υ bin in the signal region that model the multijet contribution and the MC statistical uncertainties are anti-correlated by 10–30%.

In the measurement for the fiducial region, the P_τ^{POI} and generator η parameters only show small correlations. The other correlations agree within five percent points with those in the measurement in the mass-selected region.

6.6.3 Monte Carlo Generated Pseudo Experiments

The combined fit that extracts the polarisation in the mass-selected region is tested with pseudo experiments using Monte Carlo generated data. The pseudo data are generated using the ToyMCSampler algorithm within the RooFit/RooStats framework [91, 92]. Tests are performed for the same assumed tau polarisation values as in Figure 6.50. The nuisance parameter values are randomised within the post-fit uncertainties found in the fit to the respective Asimov data. The pull, defined as

$$\text{pull} = \frac{\text{Post-fit } P_\tau^{\mathrm{POI}} - \text{assumed } P_\tau}{\text{minos uncertainty}},$$

is calculated for each pseudo experiment. The pull distribution for an assumed tau polarisation of $P_\tau = -0.14$ is shown in Figure 6.53. It resembles a Gaussian distribution with a mean of -0.02 ± 0.01 and a width of 0.99 ± 0.01, which means that the estimated tau polarisation is nearly unbiased. The results are representative for all assumed polarisation values except ±0.90, for which deviations are caused by the boundaries at ±1. The remaining pull distributions can be found in Figures E.1–E.3. The mean and width of the P_τ^{POI} distributions as a function of the assumed P_τ value is also shown in Figure 6.53.

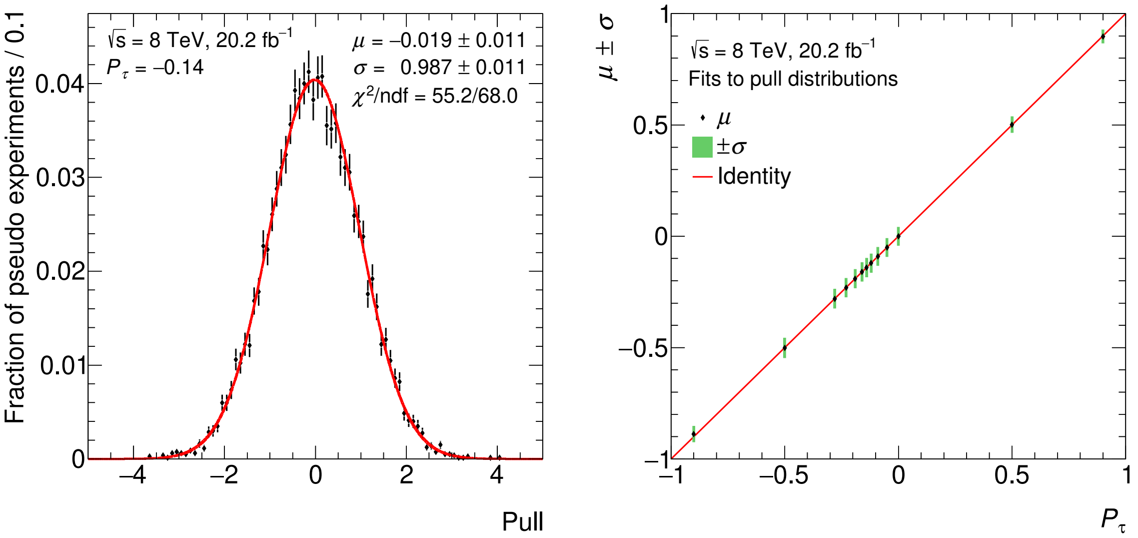

Figure 6.53: Example pull distribution (left) and results of fits to various pull distributions obtained using 10 000 pseudo experiments each with Monte Carlo generated data (right). The pull distribution is obtained using the 10 000 pseudo experiments in which $P_\tau = -0.14$ is assumed. The mean (μ) and width (σ) parameters obtained in a fit of a Gaussian function to the pull distribution as well as the χ^2 and the number of degrees of freedom in the fit are documented. The right plot shows the mean and width of Gaussian functions obtained in fits to the post-fit P_τ^{POI} distributions as a function of the assumed P_τ value in the pseudo experiments. The identity function is overlaid.

6.7 Results

The Υ distributions after the combined fit that extracts the tau polarisation in the mass-selected region are shown in Figure 6.54. The corresponding results of the measurements in the individual channels and of the measurement in the fiducial region can be found in Figures E.4–E.6. The post-fit estimates in the signal region agree with the data within the statistical uncertainties. The few discrepancies in the pre-fit distributions (see Figure 6.27) are rectified. Because the unconstrained $t_{\mathrm{b}}^{\mathrm{multijet}}$ parameters are primarily determined from the same-sign region, good agreement is reached almost by construction in this region.

The P_τ^{POI} likelihood profiles are shown in Figure 6.55 and the measured tau polarisation values are summarised in Table 6.24. These values are $P_\tau = -0.20 \pm 0.02$ (stat) $\pm$ 0.05 (syst) and $P_\tau = -0.13 \pm 0.02$ (stat) $\pm$ 0.05 (syst) for the mass-selected region in the τ_e–τ_{had} and τ_μ–τ_{had} channels, respectively. They agree at a level of 1.4 standard deviations and are compatible with each other. In this compatibility estimate only the uncertainties that are uncorrelated between the channels are considered, which are the statistical, MC statistical, and multijet estimate uncertainties. The agreement is similar for the fiducial region. The combination yields $P_\tau = -0.27 \pm 0.02$ (stat) $\pm$ 0.04 (syst) for the fiducial region and $P_\tau = -0.14 \pm 0.02$ (stat) $\pm$ 0.04 (syst) for the mass-selected region. The SM predictions of $P_\tau = -0.270 \pm 0.006$ and $P_\tau = -0.1536 \pm 0.0014$, respectively, are confirmed.

The $\sin^2\theta_{\mathrm{W}}^{\mathrm{eff}}$ value can be estimated using Eq. (2.24) by neglecting the difference between the tau polarisation in the mass-selected region and that in $Z \to \tau\tau$ events at the pole. Inserting the result of the combination in the mass-selected region yields $\sin^2\theta_{\mathrm{W}}^{\mathrm{eff}} \approx 0.232 \pm 0.005$. The LEP experiments measured $\sin^2\theta_{\mathrm{W}}^{\mathrm{eff}} = 0.23159 \pm 0.00041$ using tau polarisation [23]. The measurements in electron–positron collisions benefit from smaller backgrounds and the more accurate knowledge about the initial state compared to hadron collisions.

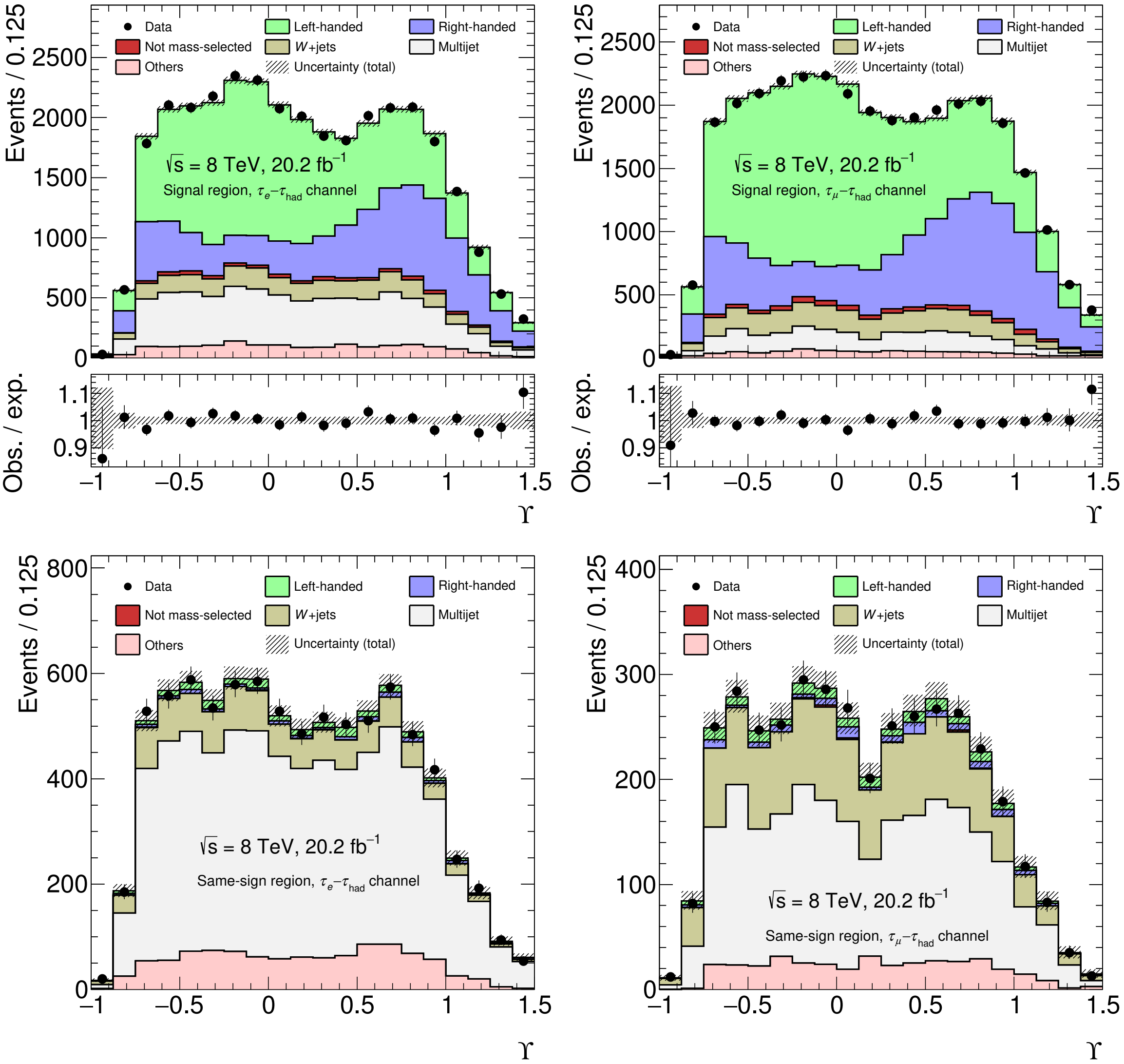

Figure 6.54: The ϒ distributions in the τ_e–τ_{had} (left) and τ_μ–τ_{had} (right) channels, and in the signal (top) and same-sign (bottom) regions after the combined fit that extracts the tau polarisation in the mass-selected region. Adapted from [25].

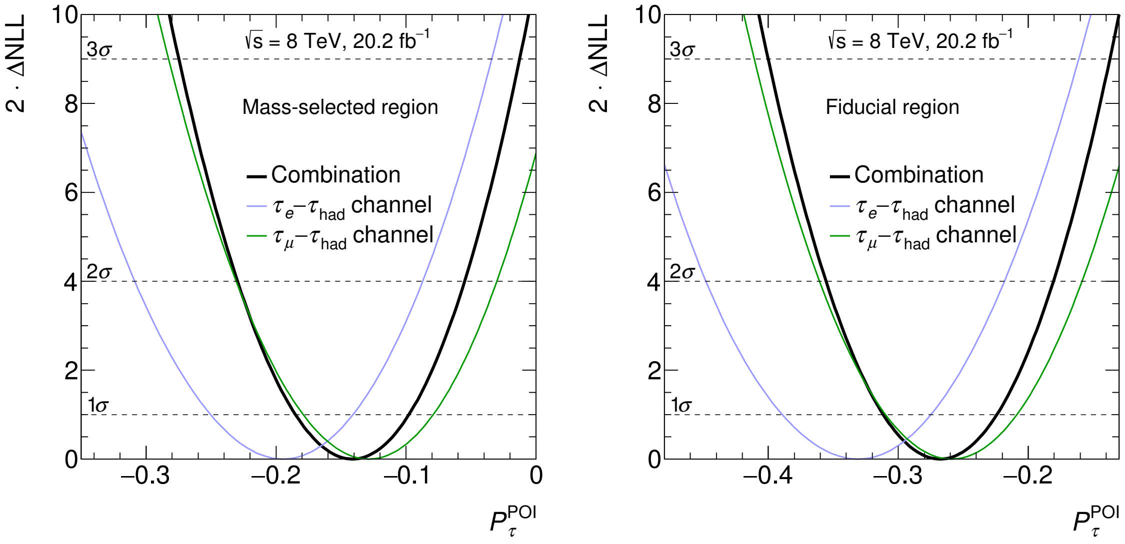

Figure 6.55: Likelihood profiles of P_τ^{POI} in the fits that extract the polarisation in the mass-selected (left) and fiducial (right) regions. The profiles are shown separately for the fits in the τ_e–τ_{had} and τ_μ–τ_{had} channels and for the combination. Adapted from [25].

Channel	P_τ in mass-selected region		P_τ in fiducial region	
τ_e–τ_{had}	−0.20	± 0.02 (stat) ± 0.05 (syst)	−0.33	± 0.03 (stat) ± 0.05 (syst)
τ_μ–τ_{had}	−0.13	± 0.02 (stat) ± 0.05 (syst)	−0.26	± 0.02 (stat) ± 0.05 (syst)
Combination	−0.14	± 0.02 (stat) ± 0.04 (syst)	−0.27	± 0.02 (stat) ± 0.04 (syst)
Prediction	−0.1536 ± 0.0014		−0.270 ± 0.006	

Table 6.24: Measured tau polarisation values, their uncertainties, and the predictions for the mass-selected and fiducial regions. Adapted from [25].

The measured α_{signal} values are 1.03 ± 0.07 in the τ_e–τ_{had} channel, 1.01 ± 0.06 in the τ_μ–τ_{had} channel, and 1.03 ± 0.06 in the combinations both in the measurements in the mass-selected and fiducial regions. The measured signal yields are consistent with the prediction.

The tau polarisation values measured in the combinations are much closer to those in the τ_μ–τ_{had} channel than to those in the τ_e–τ_{had} channel. This is due to the nuisance parameter pulls in Figures 6.56 and 6.57. The f_{cent} and TER (hadronic) parameters are pulled in the same direction in the channel-exclusive fits and the pulls are enhanced in the combinations. The P_τ^{POI} and f_{cent} parameters are anti-correlated by about ~40%, so the enhanced negative f_{cent} pulls lead to increased P_τ^{POI} values in the combination. Similarly, the P_τ^{POI} value is increased due to its ~10% positive correlation with the TER (hadronic) parameter. Further small shifts in both directions are caused by the pulls of the generator Υ ($\tau \to h^\pm\pi^0\nu$), TES (hadronic), and other parameters.

The nuisance parameter values agree well between the channel-exclusive and combined fits and between the fits in the mass-selected and fiducial regions. The parameter correlations are similar to those in the fits to Asimov data.

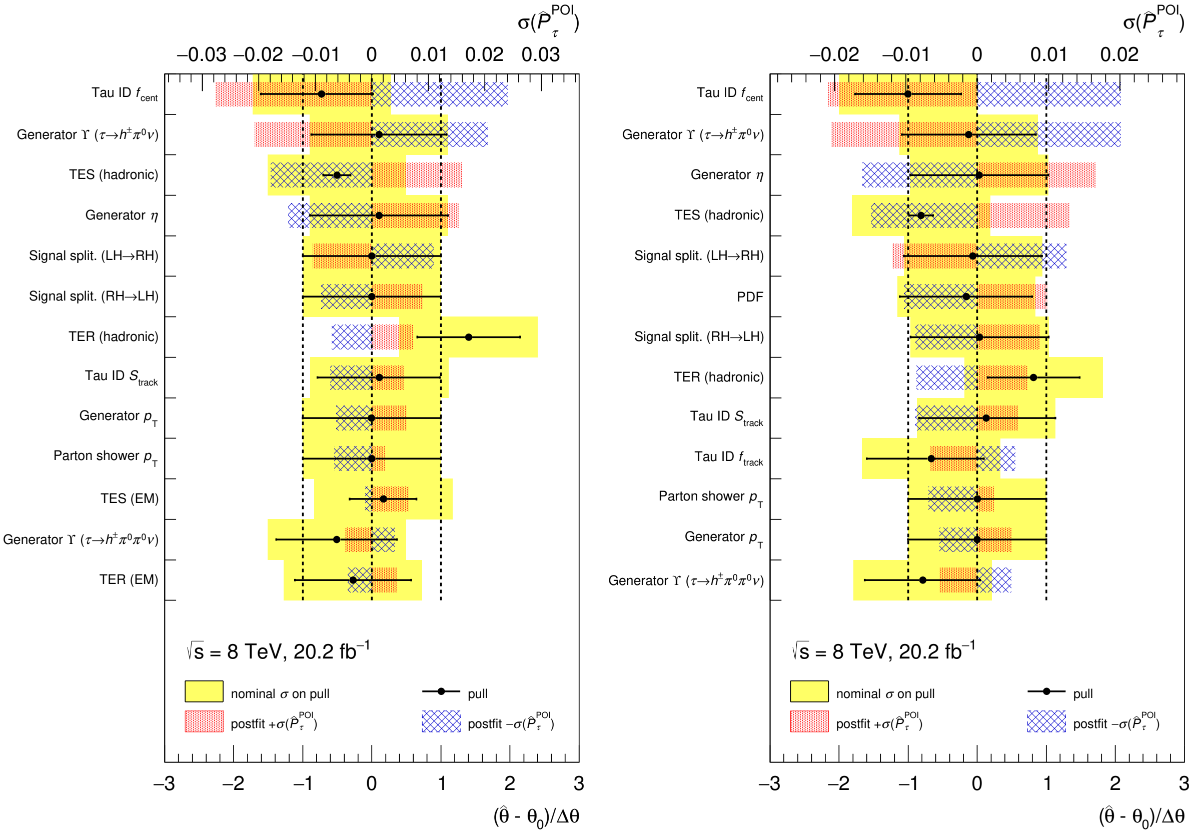

Figure 6.56: Values of Gaussian-constrained nuisance parameters and their uncertainties as well as their impact on the P_τ uncertainty in the fits to data. They are shown for the fits that extract P_τ in the mass-selected region for the τ_e–τ_{had} (left) and τ_μ–τ_{had} (right) channels. The black markers show the post-fit nuisance parameter values and uncertainties (use bottom axis). The yellow areas indicate the range covered by the post-fit nuisance parameter values with pre-fit uncertainties (use bottom axis). The red (+1) and blue (−1) areas indicate the impact of varying the nuisance parameter value by one post-fit standard deviation on the fitted polarisation value (use top axis). The nuisance parameters shown cover 99% of the P_τ uncertainty in Gaussian constrained nuisance parameters.

The pulled nuisance parameters represent uncertainties that are specific to this analysis. In particular, the partially significant pulls do not imply discrepancies with other measurements. Nevertheless, the large TER (hadronic) pulls require special attention. Because the TER was not measured previously, the assumed TER central values are taken on from the simulation and the pre-fit uncertainties are chosen ad-hoc. The values and uncertainties are to be determined in the fit. The TER (hadronic) parameter is pulled significantly, so its post-fit values may be affected significantly by the inserted pre-fit value and uncertainty.

Additional fits are performed in which the pre-fit values are altered (see Table 6.25). The results suggest that the hadronic component of the TER is underestimated by 6–7% in the simulation. The TER (hadronic) pull in the nominal fit corresponds to a smaller variation of the resolution. The possible effect on the measured tau polarisation is ~0.01. It is covered by the quoted TES and TER uncertainties and much smaller than the overall systematic uncertainties, which is judged adequate.[6] The large

---

[6] Calculating the template variations related to uncertainties other than those in the TES and TER for an assumed tau energy resolution other than that in the simulation would only be possible in a dedicated data reprocessing. In the test with an

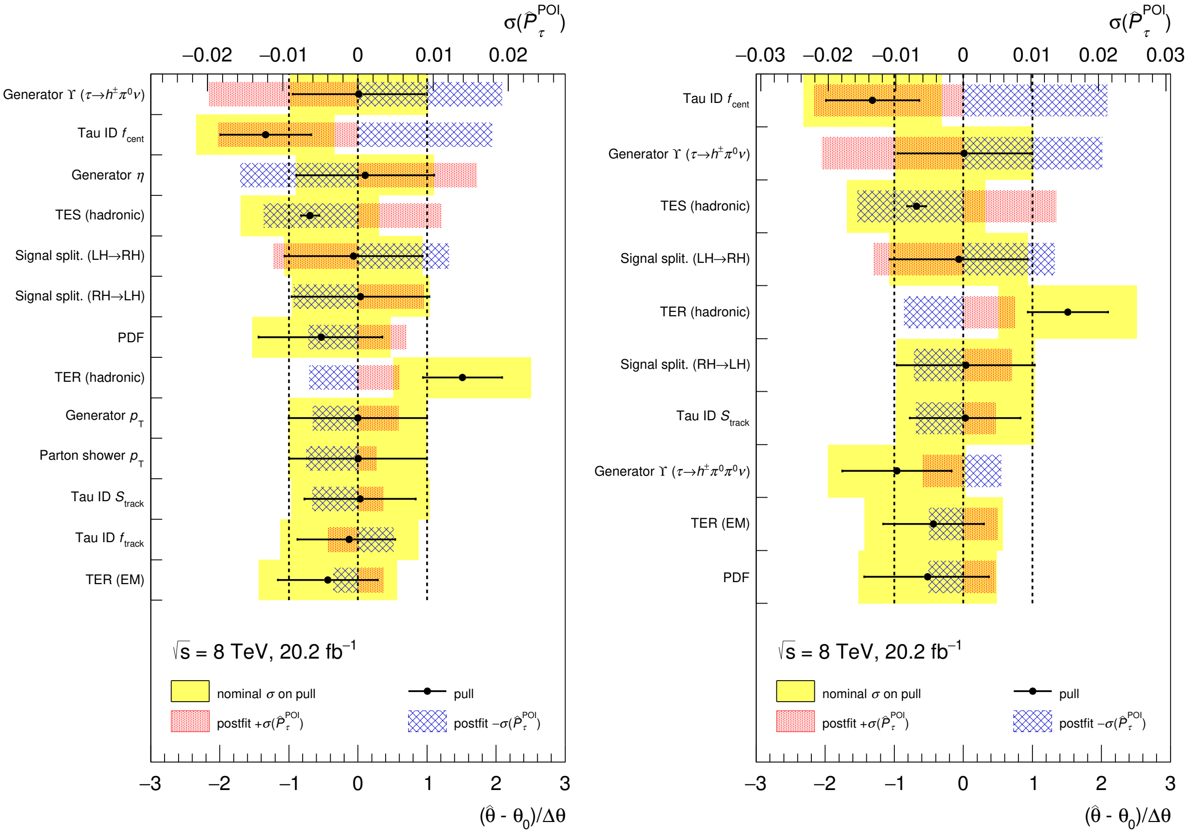

Figure 6.57: Values of Gaussian-constrained nuisance parameters and their uncertainties as well as their impact on the P_τ uncertainty in the fits to data. They are shown for the combined fits that extract P_τ in the mass-selected (left) and fiducial (right) regions. The black markers show the post-fit nuisance parameter values and uncertainties (use bottom axis). The yellow areas indicate the range covered by the post-fit nuisance parameter values with pre-fit uncertainties (use bottom axis). The red (+1) and blue (−1) areas indicate the impact of varying the nuisance parameter value by one post-fit standard deviation on the fitted polarisation value (use top axis). The nuisance parameters shown cover 99% of the P_τ uncertainty in Gaussian constrained nuisance parameters. Adapted from [25].

Pre-fit variation of resolution [%]	TER (hadronic) post-fit value	Post-fit variation of resolution [%]	P_τ^{POI} post-fit value
0.0 ± 2.5	1.5 ± 0.6	3.8 ± 1.5	-0.141 ± 0.044
0.0 ± 3.5	1.7 ± 0.4	6.0 ± 1.4	-0.130 ± 0.042
0.0 ± 6.0	1.24 ± 0.25	7.4 ± 1.5	-0.128 ± 0.044
0.0 ± 10.0	0.58 ± 0.12	5.8 ± 1.2	-0.134 ± 0.042
6.0 ± 2.5	0.15 ± 0.31	6.4 ± 0.8	-0.137 ± 0.047

Table 6.25: Results of fits with different assumptions about the hadronic TER component. The nominal combined fit that extracts the tau polarisation in the mass-selected region is documented in the first row. In the following four fits the pre-fit uncertainty is increased. The varied templates are obtained as usual except that the width, σ_s, of the Gaussian distribution from which the s values in Eq. (6.5.1) are drawn is altered. In the last fit an increased resolution is assumed. The post-fit value of the TER (hadronic) parameter, the corresponding post-fit variation of the resolution, and the measured tau polarisation are documented. The uncertainties in the post-fit parameter values are taken from the minos algorithm [92].

TER (hadronic) values reduce the discrepancies around $\Upsilon = 1$ and above, which are present before the fit (see Figure 6.27).

The impact of the various categories of uncertainties on the measurement is computed as in the fits to Asimov data and shown in Table 6.26. The TES and TER uncertainties are about 50% larger than in the fits to Asimov data, the remaining uncertainties are similar. The uncertainties for the individual channels can be found in Tables E.3 and E.4.

The measurement presented in this chapter confirms the SM predictions for the tau polarisation in $Z/\gamma^* \to \tau\tau$ decays with ditau masses close to the Z boson mass, complementing previous high-precision measurements at LEP. It provides a solid foundation for measurements that may soon be performed at the LHC. These may, for example, probe the CP properties of the Higgs boson in $H \to \tau\tau$ decays or test the SM predictions for the tau polarisation in $\tau\nu$ or $\tau\tau$ final-states with difermion masses much larger than the W and Z boson pole masses, respectively.

---

assumed pre-fit variation of 6% the template variations are approximated as in Eq. (6.8).

Source of uncertainty	σ_{P_τ} in mass-selected region	σ_{P_τ} in fiducial region
Modelling of signal process	0.026	0.022
τ_{had} identification	0.020	0.024
MC statistical	0.016	0.019
Signal sample splitting	0.015	0.015
TES and TER	0.015	0.019
Multijet estimate	0.013	0.013
PDF	0.007	0.005
W+jets shape	0.002	0.003
Other	0.008	0.003
Total systematic uncertainty	0.040	0.039
Statistical uncertainty	0.015	0.016

Table 6.26: Impact of the individual sources of uncertainty on the polarisation uncertainty σ_{P_τ} for the combined fits that extract the tau polarisation in the mass-selected and fiducial regions. Taken from [25].

CHAPTER 7

Conclusions

A measurement of the tau polarisation in $Z/\gamma^* \rightarrow \tau\tau$ decays in proton–proton collisions at ATLAS has been presented in addition to an extended reconstruction of hadronic tau decays that facilitates the determination of the decay topology and the four-momenta of the hadrons from these decays, which was developed as part of this thesis.

The extended reconstruction of hadronic tau decays determines the number and four-momenta of the charged hadrons from the tau decay using charged-particle tracks in the inner detector. The energy deposited by the charged hadrons is removed from the electromagnetic calorimeter, and the remaining energy deposits are considered neutral-pion candidates. Signal candidates are distinguished from backgrounds using multivariate techniques that identify energy deposits with shapes characteristic for electromagnetic showers. Subsequently, the information about the reconstructed charged hadrons and neutral-pion candidates is combined using multivariate techniques to determine the decay topology. A five-way classification is performed, and the decay topology is identified correctly for 75% of the reconstructed single- and three-prong decays without neutral kaons in a $Z/\gamma^* \rightarrow \tau\tau$ sample. The visible tau four-momentum is reconstructed using particle-flow techniques that combine information about charged-particle tracks from the inner detector with energy measurements, in particular of neutral pions, from the calorimeter system. The resolution of the visible energy is improved by up to a factor of two, and the directional resolution is improved by up to a factor of five with respect to the previous reconstruction. The quoted largest improvements apply to decays with small visible transverse momenta. The performance of the new method in data is described well by the simulation.

The measurement of the tau polarisation in $Z/\gamma^* \rightarrow \tau\tau$ decays utilises the ATLAS dataset recorded at a centre-of-mass energy of $\sqrt{s} = 8\,\text{TeV}$ with an integrated luminosity of $20.2\,\text{fb}^{-1}$. A signal region enhanced with signal events that contain one leptonic tau decay and one hadronic tau decay with a single charged particle in the final state is selected. The hadronic decays serve as spin analysers. The estimates of the major W+jets and multijet backgrounds are data-driven. The signal and the minor $Z/\gamma^* \rightarrow \ell\ell$ and top pair backgrounds are taken from the simulation. The largest systematic uncertainties are related to the modelling of the identification of hadronic tau decays, which is based on multivariate techniques, and that of the signal process on generator level. The uncertainties in the identification are estimated from the differences between the distributions of the identification input variables in data and simulated events. For the uncertainties in the modelling of the signal process, predictions from different event generators are compared. The tau polarisation is determined using an extended binned maximum-likelihood fit. A tau polarisation of $P_\tau = -0.27 \pm 0.02\,\text{(stat)} \pm 0.04\,\text{(syst)}$ is measured in a fiducial region, which is selected using generator-level quantities and resembles the signal region. An extrapolation to the full phase space within the mass-selected region of $66\,\text{GeV} < m_{Z/\gamma^*} < 116\,\text{GeV}$ is performed. The result is $P_\tau = -0.14 \pm 0.02$ (stat) $\pm\, 0.04$ (syst). The Standard Model predictions are $P_\tau = -0.270 \pm 0.006$ for the fiducial region and $P_\tau = -0.1536 \pm 0.0014$ for the mass-selected region, and confirmed by the measurement. The measured tau polarisation corresponds to a weak mixing angle of about $\sin^2\theta_{\mathrm{W}}^{\mathrm{eff}} = 0.232 \pm 0.005$. Here, the photon contribution and its interference with the Z boson contribution are neglected. Previous high-precision measurements at the Large Electron–Positron Collider (LEP) are complemented by this measurement. The only previous tau polarisation measurement at a hadron collider was performed in $W \to \tau\nu$ + jets decays by ATLAS using a much smaller dataset.

As an outlook, several further exciting tau polarisation measurements are or will soon be possible at the LHC. They may for example allow for studies of the CP quantum numbers of the Higgs boson in $H \to \tau\tau$ decays or the tau polarisation in ditau or tau–neutrino production processes at high masses. These measurements can benefit from the analysis techniques developed for the measurement in $Z/\gamma^* \to \tau\tau$ decays, and their sensitivity is expected to be boosted by the more detailed and accurate reconstruction of hadronic tau decays. More generally, analyses performed in final states with hadronic tau decays have benefitted from the improved reconstruction of the visible four-momentum for these decays.

Bibliography

[1] ATLAS Collaboration, *Observation of a new particle in the search for the Standard Model Higgs boson with the ATLAS detector at the LHC*, Phys. Lett. B **716** (2012) 1, arXiv: `1207.7214 [hep-ex]`.

[2] CMS Collaboration, *Observation of a new boson at a mass of 125 GeV with the CMS experiment at the LHC*, Phys. Lett. B **716** (2012) 30, arXiv: `1207.7235 [hep-ex]`.

[3] ATLAS and CMS Collaborations, *Measurements of the Higgs boson production and decay rates and constraints on its couplings from a combined ATLAS and CMS analysis of the LHC pp collision data at* $\sqrt{s} = 7$ *and* 8 *TeV*, JHEP **08** (2016) 045, arXiv: `1606.02266 [hep-ex]`.

[4] ATLAS Collaboration, *Cross-section measurements of the Higgs boson decaying to a pair of tau leptons in proton–proton collisions at* $\sqrt{s} = 13$ *TeV with the ATLAS Detector*, ATLAS-CONF-2018-021, 2018, URL: `https://cds.cern.ch/record/2621794`.

[5] CMS Collaboration, *Observation of the Higgs boson decay to a pair of* τ *leptons*, Phys. Lett. B **779** (2018) 283, arXiv: `1708.00373 [hep-ex]`.

[6] S. Berge, W. Bernreuther and S. Kirchner, *Prospects of constraining the Higgs boson's CP nature in the tau decay channel at the LHC*, Phys. Rev. D **92** (2015) 096012, arXiv: `1510.03850 [hep-ph]`.

[7] ATLAS Collaboration, *Searches for Higgs boson pair production in the* $hh \to bb\tau\tau, \gamma\gamma WW^*, \gamma\gamma bb, bbbb$ *channels with the ATLAS detector*, Phys. Rev. D **92** (2015) 092004, arXiv: `1509.04670 [hep-ex]`.

[8] ATLAS Collaboration, *A search for resonant and non-resonant Higgs boson pair production in the* $b\bar{b}\tau^+\tau^-$ *decay channel in pp collisions at* $\sqrt{s} = 13$ *TeV with the ATLAS detector*, submitted to Phys. Rev. Lett. (2018), arXiv: `1808.00336 [hep-ex]`.

[9] ATLAS Collaboration, *Search for additional heavy neutral Higgs and gauge bosons in the ditau final state produced in* 36 *fb*$^{-1}$ *of pp collisions at* $\sqrt{s} = 13$ *TeV with the ATLAS detector*, JHEP **01** (2018) 055, arXiv: `1709.07242 [hep-ex]`.

[10] ATLAS Collaboration, *Search for charged Higgs bosons decaying via* $H^\pm \to \tau^\pm\nu_\tau$ *in the* τ*+jets and* τ*+lepton final states with* 36 *fb*$^{-1}$ *of pp collision data recorded at* $\sqrt{s} = 13$ *TeV with the ATLAS experiment*, JHEP **09** (2018) 139, arXiv: `1807.07915 [hep-ex]`.

[11] ATLAS Collaboration, *Search for High-Mass Resonances Decaying to* $\tau\nu$ *in pp Collisions at* $\sqrt{s} = 13$ *TeV with the ATLAS detector*, Phys. Rev. Lett. **120** (2018) 161802, arXiv: `1801.06992 [hep-ex]`.

[12] ATLAS Collaboration, *Summary of the ATLAS experiment's sensitivity to supersymmetry after LHC Run 1 — interpreted in the phenomenological MSSM*, JHEP **10** (2015) 134, arXiv: `1508.06608 [hep-ex]`.

[13] ATLAS Collaboration, *Search for the electroweak production of supersymmetric particles in $\sqrt{s} = 8$ TeV pp collisions with the ATLAS detector*, Phys. Rev. D **93** (2016) 052002, arXiv: `1509.07152 [hep-ex]`.

[14] ATLAS Collaboration, *Search for squarks and gluinos in final states with hadronically decaying τ-leptons, jets, and missing transverse momentum using pp collisions at $\sqrt{s} = 13$ TeV with the ATLAS detector*, submitted to Phys. Rev. D (2018), arXiv: `1808.06358 [hep-ex]`.

[15] ATLAS Collaboration, *Dark matter interpretations of ATLAS searches for the electroweak production of supersymmetric particles in $\sqrt{s} = 8$ TeV proton–proton collisions*, JHEP **09** (2016) 175, arXiv: `1608.00872 [hep-ex]`.

[16] ATLAS Collaboration, *Search for the direct production of charginos and neutralinos in final states with tau leptons in $\sqrt{s} = 13$ TeV pp collisions with the ATLAS detector*, Eur. Phys. J. C **78** (2018) 154, arXiv: `1708.07875 [hep-ex]`.

[17] ATLAS Collaboration, *Search for top squarks decaying to tau sleptons in pp collisions at $\sqrt{s} = 13$ TeV with the ATLAS detector*, Phys. Rev. D **98** (2018) 032008, arXiv: `1803.10178 [hep-ex]`.

[18] ATLAS Collaboration, *Search for supersymmetry in events with four or more leptons in $\sqrt{s} = 13$ TeV pp collisions with ATLAS*, Phys. Rev. D **98** (2018) 032009, arXiv: `1804.03602 [hep-ex]`.

[19] ATLAS Collaboration, *Search for third generation scalar leptoquarks in pp collisions at $\sqrt{s} = 7$ TeV with the ATLAS detector*, JHEP **06** (2013) 033, arXiv: `1303.0526 [hep-ex]`.

[20] ATLAS Collaboration, *Search for lepton-flavour-violating decays of the Higgs and Z bosons with the ATLAS detector*, Eur. Phys. J. C **77** (2017) 70, arXiv: `1604.07730 [hep-ex]`.

[21] ATLAS Collaboration, *Search for lepton-flavor violation in different-flavor, high-mass final states in pp collisions at $\sqrt{s} = 13$ TeV with the ATLAS detector*, submitted to Phys. Rev. D (2018), arXiv: `1807.06573 [hep-ex]`.

[22] ATLAS Collaboration, *A search for lepton-flavor-violating decays of the Z boson into a τ-lepton and a light lepton with the ATLAS detector*, submitted to Phys. Rev. D (2018), arXiv: `1804.09568 [hep-ex]`.

[23] The ALEPH Collaboration, The DELPHI Collaboration, The L3 Collaboration, The OPAL Collaboration, The SLD Collaboration, The LEP Electroweak Working Group, The SLD Electroweak and Heavy Flavour Groups, *Precision electroweak measurements on the Z resonance*, Phys. Rept. **427** (2006) 257, arXiv: `hep-ex/0509008`.

[24] ATLAS Collaboration, *Measurement of τ polarization in $W \to \tau\nu$ decays with the ATLAS detector in pp collisions at $\sqrt{s} = 7$ TeV*, Eur. Phys. J. C **72** (2012) 2062, arXiv: `1204.6720 [hep-ex]`.

[25] ATLAS Collaboration, *Measurement of τ polarisation in $Z/\gamma^{*} \rightarrow \tau\tau$ decays in proton–proton collisions at $\sqrt{s} = 8$ TeV with the ATLAS detector*, Eur. Phys. J. C **78** (2018) 163, arXiv: `1709.03490 [hep-ex]`.

[26] ATLAS Collaboration, *Reconstruction of hadronic decay products of tau leptons with the ATLAS experiment*, Eur. Phys. J. C **76** (2016) 295, arXiv: `1512.05955 [hep-ex]`.

[27] M. Tanabashi et al. (Particle Data Group), *Review of Particle Physics*, Phys. Rev. D **98** (2018) 030001.

[28] A. Djouadi, *The Anatomy of Electro-Weak Symmetry Breaking. Tome I: The Higgs boson in the Standard Model*, Phys. Rept. **457** (2008) 1, arXiv: `hep-ph/0503172 [hep-ph]`.

[29] W. N. Cottingham and D. A. Greenwood, *An Introduction to the Standard Model of Particle Physics*, Cambridge University Press, 2007, ISBN: 9780521852494.

[30] F. Halzen and A. D. Martin, *Quarks & Leptons: An Introductory Course in Modern Particle Physics*, Wiley, 1984, ISBN: 0471887412.

[31] R. Tenchini and C. Verzegnassi, *The Physics of the Z and W Bosons*, World Scientific, 2008, ISBN: 9789812707024.

[32] M. Thomson, *Modern Particle Physics*, Cambridge University Press, 2013, ISBN: 9781107034266.

[33] Y. Fukuda et al., *Evidence for oscillation of atmospheric neutrinos*, Phys. Rev. Lett. **81** (1998) 1562, arXiv: `hep-ex/9807003 [hep-ex]`.

[34] Q. R. Ahmad et al., *Direct evidence for neutrino flavor transformation from neutral current interactions in the Sudbury Neutrino Observatory*, Phys. Rev. Lett. **89** (2002) 011301, arXiv: `nucl-ex/0204008 [nucl-ex]`.

[35] ATLAS Collaboration, *Search for heavy lepton resonances decaying to a Z boson and a lepton in pp collisions at $\sqrt{s} = 8$ TeV with the ATLAS detector*, JHEP **09** (2015) 108, arXiv: `1506.01291 [hep-ex]`.

[36] N. Aghanim et al., *Planck 2018 results. VI. Cosmological parameters*, submitted to Astron. Astrophys. (2018), arXiv: `1807.06209 [astro-ph.CO]`.

[37] J. Rojo et al., *The PDF4LHC report on PDFs and LHC data: Results from Run I and preparation for Run II*, J. Phys. G **42** (2015) 103103, arXiv: `1507.00556 [hep-ph]`.

[38] ATLAS Collaboration, *Measurement of the total cross section from elastic scattering in pp collisions at $\sqrt{s} = 8$ TeV with the ATLAS detector*, Phys. Lett. B **761** (2016) 158, arXiv: `1607.06605 [hep-ex]`.

[39] ATLAS Collaboration, *Summary plots from the ATLAS Standard Model physics group*, 2018, URL: `https://atlas.web.cern.ch/Atlas/GROUPS/PHYSICS/CombinedSummaryPlots/SM` (visited on 13/10/2018).

[40] M. L. Perl et al., *Evidence for Anomalous Lepton Production in $e^{+} - e^{-}$ Annihilation*, Phys. Rev. Lett. **35** (1975) 1489.

[41] ATLAS Collaboration, *Observation of Higgs boson production in association with a top quark pair at the LHC with the ATLAS detector*, Phys. Lett. B **784** (2018) 173, arXiv: `1806.00425 [hep-ex]`.

[42] CMS Collaboration, *Observation of $t\bar{t}H$ Production*, Phys. Rev. Lett. **120** (2018) 231801, arXiv: `1804.02610 [hep-ex]`.

[43] B. K. Bullock, K. Hagiwara and A. D. Martin, *Tau polarization and its correlations as a probe of new physics*, Nucl. Phys. B **395** (1993) 499.

[44] A. Stahl, *Physics With Tau Leptons*, Springer-Verlag, 2000, ISBN: 3540662677.

[45] CERN, *Member states*, 2012, URL: `https://cds.cern.ch/record/1997223`.

[46] T. Massam et al., *Experimental observation of antideuteron production*, Nuov Cim A **63** (1965) 10.

[47] D. E. Dorfan et al., *Observation of Antideuterons*, Phys. Rev. Lett. **14** (1965) 1003.

[48] G. Charpak et al., *The use of multiwire proportional counters to select and localize charged particles*, Nucl. Instrum. Meth. **62** (1968) 262.

[49] F. Hasert et al., *Search for elastic muon-neutrino electron scattering*, Phys. Lett. B **46** (1973) 121.

[50] F. Hasert et al., *Observation of neutrino-like interactions without muon or electron in the gargamelle neutrino experiment*, Phys. Lett. B **46** (1973) 138.

[51] D. Möhl, G. Petrucci, L. Thorndahl, and S. van der Meer, *Physics and technique of stochastic cooling*, Physics Reports **58** (1980) 73.

[52] UA1 Collaboration, G. Arnison et al., *Experimental observation of isolated large transverse energy electrons with associated missing energy at $s = 540$ GeV*, Phys. Lett. B **122** (1983) 103.

[53] UA2 Collaboration, M. Banner et al., *Observation of single isolated electrons of high transverse momentum in events with missing transverse energy at the CERN pp collider*, Phys. Lett. B **122** (1983) 476.

[54] UA1 Collaboration, G. Arnison et al., *Experimental observation of lepton pairs of invariant mass around 95 GeV/c^2 at the CERN SPS collider*, Phys. Lett. B **126** (1983) 398.

[55] UA2 Collaboration, P. Bagnaia et al., *Evidence for $Z^0 \to e^+e^-$ at the CERN pp collider*, Phys. Lett. B **129** (1983) 130.

[56] G. Baur et al., *Production of antihydrogen*, Phys. Lett. B **368** (1996) 251.

[57] CERN, *The birth of the web*, 2013, URL: `https://cds.cern.ch/record/1998446`.

[58] CERN, *The accelerator complex*, 2012, URL: `https://cds.cern.ch/record/1997193`.

[59] Wikimedia Commons, users: Forthommel and Dukwon, *Map of the CERN accelerator complex*, 2016, URL: `https://commons.wikimedia.org/wiki/File:Cern-accelerator-complex.svg` (visited on 13/10/2018).

[60] L. Evans and P. Bryant, *LHC Machine*, JINST **3** (2008) S08001.

[61] ATLAS Collaboration, *The ATLAS Experiment at the CERN Large Hadron Collider*, JINST **3** (2008) S08003.

[62] CMS Collaboration, *The CMS experiment at the CERN LHC*, JINST **3** (2008) S08004.

[63] A. A. Alves, Jr. et al. (LHCb Collaboration), *The LHCb Detector at the LHC*, JINST **3** (2008) S08005.

[64] K. Aamodt et al. (ALICE Collaboration), *The ALICE experiment at the CERN LHC*, JINST **3** (2008) S08002.

[65] G. Anelli et al. (TOTEM Collaboration), *The TOTEM Experiment at the CERN Large Hadron Collider*, JINST **3** (2008) S08007.

[66] O. Adriani et al. (LHCf Collaboration), *The LHCf detector at the CERN Large Hadron Collider*, JINST **3** (2008) S08006.

[67] J. Pinfold et al. (MoEDAL Collaboration), *Technical Design Report of the MoEDAL Experiment*, tech. rep. CERN-LHCC-2009-006, 2009, URL: `https://cds.cern.ch/record/1181486`.

[68] ATLAS Collaboration, *LuminosityPublicResults*, 2018, URL: `https://twiki.cern.ch/twiki/bin/view/AtlasPublic/LuminosityPublicResults` (visited on 22/03/2018).

[69] ATLAS Collaboration, *LuminosityPublicResultsRun2*, 2018, URL: `https://twiki.cern.ch/twiki/bin/view/AtlasPublic/LuminosityPublicResultsRun2` (visited on 22/03/2018).

[70] R. Steerenberg and I. Raynova, *LHC Report: An eventful and successful 2017*, 2017, URL: `https://cds.cern.ch/record/2299299`.

[71] ATLAS Collaboration, *Alignment of the ATLAS Inner Detector and its Performance in 2012*, ATLAS-CONF-2014-047, 2014, URL: `https://cds.cern.ch/record/1741021`.

[72] ATLAS Collaboration, *Topological cell clustering in the ATLAS calorimeters and its performance in LHC Run 1*, Eur. Phys. J. C **77** (2017) 490, arXiv: `1603.02934 [hep-ex]`.

[73] ATLAS Collaboration, *Measurement of the muon reconstruction performance of the ATLAS detector using 2011 and 2012 LHC proton–proton collision data*, Eur. Phys. J. C **74** (2014) 3130, arXiv: `1407.3935 [hep-ex]`.

[74] ATLAS Collaboration, *Performance of the ATLAS Trigger System in 2010*, Eur. Phys. J. C **72** (2012) 1849, arXiv: `1110.1530 [hep-ex]`.

[75] ATLAS Collaboration, *ATLAS Insertable B-Layer Technical Design Report Addendum*, tech. rep. CERN-LHCC-2012-009. ATLAS-TDR-19-ADD-1, Addendum to CERN-LHCC-2010-013, ATLAS-TDR-019, 2012, URL: `https://cds.cern.ch/record/1451888`.

[76] ATLAS Collaboration, *Performance of the ATLAS trigger system in 2015*, Eur. Phys. J. C **77** (2017) 317, arXiv: `1611.09661 [hep-ex]`.

[77] ATLAS Collaboration, *Performance of the ATLAS Inner Detector Track and Vertex Reconstruction in High Pile-Up LHC Environment*, ATLAS-CONF-2012-042, 2012, URL: `https://cds.cern.ch/record/1435196`.

[78] M. Cacciari, G. P. Salam and G. Soyez, *The anti-k_t jet clustering algorithm*, JHEP **04** (2008) 063, arXiv: `0802.1189 [hep-ph]`.

[79] M. Cacciari, G. P. Salam and G. Soyez, *FastJet User Manual*, Eur. Phys. J. C **72** (2012) 1896, arXiv: `1111.6097 [hep-ph]`.

[80] ATLAS Collaboration, *Jet energy measurement and its systematic uncertainty in proton–proton collisions at $\sqrt{s} = 7$ TeV with the ATLAS detector*, Eur. Phys. J. C **75** (2015) 17, arXiv: `1406.0076 [hep-ex]`.

[81] ATLAS Collaboration, *Electron efficiency measurements with the ATLAS detector using 2012 LHC proton–proton collision data*, Eur. Phys. J. C **77** (2017) 195, arXiv: `1612.01456 [hep-ex]`.

[82] ATLAS Collaboration, *Identification and energy calibration of hadronically decaying tau leptons with the ATLAS experiment in pp collisions at $\sqrt{s} = 8$ TeV*, Eur. Phys. J. C **75** (2015) 303, arXiv: `1412.7086 [hep-ex]`.

[83] N. Wermes, *Tau Decay*, 2014, URL: `https://twiki.cern.ch/twiki/bin/view/AtlasProtected/TauWG` (visited on 13/10/2018).

[84] M. Trottier-McDonald, *Evidence for the Standard Model Higgs Boson Decaying to One Semi-hadronically Decaying Tau and One Leptonically Decaying Tau at ATLAS*, CERN-THESIS-2014-055, PhD Thesis: Simon Fraser University, 2014, URL: `https://cds.cern.ch/record/1709068`.

[85] ATLAS Collaboration, *Performance of missing transverse momentum reconstruction in proton–proton collisions at $\sqrt{s} = 7$ TeV with ATLAS*, Eur. Phys. J. C **72** (2012) 1844, arXiv: `1108.5602 [hep-ex]`.

[86] ATLAS Collaboration, *Measurement of the photon identification efficiencies with the ATLAS detector using LHC Run-1 data*, Eur. Phys. J. C **76** (2016) 666, arXiv: `1606.01813 [hep-ex]`.

[87] A. Hoecker et al., *TMVA - Toolkit for Multivariate Data Analysis*, PoS **ACAT** (2007) 040, arXiv: `physics/0703039 [physics.data-an]`.

[88] C. Deutsch, *Identification and Classification of Hadronic Tau Lepton Decays in the ATLAS Experiment for Run 2 of the LHC*, Master Thesis: Universität Bonn, 2017.

[89] T. Hastie, R. Tibshirani and J. Friedman, *The Elements of Statistical Learning*, Springer Science+Business Media, 2009, ISBN: 9780387848587.

[90] K. Cranmer et al., *HistFactory: A tool for creating statistical models for use with RooFit and RooStats*, CERN-OPEN-2012-016, 2012, URL: `https://cds.cern.ch/record/1456844/`.

[91] W. Verkerke and D. P. Kirkby, *The RooFit toolkit for data modeling*, 2003, arXiv: `physics/0306116`.

[92] L. Moneta et al., *The RooStats Project*, PoS **ACAT** (2010) 057, arXiv: `1009.1003 [physics.data-an]`.

[93] R. Barlow and C. Beeston, *Fitting using finite Monte Carlo samples*, Comput. Phys. Commun. **77** (1993) 219.

[94] ATLAS Collaboration, *Measurement of the $t\bar{t}$ production cross section in the τ + jets final state in pp collisions at $\sqrt{s} = 8$ TeV using the ATLAS detector*, Phys. Rev. D **95** (2017) 072003, arXiv: `1702.08839 [hep-ex]`.

[95] ATLAS Collaboration, *Measurement of the top quark branching ratios into channels with leptons and quarks with the ATLAS detector*, Phys. Rev. D **92** (2015) 072005, arXiv: `1506.05074 [hep-ex]`.

[96] ATLAS Collaboration,
Measurement of the top quark pair cross section with ATLAS in pp collisions at $\sqrt{s} = 7$ *TeV using final states with an electron or a muon and a hadronically decaying* τ *lepton*,
Phys. Lett. B **717** (2012) 89, arXiv: `1205.2067 [hep-ex]`.

[97] ATLAS Collaboration, *Measurement of the* $W \rightarrow \tau\nu_\tau$ *cross section in pp collisions at* $\sqrt{s} = 7$ *TeV with the ATLAS experiment*, Phys. Lett. B **706** (2012) 276,
arXiv: `1108.4101 [hep-ex]`.

[98] ATLAS Collaboration, *Measurement of the* $Z \rightarrow \tau\tau$ *cross section with the ATLAS detector*,
Phys. Rev. D **84** (2011) 112006, arXiv: `1108.2016 [hep-ex]`.

[99] ATLAS Collaboration,
Evidence for the Higgs-boson Yukawa coupling to tau leptons with the ATLAS detector,
JHEP **04** (2015) 117, arXiv: `1501.04943 [hep-ex]`.

[100] ATLAS Collaboration,
Search for the standard model Higgs boson produced in association with a vector boson and decaying into a tau pair in pp collisions at $\sqrt{s} = 8$ *TeV with the ATLAS detector*,
Phys. Rev. D **93** (2016) 092005, arXiv: `1511.08352 [hep-ex]`.

[101] ATLAS Collaboration, *Test of CP Invariance in vector-boson fusion production of the Higgs boson using the Optimal Observable method in the ditau decay channel with the ATLAS detector*,
Eur. Phys. J. C **76** (2016) 658, arXiv: `1602.04516 [hep-ex]`.

[102] ATLAS Collaboration, *Search for charged Higgs bosons decaying via* $H^\pm \rightarrow \tau^\pm\nu$ *in fully hadronic final states using pp collision data at* $\sqrt{s} = 8$ *TeV with the ATLAS detector*,
JHEP **03** (2015) 088, arXiv: `1412.6663 [hep-ex]`.

[103] ATLAS Collaboration, *Search for neutral Higgs bosons of the minimal supersymmetric standard model in pp collisions at* $\sqrt{s} = 8$ *TeV with the ATLAS detector*, JHEP **11** (2014) 056,
arXiv: `1409.6064 [hep-ex]`.

[104] ATLAS Collaboration, *Search for charged Higgs bosons through the violation of lepton universality in* $t\bar{t}$ *events using pp collision data at* $\sqrt{s} = 7$ *TeV with the ATLAS experiment*,
JHEP **03** (2013) 076, arXiv: `1212.3572 [hep-ex]`.

[105] ATLAS Collaboration, *Search for direct top squark pair production in final states with two tau leptons in pp collisions at* $\sqrt{s} = 8$ *TeV with the ATLAS detector*, Eur. Phys. J. C **76** (2016) 81,
arXiv: `1509.04976 [hep-ex]`.

[106] ATLAS Collaboration,
Search for supersymmetry in events with large missing transverse momentum, jets, and at least one tau lepton in 20 fb^{-1} *of* $\sqrt{s} = 8$ *TeV proton–proton collision data with the ATLAS detector*,
JHEP **09** (2014) 103, arXiv: `1407.0603 [hep-ex]`.

[107] ATLAS Collaboration, *Search for the direct production of charginos, neutralinos and staus in final states with at least two hadronically decaying taus and missing transverse momentum in pp collisions at* $\sqrt{s} = 8$ *TeV with the ATLAS detector*, JHEP **10** (2014) 096,
arXiv: `1407.0350 [hep-ex]`.

[108] ATLAS Collaboration, *Search for a heavy narrow resonance decaying to* $e\mu$, $e\tau$, *or* $\mu\tau$ *with the ATLAS detector in* $\sqrt{s} = 7$ *TeV pp collisions at the LHC*, Phys. Lett. B **723** (2013) 15,
arXiv: `1212.1272 [hep-ex]`.

[109] ATLAS Collaboration, *A search for high-mass resonances decaying to $\tau^+\tau^-$ in pp collisions at $\sqrt{s} = 8$ TeV with the ATLAS detector*, JHEP **07** (2015) 157, arXiv: `1502.07177 [hep-ex]`.

[110] ATLAS Collaboration, *Search for new phenomena in events with three or more charged leptons in pp collisions at $\sqrt{s} = 8$ TeV with the ATLAS detector*, JHEP **08** (2015) 138, arXiv: `1411.2921 [hep-ex]`.

[111] ALEPH Collaboration, S. Schael et al., *Branching ratios and spectral functions of tau decays: Final ALEPH measurements and physics implications*, Phys. Rept. **421** (2005) 191, arXiv: `hep-ex/0506072 [hep-ex]`.

[112] OPAL Collaboration, R. Akers et al., *Measurement of the $\tau^- \to h^-\pi^0\nu_\tau$ and $\tau^- \to h^- \geq 2\pi^0\nu_\tau$ branching ratios*, Phys. Lett. B **328** (1994) 207.

[113] DELPHI Collaboration, J. Abdallah et al., *A Measurement of the tau hadronic branching ratios*, Eur. Phys. J. C **46** (2006) 1, arXiv: `hep-ex/0603044 [hep-ex]`.

[114] L3 Collaboration, M. Acciarri et al., *Measurement of tau polarization at LEP*, Phys. Lett. B **429** (1998) 387.

[115] A. Elagin et al., *Probabilistic Particle Flow Algorithm for High Occupancy Environment*, Nucl. Instrum. Meth. A **705** (2013) 93, arXiv: `1207.4780 [hep-ex]`.

[116] D0 Collaboration, V.M. Abazov et al., *Measurement of $\sigma(p\bar{p} \to Z + X)$ Br($Z \to \tau^+\tau^-$) at $\sqrt{s}$ = 1.96 TeV*, Phys. Lett. B **670** (2009) 292, arXiv: `0808.1306 [hep-ex]`.

[117] CMS Collaboration, *Reconstruction and identification of τ lepton decays to hadrons and ν_τ at CMS*, JINST **11** (2016) P01019, arXiv: `1510.07488 [hep-ex]`.

[118] T. Sjöstrand, S. Mrenna and P. Z. Skands, *A brief introduction to PYTHIA 8.1*, Comput. Phys. Commun. **178** (2008) 852, arXiv: `0710.3820 [hep-ph]`.

[119] B. Winter, *Reconstruction of neutral pions in hadronic tau lepton decays in the ATLAS detector*, BONN-IB-2013-04, Master Thesis: Universität Bonn, 2012, URL: `https://web.physik.uni-bonn.de/group/view.php?&group=2&lang=en&c=t&id=486`.

[120] S. Yuen, *Improving the Reconstruction of Neutral Pions in Tau Decays Using the Strip Layer of the ATLAS Electromagnetic Calorimeter*, Master Thesis: Universität Bonn, 2013.

[121] C. Limbach, *Development of a new reconstruction and classification method for Tau leptons and its application in the ATLAS detector at the LHC*, BONN-IR-2015-03, PhD Thesis: Universität Bonn, 2015, URL: `https://web.physik.uni-bonn.de/group/view.php?&group=1&lang=de&c=t&id=62`.

[122] S. Jadach, J. H. Kuhn and Z. Was, *TAUOLA: A Library of Monte Carlo programs to simulate decays of polarized tau leptons*, Comput. Phys. Commun. **64** (1990) 275.

[123] E. Barberio, B. van Eijk and Z. Was, *PHOTOS: A Universal Monte Carlo for QED radiative corrections in decays*, Comput. Phys. Commun. **66** (1991) 115.

[124] ATLAS Collaboration, *The ATLAS Simulation Infrastructure*, Eur. Phys. J. C **70** (2010) 823, arXiv: `1005.4568 [physics.ins-det]`.

[125] S. Agostinelli et al., *GEANT4 - a simulation toolkit*, Nucl. Instrum. Meth. A **506** (2003) 250.

[126] J. Pumplin et al.,
New generation of parton distributions with uncertainties from global QCD analysis,
JHEP **07** (2002) 012, arXiv: `hep-ph/0201195`.

[127] ATLAS Collaboration, *Summary of ATLAS Pythia 8 tunes*, ATL-PHYS-PUB-2012-003, 2012,
URL: `https://cds.cern.ch/record/1474107`.

[128] M. L. Mangano et al.,
ALPGEN, a generator for hard multiparton processes in hadronic collisions,
JHEP **07** (2003) 001, arXiv: `hep-ph/0206293`.

[129] P. Z. Skands, *Tuning Monte Carlo Generators: The Perugia tunes*,
Phys. Rev. D **82** (2010) 074018, arXiv: `1005.3457 [hep-ph]`.

[130] S. Frixione and B. R. Webber,
Matching NLO QCD computations and parton shower simulations, JHEP **0206** (2002) 29,
arXiv: `hep-ph/0204244`.

[131] S. Frixione et al., *Single-top production in MC@NLO*, JHEP **0603** (2006) 92,
arXiv: `hep-ph/0512250`.

[132] S. Frixione et al., *Single-top hadroproduction in association with a W boson*,
JHEP **0807** (2008) 29, arXiv: `0805.3067 [hep-ph]`.

[133] G. Corcella et al., *HERWIG 6: an event generator for hadron emission reactions with interfering gluons (including supersymmetric processes)*, JHEP **01** (2001) 010, arXiv: `hep-ph/0011363`.

[134] J. M. Butterworth, J. R. Forshaw and M. H. Seymour,
Multiparton interactions in photoproduction at HERA, Z. Phys. C **72** (1996) 637,
arXiv: `hep-ph/9601371`.

[135] H.-L. Lai et al., *New parton distributions for collider physics*, Phys.Rev. D **82** (2010) 074024,
arXiv: `1007.2241 [hep-ph]`.

[136] S. Yuen, *Analysis of the Higgs boson coupling and CP properties in the* $H \to \tau_{had}\tau_{had}$ *channel in collisions recorded at center-of-mass energies of* $\sqrt{s} = 13\,\text{TeV}$ *with the ATLAS detector*,
PhD Thesis in preparation, private communication: Universität Bonn, 2018.

[137] ATLAS Collaboration,
Reconstruction of hadronic decay products of tau leptons with the ATLAS experiment,
tech. rep. ATL-COM-PHYS-2015-245, 2015, URL: `https://cds.cern.ch/record/2007886`.

[138] ATLAS Collaboration, *Measurement of the tau lepton reconstruction and identification performance in the ATLAS experiment using pp collisions at* $\sqrt{s} = 13$ *TeV*,
ATLAS-CONF-2017-029, 2017, URL: `https://cds.cern.ch/record/2261772`.

[139] D. Duschinger, *Search for neutral bosons decaying into the fully hadronic di-tau final state with the ATLAS detector at the LHC*, PhD Thesis: Technische Universität Dresden, 2018.

[140] T. Sjöstrand, S. Mrenna and P. Z. Skands, *PYTHIA 6.4 physics and manual*, JHEP **05** (2006) 026,
arXiv: `hep-ph/0603175`.

[141] N. Davidson et al., *Universal interface of TAUOLA: Technical and physics documentation*,
Comput. Phys. Commun. **183** (2012) 821, arXiv: `1002.0543 [hep-ph]`.

[142] P. Nason, *A New method for combining NLO QCD with shower Monte Carlo algorithms*,
JHEP **11** (2004) 040, arXiv: `hep-ph/0409146`.

[143] S. Frixione, P. Nason and C. Oleari, *Matching NLO QCD computations with Parton Shower simulations: the POWHEG method*, JHEP **11** (2007) 070, arXiv: 0709.2092 [hep-ph].

[144] S. Alioli et al., *A general framework for implementing NLO calculations in shower Monte Carlo programs: the POWHEG BOX*, JHEP **06** (2010) 043, arXiv: 1002.2581 [hep-ph].

[145] ATLAS Collaboration, *New ATLAS event generator tunes to 2010 data*, ATL-PHYS-PUB-2011-008, 2011, URL: https://cds.cern.ch/record/1345343.

[146] Z. Czyczula, T. Przedzinski and Z. Was, *TauSpinner Program for Studies on Spin Effect in tau Production at the LHC*, Eur. Phys. J. C **72** (2012) 1988, arXiv: 1201.0117 [hep-ph].

[147] A. Sherstnev and R. S. Thorne, *Parton Distributions for LO Generators*, Eur. Phys. J. C **55** (2008) 553, arXiv: 0711.2473 [hep-ph].

[148] A. Kaczmarska et al., *Application of TauSpinner for Studies on tau-Lepton Polarization and Spin Correlations in Z, W and H Decays at the LHC*, Acta Phys. Polon. B **45** (2014) 1921, arXiv: 1402.2068 [hep-ph].

[149] J. Kalinowski et al., *Production of τ lepton pairs with high pT jets at the LHC and the TauSpinner reweighting algorithm*, Eur. Phys. J. C **76** (2016) 540, arXiv: 1604.00964 [hep-ph].

[150] CMS Collaboration, *A search for Higgs boson pair production in the $bb\tau\tau$ final state in proton–proton collisions at $\sqrt{(s)} = 8$ TeV*, Phys. Rev. D **96** (2017) 072004, arXiv: 1707.00350 [hep-ex].

[151] S. Catani et al., *Vector boson production at hadron colliders: a fully exclusive QCD calculation at NNLO*, Phys. Rev. Lett. **103** (2009) 082001, arXiv: 0903.2120 [hep-ph].

[152] ATLAS Collaboration, *Search for anomalous couplings in the Wtb vertex from the measurement of double differential angular decay rates of single top quarks produced in the t-channel with the ATLAS detector*, JHEP **04** (2016) 023, arXiv: 1510.03764 [hep-ex].

[153] CMS Collaboration, *Measurement of the Inclusive Z Cross Section via Decays to Tau Pairs in pp Collisions at $\sqrt{s} = 7$ TeV*, JHEP **08** (2011) 117, arXiv: 1104.1617 [hep-ex].

[154] CMS Collaboration, *Evidence for the* 125 *GeV Higgs boson decaying to a pair of τ leptons*, JHEP **05** (2014) 104, arXiv: 1401.5041 [hep-ex].

[155] J. Kraus, *$W \to \tau\nu_\tau$ Cross Section Measurement and Search for the Standard Model Higgs Boson in the $\tau_{lep}\tau_{had}$ Final State with the ATLAS Detector*, BONN-IR-2015-02, PhD Thesis: Universität Bonn, 2015, URL: https://web.physik.uni-bonn.de/group/view.php?&group=2&lang=en&c=t&id=561.

[156] CMS Collaboration, *Search for neutral MSSM Higgs bosons decaying to a pair of tau leptons in pp collisions*, JHEP **10** (2014) 160, arXiv: 1408.3316 [hep-ex].

[157] CMS Collaboration, *Search for heavy resonances decaying to tau lepton pairs in proton–proton collisions at $\sqrt{s} = 13$ TeV*, JHEP **02** (2017) 048, arXiv: 1611.06594 [hep-ex].

[158] A. Buckley et al., *LHAPDF6: parton density access in the LHC precision era*, Eur. Phys. J. C **75** (2015) 132, arXiv: `1412.7420 [hep-ph]`.

[159] R. D. Ball et al., *Parton distributions for the LHC Run II*, JHEP **04** (2015) 040, arXiv: `1410.8849 [hep-ph]`.

[160] L. A. Harland-Lang et al., *Parton distributions in the LHC era: MMHT 2014 PDFs*, Eur. Phys. J. **C75** (2015) 204, arXiv: `1412.3989 [hep-ph]`.

[161] S. Dulat et al., *New parton distribution functions from a global analysis of quantum chromodynamics*, Phys. Rev. **D93** (2016) 033006, arXiv: `1506.07443 [hep-ph]`.

[162] ATLAS Collaboration, *Measurement of the k_t splitting scales in $Z \to \ell\ell$ events in pp collisions at $\sqrt{s} = 8$ TeV with the ATLAS detector*, JHEP **08** (2017) 026, arXiv: `1704.01530 [hep-ex]`.

[163] ATLAS Collaboration, *Measurement of the Drell–Yan triple-differential cross section in pp collisions at $\sqrt{s} = 8$ TeV*, JHEP **12** (2017) 059, arXiv: `1710.05167 [hep-ex]`.

[164] ATLAS Collaboration, *Measurement of the effective leptonic weak mixing angle using electron and muon pairs from Z-boson decay in the ATLAS experiment at $\sqrt{s} = 8$ TeV*, ATLAS-CONF-2018-037, 2018, URL: `https://cds.cern.ch/record/2630340`.

[165] ATLAS Collaboration, *Measurements of the production cross section of a Z boson in association with jets in pp collisions at $\sqrt{s} = 13$ TeV with the ATLAS detector*, Eur. Phys. J. C **77** (2017) 361, arXiv: `1702.05725 [hep-ex]`.

[166] CMS Collaboration, *Measurement of differential cross sections in the kinematic angular variable ϕ^* for inclusive Z boson production in pp collisions at $\sqrt{s} = 8$ TeV*, JHEP **03** (2018) 172, arXiv: `1710.07955 [hep-ex]`.

[167] CMS Collaboration, *Measurement of the weak mixing angle using the forward-backward asymmetry of Drell–Yan events in pp collisions at* 8 *TeV*, Eur. Phys. J. C **78** (2018) 701, arXiv: `1806.00863 [hep-ex]`.

[168] CMS Collaboration, *Measurement of differential cross sections for Z boson production in association with jets in proton–proton collisions at $\sqrt{s} = 13$ TeV*, submitted to Eur. Phys. J. C (2018), arXiv: `1804.05252 [hep-ex]`.

[169] ATLAS Collaboration, *Measurement of the inclusive and fiducial $t\bar{t}$ production cross-sections in the lepton+jets channel in pp collisions at $\sqrt{s} = 8$ TeV with the ATLAS detector*, Eur. Phys. J. C **78** (2018) 487, arXiv: `1712.06857 [hep-ex]`.

[170] ATLAS Collaboration, *Measurements of differential cross sections of top quark pair production in association with jets in pp collisions at $\sqrt{s} = 13$ TeV using the ATLAS detector*, submitted to JHEP (2018), arXiv: `1802.06572 [hep-ex]`.

[171] CMS Collaboration, *Measurement of double-differential cross sections for top quark pair production in pp collisions at $\sqrt{s} = 8$ TeV and impact on parton distribution functions*, Eur. Phys. J. C **77** (2017) 459, arXiv: `1703.01630 [hep-ex]`.

[172] CMS Collaboration, *Measurements of differential cross sections of top quark pair production as a function of kinematic event variables in proton–proton collisions at $\sqrt{s} = 13$ TeV*, JHEP **06** (2018) 002, arXiv: `1803.03991 [hep-ex]`.

[173] CMS Collaboration, *Measurement of differential cross sections for the production of top quark pairs and of additional jets in lepton+jets events from pp collisions at* $\sqrt{s} = 13$ *TeV*, Phys. Rev. D **97** (2018) 112003, arXiv: `1803.08856 [hep-ex]`.

[174] L. Schildgen, *Measurement of the* τ *Lepton Polarisation in* $Z \rightarrow \tau_{lep}\tau_{had}$ *Decays with the ATLAS Detector*, Master Thesis: Universität Bonn, 2015, URL: `https://web.physik.uni-bonn.de/group/view.php?&group=1&lang=de&c=t&id=66`.

[175] ATLAS Collaboration, *Search for the Standard Model Higgs boson in the* $H \rightarrow \tau^+\tau^-$ *decay mode in* $\sqrt{s} = 7$ *TeV pp collisions with ATLAS*, JHEP **09** (2012) 070, arXiv: `1206.5971 [hep-ex]`.

[176] ATLAS Collaboration, *Search for anomalous production of prompt same-sign lepton pairs and pair-produced doubly charged Higgs bosons with* $\sqrt{s} = 8$ *TeV pp collisions using the ATLAS detector*, JHEP **03** (2015) 041, arXiv: `1412.0237 [hep-ex]`.

[177] ATLAS Collaboration, *Performance of b-jet identification in the ATLAS experiment*, JINST **11** (2016) P04008, arXiv: `1512.01094 [hep-ex]`.

[178] ATLAS Collaboration, *Luminosity determination in pp collisions at* $\sqrt{s} = 8$ *TeV using the ATLAS detector at the LHC*, Eur. Phys. J. C **76** (2016) 653, arXiv: `1608.03953 [hep-ex]`.

[179] J. Alwall et al., *The automated computation of tree-level and next-to-leading order differential cross sections, and their matching to parton shower simulations*, JHEP **07** (2014) 079, arXiv: `1405.0301 [hep-ph]`.

[180] ATLAS Collaboration, *Simultaneous measurements of the* $t\bar{t}$, W^+W^-, *and* $Z/\gamma^* \rightarrow \tau\tau$ *production cross-sections in pp collisions at* $\sqrt{s} = 7$ *TeV with the ATLAS detector*, Phys. Rev. D **91** (2015) 052005, arXiv: `1407.0573 [hep-ex]`.

[181] ATLAS Collaboration, $Z \rightarrow \tau\tau$ *cross section measurement in proton–proton collisions at* 7 *TeV with the ATLAS experiment*, ATLAS-CONF-2012-006, 2012, URL: `https://cds.cern.ch/record/1426991`.

APPENDIX A

Reconstruction of Visible Decay Products in τ_{had} Decays

A.1 Charged-Hadron Shower Subtraction Using Strip Layer Hits

If a charged hadron deposits a noticeable amount of energy in the strip layer, the energy deposit is local similar as for photons. Such energy deposits are identified by performing a geometric matching of strip layer hits (see Section 5.4) and charged-particle tracks. Energy in the seed cell and in the two neighbouring cells in η direction on each side (five cells in total) is removed.[1] Otherwise, no energy is subtracted in the strip layer. The difference of $E^{\pm}_{Ecal}$ and the energy found in a potential matched strip layer hit is subtracted in the Ecal2 layer. No energy is subtracted in the presampler, in which charged hadrons rarely deposit a noticeable amount of energy. This subtraction procedure adapts to the charged-hadron shower in the *Ecal*. The overall probability to find a hit matched to a given track is mostly dependent on the largest allowed $|\Delta\eta(\text{track, strip layer hit})|$ for a match. It is 20% (33%) if $|\Delta\eta| < 0.002$ ($|\Delta\eta| < 0.005$) is required in simulated $Z/\gamma^* \rightarrow \tau\tau$ decays. These values differ by less than one percent point between decays with and without neutral pions, which indicates that hits from charged hadrons are found frequently, and that few hits from neutral pions are removed accidentally. Nevertheless, the algorithm's performance is only marginally improved when using this subtraction procedure.

A.2 Specific Contributions in Development of TauPi0Rec Algorithm

Subsequent to my master thesis [119], the TauPi0Rec algorithm was developed by Stephanie Yuen [120, 136] and me. The extension to three-prong decays (Section 5.3.1) and the cell-level charged-hadron shower subtraction (Section 5.3.2) were developed by me. I initially conceived the cluster-level subtraction, which was created by Stephanie (see Section 5.3.3). The neutral-pion identification was improved both by Stephanie and me (Section 5.3.4). Stephanie designed the reconstruction of hits in the strip layer (Section 5.4) during her master thesis [120]. I helped supervising her at the time. The subtraction using strip layer hits (Appendix A.1) was created by Stephanie and me. I helped supervising Christopher Deutsch during his master thesis [88], from which some of the results in Section 5.7 are taken.

---

[1] If the hit was seeded by two neighbouring cells in ϕ direction, the energy in the seed cells and in their two neighbouring cells in η direction on each side is removed.

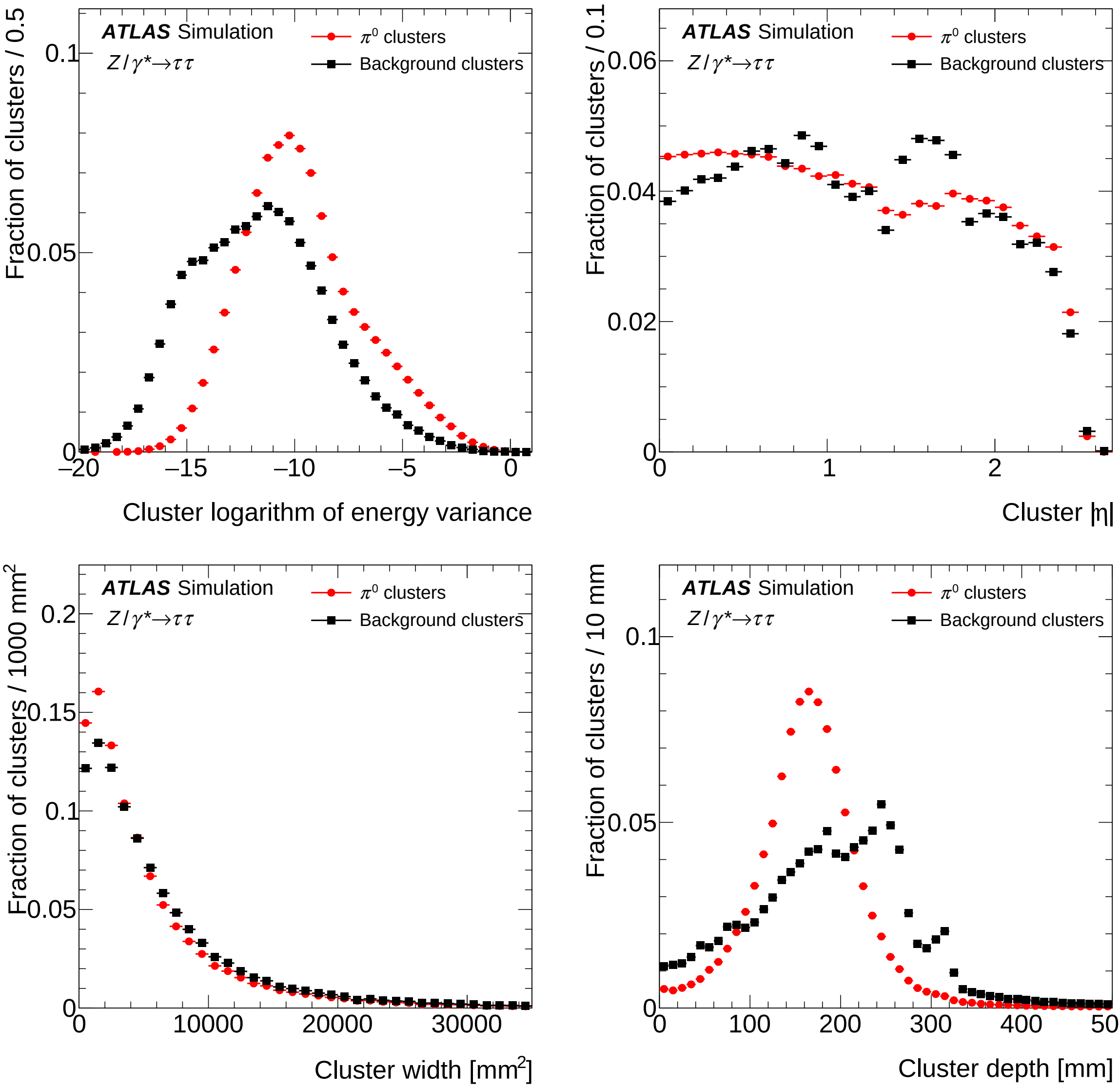

Figure A.1: Distributions of the $\log\langle\rho^2\rangle^{\text{clus}}$ (top left), $|\eta^{\text{clus}}|$ (top right), $\langle r^2\rangle^{\text{clus}}$ (bottom left), and $\lambda^{\text{clus}}_{\text{centre}}$ (bottom right) variables for tagged signal and background neutral-pions candidates. Taken from [26].

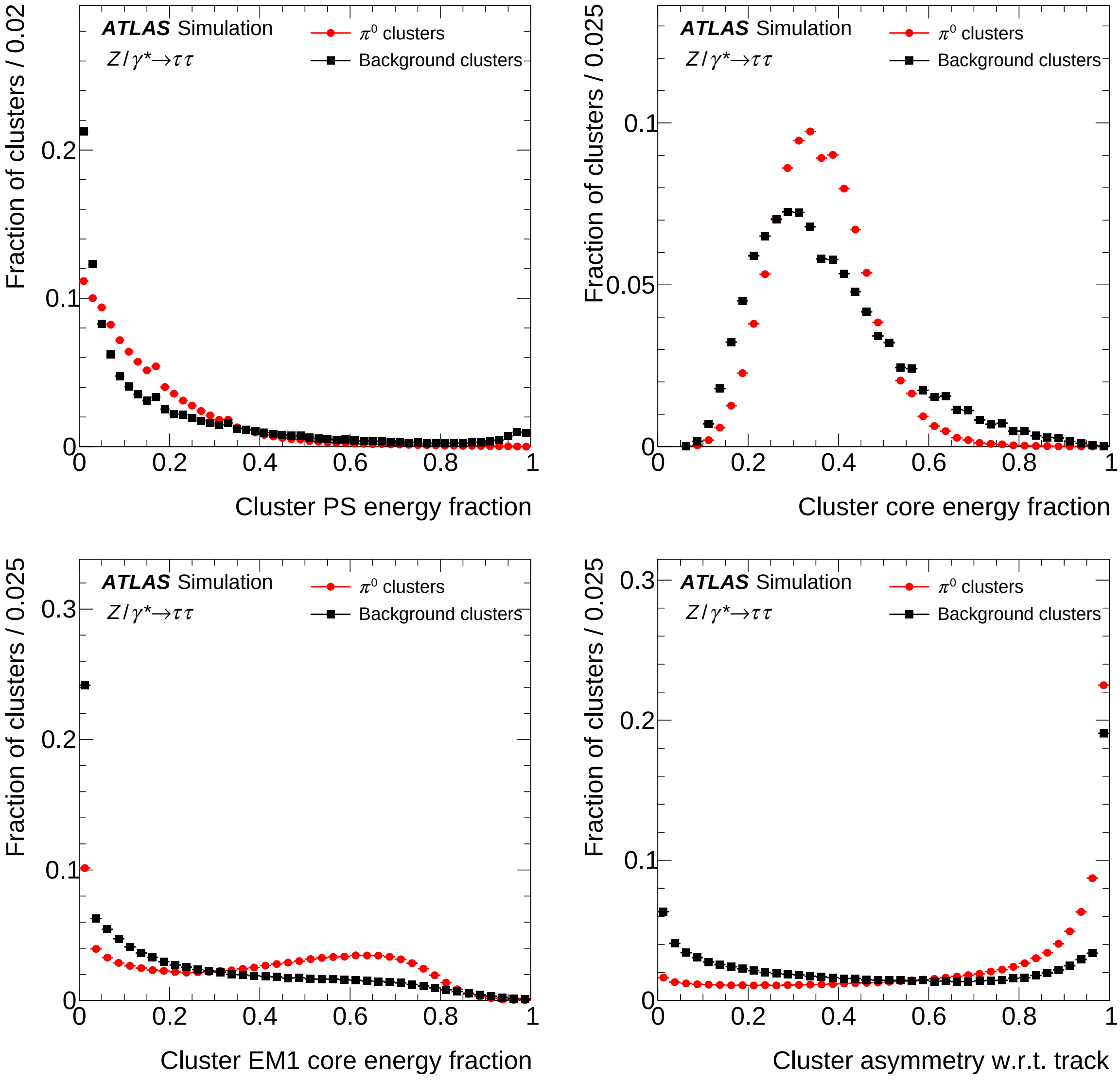

Figure A.2: Distributions of the $f_{\mathrm{PS}}^{\mathrm{clus}}$ (top left), $f_{\mathrm{core}}^{\mathrm{clus}}$ (top right), $f_{\mathrm{core,strip}}^{\mathrm{clus}}$ (bottom left), and $\mathcal{A}_{\mathrm{track}}^{\mathrm{clus}}$ (bottom right) variables for tagged signal and background neutral-pions candidates. Taken from [26].

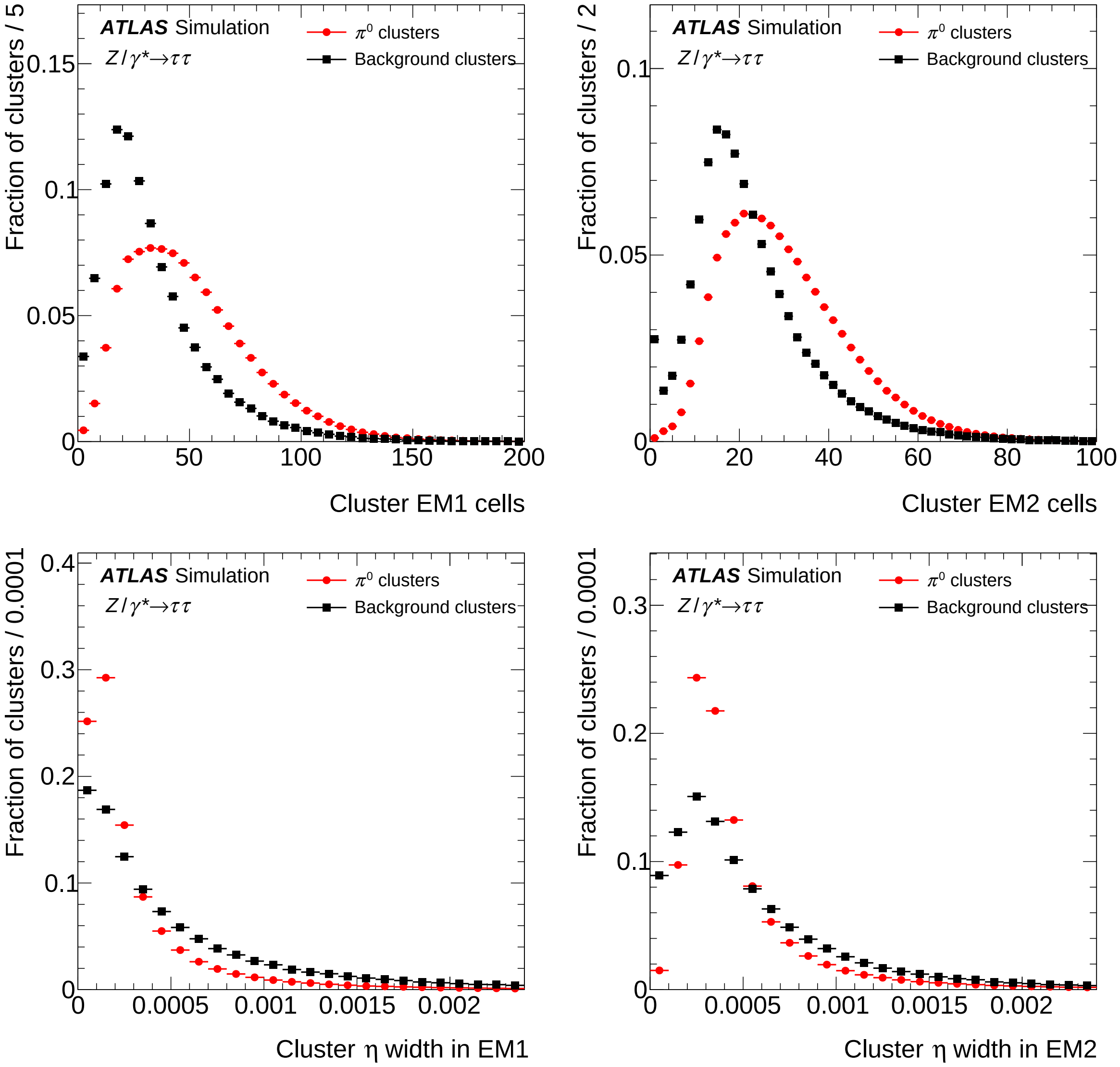

Figure A.3: Distributions of the $N_{\text{strip}}^{\text{clus}}$ (top left), $N_{\text{Ecal2}}^{\text{clus}}$ (top right), $\langle\eta_{\text{strip}}^2\rangle^{\text{clus}}$ (bottom left), and $\langle\eta_{\text{Ecal2}}^2\rangle^{\text{clus}}$ (bottom right) variables for tagged signal and background neutral-pions candidates. Taken from [26].

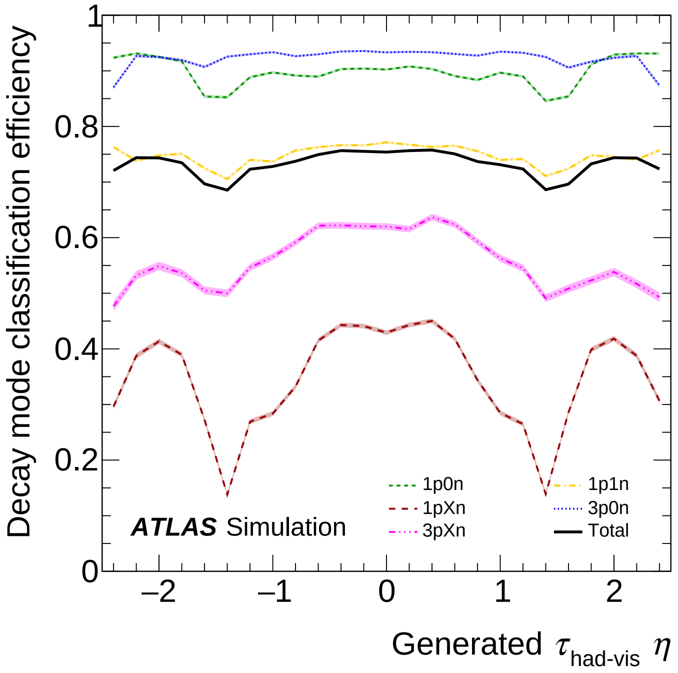

Figure A.4: Stability of decay topology classification vs. η. The $\tau \to h^{\pm}\nu$, $\tau \to h^{\pm}\pi^{0}\nu$, $\tau \to h^{\pm} \geq 2\pi^{0}\nu$, $\tau \to h^{\pm}h^{+}h^{-}\nu$, and $\tau \to h^{\pm}h^{+}h^{-} \geq 1\pi^{0}\nu$ decay topologies are labelled 1p0n, 1p1n, 1pXn, 3p0n, and 3pXn, respectively. The shown uncertainties are statistical. Taken from [26].

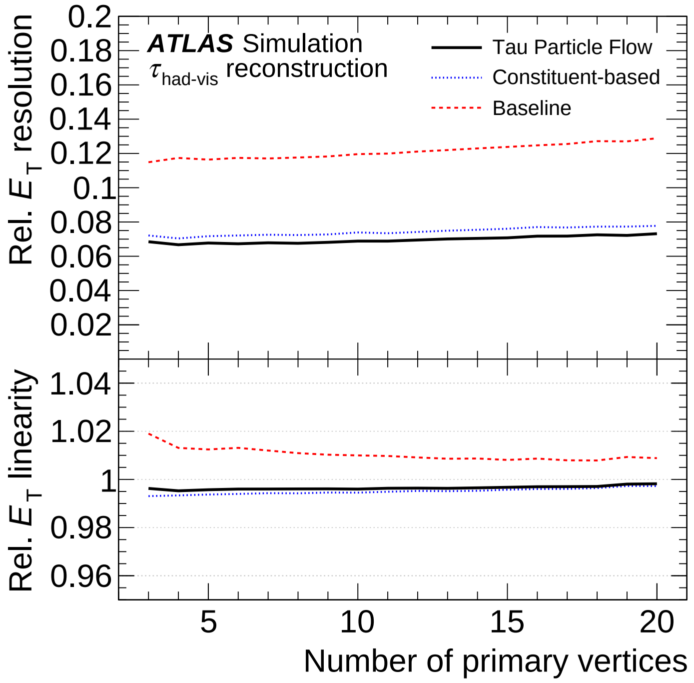

Figure A.5: Stability of the $E_{\text{T}}^{\tau_{\text{had-vis}}}$ reconstruction vs. pile-up. Taken from [26].

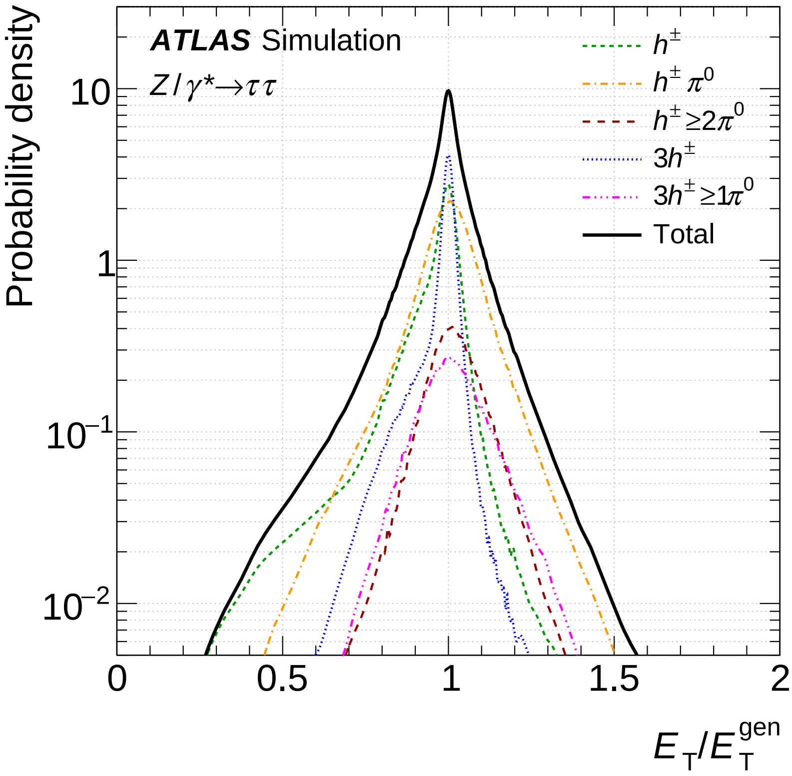

Figure A.6: Relative Tau Particle Flow residual E_{T} distribution split into reconstructed decay topologies, which are labelled by the reconstructed hadrons. Taken from [26].

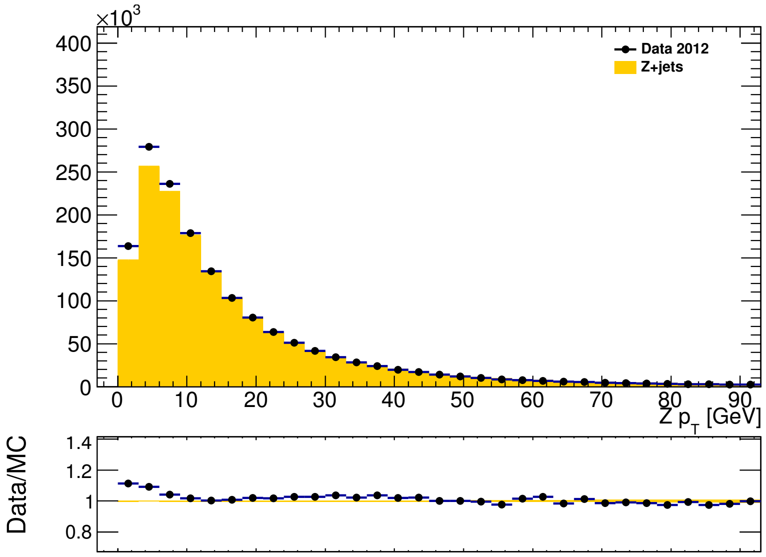

Figure A.7: The data and simulated p_{T} distribution of the Z boson before the reweighting. Adapted from Ref. [137], the ATLAS internal documentation for Ref. [26].

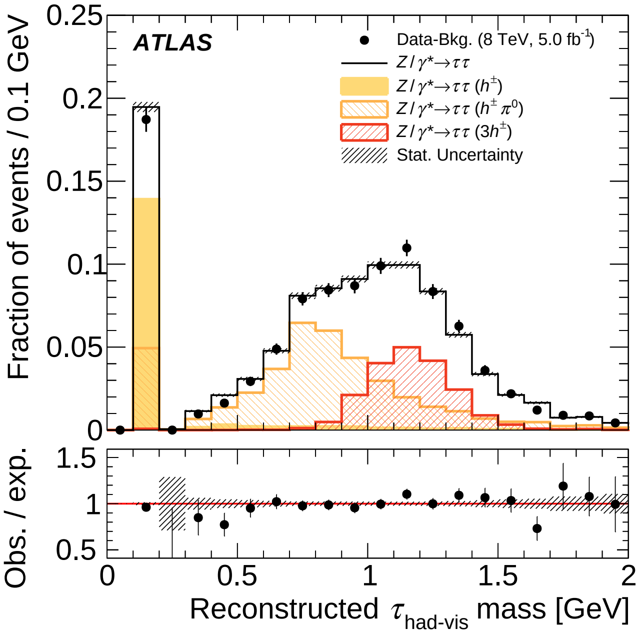

Figure A.8: Distribution of the $\tau_{\text{had-vis}}$ mass reconstructed by Tau Particle Flow in the $Z/\gamma^* \to \tau\tau$ tag-and-probe analysis. The estimated background contribution has been subtracted from the data. The simulated $Z/\gamma^* \to \tau\tau$ sample is normalised to the background-subtracted data. The contributions from generated $\tau \to h^\pm\nu$, $\tau \to h^\pm\pi^0\nu$, and $\tau \to h^\pm h^+ h^- \nu$ decays are overlaid. The shown uncertainties are statistical. Taken from [26].

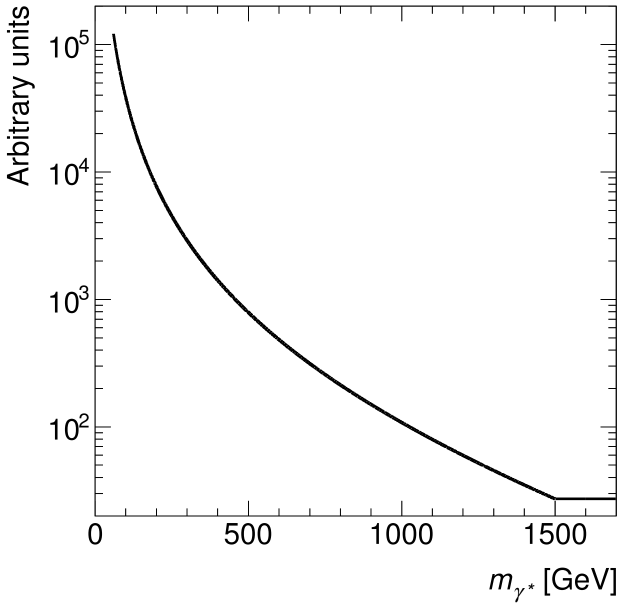

Figure A.9: Mass spectrum set in the $\gamma^* \to \tau_{\text{had}}\tau_{\text{had}}$ sample. It is $\propto (m_{\gamma^*}/\sqrt{s})^{-4.18717} \cdot (1 - m_{\gamma^*}/\sqrt{s})^{11.5811} \cdot (m_{\gamma^*}/\sqrt{s})^2$ for $60 < m_{\gamma^*} < 1\,500$ GeV, constant in the range 1 500–7 000 GeV, and zero outside these ranges. The last factor in the formula artificially increases contributions at high masses. The first two factors parametrise the pure photon contribution in the SM.

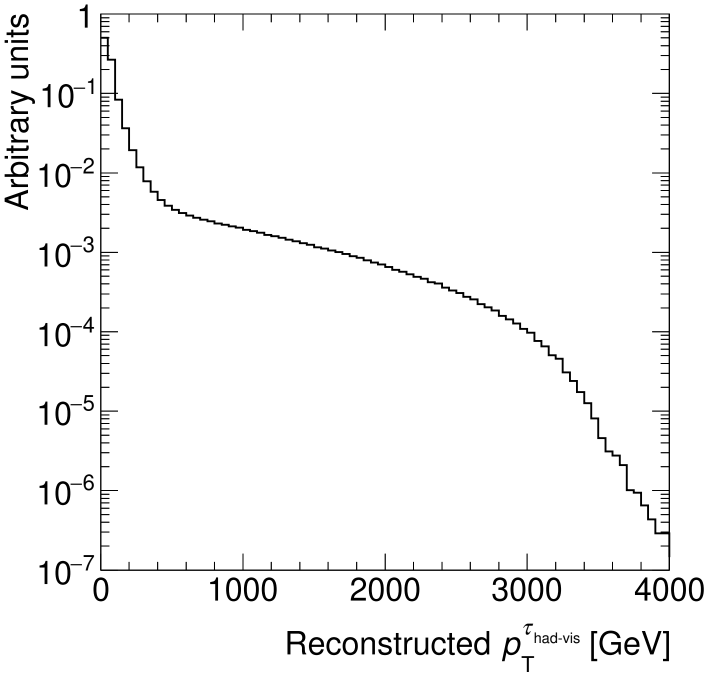

Figure A.10: Reconstruction-level $p_T^{\tau_{\text{had-vis}}}$ spectrum in the $\gamma^* \to \tau_{\text{had}}\tau_{\text{had}}$ sample.

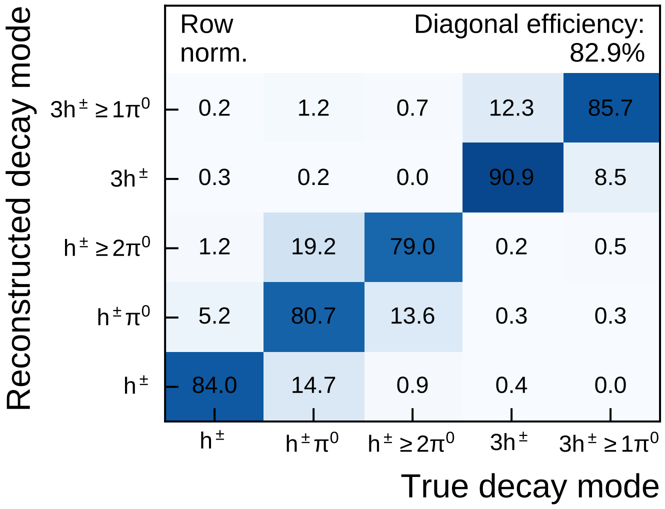

Reconstructed decay mode \ True decay mode	$h^\pm$	$h^\pm\pi^0$	$h^\pm \geq 2\pi^0$	$3h^\pm$	$3h^\pm \geq 1\pi^0$
$3h^\pm \geq 1\pi^0$	0.2	1.2	0.7	12.3	85.7
$3h^\pm$	0.3	0.2	0.0	90.9	8.5
$h^\pm \geq 2\pi^0$	1.2	19.2	79.0	0.2	0.5
$h^\pm\pi^0$	5.2	80.7	13.6	0.3	0.3
$h^\pm$	84.0	14.7	0.9	0.4	0.0

Figure A.11: Decay topology classification performance possible with recurrent neural networks after applying the *medium* level of τ_{had} identification. The sample and selection are the same as in Figure 5.26 and specified in Section 5.7. The fraction of τ_{had} candidates of a given classified topology that originated from a particular generated topology in simulated $\gamma^* \to \tau_{\text{had}}\tau_{\text{had}}$ events is shown in percent. The decay topologies are labelled by the final state hadrons. Decays with neutral kaons are omitted. The statistical uncertainties are negligible. Taken from [88].

APPENDIX B

Simulated Samples in the Tau Polarisation Measurement

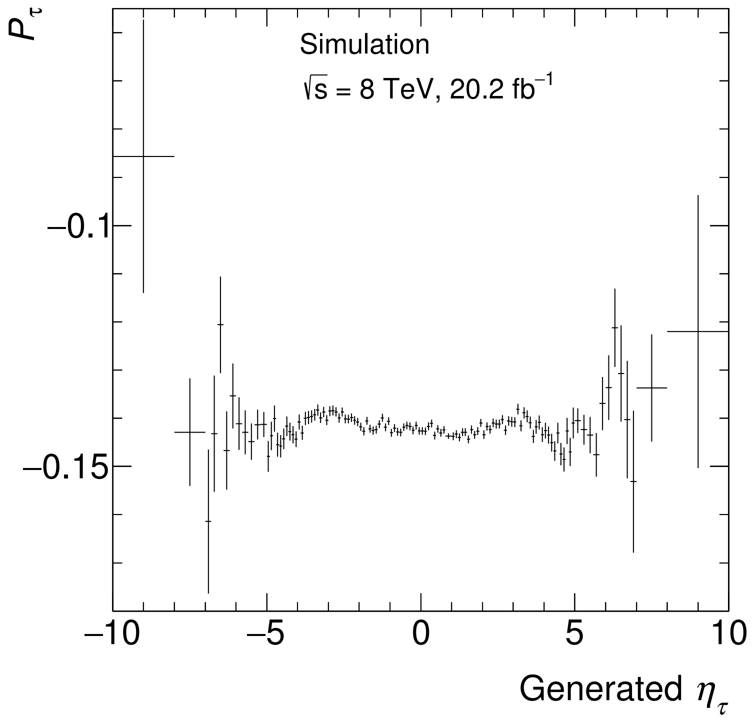

Figure B.1: Dependence of the tau polarisation on the tau pseudorapidity in the nominal simulated signal sample.

Process	Generators	Cross-section [pb]	Number of events	Int. luminosity [fb^{-1}]
$Z/\gamma^* \to \tau\tau$ +0 partons	Alpgen+Pythia6	848.27	34994149	41.3
$Z/\gamma^* \to \tau\tau$ +1 parton	Alpgen+Pythia6	207.39	9999983	48.2
$Z/\gamma^* \to \tau\tau$ +2 partons	Alpgen+Pythia6	69.45	3699987	53.3
$Z/\gamma^* \to \tau\tau$ +3 partons	Alpgen+Pythia6	18.49	1099896	59.5
$Z/\gamma^* \to \tau\tau$ +4 partons	Alpgen+Pythia6	4.73	398795	84.2
$Z/\gamma^* \to \tau\tau$ +5 or 6 partons	Alpgen+Pythia6	1.48	219995	148.4
$Z/\gamma^* \to \tau\tau$ +0 partons	Alpgen+Jimmy	848.27	6607086	7.8
$Z/\gamma^* \to \tau\tau$ +1 parton	Alpgen+Jimmy	207.39	1334896	6.4
$Z/\gamma^* \to \tau\tau$ +2 partons	Alpgen+Jimmy	69.45	404900	5.8
$Z/\gamma^* \to \tau\tau$ +3 partons	Alpgen+Jimmy	18.49	110000	5.9
$Z/\gamma^* \to \tau\tau$ +4 partons	Alpgen+Jimmy	4.73	28999	6.1
$Z/\gamma^* \to \tau\tau$ +5 or 6 partons	Alpgen+Jimmy	1.48	10000	6.7
$Z/\gamma^* \to \tau\tau$	Pythia8	1149.82	14968566	13.0
$Z/\gamma^* \to \tau\tau$	Powheg+Pythia8	1109.90	4999692	4.5
$Z/\gamma^* \to ee$ +0 partons	Alpgen+Pythia6	848.38	6298988	7.4
$Z/\gamma^* \to ee$ +1 parton	Alpgen+Pythia6	207.33	8199476	39.5
$Z/\gamma^* \to ee$ +2 partons	Alpgen+Pythia6	69.47	3175991	45.7
$Z/\gamma^* \to ee$ +3 partons	Alpgen+Pythia6	18.46	894995	48.5
$Z/\gamma^* \to ee$ +4 partons	Alpgen+Pythia6	4.73	398597	84.1
$Z/\gamma^* \to ee$ +5 or 6 partons	Alpgen+Pythia6	1.49	229700	154.6
$Z/\gamma^* \to \mu\mu$ +0 partons	Alpgen+Pythia6	848.61	6298796	7.4
$Z/\gamma^* \to \mu\mu$ +1 parton	Alpgen+Pythia6	207.37	8198384	39.5
$Z/\gamma^* \to \mu\mu$ +2 partons	Alpgen+Pythia6	69.48	3175488	45.7
$Z/\gamma^* \to \mu\mu$ +3 partons	Alpgen+Pythia6	18.49	894799	48.4
$Z/\gamma^* \to \mu\mu$ +4 partons	Alpgen+Pythia6	4.73	398200	84.2
$Z/\gamma^* \to \mu\mu$ +5 or 6 partons	Alpgen+Pythia6	1.48	229200	154.8
$W \to e\nu$ +0 partons	Alpgen+Pythia6	9346.40	11984873	1.3
$W \to e\nu$ +1 parton	Alpgen+Pythia6	2061.84	26298052	12.8
$W \to e\nu$ +2 partons	Alpgen+Pythia6	623.65	17569347	28.2
$W \to e\nu$ +3 partons	Alpgen+Pythia6	169.80	4985287	29.4
$W \to e\nu$ +4 partons	Alpgen+Pythia6	43.41	2553792	58.8
$W \to e\nu$ +5 or 6 partons	Alpgen+Pythia6	13.07	799192	61.1
$W \to \mu\nu$ +0 partons	Alpgen+Pythia6	9346.17	12079285	1.3
$W \to \mu\nu$ +1 parton	Alpgen+Pythia6	2061.72	26271747	12.7
$W \to \mu\nu$ +2 partons	Alpgen+Pythia6	623.92	17601454	28.2
$W \to \mu\nu$ +3 partons	Alpgen+Pythia6	169.81	4966077	29.2
$W \to \mu\nu$ +4 partons	Alpgen+Pythia6	43.42	2556595	58.9
$W \to \mu\nu$ +5 or 6 partons	Alpgen+Pythia6	13.72	788898	60.3
$W \to \tau\nu$ +0 partons	Alpgen+Pythia6	9346.17	11993080	1.3
$W \to \tau\nu$ +1 parton	Alpgen+Pythia6	2061.38	26298935	12.7
$W \to \tau\nu$ +2 partons	Alpgen+Pythia6	623.54	17601943	28.2
$W \to \tau\nu$ +3 partons	Alpgen+Pythia6	169.79	4987982	29.4
$W \to \tau\nu$ +4 partons	Alpgen+Pythia6	43.40	2558295	58.9
$W \to \tau\nu$ +5 or 6 partons	Alpgen+Pythia6	13.69	799096	61.1
Top pair	Powheg+Pythia6	137.32	14996424	109.2

Table B.1: List of simulated samples. The cross-sections used to normalise the samples, the generated number of events, and the corresponding integrated luminosities are listed. The latter value does not account for losses of effective statistical precision due to pile-up reweighting. The Alpgen event generator creates subsamples with different numbers of final-state partons separately. They are combined and treated as one sample subsequently.

APPENDIX C

Details about Background Estimates

C.1 Properties of $Z/\gamma^* \rightarrow \ell\ell$ and Top Pair Backgrounds

The $Z/\gamma^* \rightarrow \ell\ell$ (jet $\rightarrow \tau_{\text{had}}$) contribution is larger in the τ_e–τ_{had} channel than in the τ_μ–τ_{had} channel (see Table 6.3). The reconstruction and identification efficiencies are smaller for electrons than for muons, which makes it more likely to miss one of the leptons in $Z/\gamma^* \rightarrow ee$ events. In contrast, the number and properties of the jets and hence the probabilities to misidentify them as τ_{had} decays are the same in $Z/\gamma^* \rightarrow ee$ and $Z/\gamma^* \rightarrow \mu\mu$ events. and similar in W+jets events. The τ_{had} candidates often originate from the outgoing quark in t-channel diagrams like that in Figure 2.4. Especially, they mostly originate from light quarks, which are the most common quarks in the proton (see Figure 2.2). The origin compositions of the selected τ_{had} candidates are shown in Table C.1. The efficiencies of most requirements in the signal region selection are alike in both channels. For example, the requirement of opposite lepton and τ_{had} candidate charges provides a suppression by a factor of two, because the probability to miss a lepton is mostly independent of its charge. The efficiency of the m_{T} cut is about 2.5 times smaller in the τ_μ–τ_{had} channel than in the τ_e–τ_{had} channel. Presumably, large fractions of the momenta of unidentified muons remain unobserved and fallacious $E_{\text{T}}^{\text{miss}}$ vectors, which are collinear with the p_{T} vectors of the missed muons, are reconstructed. Then the reconstructed event topologies resemble those in $W \rightarrow \mu\nu$ + jets events, which preferentially have high m_{T} values. In contrast, the energy of unidentified electrons should still be detected making it more likely for $Z/\gamma^* \rightarrow ee$ (jet $\rightarrow \tau_{\text{had}}$) events to pass the m_{T} requirement.

The $Z/\gamma^* \rightarrow \ell\ell$ ($\ell \rightarrow \tau_{\text{had}}$) contribution in the τ_e–τ_{had} channel is larger than that in the τ_μ–τ_{had} channel (see Table 6.3) because electrons are more likely to be misidentified as τ_{had} decays than muons [82]. As to be expected for events with τ_{had} candidates mimicked by different particles, the efficiencies of the τ_{had} object requirements in the signal region selection differ noticeably between the channels. The efficiencies to pass the m_{T} and m_{vis} cuts also differ between the channels. The m_{vis} distributions before and after the m_{T} requirement (see Figure C.1) peak at the Z boson mass in the τ_e–τ_{had} channel. This means that the reconstructed electron and τ_{had} momenta typically agree well with the momenta of the real electrons. In $Z/\gamma^* \rightarrow \mu\mu$ ($\mu \rightarrow \tau_{\text{had}}$) events, there is an abundance of events with smaller m_{vis} values, in particular before the m_{T} cut. In these events, the muon that mimics the τ_{had} candidate is not fully stopped in the calorimeter, which causes the reconstructed τ_{had} momentum to be smaller than that of the muon. The effect can be seen in the Υ distribution before the m_{T} cut (see Figure C.2): Υ values above one mean that $p_{\text{T}}^{\tau_{\text{had-vis}}}$ is smaller than $p_{\text{T}}^{\text{track}}$. Events with such τ_{had} candidates are suppressed by the m_{T} requirement (compare left and right in Figures C.1 and C.2). It can be assumed that the reconstructed $E_{\text{T}}^{\text{miss}}$ vector is preferentially collinear with the direction of the τ_{had} candidate and opposite

τ_e–τ_{had} channel						
Origin	$Z/\gamma^* \to \tau\tau$	$Z/\gamma^* \to \ell\ell$	$Z/\gamma^* \to \ell\ell$ (jet $\to \tau_{\text{had}}$)	Top pair	Top pair (jet $\to \tau_{\text{had}}$)	W+jets
Real τ_{had} decay	99.6	0	0	58	0	0
b quark	0.0	0	0	6	15	0
c quark	0.0	2	2	2	5	4
u, d, or s quark	0.3	56	77	31	74	80
Gluon	0.0	7	9	2	5	7
Electron	0.0	28	0	0	0	0
Muon	0.0	0	0	0	0	0
Not matched	0.0	8	11	1	2	9

τ_μ–τ_{had} channel						
Origin	$Z/\gamma^* \to \tau\tau$	$Z/\gamma^* \to \ell\ell$	$Z/\gamma^* \to \ell\ell$ (jet $\to \tau_{\text{had}}$)	Top pair	Top pair (jet $\to \tau_{\text{had}}$)	W+jets
Real τ_{had} decay	99.5	0	0	60	0	0
b quark	0.0	0	0	6	15	0
c quark	0.0	1	1	2	6	3
u, d, or s quark	0.3	60	79	29	72	79
Gluon	0.1	6	8	2	5	9
Electron	0.0	0	0	1	0	0
Muon	0.0	23	0	0	0	0
Not matched	0.0	10	12	1	3	10

Table C.1: Origin compositions of τ_{had} candidates in signal and background processes in the signal region in the τ_e–τ_{had} (top) and τ_μ–τ_{had} (bottom) channels. The relative contributions are estimated from the simulation and given in percent. For the $Z/\gamma^* \to \ell\ell$ (jet $\to \tau_{\text{had}}$) and top pair contributions they are shown inclusively and for jets that are misidentified as τ_{had}. The τ_{had} candidates are matched at stable-particle level. The unmatched candidates may originate from pile-up. The composition for multijet events is not shown, because no simulated sample is available.

to the identified muon in these events. The reconstructed event topologies are similar to those previously discussed for $Z/\gamma^* \to \mu\mu$ (jet $\to \tau_{\text{had}}$) events and lead to a reduced m_{T} cut efficiency. The effect is less pronounced in $Z/\gamma^* \to \mu\mu$ ($\mu \to \tau_{\text{had}}$) events because the $p_{\text{T}}^{\tau_{\text{had-vis}}}$ requirement rejects events in which a large fraction of the muon momentum is lost.

Most top pair events involve two $t \to bW$ decays. Their signature depends strongly on how the W bosons decay subsequently. Specifically, it depends on the combination of hadronic ($W \to$ quarks), leptonic ($W \to \ell\nu$), and $W \to \tau\nu$ decays. In top pair background events the lepton originates from a leptonic W decay or from a $W \to \tau\nu$ decay that is followed by a τ_{lep} decay. Additionally, there is a $W \to \tau\nu$ decay that is followed by a τ_{had} decay or the second W boson decays hadronically. The former leads to a top pair background component in which the τ_{had} candidate is real. The latter leads to a component in which a jet is misidentified as a τ_{had} decay. The jet originates from the hadronic W decay, the bottom quarks produced in the top decays, or additional quarks or gluons. Although there are two or more bottom quarks produced in most top pair events and even though bottom quark-initiated jets involve weak decays with observable flight lengths[1] only about 15% of the misidentified τ_{had} candidates originate from bottom quarks (see Table C.1). They are likely suppressed by the τ_{had} identification and single-prong requirements, because the particle multiplicities are larger in typical bottom hadron (and subsequent) decays than in decays of other hadrons. Additionally, bottom hadron masses are larger than

---

[1] Jets with single bottom quarks involve hadrons that decay via the weak interaction, such as $B^\pm$, B^0, or B_s mesons or Λ_b baryons. They have ranges of about $c\tau = 400$–$500\,\mu$m [27], which are of the same order as those of taus ($c\tau = 87\,\mu$m).

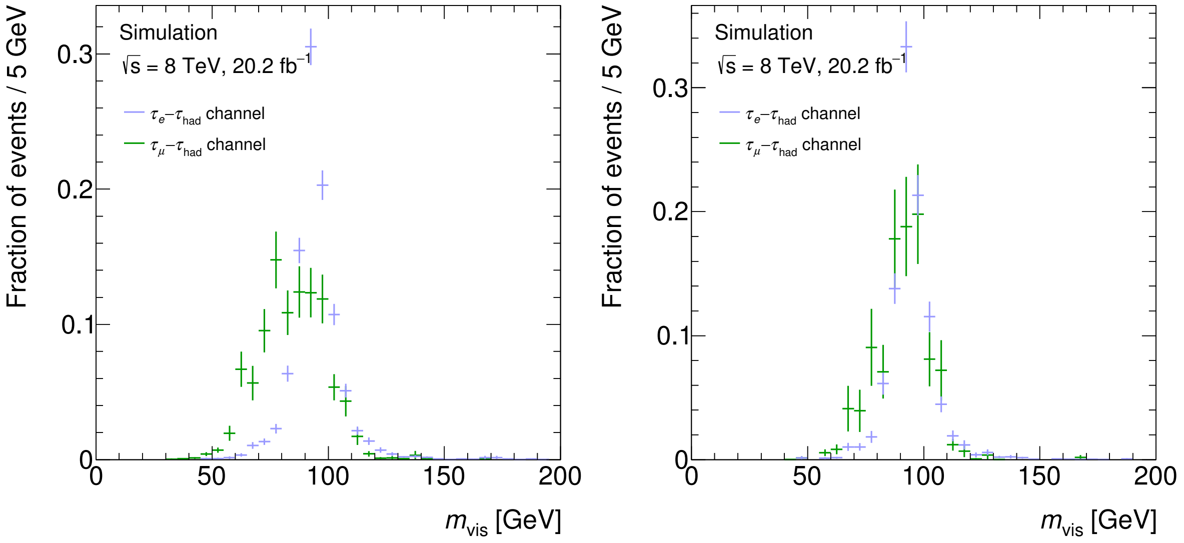

Figure C.1: Normalised m_{vis} distributions in $Z/\gamma^* \rightarrow \ell\ell$ ($\ell \rightarrow \tau_{\text{had}}$) events before the m_{T}, $\sum \Delta\phi$, and m_{vis} requirement (left) and before the $\sum \Delta\phi$ and m_{vis} requirements (right). The remaining cuts in the signal region selection are applied. The statistical uncertainties are shown.

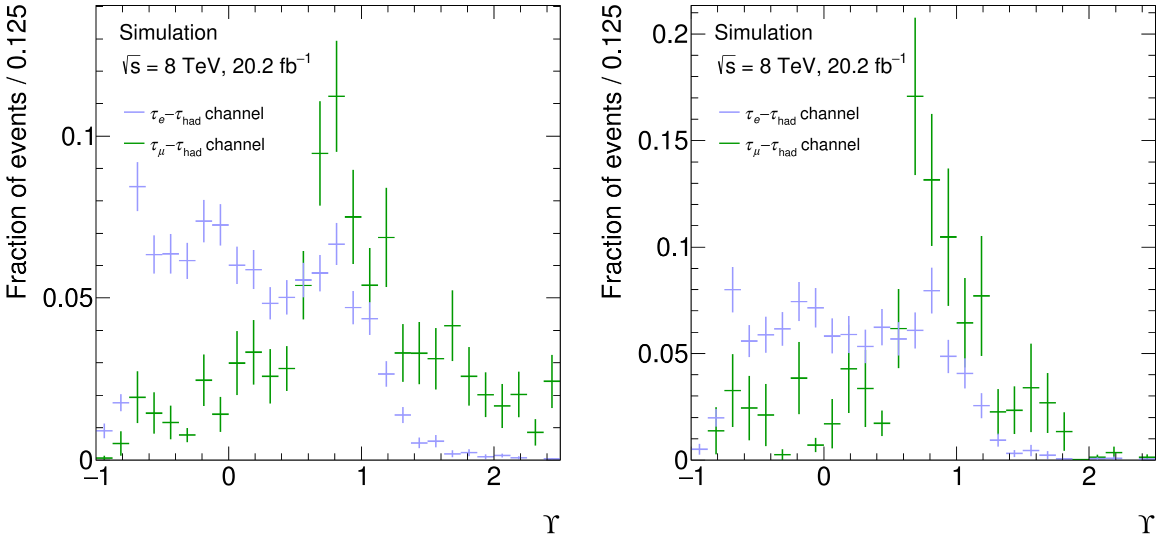

Figure C.2: Normalised Υ distributions in $Z/\gamma^* \rightarrow \ell\ell$ ($\ell \rightarrow \tau_{\text{had}}$) events before the m_{T}, $\sum \Delta\phi$, and m_{vis} requirement (left) and before the $\sum \Delta\phi$ and m_{vis} requirements (right). The remaining cuts in the signal region selection are applied. The distributions are exceptionally shown in a wider range (otherwise $-1.0 \leq \Upsilon \leq 1.5$). The statistical uncertainties are shown.

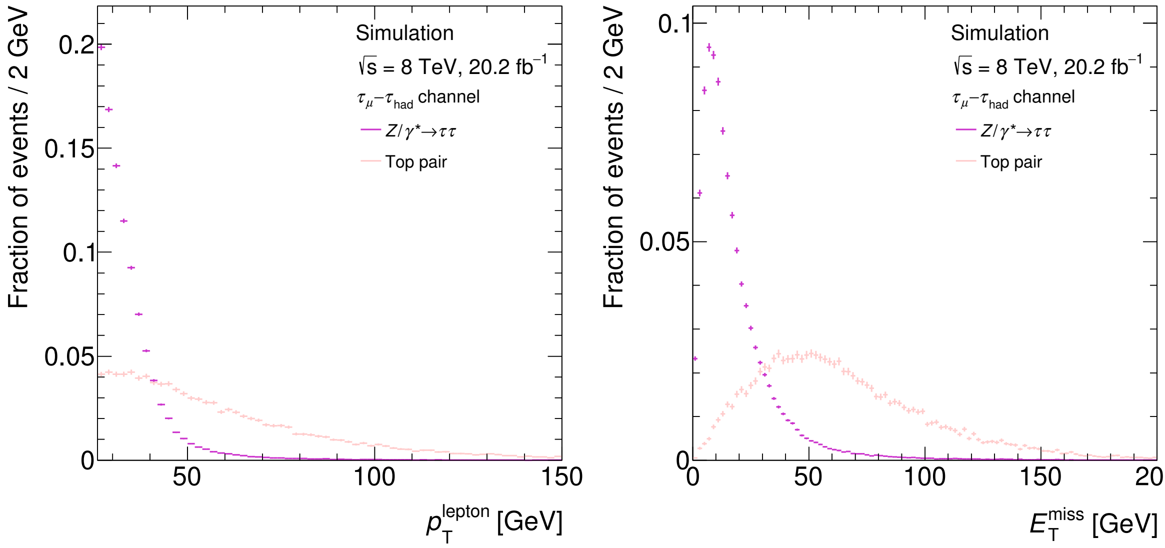

Figure C.3: Normalised distributions of $p_{\mathrm{T}}^{\text{lepton}}$ (left) and $E_{\mathrm{T}}^{\text{miss}}$ (right) in top pair events in the τ_μ–τ_{had} channel before the m_{T}, $\sum\Delta\phi$, and m_{vis} cuts. The remaining cuts in the signal region selection are applied. The corresponding distributions for signal events are shown for comparison and the statistical uncertainties are indicated.

other hadron masses and further away from the tau mass. In contrast to $Z/\gamma^* \to \ell\ell$ events no failed reconstruction or misidentification of leptons are needed to mimic the signal topology in top pair events. Hence, the top pair background has similar properties in both channels. Because top quarks are much heavier than bottom quarks and W bosons, their decay products are boosted. Consequently, the leptons often have large transverse momenta (see Figure C.3). Contributions to $E_{\mathrm{T}}^{\text{miss}}$ arise from $W \to \ell_\tau\nu$ decays, possible subsequent tau decays, and possible (semi-)leptonic decays of hadrons within bottom or charm quark jets. The $E_{\mathrm{T}}^{\text{miss}}$ distribution reaches its maximum around 50 GeV (see Figure C.3). The large $p_{\mathrm{T}}^{\text{lepton}}$ and $E_{\mathrm{T}}^{\text{miss}}$ values typically result in large m_{T} values, so the top pair background is suppressed effectively by the m_{T} cut (Table 6.3).

C.2 Estimation of *W*+jets Background

The W+jets contributions in the same-sign region are estimated analogous to those in the signal region:

- The event yields are estimated using Eq. (6.4). The k_W factors are taken from the same-sign W+jets control region (see Table 6.9).
- The W+jets Υ distributions in the same-sign W+jets control region are estimated from the data in that region (see Figure C.4).
- The shape corrections for the transfer from the same-sign W+jets control region to the same-sign region are estimated as shown in Figure C.5. The fits to the ratios are repeated after the corrections from Figure C.5 are applied to the distributions in the same-sign W+jets control region. The statistical uncertainties in these fits are taken on as preliminary uncertainties in the shape corrections.

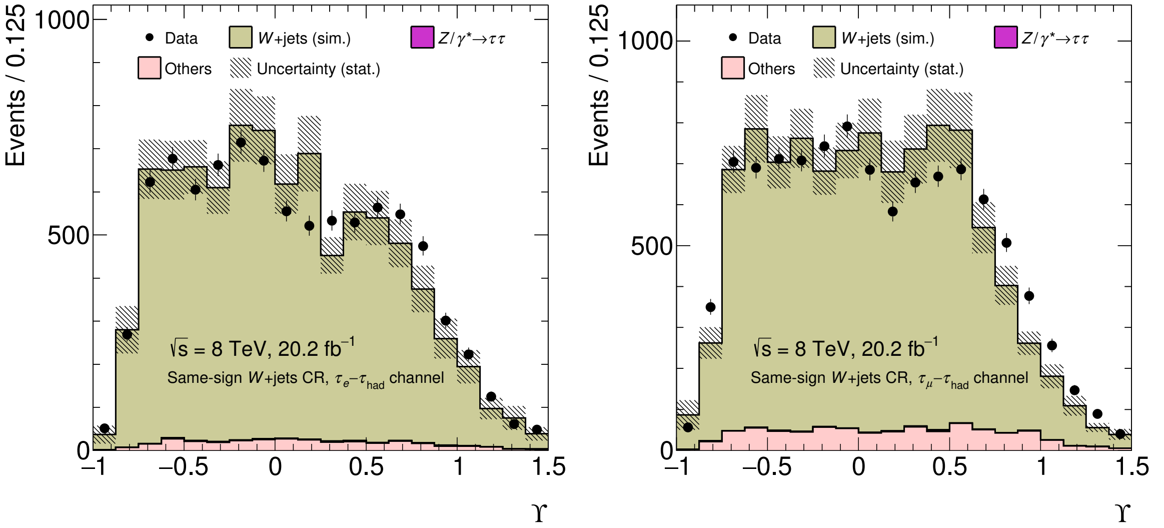

Figure C.4: The Υ distribution in the same-sign W+jets control region in the τ_e–τ_{had} (left) and τ_μ–τ_{had} (right) channel. The contributions of $Z/\gamma^* \rightarrow \tau\tau$ and of $Z/\gamma^* \rightarrow \ell\ell$ and top pair (other) events are estimated from the simulation. The estimated W+jets contribution corresponds to the difference of the data and the aforementioned contributions. The W+jets distribution obtained from simulation is shown for comparison. It is normalised using Eq. (6.4), i.e. such that the total estimated event yield matches the observed yield. The statistical uncertainties are shown.

- The W+jets Υ distributions from the data in the same-sign W+jets control region are corrected using the linear functions obtained in Figure C.5 and normalised to the event yields found with Eq. (6.4). The results are the final predicted W+jets Υ distributions in the same-sign region.
- The final shape correction uncertainties are determined. For this, additional linear fits are performed to the ratios of the normalised Υ distributions in simulated W+jets events in the same-sign W+jets validation W+jets control regions. The preliminary uncertainties are inflated such that the slopes found in the additional fits are covered.

The slopes for the linear corrections and their final uncertainties are included in Table 6.10.

The parameters obtained in the linear fits performed to estimate the W+jets background in the signal and same-sign regions are summarised in Table C.2.

C.3 Estimation of Multijet Background

The Υ distribution in the multijet control region in the τ_e–τ_{had} channel is shown in Figure C.6. The $f_{p_{\text{T}},\text{iso}}$ and $f_{E_{\text{T}},\text{iso}}$ distributions in the multijet control regions are shown in Figures C.7 and C.8. The double-peak structures originate from requiring that $f_{p_{\text{T}},\text{iso}} \geq 0.06$ or $f_{E_{\text{T}},\text{iso}} \geq 0.06$. Lepton candidates with $f_{E_{\text{T}},\text{iso}} \geq 0.06$ often have $f_{p_{\text{T}},\text{iso}}$ close to zero. The abundance of values right above $f_{p_{\text{T}},\text{iso}} = 0.06$ results from events that pass the $f_{p_{\text{T}},\text{iso}} \geq 0.06$ requirement. Analogous considerations apply to the $f_{E_{\text{T}},\text{iso}}$ distribution.

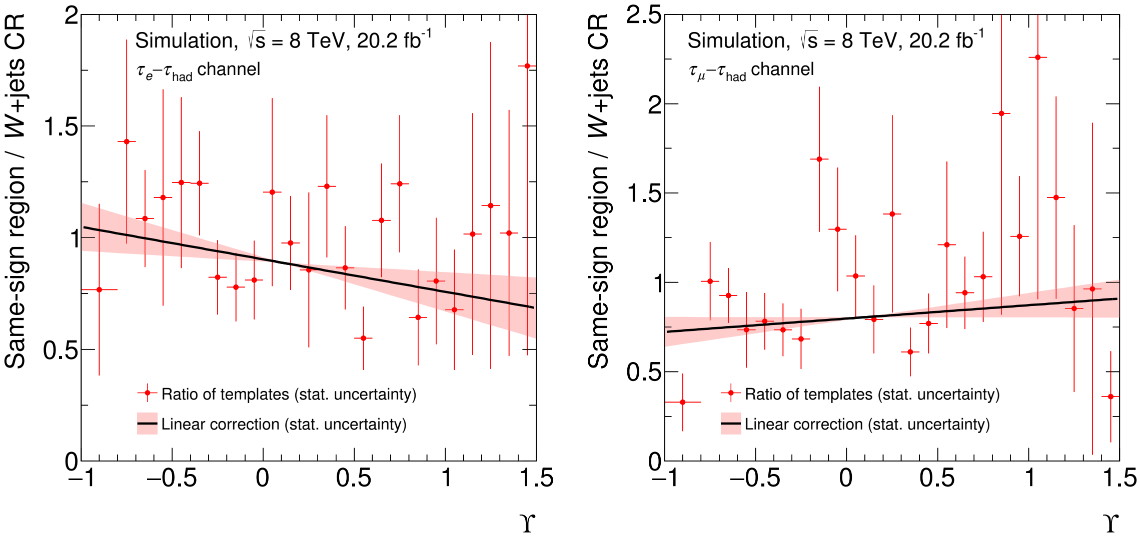

Figure C.5: Ratios of normalised, simulated ϒ distributions in W+jets events in the same-sign region and in the same-sign W+jets control region for the τ_e–τ_{had} (left) and τ_μ–τ_{had} (right) channels. Linear functions are fit to the ratios. The fitted functions are shown and the statistical uncertainties in the slopes are indicated. The fit parameters are given in Table C.2.

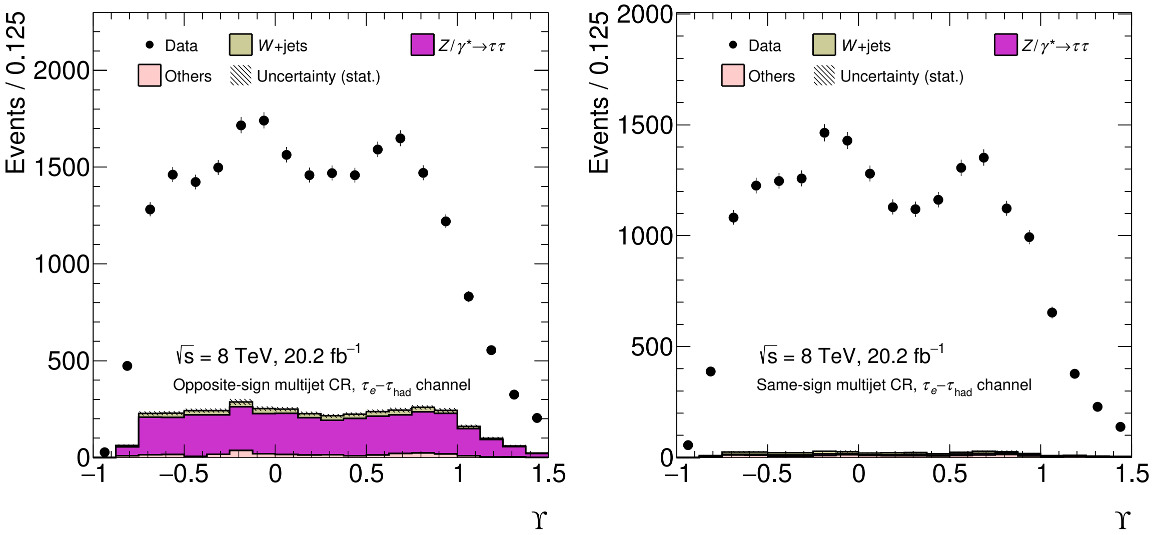

Figure C.6: The ϒ distribution in the opposite-sign multijet control region (left) and the same-sign multijet control region (right) in the τ_e–τ_{had} channel. The contributions of $Z/\gamma^* \to \tau\tau$ and of $Z/\gamma^* \to \ell\ell$ and top pair (other) events are estimated from the simulation. The W+jets contribution is estimated as described in Section 6.4.2. The estimated multijet contribution corresponds to the difference of the data and the aforementioned contributions. The statistical uncertainties are shown.

τ_e–τ_{had} channel

Fitted ratio	e and τ_{had} charges	Slope	Offset at $\Upsilon = 0$	χ^2
Signal region/W+jets CR	opposite	0.03 ± 0.05	0.954 ± 0.030	12.0
Same after correction	opposite	0.00 ± 0.05	0.959 ± 0.031	12.0
W+jets VR1/W+jets CR	opposite	0.006 ± 0.032	0.986 ± 0.021	18.5
W+jets VR2/W+jets CR	opposite	0.03 ± 0.04	0.967 ± 0.027	22.3
Same-sign region/W+jets CR	same	−0.15 ± 0.10	0.90 ± 0.05	16.7
Same after correction	same	−0.03 ± 0.10	0.90 ± 0.05	16.7
W+jets VR1/W+jets CR	same	−0.02 ± 0.07	0.92 ± 0.04	23.7
W+jets VR2/W+jets CR	same	−0.05 ± 0.07	0.88 ± 0.04	21.7

τ_μ–τ_{had} channel

Fitted ratio	μ and τ_{had} charges	Slope	Offset at $\Upsilon = 0$	χ^2
Signal region/W+jets CR	opposite	−0.02 ± 0.05	0.974 ± 0.033	12.7
Same after correction	opposite	0.00 ± 0.05	0.971 ± 0.032	12.7
W+jets VR1/W+jets CR	opposite	0.019 ± 0.030	0.991 ± 0.019	16.5
W+jets VR2/W+jets CR	opposite	0.06 ± 0.04	0.967 ± 0.022	16.6
Same-sign region/W+jets CR	same	0.07 ± 0.08	0.80 ± 0.05	31.5
Same after correction	same	0.01 ± 0.07	0.80 ± 0.05	31.5
W+jets VR1/W+jets CR	same	−0.13 ± 0.07	0.95 ± 0.04	19.5
W+jets VR2/W+jets CR	same	−0.02 ± 0.07	0.90 ± 0.05	20.6

Table C.2: Summary of linear fits performed for the W+jets background estimate to evaluate differences between the Υ distributions in the W+jets control and signal regions as well as the related systematic uncertainties. The results are shown for the fits in the τ_e–τ_{had} (top) and τ_μ–τ_{had} (bottom) channels. The slopes and offsets and their statistical uncertainties are documented. Additionally, the χ^2 values are shown. All fits have 22 degrees of freedom.

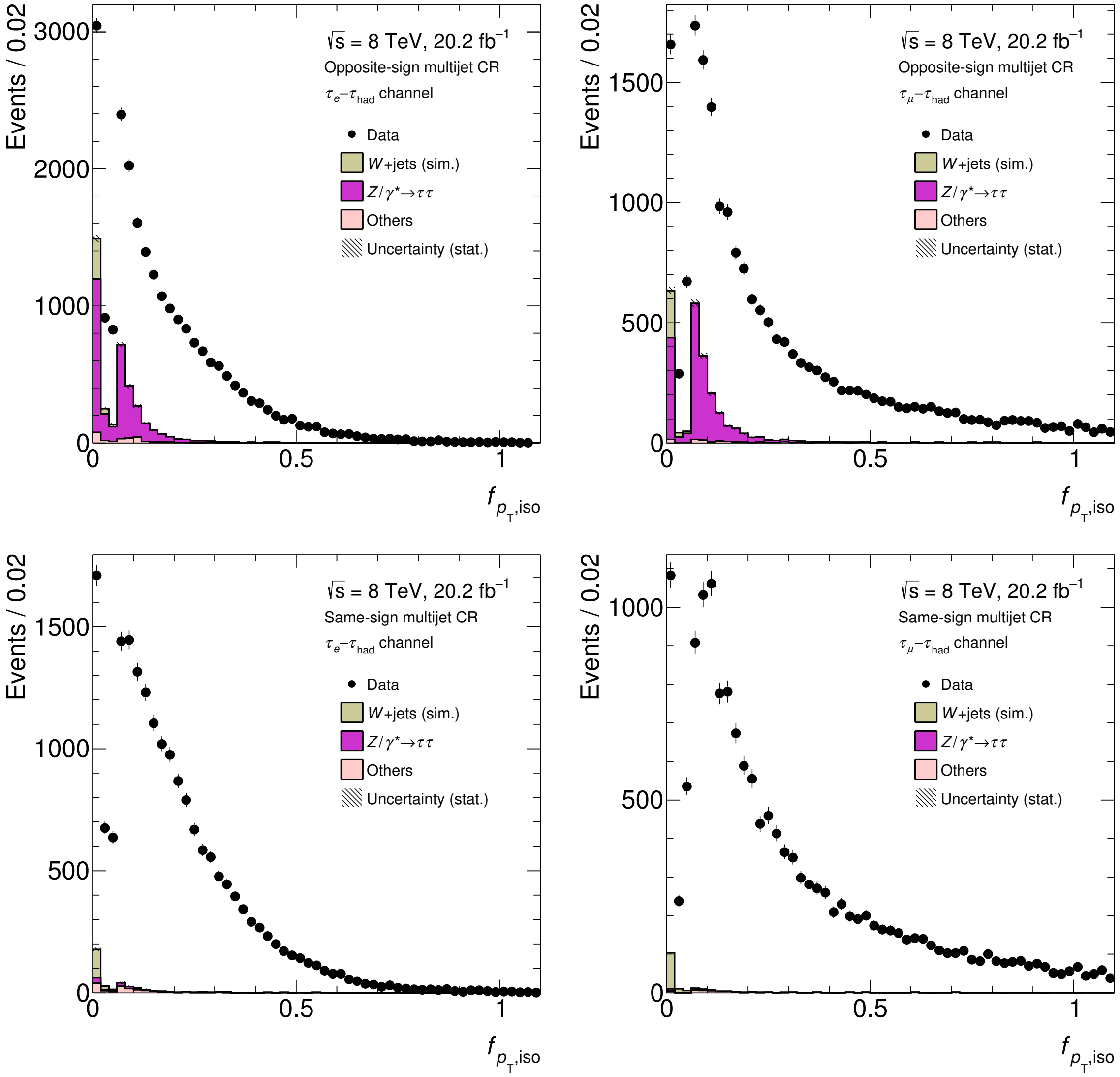

Figure C.7: Distributions of $f_{p_{\rm T},\rm iso}$ in the multijet control regions in the τ_e–$\tau_{\rm had}$ (left) and τ_μ–$\tau_{\rm had}$ (right) channels and for events with opposite (top) and same (bottom) lepton and $\tau_{\rm had}$ candidate charges. The estimated multijet contribution is given by the difference of the data and the remaining contributions.

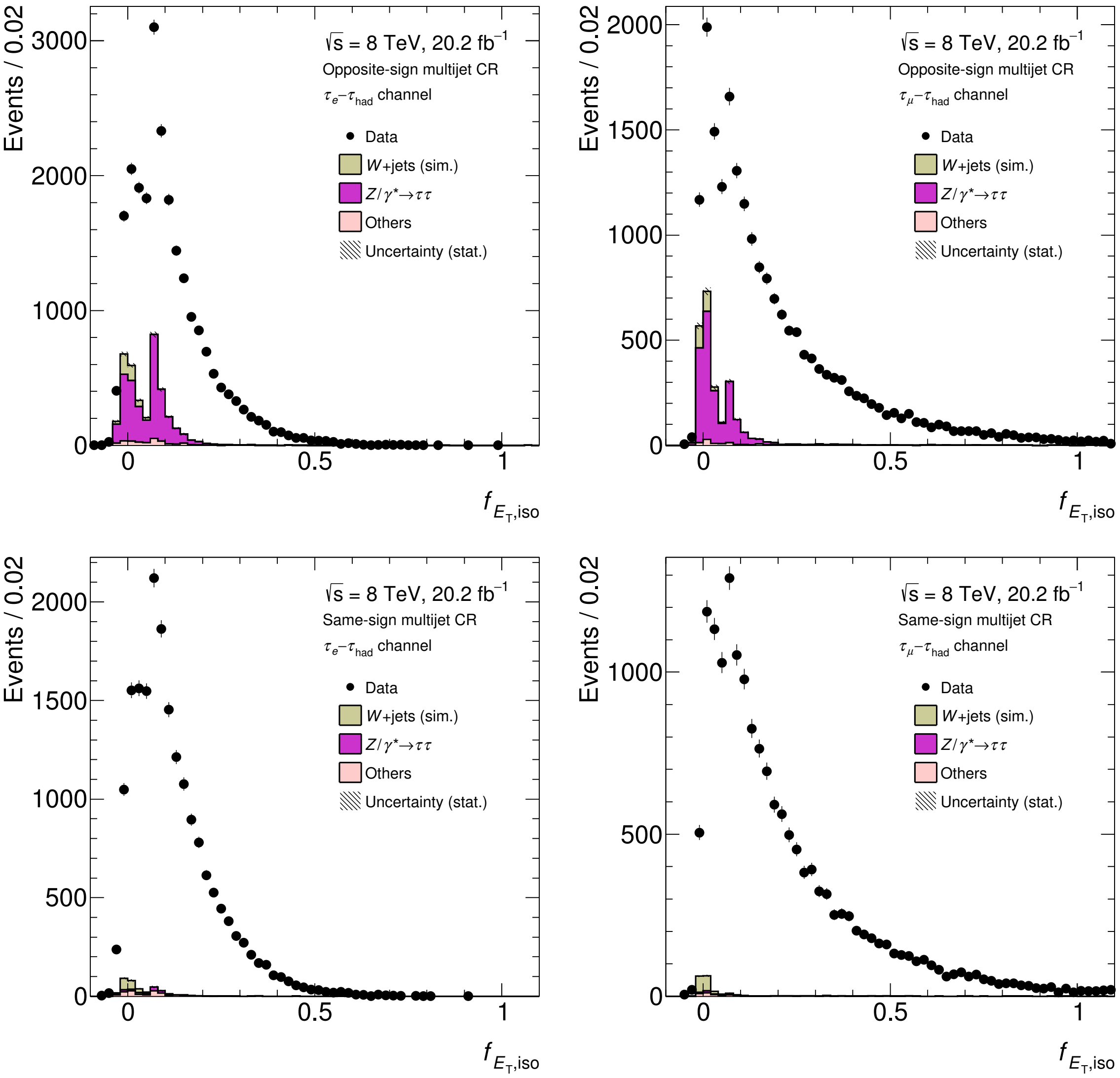

Figure C.8: Distributions of $f_{E_T,\text{iso}}$ in the multijet control regions in the τ_e–τ_{had} (left) and τ_μ–τ_{had} (right) channels and for events with opposite (top) and same (bottom) lepton and τ_{had} candidate charges. The estimated multijet contribution is given by the difference of the data and the remaining contributions. The few negative $f_{E_T,\text{iso}}$ values stem from events in which a negative amount of energy is measured around the lepton candidate. This can be caused by out-of-time pile-up or electronic noise in the readout system of the calorimeter.

APPENDIX D

Further Information about Systematic Uncertainties

D.1 Estimation of Uncertainties in τ_{had} Identification Input Variables

The distributions of the τ_{had} identification input variables in the top pair validation region are shown in Figures D.1 and D.2.

The uncertainties in the integer input variables are determined using the difference of the data and estimated cumulative distribution functions

$$d(n) = \text{CDF}_{\text{data}}(n+1) - \text{CDF}_{\text{sim}}(n+1).$$

If $d(n)$ is positive, the variable value is incremented by 1 for the fraction

$$f^{+1\sigma}_{\text{pos }d}(n) = \frac{d(n)}{\text{CDF}_{\text{est}}(n+1) - \text{CDF}_{\text{est}}(n)}$$

of simulated signal events with variable value n. The denominator corresponds to the number of estimated events with variable value n. Similarly, the variable value is decremented by one for the fraction

$$f^{+1\sigma}_{\text{neg }d}(n+1) = \frac{-d(n)}{\text{CDF}_{\text{est}}(n+2) - \text{CDF}_{\text{est}}(n+1)}$$

of simulated signal events with variable value $(n+1)$ if $d(n)$ is negative. The events in which the values are altered are selected randomly. If this method was applied to the estimate in the kinematic region in which the fractions are determined, the resulting input variable distribution would match the data in that region. In particular, the number of events with variable value $\leq n$ is increased (decreased) in the estimate if $d(n)$ is positive (negative). The impact of this variation on the signal in the signal region is evaluated as for the continuous variables. It is considered as a $+1\sigma$ variation. The impact of the opposite variation is computed by decrementing the variable value by one for the fraction

$$f^{-1\sigma}_{\text{pos }d}(n+1) = \frac{d(n)}{\text{CDF}_{\text{est}}(n+2) - \text{CDF}_{\text{est}}(n+1)}$$

of simulated signal events with variable value $(n+1)$ if $d(n)$ is positive. Simultaneously, the variable

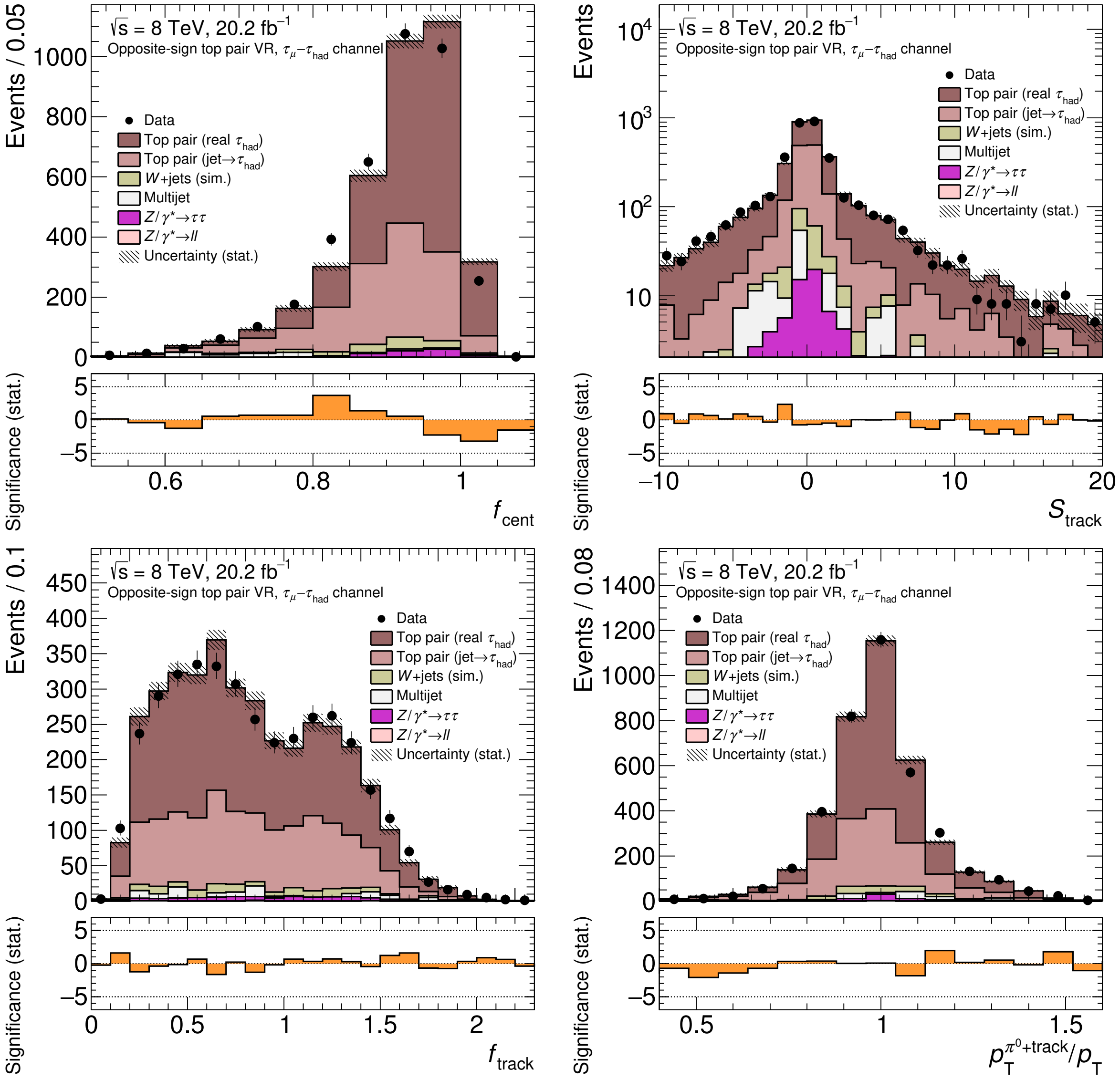

Figure D.1: Distributions of τ_{had} identification input variables in the top pair validation control region for the τ_μ–τ_{had} channel.

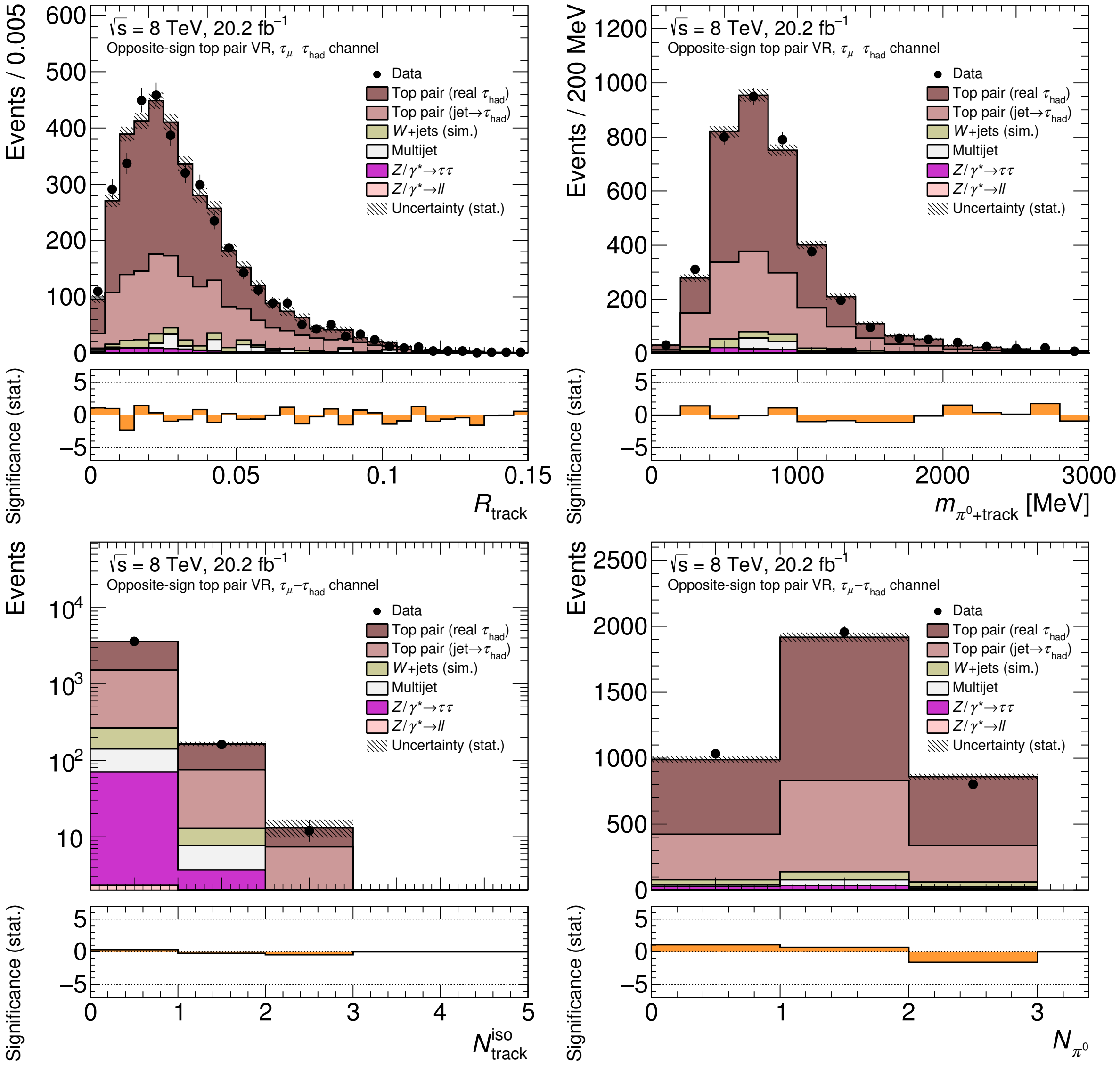

Figure D.2: Distributions of τ_{had} identification input variables in the top pair validation region for the τ_{μ}–τ_{had} channel.

value is incremented by one for the fraction of simulated signal events

$$f_{\text{neg }d}^{-1\sigma}(n) = \frac{-d(n)}{\text{CDF}_{\text{est}}(n+1) - \text{CDF}_{\text{est}}(n)}$$

with variable value n if $d(n)$ is negative. Now the number of events with variable value $\leq n$ is decreased (increased) if $d(n)$ is positive (negative).

The effect of the uncertainties in the f_{cent}, S_{track}, and f_{track} variables on the signal outside the mass-selected region is shown in Figure D.3. The impact on the tau polarisation uncertainty is much smaller than for the signal inside the mass-selected region. The effect of the uncertainties in these variables from the top pair validation region are shown in Figure D.4. The τ_{had} identification uncertainties in the tau polarisation are reduced by a factor of two if the uncertainties from the top pair control region instead of those from the W+jets control region are considered. The effect of the input variable uncertainties on the left-handed signal in the τ_e–τ_{had} channel is shown in Figure D.5. As expected for uncertainties in the modelling of τ_{had} decays there are no large differences between the two channels. The effect of the uncertainties in the f_{cent}, S_{track}, and f_{track} variables on the left-handed signal inside the fiducial region is shown in Figure D.6. The signal in the fiducial region coincides with the signal inside the mass-selected region to a large extend. Hence there are no large differences between the shape variations between the measurements of the polarisation inside the fiducial region and inside the mass-selected region. The impact of the uncertainties in the remaining τ_{had} identification input variables on the left-handed signal inside the mass-selected region is shown in Figures D.7 and D.8.

D.2 Estimation of Uncertainties in Modelling of Signal Process

The Υ modelling uncertainties in the templates for events with left- and right-handed taus inside the fiducial region are shown in Figure D.9.

D.3 Estimation of Uncertainties in Splitting of Signal Sample

D.3.1 Calculation of σ_{LR} and σ_{RL}

The fraction of events with left-handed (right-handed) taus in the signal sample is denoted as f_{L} (f_{R}). The generated tau polarisation is given by $P_\tau^{\text{gen}} = f_{\text{R}} - f_{\text{L}}$. If the uncertainty in the relative net migration from the left-handed to the right-handed subsample is σ_{LR} and the uncertainty in the opposite migration vanishes, the uncertainty in the tau polarisation determined by the TauSpinner algorithm is

$$\sigma_{P_\tau^{\text{TS}}} = (f_{\text{R}} + \sigma_{\text{LR}} f_{\text{L}} - (1 - \sigma_{\text{LR}})\, f_{\text{L}}) - (f_{\text{R}} - f_{\text{L}}) = 2\sigma_{\text{LR}} f_{\text{L}}.$$

The tau polarisation in the signal sample is around −0.14, so $f_{\text{L}} \approx 0.5 \approx f_{\text{R}}$ and $\Delta P_\tau \approx \sigma_{\text{LR}}$. Analogously, a relative net migration from the right-handed to the left-handed subsample of σ_{RL} and a vanishing σ_{LR} lead to an uncertainty of $\sigma_{P_\tau^{\text{TS}}} = 2\sigma_{\text{RL}} f_{\text{R}} \approx \sigma_{\text{RL}}$.

The uncertainty in the tau polarisation determined by the TauSpinner algorithm is 0.007 (see Section 6.5.2). It is covered by the uncertainties in the migration in either direction if $\sigma_{\text{LR}} = \sigma_{\text{RL}} = 0.007$.

D.3.2 Calculation of Template Variations

The expected signal contributions in the signal region and within the mass-selected or fiducial region are denoted as $F_{\text{left,SR}}^{\text{nominal}}$ and $F_{\text{right,SR}}^{\text{nominal}}$ for events with left- and right-handed taus, respectively. They are scaled

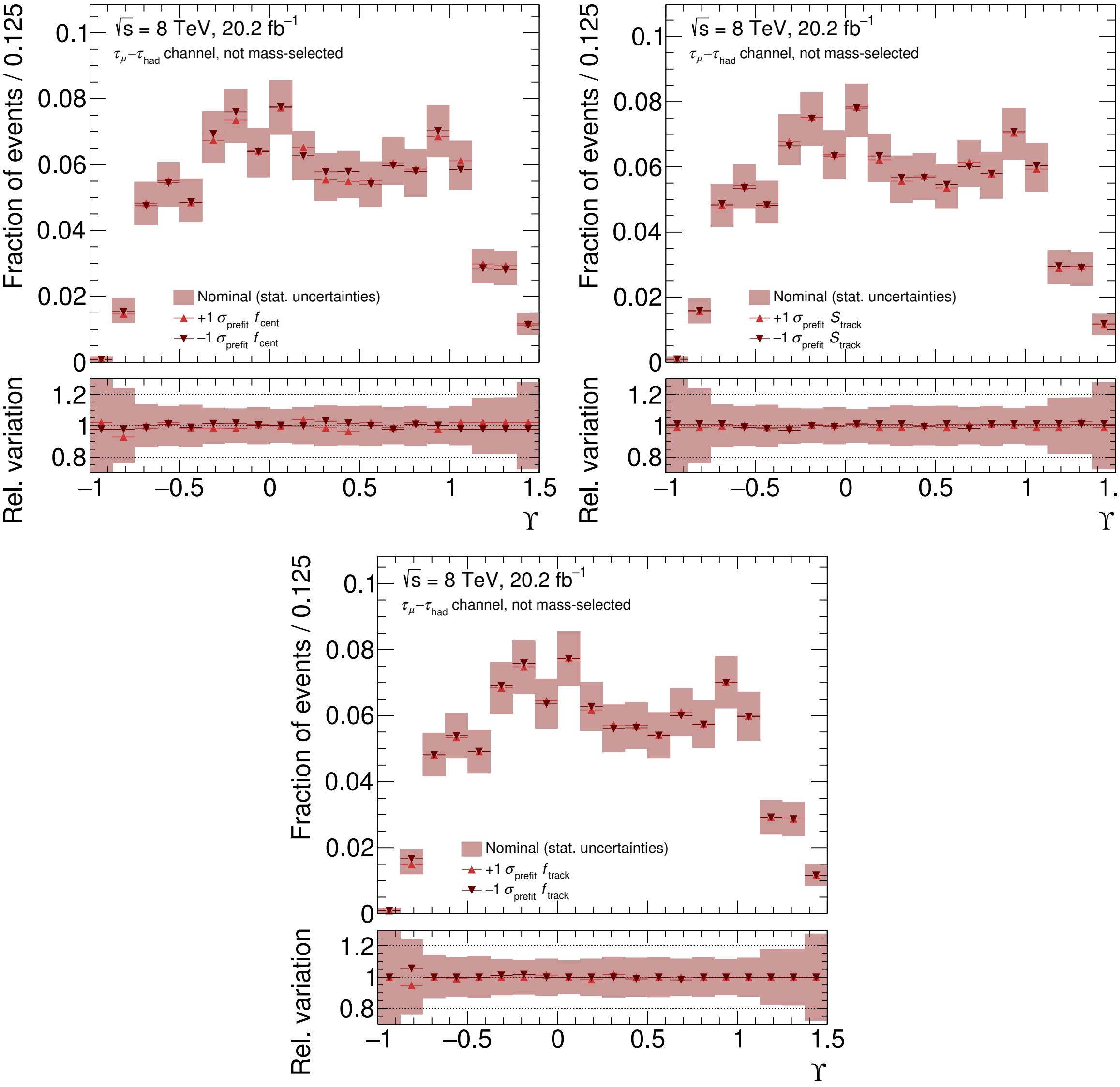

Figure D.3: Impact of the uncertainties in the f_{cent} (top left), S_{track} (top right), and f_{track} (bottom) variables on signal in the signal region for the τ_μ–τ_{had} channel. The impact on the shape of the Υ distribution for events outside the mass-selected region is shown. The uncertainties from the W+jets control region are used.

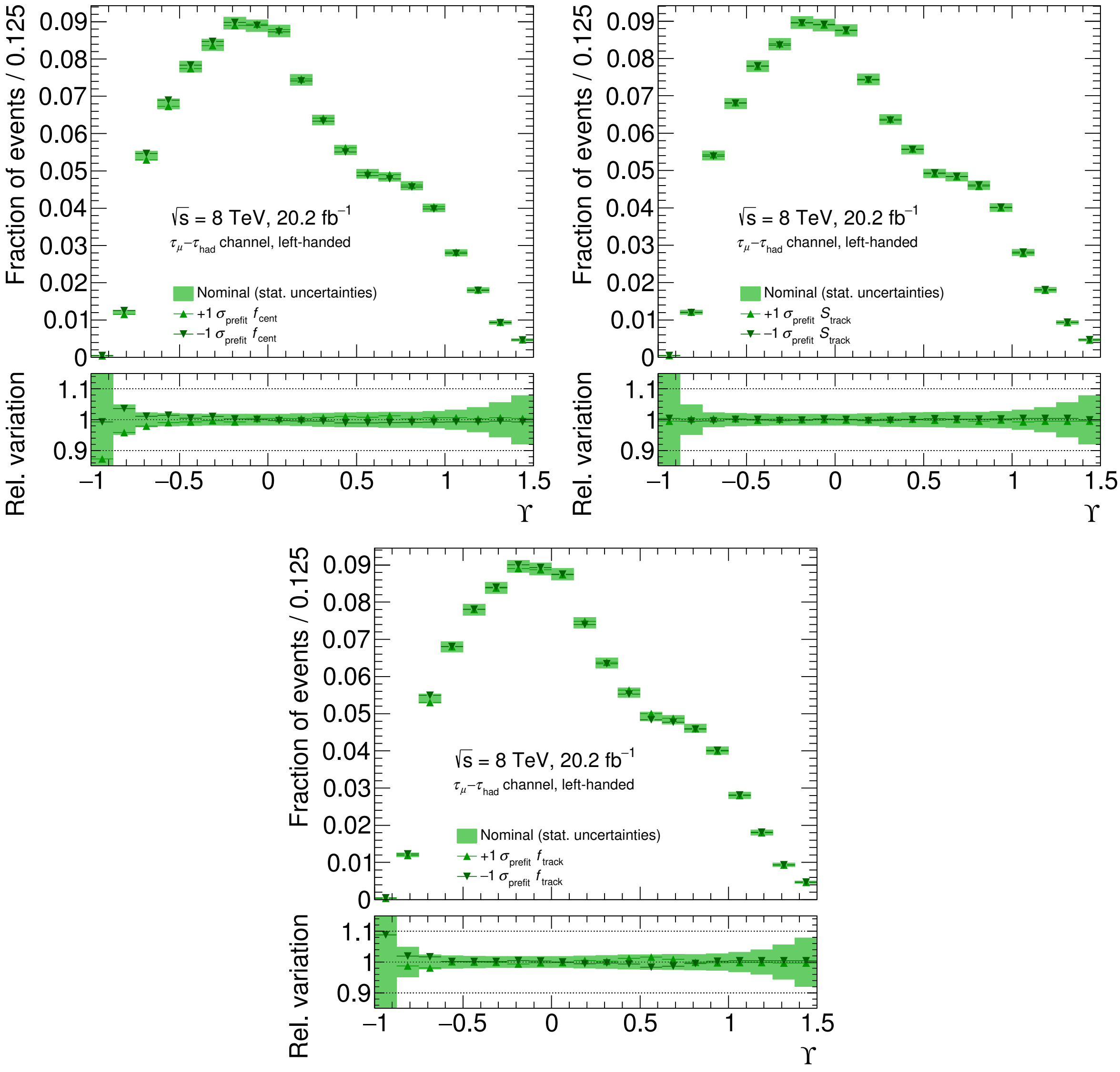

Figure D.4: Impact of the uncertainties in the $f_{\rm cent}$ (top left), $S_{\rm track}$ (top right), and $f_{\rm track}$ (bottom) variables on the left-handed, mass-selected signal in the signal region for the τ_μ–$\tau_{\rm had}$ channel. The impact on the shape of the Υ distribution is shown. The uncertainties from the top pair validation region are used.

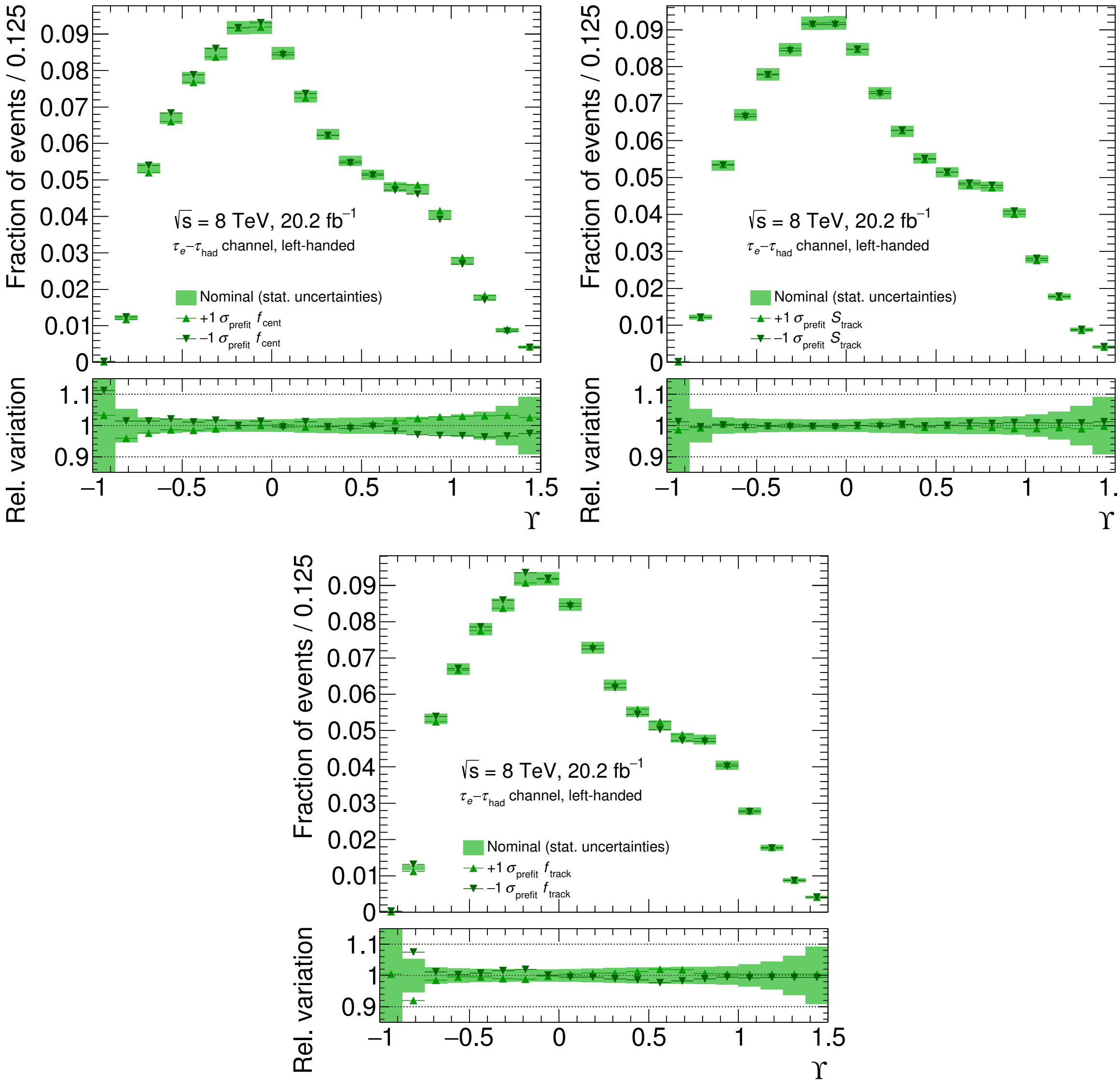

Figure D.5: Impact of the uncertainties in the f_{cent} (top left), S_{track} (top right), and f_{track} (bottom) variables on the left-handed, mass-selected signal in the signal region for the τ_e–τ_{had} channel. The impact on the shape of the Υ distribution is shown. The uncertainties from the W+jets control region are used.

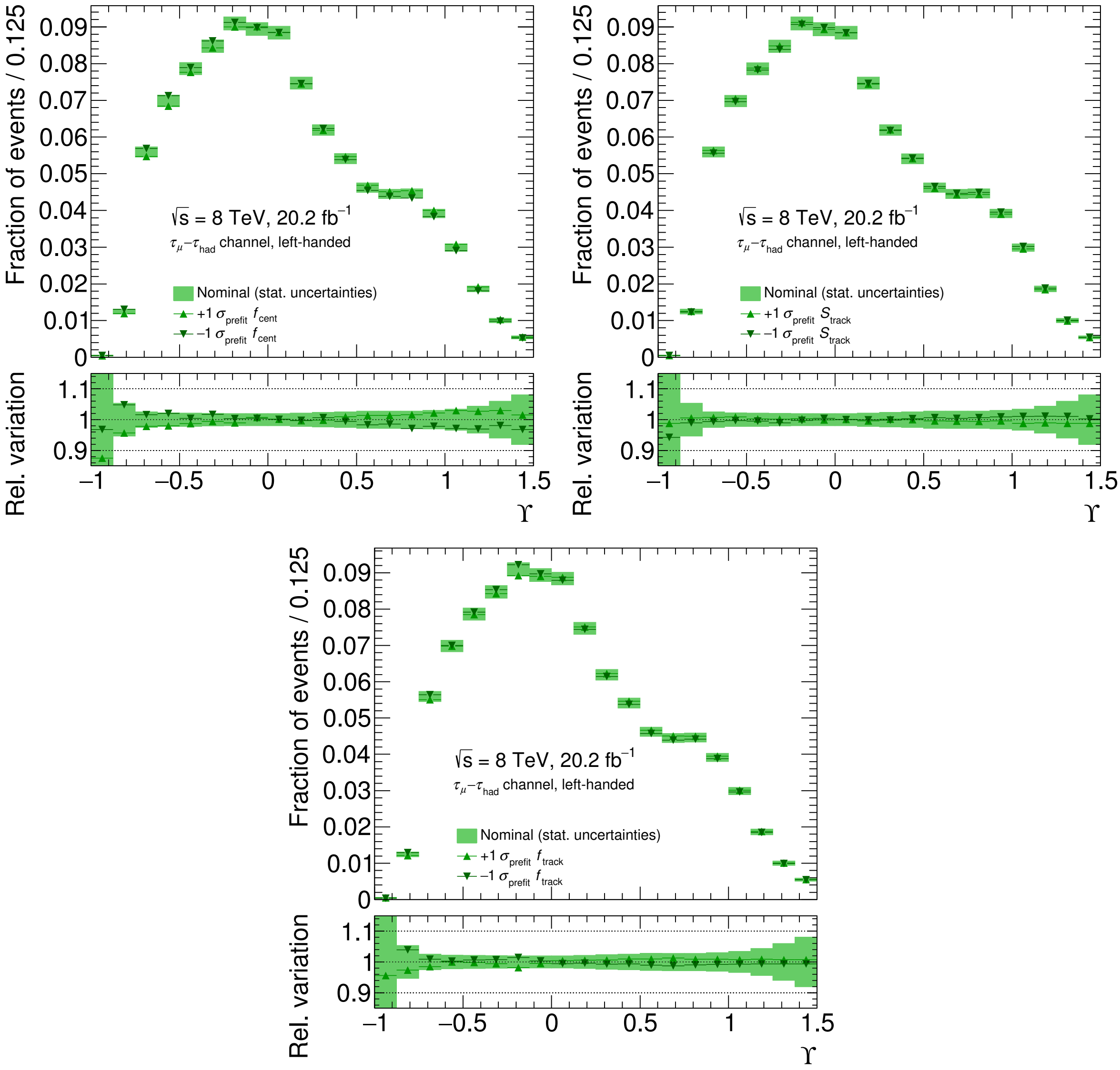

Figure D.6: Impact of the uncertainties in the f_{cent} (top left), S_{track} (top right), and f_{track} (bottom) variables on the left-handed signal inside the fiducial and signal regions for the τ_μ–τ_{had} channel. The impact on the shape of the ϒ distribution is shown. The uncertainties from the W+jets control region are used.

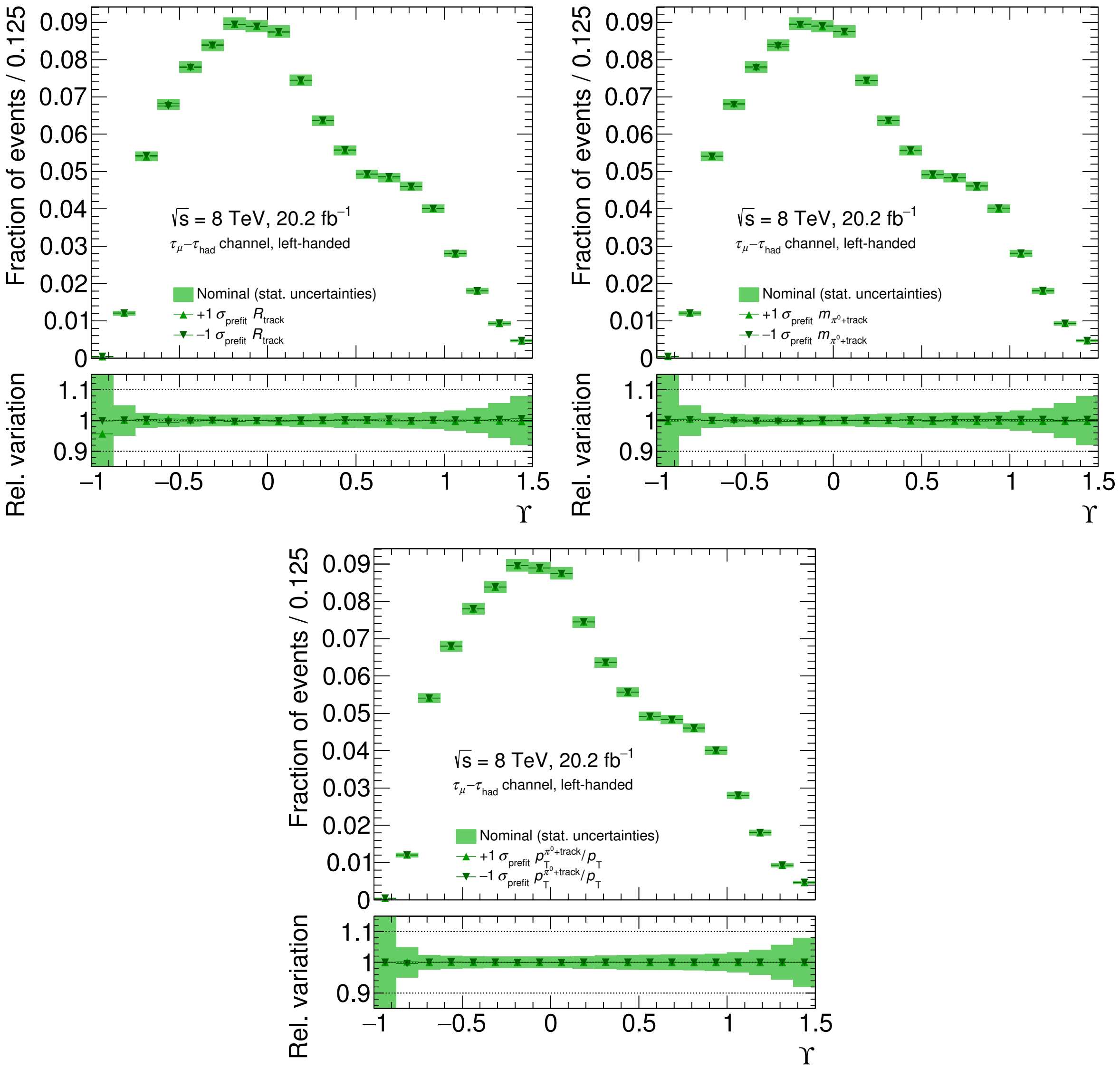

Figure D.7: Impact of the uncertainties in the R_{track} (top left), $m_{\pi^0\text{+track}}$ (top right), and $p_{\text{T}}^{\pi^0\text{+track}}/p_{\text{T}}$ (bottom) variables on the left-handed signal inside the fiducial and signal regions for the τ_{μ}–τ_{had} channel. The impact on the shape of the Υ distribution is shown. The uncertainties from the W+jets control region are used.

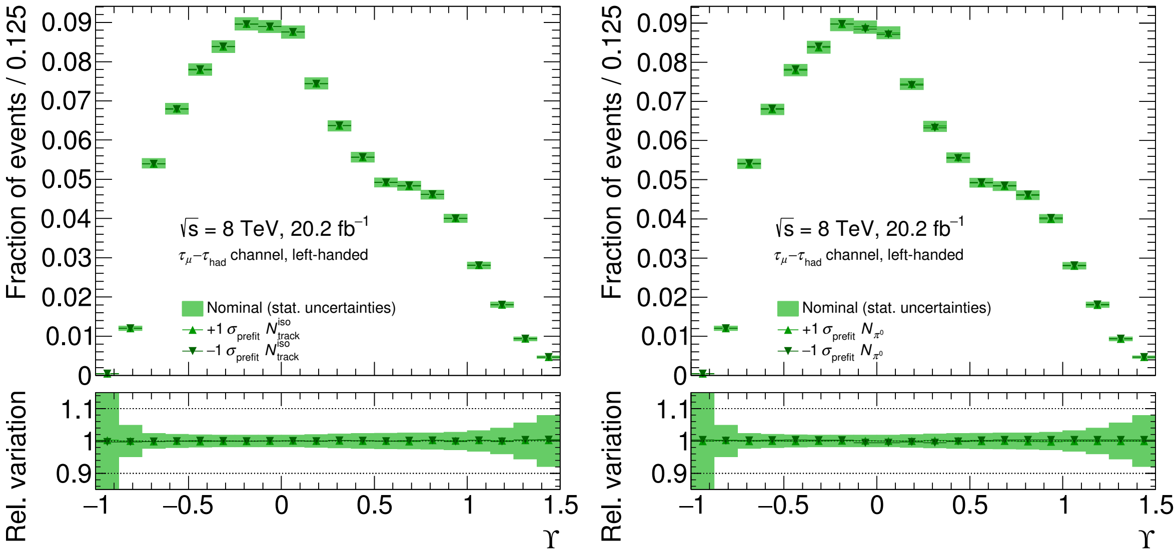

Figure D.8: Impact of the uncertainties in the $N^{\mathrm{iso}}_{\mathrm{track}}$ (left) and N_{π^0} (right) variables on the left-handed signal inside the fiducial and signal regions for the τ_μ–τ_{had} channel. The impact on the shape of the Υ distribution is shown. The uncertainties from the W+jets control region are used.

to the full $Z/\gamma^* \to \tau\tau$ cross-section within the mass-selected or fiducial region to obtain the templates utilised in the fit

$$F^{\mathrm{nominal}}_{\mathrm{left}} = \frac{1}{1-f^{\mathrm{rep}}_{\mathrm{R}}} F^{\mathrm{nominal}}_{\mathrm{left,SR}} \qquad \text{and} \qquad F^{\mathrm{nominal}}_{\mathrm{right}} = \frac{1}{f^{\mathrm{rep}}_{\mathrm{R}}} F^{\mathrm{nominal}}_{\mathrm{right,SR}}.$$

Here, $f^{\mathrm{rep}}_{\mathrm{R}}$ is the fraction of signal events with right-handed taus determined by the TauSpinner algorithm.

A net migration of σ_{LR} from the left-handed to the right-handed subsample leads to the following varied signal contributions in the signal region

$$F'_{\mathrm{left,SR}} = (1-\sigma_{\mathrm{LR}})\, F^{\mathrm{nominal}}_{\mathrm{left,SR}} \qquad \text{and} \qquad F'_{\mathrm{right,SR}} = F^{\mathrm{nominal}}_{\mathrm{right,SR}} + \sigma_{\mathrm{LR}} F^{\mathrm{nominal}}_{\mathrm{left,SR}}.$$

The tau polarisation determined by the TauSpinner algorithm is altered by $2\sigma_{\mathrm{LR}}(1-f^{\mathrm{rep}}_{\mathrm{R}})$ and the altered right-handed fraction is $f^{\mathrm{rep}\prime}_{\mathrm{R}} = f^{\mathrm{rep}}_{\mathrm{R}} + \sigma_{\mathrm{LR}}(1-f^{\mathrm{rep}}_{\mathrm{R}})$. Normalising $F'_{\mathrm{left,SR}}$ to the full $Z/\gamma^* \to \tau\tau$ cross-section using $f^{\mathrm{rep}\prime}_{\mathrm{R}}$ gives

$$F'_{\mathrm{left}} = \frac{1}{1-f^{\mathrm{rep}\prime}_{\mathrm{R}}} F'_{\mathrm{left,SR}} = \frac{1-\sigma_{\mathrm{LR}}}{1-f^{\mathrm{rep}}_{\mathrm{R}} - \sigma_{\mathrm{LR}}\left(1-f^{\mathrm{rep}}_{\mathrm{R}}\right)} F^{\mathrm{nominal}}_{\mathrm{left,SR}} = \frac{1}{1-f^{\mathrm{rep}}_{\mathrm{R}}} F^{\mathrm{nominal}}_{\mathrm{left,SR}} = F^{\mathrm{nominal}}_{\mathrm{left}},$$

so the left-handed template remains unaltered. The normalised, right-handed template is altered as follows

$$\begin{aligned} F'_{\mathrm{right}} = \frac{1}{f^{\mathrm{rep}\prime}_{\mathrm{R}}} F'_{\mathrm{right,SR}} &= \frac{1}{1-f^{\mathrm{rep}}_{\mathrm{R}} - \sigma_{\mathrm{LR}}\left(1-f^{\mathrm{rep}}_{\mathrm{R}}\right)} \left(F^{\mathrm{nominal}}_{\mathrm{right,SR}} + \sigma_{\mathrm{LR}} F^{\mathrm{nominal}}_{\mathrm{left,SR}}\right) \\ &= F^{\mathrm{nominal}}_{\mathrm{right}} + \frac{\sigma_{\mathrm{LR}}\left(1-f^{\mathrm{rep}}_{\mathrm{R}}\right)}{f^{\mathrm{rep}}_{\mathrm{R}} + \sigma_{\mathrm{LR}}\left(1-f^{\mathrm{rep}}_{\mathrm{R}}\right)} \left(F^{\mathrm{nominal}}_{\mathrm{left}} - F^{\mathrm{nominal}}_{\mathrm{right}}\right). \end{aligned}$$

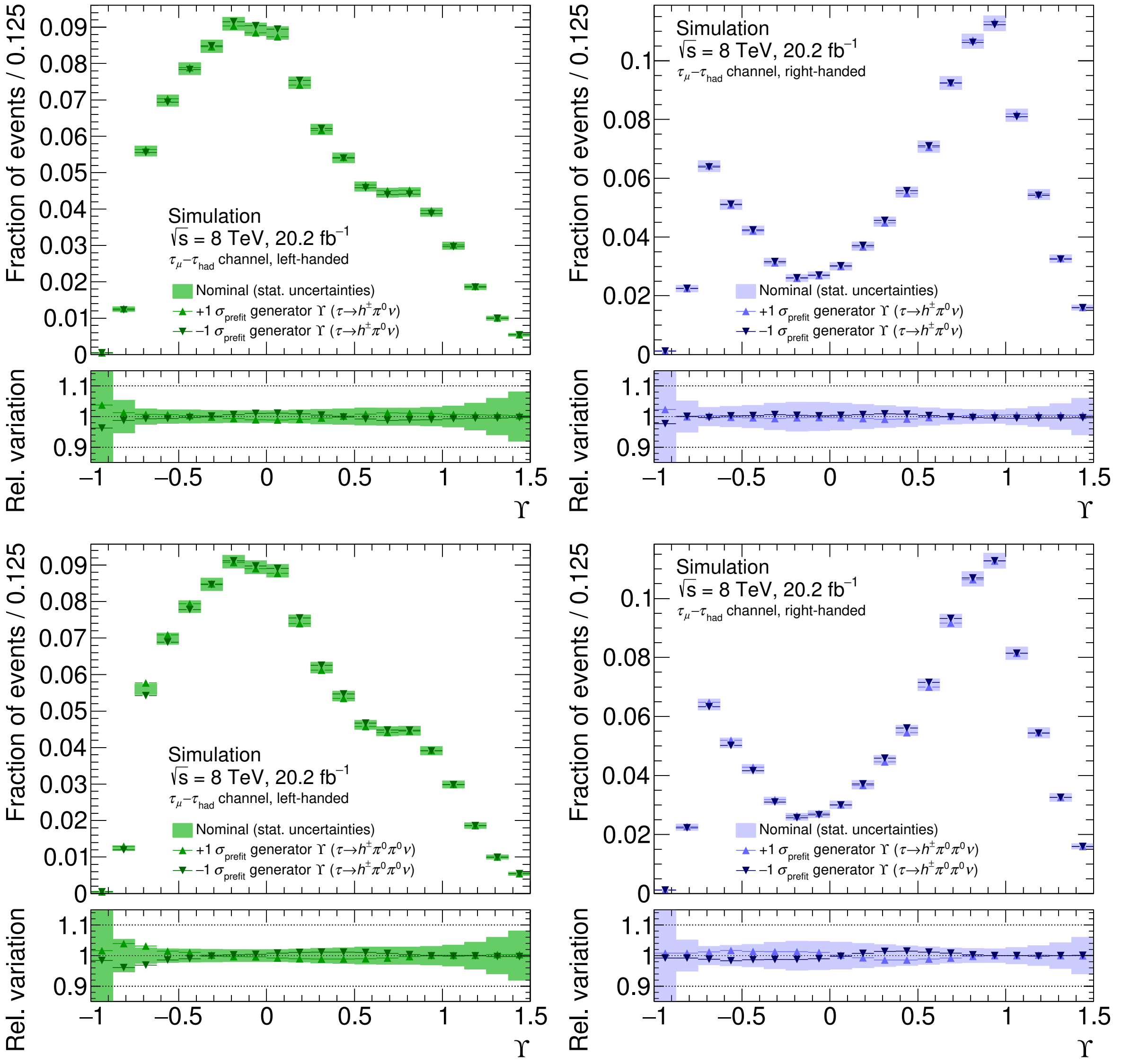

Figure D.9: Impact of the Υ modelling uncertainties in signal events with $\tau \to h^{\pm}\pi^{0}\nu$ (top) and $\tau \to h^{\pm}\pi^{0}\pi^{0}\nu$ (bottom) decays in the signal region for the τ_{μ}–τ_{had} channel. The impact on the shape of the Υ distributions for events inside fiducial the region with left-handed (left) and right-handed (right) taus is shown.

Left-handed	Right-handed	Not fiducial
$^{+4.0}_{-4.0}$ PDF	$^{+4.2}_{-4.2}$ PDF	$^{+3.7}_{-3.7}$ PDF
$^{+1.4}_{-1.2}$ TES (hadronic)	$^{+1.6}_{-1.9}$ TES (hadronic)	$^{+9.1}_{-6.3}$ TES (hadronic)
$^{+0.7}_{-0.6}$ TES (electromagnetic)	$^{+0.5}_{-0.5}$ TES (electromagnetic)	$^{+4.6}_{-3.5}$ TES (electromagnetic)
$^{0.0}_{0.0}$ TER (hadronic)	$^{-0.2}_{+0.2}$ TER (hadronic)	$^{+1.3}_{-1.3}$ TER (hadronic)
$^{+0.1}_{-0.1}$ TER (electromagnetic)	$^{0.0}_{0.0}$ TER (electromagnetic)	$^{+0.4}_{-0.4}$ TER (electromagnetic)
$^{+0.6}_{-0.6}$ generator η	$^{+0.6}_{-0.6}$ generator η	$^{+0.6}_{-0.6}$ generator η
$^{+2.5}_{-2.5}$ tau ID (syst)	$^{+2.5}_{-2.5}$ tau ID (syst)	$^{+2.5}_{-2.5}$ tau ID (syst)
$^{+1.9}_{-1.9}$ luminosity	$^{+1.9}_{-1.9}$ luminosity	$^{+1.9}_{-1.9}$ luminosity
$^{+1.4}_{-1.4}$ tau ID (stat)	$^{+1.4}_{-1.4}$ tau ID (stat)	$^{-2.0}_{+0.8}$ electron scale (3)
$^{+1.0}_{-1.0}$ electron ID	$^{+1.0}_{-1.0}$ electron ID	$^{+0.8}_{-1.9}$ electron scale (1)
$^{+0.9}_{-0.9}$ electron trigger	$^{+0.9}_{-0.9}$ electron trigger	$^{+1.4}_{-1.4}$ tau ID (stat)
$^{+0.8}_{-0.8}$ pile-up	$^{+0.9}_{-0.9}$ pile-up	$^{+1.4}_{-0.6}$ electron resolution
$^{+0.8}_{-0.8}$ electron isolation	$^{+0.8}_{-0.8}$ electron isolation	
$^{+0.3}_{+1.0}$ electron scale (3)		
$^{+0.5}_{-0.3}$ generator p_T		

Table D.1: Relative signal normalisation uncertainties in the signal region for the τ_e–τ_{had} channel for the fit that extracts the tau polarisation in the fiducial region. All numbers are given in %. The upper (lower) number for each uncertainty corresponds to a variation by $+1\sigma$ (-1σ). The uncertainties listed above the line also have shape components for the respective contribution. The absolute normalisation variations for the signal sample splitting uncertainties are smaller than 0.1%.

The value of σ_{LR} can vary within ±0.007 as estimated in Appendix D.3.1. Positive values correspond to the type of migration in which events with kinematic configurations that are more common for events with left-handed taus are classified as right-handed too often. Negative values correspond to the type of migration in which events with kinematic configurations that are more common for events with left-handed taus are classified as right-handed too rarely.

D.3.3 Signal Normalisation Uncertainties in Measurement of Polarisation in Fiducial Region

Left-handed	Right-handed	Not fiducial
$^{+3.3}_{-3.3}$ PDF	$^{+3.4}_{-3.4}$ PDF	$^{+3.2}_{-3.2}$ PDF
$^{+1.7}_{-1.6}$ TES (hadronic)	$^{+1.7}_{-1.8}$ TES (hadronic)	$^{+9.6}_{-7.0}$ TES (hadronic)
$^{+0.9}_{-0.9}$ TES (electromagnetic)	$^{+0.6}_{-0.5}$ TES (electromagnetic)	$^{+4.8}_{-3.4}$ TES (electromagnetic)
$^{+0.1}_{-0.1}$ TER (hadronic)	$^{+0.1}_{-0.1}$ TER (hadronic)	$^{+0.5}_{-0.5}$ TER (hadronic)
$^{-0.1}_{+0.1}$ TER (electromagnetic)	$^{+0.1}_{-0.1}$ TER (electromagnetic)	$^{+0.2}_{-0.2}$ TER (electromagnetic)
$^{-0.2}_{+0.2}$ generator η	$^{-0.4}_{+0.4}$ generator η	$^{-0.3}_{+0.3}$ generator η
$^{+2.5}_{-2.5}$ tau ID (syst)	$^{+2.6}_{-2.6}$ tau ID (syst)	$^{+2.5}_{-2.5}$ tau ID (syst)
$^{+1.9}_{-1.9}$ luminosity	$^{+1.9}_{-1.9}$ luminosity	$^{+1.9}_{-1.9}$ luminosity
$^{+1.8}_{-1.8}$ muon trigger	$^{+1.8}_{-1.8}$ muon trigger	$^{+1.8}_{-1.8}$ muon trigger
$^{+1.5}_{-1.5}$ tau ID (stat)	$^{+1.5}_{-1.5}$ tau ID (stat)	$^{+1.4}_{-1.4}$ tau ID (stat)
$^{+1.1}_{-1.1}$ muon isolation	$^{+1.1}_{-1.1}$ muon isolation	$^{+1.1}_{-1.1}$ muon isolation
$^{+0.7}_{-0.6}$ generator p_{T}	$^{+0.6}_{-0.5}$ generator p_{T}	

Table D.2: Relative signal normalisation uncertainties in the signal region for the τ_μ–τ_{had} channel for the fit that extracts the tau polarisation in the fiducial region. All numbers are given in %. The upper (lower) number for each uncertainty corresponds to a variation by $+1\sigma$ (-1σ). The uncertainties listed above the line also have shape components for the respective contribution. The absolute normalisation variations for the signal sample splitting uncertainties are smaller than 0.1%.

APPENDIX E

Fit Model and Results

Source of uncertainty	σ_{P_τ} in mass-selected region	σ_{P_τ} in fiducial region
Modelling of signal process	±0.026	±0.021
τ_{had} identification	±0.028	±0.032
MC statistical	±0.020	±0.023
Signal sample splitting	±0.014	±0.015
TES and TER	±0.016	±0.018
Multijet estimate	±0.020	±0.020
PDF	±0.007	±0.005
W+jets shape	±0.003	±0.003
Other	±0.006	±0.005
Total systematic uncertainty	±0.051	±0.050
Statistical uncertainty	±0.024	±0.026

Table E.1: Impact of the individual sources of uncertainty on the polarisation uncertainty σ_{P_τ} for the fits that extract the tau polarisation in the mass-selected and fiducial regions for the τ_e–τ_{had} channel. The results stem from fits to Asimov data.

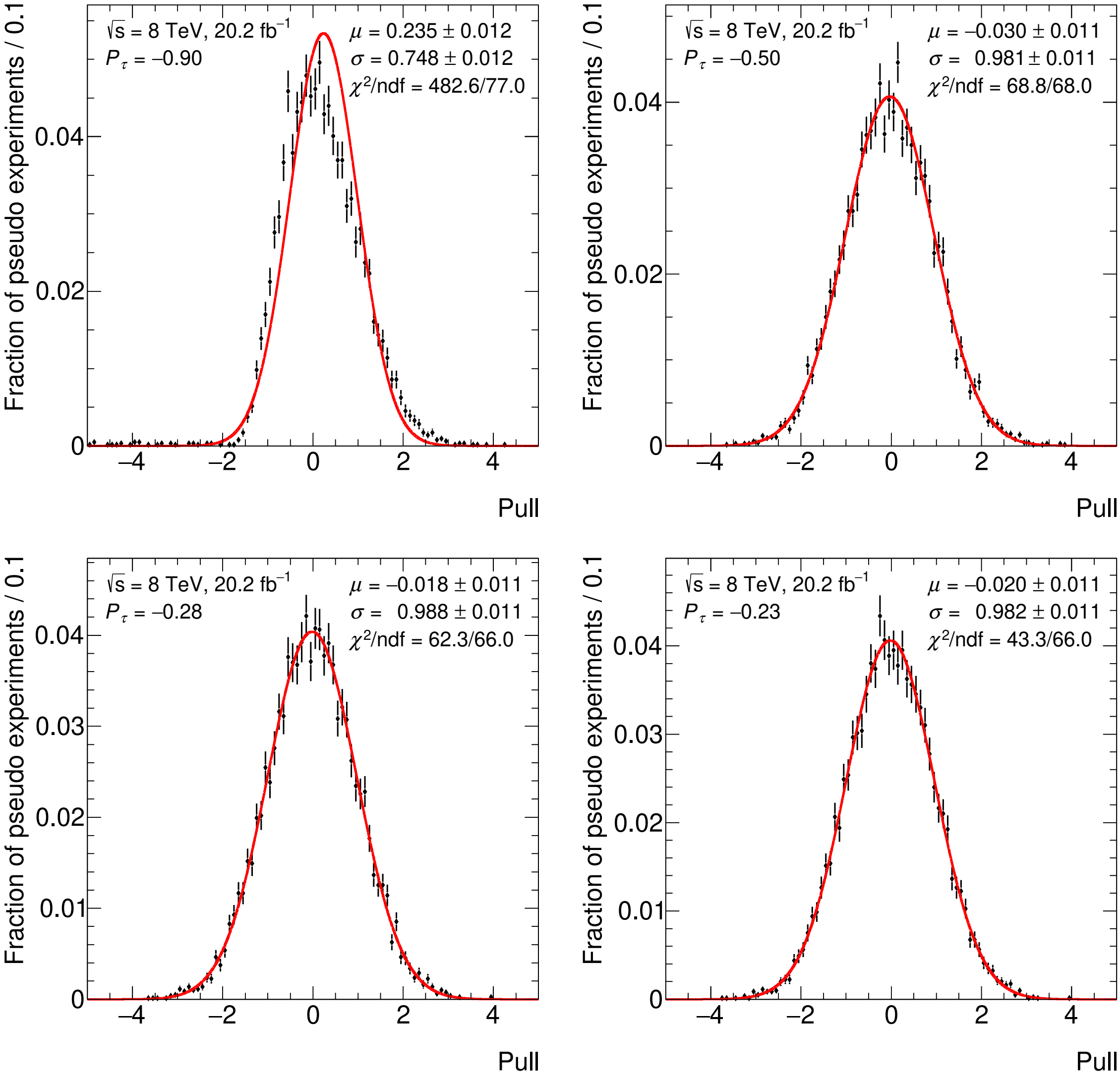

Figure E.1: Pull distributions after 10 000 pseudo experiments each with Monte Carlo generated data for assumed polarisation values of $P_\tau = -0.90$ (top left), $P_\tau = -0.50$ (top right), $P_\tau = -0.28$ (bottom left), and $P_\tau = -0.23$ (bottom right). The mean (μ) and width (σ) parameters obtained in fits of Gaussian functions to the pull distributions as well as the χ^2 and the number of degrees of freedom in the fits are documented.

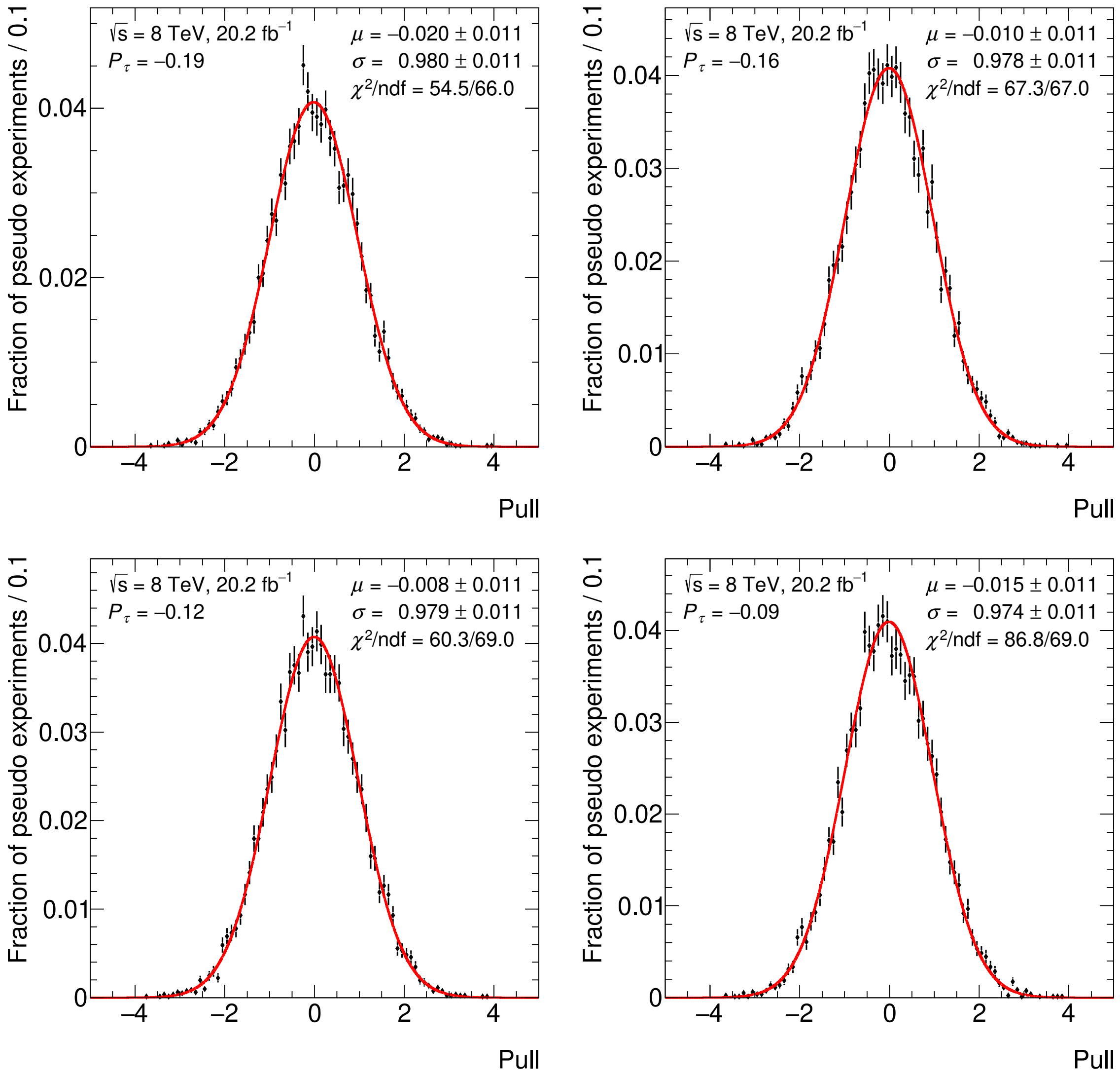

Figure E.2: Pull distributions after 10 000 pseudo experiments each with Monte Carlo generated data for assumed polarisation values of $P_\tau = -0.19$ (top left), $P_\tau = -0.16$ (top right), $P_\tau = -0.12$ (bottom left), and $P_\tau = -0.09$ (bottom right). The mean (μ) and width (σ) parameters obtained in fits of Gaussian functions to the pull distributions as well as the χ^2 and the number of degrees of freedom in the fits are documented.

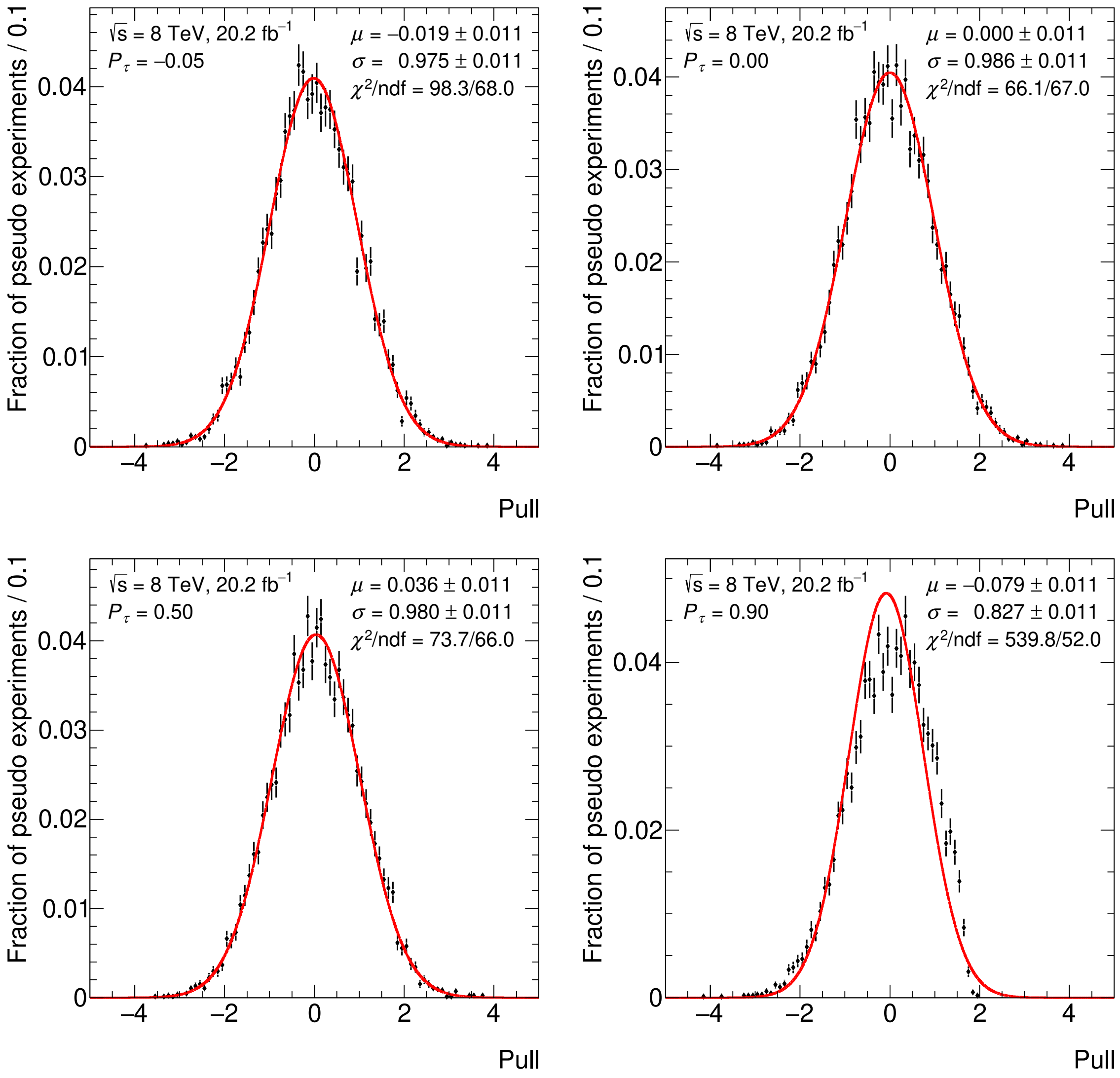

Figure E.3: Pull distributions after 10 000 pseudo experiments each with Monte Carlo generated data for assumed polarisation values of $P_\tau = -0.05$ (top left), $P_\tau = 0.00$ (top right), $P_\tau = 0.50$ (bottom left), and $P_\tau = 0.90$ (bottom right). The mean (μ) and width (σ) parameters obtained in fits of Gaussian functions to the pull distributions as well as the χ^2 and the number of degrees of freedom in the fits are documented.

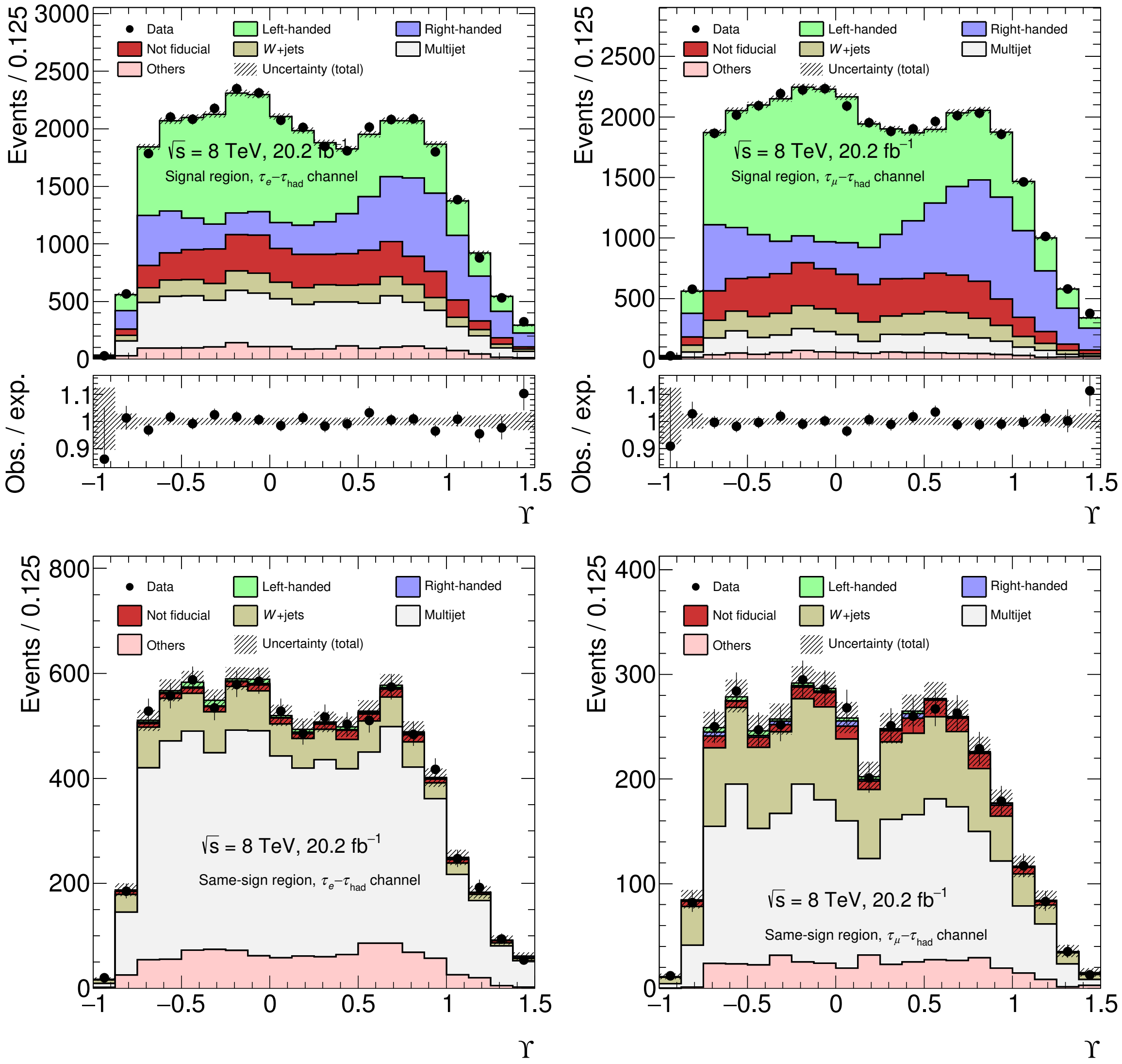

Figure E.4: The ϒ distributions in the τ_e–τ_{had} (left) and τ_μ–τ_{had} (right) channels, and in the signal (top) and same-sign (bottom) regions after the combined fit that extracts the tau polarisation in the fiducial region. Adapted from [25].

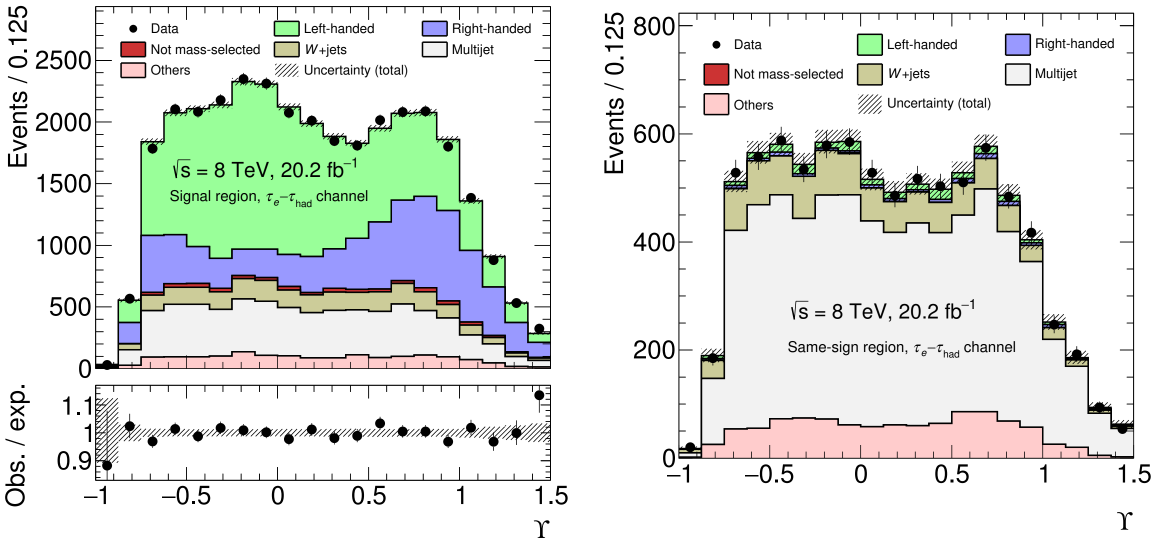

Figure E.5: The Υ distributions in the signal (left) and same-sign (right) regions after the τ_e–τ_{had}-channel-exclusive fit that extracts the tau polarisation in the fiducial region.

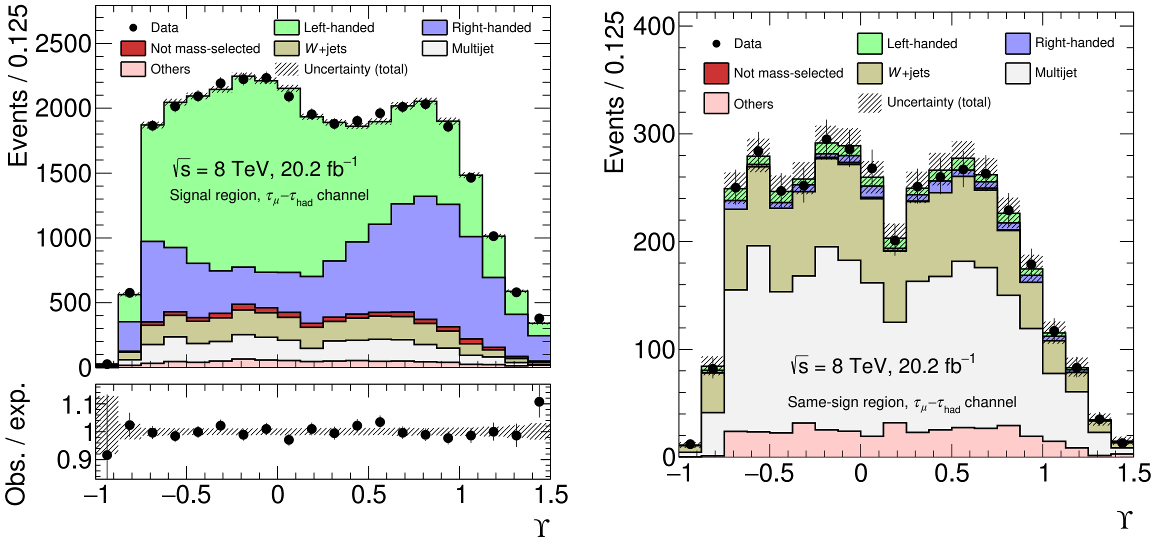

Figure E.6: The Υ distributions in the signal (left) and same-sign (right) regions after the τ_μ–τ_{had}-channel-exclusive fit that extracts the tau polarisation in the fiducial region.

Source of uncertainty	σ_{P_τ} in mass-selected region	σ_{P_τ} in fiducial region
Modelling of signal process	±0.026	±0.021
τ_{had} identification	±0.021	±0.024
MC statistical	±0.019	±0.020
Signal sample splitting	±0.015	±0.015
TES and TER	±0.013	±0.015
Multijet estimate	±0.012	±0.012
PDF	±0.007	±0.005
W+jets shape	±0.003	±0.004
Other	±0.007	±0.001
Total systematic uncertainty	±0.045	±0.045
Statistical uncertainty	±0.020	±0.021

Table E.2: Impact of the individual sources of uncertainty on the polarisation uncertainty σ_{P_τ} for the fits that extract the tau polarisation in the mass-selected and fiducial regions for the τ_μ–τ_{had} channel. The results stem from fits to Asimov data.

Source of uncertainty	σ_{P_τ} in mass-selected region	σ_{P_τ} in fiducial region
Modelling of signal process	±0.027	±0.023
τ_{had} identification	±0.029	±0.034
MC statistical	±0.020	±0.023
Signal sample splitting	±0.014	±0.014
TES and TER	±0.020	±0.024
Multijet estimate	±0.019	±0.020
PDF	±0.007	±0.005
W+jets shape	±0.003	±0.003
Other	±0.008	±0.006
Total systematic uncertainty	±0.050	±0.050
Statistical uncertainty	±0.024	±0.026

Table E.3: Impact of the individual sources of uncertainty on the polarisation uncertainty σ_{P_τ} for the fits that extract the tau polarisation in the mass-selected and fiducial regions for the τ_e–τ_{had} channel. Taken from [25].

Source of uncertainty	σ_{P_τ} in mass-selected region	σ_{P_τ} in fiducial region
Modelling of signal process	±0.027	±0.024
τ_{had} identification	±0.024	±0.027
MC statistical	±0.021	±0.022
Signal sample splitting	±0.015	±0.016
TES and TER	±0.018	±0.022
Multijet estimate	±0.014	±0.014
PDF	±0.007	±0.005
W+jets shape	±0.003	±0.004
Other	±0.007	±0.001
Total systematic uncertainty	±0.050	±0.050
Statistical uncertainty	±0.020	±0.021

Table E.4: Impact of the individual sources of uncertainty on the polarisation uncertainty σ_{P_τ} for the fits that extract the tau polarisation in the mass-selected and fiducial regions for the τ_μ–τ_{had} channel. Taken from [25].

List of Figures

List of Tables

Acknowledgements

It is a pleasure to thank Prof. Jochen Dingfelder for allowing me to be part of his group, for which Jochen is the basis of a highly inspiring, enjoyable, and productive atmosphere. Without his immense and continuous support throughout my master and PhD studies, this thesis would never have been possible. I would also like to thank Jochen for coming up with exciting topics that played to my strengths and taught me a wealth of skills, and for finding ingenious solutions for several problems that had appeared to be persistent.

I am incredibly lucky to have shared almost the entire period with Dr. William Davey, who guided me on a day-to-day basis from the first steps of research and coding to the completion of the projects presented in this thesis. At the beginning, Will provided the perfect balance of plug-and-play solutions and leaving things for me to discover on my own. With time, we enjoyed more and more constructive sessions in which we brainstormed and improved each other's ideas, and time outside the office. Thanks, pal!

Thanks to the members of Jochen's group, I enjoyed almost every day at work. Several of my colleagues have become good friends outside the office as well. For this I would like to thank in particular: Patrick Ahlburg, Mario Arndt, Florian Beisiegel, Florian Bernlochner, Simon Blanke, Clara Callenberg, Michael Daas, Bruno Deschamps, Christopher Deutsch, Stephan Duell, Stephan Ehlers, Alexander Ermakov, Saskia Falke, Valja Gebhardt, Jan Hasenbusch, Verena Muckhoff, Sonja Lambertz, Florian Lütticke, Carlos Marinas, Christian Oswald, Niko Owtscharenko, Botho Paschen, Luis Pesantez, Michael Schnell, Federico Scutti, Emily Thompson, Eckhard von Törne, Christos Vergis, Tan Wang, Christian Wessel, and Liv Wiik–Fuchs. Special credit goes to Stephanie Yuen, with who I enjoyed sharing an office for many years, and collaborating closely on several projects.

The works presented in this thesis are the result of a pleasant, close, and productive collaboration with the group of Prof. Klaus Desch. For this, I would like to thank Klaus, who furthermore agreed to be a referee for this thesis, Philip Bechtle, Christian Limbach, Lara Schildgen, and Peter Wagner in particular.

Prof. Manuel Drees and Prof. Andreas Hense agreed to be members of the PhD committee as well, for which I am very grateful.

For further incredibly valuable and friendly support of this thesis, I would like to thank representatively: Attilio Andreazza, Ludovica Bella, Ulla Blumenschein, Ian C. Brock, Pawel Bruckman de Renstrom, Quentin Buat, Markus Cristinziani, Jane Cummings, Chiara Debenedetti, Sarah Demers, Pier–Olivier DeViveiros, Dirk Duschinger, Luca Fiorini, Martin Flechl, Felix Friedrich, Cristina Galea, Mark Hodgkinson, David Hohn, Michel Janus, Carl Jeske, Anna Kaczmarska, Jana Kraus, Jan Kretzschmar, Jürgen Kroseberg, Stan Lai, Pawel Malecki, Theresa Obermann, Elzbieta Richter–Was, Eram Rizvi, Nils Ruthmann, Kristof Schmieden, Elisabeth Schopf, Matthias Schott, Thomas Schwindt, Federico Sforza, Eric Torrence, Michel Trottier–McDonald, Barbara Valeriani–Kaminski, Zbigniew Was, Norbert Wermes, Peter Wienemann, Marcin Wolter, and Stefania Xella.

After my PhD studies, the group of Prof. Karl Jakobs, Christian Weiser, and Karsten Köneke has offered a warm welcome entrusting me with fascinating projects that bear new challenges. I am highly grateful for this and, in the context of this thesis, for having been offered time to finalise it. I am very much looking forward to the years ahead in Freiburg.

My family and friends I thank for all the amazing times we have shared, and for their whole-hearted and dependable support.

Finally, I acknowledge the Rheinische Friedrich–Wilhelms–University of Bonn, the Bonn–Cologne Graduate School of Physics and Astronomy, and the Federal Ministry for Education and Research of the Federal Republic of Germany for their generous support of this thesis.